Cellular Summer Camp: How Young Neurons Learn to Communicate and Interact With Their Environments

A Dissertation

Presented in Partial Fulfillment of the Requirements for the

Degree of Doctor of Philosophy

with a major in

Microbiology, Molecular Biology, & Biochemistry

in the

College of Graduate Studies

University of Idaho

by

Joshua Muller Sukeena

Major Professor: Peter G. Fuerst, Ph.D.

Committee Members: Deborah Stenkamp, Ph.D., Allan Caplan, Ph.D., Barrie Robison, Ph.D.

Department Administrator: James Nagler, Ph.D.

May 2017

Authorization to Submit Dissertation

This dissertation of Joshua Sukeena, submitted for the degree of Doctorate with a major in Microbiology, Molecular Biology and Biochemistry and titled, "Cellular Summer Camp: How Young Neurons Learn to Communicate and Interact With Their Environments" has been reviewed in final form. Permission, as indicated by the signatures and dates given below, is now granted to submit final copies to the College of Graduate Studies for approval.

Major Professor: _____ Date: _____

Peter Fuerst, Ph.D.

Committee Members: _____ Date: _____

Deborah Stenkamp, Ph.D.

_____ Date: _____

Barrie Robison, Ph.D.

_____ Date: _____

Allan Caplan, Ph.D.

Department Administrator:

_____ Date: _____

James Nagler, Ph.D.

Abstract

The primary sense of humans is vision, and the visual system begins in the retina. The retina is the major light-sensing tissue of the central nervous system that responds to light in the environment and aids in its conversion into visual information. The retina is composed almost entirely of neurons, and is part of the central nervous system proper. It is a major focus of biomedical research due to the debilitating eye diseases that are associated with it. Its complex circuitry and wiring are ideal for understanding cellular mechanisms of neural development. The work in this dissertation presents multiple novel cellular interactions in the developing nervous system and promotes a possible system for understanding the role that evolution has played in the highly complex teleost retina.

The first chapter gives a brief overview of retina development and why it is a great model system to use in basic science. The second chapter is a review of bipolar cells across species. Here we will review basic development and organization of bipolar cells, followed by physiology and how bipolar cells communicate with cells in the retina. We will also summarize the common model systems used in research today including rodents, teleost fish, and primates. We also use figures to give a thorough and in depth review of their vertical organization and summarize their current classification system.

The third chapter presents a possible compensatory mechanism to preserve cone predictive field in the developing mouse retina following the failure of Bax-mediated programmed cell death. We present a possible feedback mechanism between cones and bipolar cells to ensure tiling organization despite an increase in cellular density. The fourth chapter presents additional roles for an important regulator of neurite targeting, Down syndrome cell adhesion molecular (Dscam). Loss of function assays reveal its role in neurite refinement in the developing mouse retina. We find it necessary for proper refinement and subsequent lamination of type 2 dopaminergic amacrine cells in the inner retina. Gain of function assays with DSCAM also reveal it is not sufficient to drive cell death, increase spatial organization, prevent cell-to-cell pairing, or promote active avoidance in the retina.

The fifth chapter characterizes the expression of *dscam* and *sdk* paralogs in the zebrafish (*Danio rerio*) retina for their potential role in its highly ordered cellular organization. Adding to that, the full cDNA sequences for *dscama* and *dscamb* in the zebrafish retina have been cloned for use in cellular interaction assays. Furthermore, the sixth chapter of this work

identifies a potential new model system, the spotted gar (*Lepisosteus oculatus*), for research regarding the evolution of the visual system.

Acknowledgements

I would like to acknowledge my major advisor, Dr. Peter Fuerst. You took a chance on me when I had a dream of becoming a scientist, and I had no clue what I was doing. I still probably don't know what I'm doing, but your guidance has helped me develop into an actual scientist. Your dedication to the craft of training young scientists is admirable, and I am so thankful that I made the decision to come and work with you. Your ability to think outside the box, and approach problems from a new perspective were invaluable to my projects. Your dedication to my training despite my mistakes and struggles are the reason I can call myself a scientist. Your understanding and support during the times that required me to focus all of my attention on my family are things I'll never be able to properly thank you for. Thank you for the guidance and for the training you provided me.

I would also like to acknowledge my Ph.D. committee members, Dr. Deborah Stenkamp, Dr. Barrie Robison, and Dr. Allan Caplan. You were all an invaluable part of my training, and I can't thank you enough for the support and guidance on my projects and research training. I am so thankful to have you all as mentors.

I'd also like to acknowledge the members of the Fuerst Lab, who provided constant support and friendship during my training. Aaron Simmons, you have been an incredible friend through everything, and I'll truly miss our daily interactions. Carlos, you deserve a part of my doctorate. You are an outstanding scientist, and an even better friend. Shuai Li, your positivity was contagious each and every day in the lab, and I want to thank you for your dedication to helping me learn and grow early on. Sam Bloomsburg, thank you for your critical input on both my research projects and my political opinions. I'd also like to thank the other lab members who I had the pleasure of working with over the last four years including Ethan Hansen, Jake Wilson, Donson Cook-Gallardo, Morgan Merrill, CJ Miller, Sam Billingslea, Ryan Rounds, Jamie Doyle, Eric Cliff, Lance Fredericks, Alex Williams, and the many others who were a part of our lab. You all made contributions to my work and my life, and for that I am grateful. I'd also like to acknowledge Gina Tingley and Kristi Accola for the good conversations and always ensuring that my path to graduation was as smooth as possible.

Dedication

This work is dedicated to my wife, Abbey. Without you, I would have never been able to get through the roller coaster that is graduate school. Your support and love has always been the one constant thing I could count on each and every day. You have been my rock and my best friend through everything, and I will never be able to thank you enough.

I'd also like to dedicate this to my beautiful daughter Savanna whose entrance into this world would be a test of epic proportions to anyone, let alone someone finishing a doctorate. Thank you for teaching me that no matter how much stress and anxiety I have about my research, there is no greater joy in this world than laughing with my child.

Lastly, I'd like to dedicate this to my parents, Curt and Vicki. You guys literally taught me how to be a person, and I'll always be grateful for your support and guidance. Thank you for always picking up the phone when I need to talk out my anxiety, and also for just being there.

Table of Contents

List of Figures

List of Tables

Chapter 1: Introduction

Neuronal communication in the central nervous system (CNS) requires cells to establish and maintain extremely specific signaling pathways. The complexity of these neural pathways can be seen in the retina, the light sensing tissue of the CNS that is located at the back of the eye. The retina is responsible for converting light stimuli from the environment into a signal that can be interpreted by the brain. The retina is dually beneficial in biomedical research. First, with vision being the primary sense in humans, understanding the retina is critical for the treatment of diseases that result in vision loss. Secondly, the retina is a great scientific model system as it is made up almost entirely of neurons, it has distinct and conserved structure that consists of three nuclear layers and two synaptic layers, and it is part of the central nervous system. The light sensing tissue is an ideal system for researchers from many different fields including clinical medicine, pharmacology, neuroscience, developmental biology, and physiology.

The retina is a system within the CNS where cellular interactions and synaptogenesis can be focused on and directly observed by researchers. One way in which cells can interact with their neighbors is through cell adhesion molecules (CAMs). CAMs are transmembrane proteins with extracellular domains that allow for communication via protein-protein interactions between cells. Understanding the roles that CAMs play in retinal development is growing. One of the many families of CAMs is the immunoglobulin superfamily (IgSF). The IgSF includes a critical protein involved in neural development, the Down syndrome cell adhesion molecule (DSCAM). Dscam is named such due to its location in the Down syndrome critical region of chromosome 21, and has previously been shown to play roles in neuron spacing, neurite avoidance, and programmed cell death (PCD). In this dissertation, we show that DSCAM plays an important role in neurite refinement during early development of the inner plexiform layer (IPL). It provides organization through repulsion. Due to the role that DSCAM plays in PCD, we also looked at the role of cell death protein, BAX, in IPL lamination. In the OPL, we observed that the loss of BAX-mediated PCD resulted in changes to the cone terminals and the wiring of type 4 OFF BCs through an increase in the number of multiply-innervated cones.

In the last two decades, DSCAM has become a well understood protein in the mouse as well as chick and drosophila. In addition to working with DSCAM, another member of the IgSF, Sidekick (SDK), has been shown to play a role in proper laminar targeting of ACs and

RGCs in the IPL. However, little work has been done to look at the expression and/or functions of these proteins in zebrafish or any other teleost fish. CAM proteins become particularly interesting in the zebrafish due to them being involved in a large scale genomic rearrangement that occurred approximately 300 million years ago called the teleost genome duplication (TGD). This resulted in a major increase of genetic material for the lineages involved, and an explosion of diversity followed for teleost fish. The visual system of the zebrafish and other teleost lineages have features consistent with increased complexity compared to mammals, such as an increased number of cellular organization and cell types as well as a regenerative ability to an extent that is not seen in mammals. Therefore, it is an enticing research question as to whether this increase in genetic material facilitated expansion of complexity within these lineages. Working with *dscam* and other CAMS in the IgSF allow us to focus our observations on specific aspects of neuronal development such as cellular interactions and synaptic organization during neural development.

When a gene is duplicated, there are three possible outcomes: Pseudogenization, subfunctionalization, and neofunctionalization. Pseudogenization is a loss of one daughter copy through functional redundancy. Subfunctionalization is the daughter genes adopting part of the parent gene function, and/or differential tissue expression. Neofunctionalization is the development of wholly new functions by one of the duplicated genes. Using basal model systems for compare gene function(s) with teleost fish, we can observe evolution in action by determining potential outcome possibilities for genes involved in development. As the teleost retina is assumed to be a complex system, a baseline for comparison is required. In this work, we propose the spotted gar as a possible model for this type of research as it contains a single genome, and diverged in lineage prior to the TGD. Characterization of the spotted gar's retina provides researchers with a baseline for comparison to the more complex organization that has been observed in the teleost fish lineage. It has a genome that is similar to mammalian genome, as it contains a single genome but has spent the last 300 million years in an environment more similar to teleost fish. This work highlights some specific examples of this in action including expression patterns of predicted opsin genes, displaced neuron cell populations, and organization of photoreceptors and other cells in the retina.

The work in this dissertation approaches neural development using multiple model organisms to ask questions regarding cellular communication and organization. Neurological disorders continue to be major challenges in modern medicine and in order to address these

issues, it will be important to have a solid understanding of how the CNS is organized and how the organization evolved.

Chapter 2: Retinal Bipolar Cells Form and Function Across Model Species

Joshua M. Sukeena[1] and Peter G. Fuerst[1, 2]

1 University of Idaho, Department of Biological Sciences, Moscow, Idaho 83844, USA, 2 University of Washington School of Medicine, WWAMI Medical Education Program, Moscow, Idaho 83844, USA.

Abstract

Objective: The purpose of this review is to assist researchers interested in learning the basics of bipolar cell biology and covers the form and function of retinal bipolar cell types in several well characterized model organisms.

Background: Bipolar cells are the sole excitatory connection between photoreceptors and retinal ganglion cells (RGCs), thereby connecting the outer and inner retina. Because of their central role in information flow, and because common blinding diseases destroy photoreceptors or retinal ganglion cells, understanding and restoring bipolar cell-mediated information flow between RGCs and photoreceptors will be essential to cell therapy approaches to restoring lost vision.

Results: The development, organization and physiology of the ON and OFF pathway was reviewed in text and figure depiction. The role of bipolar cells and their inhibitory inputs or targets in generating center surround and direction selectivity is reviewed. Finally, we detail the classification of BCs in the model systems of mouse, zebrafish, goldfish, and primate.

Conclusion: This review will serve to introduce or remediate students and researchers interested in bipolar cell biology. Bipolar cells' role in conveying information between photoreceptors and ganglion cells marks them as an important neuron population for studies into regeneration of the retina. Their increasingly well characterized physiology makes them

an excellent model cell type to study basic principles of neuroscience. Finally, the classification of bipolar cell types is nearing completion in several model species, making this cell population an excellent target of connectomic studies.

Introduction

Retinal Bipolar cells mediate communication between photoreceptors and retinal ganglion cells (RGCs). Because common blinding diseases such as glaucoma, diabetic retinopathy and macular degeneration are caused by damage to photoreceptors and retinal ganglion cells (RGC), restoring bipolar cell-mediated information flow between RGCs and photoreceptors will be essential to cell therapy and other approaches to restoring lost vision. Herein we review the form and function of BC types in the retina of several well-characterized model organisms.

The retina is composed of three nuclear layers and two synaptic layers (Figure 1). The outer nuclear layer (ONL), proximal to the eye socket, contains the cell bodies of cone and rod photoreceptors, the primary light detecting cells of the retina. The inner nuclear layer (INL) contains the soma of amacrine cells (AC), horizontal cells (HC) Müller glia (MG) and BCs. HCs and ACs are mostly inhibitory inner neurons, while Müller glia provide structural and metabolic support to retina neurons. The innermost nuclear layer, closest to the interior of the eye, the retinal ganglion cell layer (RGL), contains retinal ganglion cells (RGC), ACs and astrocytes. The RGCs axons, which form the optic nerve, carry information from the retina to the vision processing areas of the brain. The two synaptic layers of the retina are the outer plexiform layer (OPL) and the inner plexiform layer (IPL). The OPL is located between the ONL and INL and contains the synapses between photoreceptors, BCs, and HCs. The IPL is located between the RGL and INL and contains the synapses between BCs, ACs, and RGCs (Figure 1). The IPL is notable in that it is spatially divided into two halves that contain circuitry devoted to light increment (ON) and light decrement (OFF).

Organization and Development

BC development is different in several regards compared to other retinal neurons. Following nuclear migration, the BC establishes contacts in the OPL with photoreceptors and in the IPL with ACs and RGCs (Figure 2A). Unlike retinal neurons such as amacrine cells, which migrate to their final location, BCs initially span the retina and resemble neuroepithelial cells (Morgan et al., 2006). BCs then retract their apical and basal processes and stabilize at the level at which their axons and dendrites arborize (Figure 2A), a process that has been shown to be regulated in the IPL by differential expression of cadherin molecules for at least two types of BC (Duan et al., 2014).

During development, BCs organize across both the horizontal (i.e., perpendicular to a line drawn from the RGL to ONL) and vertical planes of the retina (i.e., parallel to a line drawn from the RGL to the ONL). Spacing of BC soma and organization of their axons and dendrites differs from most other retinal neurons. Most non-BC retinal neurons have an organized distribution of their soma such that their soma are spaced to increase the distance with respect to other cells of the same subtype compared to a random distribution, but have dendritic arbors that overlap extensively (Figure 2B) (Keeley & Reese, 2010; Lefebvre et al., 2012). BCs on the other hand, do not space their somas, which are often located directly abutting other BCs of the same type, but have tiled dendritic and axonal arbors, in which the dendritic and axonal arbors do not overlap (Figure 2C) (Wässle et al., 2009; Lee et al., 2011; Keeley et al., 2017). Tiling occurs between the axonal and dendritic arbors of BCs of the same type, and the mechanism behind their organization is based on both cellular and molecular cues (Fuerst et al., 2009; Lee et al., 2011; Dunn & Wong, 2012; de Andrade et al., 2014; Keeley et al., 2014).

Bipolar Cell Synaptic Anatomy in the OPL

Synaptic input to BCs originates at cone and rod photoreceptors. BCs in mammalian species are categorized as either cone bipolar cells (CBCs) or rod bipolar cells (RBCs), depending on the nature of their upstream synaptic contacts. BCs in the vertebrate retina are also categorized into ON or OFF CBC categories, depending on their IPL lamination patterns.

The physiological basis of the OFF and ON pathways originates in the synapses between photoreceptors and bipolar cells. Photoreceptors tonically release glutamate when unstimulated, activating OFF BCs and the OFF pathway (Figure 3A). This will result in OFF BC depolarization and the subsequent release of glutamate from the OFF BC axon. Light increment results in hyperpolarization of photoreceptors, which cease to release glutamate, thereby inactivating the OFF channel and activating the ON pathway (Figure 3B). Glutamate acts as an inhibitory neurotransmitter at the ON BC synapse by binding to mGluR6, which results in inactivation of the TRPM1 channel, resulting in hyperpolarization of the cell (Bellone et al., 2008; Koike et al., 2010; Morgans et al., 2009). It should be noted that some ON BCs make a number of OFF contacts as they pass through the IPL (Hoshi et al., 2009; Dumitrescu et al., 2012).

CBCs receive their dominant input from contacts with cone photoreceptors, while RBCs receive their dominant input from contacts with rods. Cones form synapses with BCs at the cone axon terminal, the cone pedicle (Figure 4A). The cone pedicle contains multiple synaptic hubs at which BCs make invaginating contacts along with paired HC dendrite tips, terminating at cone ribbon synapses (Figure 4A-B). In some lineages, such as mammals, only ON BCs make invaginating contacts, and OFF cells make flat contacts at the base of the invagination, while in others, such as teleost fish species, both ON and OFF cells make

invaginating contacts (Sakai & Naka, 1983; Saito et al., 1985). Some OFF CBCs in mammals, including mouse and primates, also make direct flat contacts at rod terminals, the significance of which are still being elucidated (Soucy et al., 1998; Martaruga et al. 2007; Haverkamp et al., 2008; Tsukamoto & Omi, 2014). RBC dendritic tips and horizontal cell axon tips synapse at invaginated pits in the rod axon terminal, the rod spherule (Kolb, 1970) (Figure 4C-D).

Bipolar Cell Synaptic Pathways

BCs send glutamatergic signal to RGCs and ACs through 4 different pathways. The first pathway involves chemical synapse coupling of cones to ON and OFF BCs (Figure 5A). ON and OFF BCs transmit visual stimuli at chemical synapse connections with RGCs in the IPL (Figure 5A). The second pathway, the direct rod pathway, found in the mammalian retina, involves propagation of signal from rods to RGCs through RBCs (Figure 5B). RBCs, an ON BC type, are unusual in that they don't make direct chemical synapses with RGCs, but rather signal through AII ACs. AII ACs are abundant in mammalian retinas, and make connections with OFF CBCs, ON CBCs, and OFF RGCs. Signal from AII ACs is conveyed to ON BPCs via gap junctions, and then from ON BCs to the RGCs through chemical synapses in the IPL (Figure 5B) (Kolb & Famigletti, 1974; Famigletti & Kolb, 1975; Sterling, 1983; Strettoi et al., 1992; Seeliger et al., 2011; Ke et al., 2014). The A17 AC is also involved in the rod pathway in the mammalian retina. It plays an important role in the modulation of RBC signal to AII ACs and CBCs through reciprocal chemical synapses (Pourcho & Goebel, 1983; Hartveit, 1999; Dong & Hare, 2003; Grimes et al., 2009; Grimes et al., 2010). The mammalian retina also utilizes two alternate pathways in order to propagate rod photoreceptor signal through the retina (Figure 5C-D). The first of these (Figure 5C) is the alternative rod pathway, in which cones and rod termini are connected through gap junctions, thereby connecting rods to cones to CBCs (Yang & Wu, 1989; Sharpe & Stockman, 1999;

Bloomfield & Dacheux, 2001; Deans et al., 2002; Ribelayga et al., 2008). This allows signal from the rods in scotopic conditions to be sent to a neighboring cone to then be propagated to OFF and ON CBCs. The last rod pathway has recently been discovered. It has been observed that the rod photoreceptors make direct contacts with certain OFF BCs (type 3a, 3b, and 4 in mouse, type DB3b in primate) (Figure 5D) (Soucy et al., 1998; Hack et al., 1999; Tsukamoto et al., 2001; Mataruga et al., 2007; Strettoi et al., 2010; Pang et al., 2010).

BC Inhibitory Connectivity

BC pathways are influenced by GABAergic and glycinergic synapses with ACs in the IPL (Yang & Wu, 1991; Lukasiewicz& Werblin, 1994; Pan & Lipton, 1995; Dong & Werblin, 1998; Euler & Masland, 2000; Marc & Liu, 2000; Molnar & Werblin, 2007; Chavez & Diamond, 2008; Molnar et al., 2009; Chavez et al., 2010). Various models explaining HC inhibition of BCs in the OPL have also been proposed, including GABAergic signaling, ephaptic interactions, and pH changes in the synaptic cleft (Kamermans et al., 2001; Hirasawa & Kaneko, 2003; Kamermans & Fahrenfort, 2004; Hirasawa et al., 2012). These inhibitory connections contribute to the shaping of visual response through lateral inhibition, a process by which cells adjacent to those that are stimulated are inhibited. HC mediated inhibition of BCs alters signal as it passes through the retina and is thought to underlie several features of visual encoding such as center surround (Figure 6A-B). Lateral inhibition is thought to act in a similar fashion in the IPL (Werblin, 1972; Barnes & Werblin, 1997; Cook & McReynolds, 1998, Jacobs & Werblin, 1998; Taylor, 1999; Bloomfield & Xin, 2000; Franke & Baden, 2017).

BCs and Direction Selectivity

Within the retina, specific cell circuits are able to process visual information based on the direction of the stimuli. For example, ON-OFF direction-selective ganglion cells (DSGC)

respond differently based on the direction of motion from stimuli, with a stronger response being elicited by movement in a preferred direction (Figure 6C) (Barlow and Levick, 1965; Briggman et al., 2011; Vaney, 2012). There is growing evidence that signaling from BCs to DSGCs is the origin of DS signal. Recent findings show that glutamate signaling in the IPL likely does not lead to DS in the DSGC (Park et al., 2014), but rather through activity of starburst amacrine cells (SACs) (Ding et al., 2016, Greene et al., 2016; Kim et al., 2014). SACs receive BC input that is spatiotemporal segregated with respect to the SAC proximal and distal dendrites (Fransen & Borghuis, 2017). More specifically, contacts from distinct BCs proximal and distal to the SAC cell body resulted in differences in sustained (proximal) and transient (distal) signaling. This results in differences in excitatory responses for SACs, and subsequent changes to DS signaling to the DSGC (Figure 6D).

Overview of Bipolar Cells in Model Organisms

The identification and classification of BCs is reaching completion in several model organisms, described below. The classification of ON and OFF pathways remains consistent from species to species, however many differences in the types of BCs are noted across species. Here we review classification of BCs in several popular model systems.

Bipolar Cells of the Rodent Retina

The mouse retina is rod dominant, containing ~98% rods and ~2% cone photoreceptors (Carter-Dawson & La Vail, 1979). It possesses three types of cone photoreceptors: blue & green opsin cones (traditionally considered blue cones), green opsin cones, and blue opsin cones (blue cones that produce no green opsin), which are often referred to as “true blue” cones (Haverkamp et al., 2005). The densities of these cone types are highly variable across the retina. In the dorsal retina, green opsin cones are predominant (~95%) and intermixed with a small number of true blue cones. In the ventral retina,

blue/green opsin cones are predominant (Szel et al., 1992; Haverkamp et al., 2005), again with true blue cones composing about 5% of the cones. It is thought, with some exceptions mentioned below, that each cone is typically sampled by at least one of each type of mouse CBC (Wässle et al., 2009).

Current tallies of mouse BCs include at least 9 types of cone BC and 1 rod BC (Ghosh et al., 2004; Wässle et al., 2009). The OFF BC types are types 1, 2, 3a, 3b, and 4. Type 1 are notable in that they do not appear to contact true blue cones, and are therefore “green OFF” cells (Li and DeVries, 2006; Breuninger et al., 2011). Types 3a, 3b and 4 are notable in that they make flat contacts at both rods and cones (Mataruga et al., 2007; Haverkamp et al., 2008). An interplexiform cell that appears to developmentally resemble a bipolar cell, and yet lacking dendrites, has recently been discovered, the GluMI cell (Della Santina et al., 2016; Baden & Euler, 2016), although its ultimate cellular classification remains uncertain at this point.

Five classes of ON CBCs have been described including the type 5 BC, since reclassified into up to 4 types and types 6, 7, 8 and 9 (Ghosh et al., 2004; Wässle et al., 2009) (Figure 7). The four categories of type 5 BCs reported by Shekhar and colleagues appear to match the 5T, 5O, 5I and BCX cells reported by Behrens and colleagues (Shekhar et al., 2016; Behrens et al., 2016). The BC5d/BCX cell observed by these groups is remarkable in that its axon terminates in the ON strata of the IPL, and yet the BC makes flat contacts similar to the OFF type bipolar cells (Euler et al., 2014). Type 9 ON cells are notable in that they are the mouse “blue ON” BC and only contact true blue cones. Blue OFF only or green ON only BCs have not been reported in the mouse retina to date.

BCs in the rat retina were well described by Euler & Wässle (1995) with 10 total types including RBPCs and are very similar to what is known about the organization of the mouse retina.

A notable and useful addition to rodent models for vision research is the ground squirrel. The ground squirrel possesses a cone-dominant retina, and has therefore emerged as a valuable model system in retinal research. Thirteen types of BC have been described in ground squirrels. These include six types of BCs laminating in the OFF region of the IPL: 1a, 1b, 2, 3a, and 3b, and X. The seven types of ON BCs are 5a, 5b, 6a, 6b, 7a, 7b, and blue cone (BB). A rod bipolar cell type has also been characterized (West, 1976; Cuenca et al. 2002; Puller et al. 2011).

Bipolar Cells of the Teleost Retina

BCs have been extensively studied in several species of fish including zebrafish and goldfish. A combination of morphology and IPL lamination patterns were used to characterize BCs. The results identified six types of ON BCs, seven OFF BCs, and 4 OFF/ON BCs for a total of 17 types (Connaughton et al., 2004).

Further work by Connaughton et al. (2004) group examined receptor expression and physiological response and found these matched with their morphology results. More recently, BCs in the zebrafish retina were classified based on their connectivity with photoreceptors and their IPL lamination. Here, twenty-one BCs were characterized by a combination of OFF and ON IPL lamination and nine categories of photoreceptor connections (Li & Dowling, 2013). Cells were first given a distinction based on which IPL sublaminae(s) they terminate in and whether they were mono-stratified to triple-stratified. The authors then paired this information with nine possible combinations of green cones (G), red cones (R), blue cones (B), ultraviolet cones (UV), and rhodopsin-positive photoreceptors

(rod): G, RGB, GBUV, RG, RGBUV, RGBrod, RGBUVrod, RGrod, and Rrod and combined these classifications to propose 21 types of BC in the zebrafish retina (Figure 8A).

Early researchers made important observations to begin the characterization and identification of BCs in the goldfish retina (Kaneko, 1970; Kaneko, 1973; Ishida et al., 1980; Suzuki & Kaneko, 1990; Marc et al., 1990). The goldfish retina was most recently characterized by Sherry & Yazulla (1993) with 15 total BC types in two categories described: Cone BPCs and Mixed BPCs. Cone BPCs contain 9 types in 4 groups: C1, C1a-W, C2a, C2b, C2ab, C3a, C3b, C3ab, and C4ab. Mixed BPCs constitute 6 types of cells: Ma, Ma-L, Mb1, Mb2, Mb3, and MbL (Figure 8B).

An interesting difference comparing fish BCs to mammalian BCs is that fish OFF BCs make invaginating contacts, versus the flat contacts that OFF BCs make in mammalian species. Work characterizing BC organization in basal fish species has identified populations of displaced BCs localized in the ONL and the functional difference, if any, between these and other BCs is currently unknown (Ali & Anctil, 1976; Sukeena et al., 2016).

Bipolar Cells of the Primate Retina

10 types of CBCs have been described in the primate retina, including diffuse and midget types of BCs (Figure 9) (Boycott & Wässle, 1991). The diffuse category refers to BCs that make contacts with all cones in their “dendritic field” with no preference for specific opsin types. Diffuse BCs vary slightly in their connectivity with cones and densities throughout the retina. There are six types of diffuse bipolar cells (DB): DB1, DB2, DB3, DB4, DB5, and DB6. Recently, DB3 BCs were split as DB3a and DB3b due to their stratification pattern, and can be distinguished by their differential expression of calbindin (Puthussery, 2013). Midget BCs are unique to the primate retina. They possess a small axon terminal and contact a single cone. The two types of midget BCs in the primate retina are named for their respective

connectivity at the pedicle; the flat midget BPC (FMB) and invaginating midget BPC (IMB). The primate retina contains a blue cone-specific BC (BB), which make contacts with only blue cones. The primate retina also contains rod BCs (RB), which contact only rod photoreceptors (Boycott and Wässle, 1991). Recently, a twelfth BC type was added to the characterization from macaque retina. It has been termed the giant bipolar cell due to its large dendrite field. Through an unknown selectivity model, it only contacts about half of the cones within its dendritic field (Joo et al., 2011).

Conclusion

BCs role in conveying information between photoreceptors and ganglion cells marks them as an important neuron population for studies into reconnecting and regenerating damaged retina neurons. Ongoing development of cell type specific transgenic markers and antibodies will greatly benefit ongoing research.

References

Ali, M. A., & Anctil, M. (1976). *Retinas of fishes: An atlas*. Berlin: Springer-Verlag

Baden, T., & Euler, T. (2016). Retinal Physiology: Non-Bipolar-Cell Excitatory Drive in the Inner Retina. Current Biology, 26(15), R706-R708.

Barnes, S., & Werblin, F. (1987). Direct excitatory and lateral inhibitory synaptic inputs to amacrine cells in the tiger salamander retina. Brain research, 406(1), 233-237.

Barlow, H. B., & Levick, W. R. (1965). The mechanism of directionally selective units in rabbit's retina. *The Journal of Physiology*, *178*(3), 477–504.

Behrens, C., Schubert, T., Haverkamp, S., Euler, T., & Berens, P. (2016). Connectivity map of bipolar cells and photoreceptors in the mouse retina. *bioRxiv*, 65722.

Bellone, R. R., Brooks, S. A., Sandmeyer, L., Murphy, B. A., Forsyth, G., Archer, S., Grahn, B. (2008). Differential gene expression of TRPM1, the potential cause of congenital stationary night blindness and coat spotting patterns (LP) in the appaloosa horse (Equus caballus). *Genetics*, *179*(4), 1861–1870.

Bloomfield, S. A., & Xin, D. (2000). Surround inhibition of mammalian AII amacrine cells is generated in the proximal retina. *J Physiol*, *523 Pt 3*, 771–783.

Bloomfield, S. A., & Dacheux, R. F. (2001). Rod vision: Pathways and processing in the mammalian retina. *Progress in Retinal and Eye Research*, *20*(3), 351–384.

Boycott, B. B., & Wassle, H. (1991). Morphological Classification of Bipolar Cells of the Primate Retina. *European Journal of Neuroscience*, *3*(11), 1069–1088.

Breuninger, T., Puller, C., Haverkamp, S., & Euler, T. (2011). Chromatic Bipolar Cell Pathways in the Mouse Retina. *Journal of Neuroscience*, *31*(17), 6504–6517.

Briggman, K. L., Helmstaedter, M., & Denk, W. (2011). Wiring specificity in the direction-selectivity circuit of the retina. *Nature*, *471*(7337), 183–188.

Carter-Dawson, L. D., & Lavail, M. M. (1979). Rods and cones in the mouse retina. I. Structural analysis using light and electron microscopy. *The Journal of Comparative Neurology*, *188*(2), 245–262.

Chavez, A. E., & Diamond, J. S. (2008). Diverse mechanisms underlie glycinergic feedback transmission onto rod bipolar cells in rat retina. *J Neurosci*, *28*(31), 7919–7928.

Chavez, A. E., Grimes, W. N., & Diamond, J. S. (2010). Mechanisms underlying lateral GABAergic feedback onto rod bipolar cells in rat retina. *J Neurosci*, *30*(6), 2330–2339.

Connaughton, V. P., Graham, D., & Nelson, R. (2004). Identification and morphological classification of horizontal, bipolar, and amacrine cells within the zebrafish retina. *Journal of Comparative Neurology*, *477*(4), 371–385.

Cook, P. B., & McReynolds, J. S. (1998). Lateral inhibition in the inner retina is important for spatial tuning of ganglion cells. *Nature Neuroscience*, *1*(8), 714–719.

Cuenca, N., Deng, P., Linberg, K. A., Lewis, G. P., Fisher, S. K., & Kolb, H. (2002). The neurons of the ground squirrel retina as revealed by immunostains for calcium binding proteins and neurotransmitters. *Journal of neurocytology*, *31*(8-9), 649-666.

De Andrade, G. B., Long, S. S., Fleming, H., Li, W., & Fuerst, P. G. (2014). DSCAM localization and function at the mouse cone synapse. *Journal of Comparative Neurology*, *522*(11), 2609–2633.

Deans, M. R., Volgyi, B., Goodenough, D. A., Bloomfield, S. A., & Paul, D. L. (2002). Connexin36 Is Essential for Transmission of Rod-Mediated Visual Signals in the Mammalian Retina. *Neuron*, *36*, 703–712.

Della Santina, L., Kuo, S. P., Yoshimatsu, T., Okawa, H., Suzuki, S. C., Hoon, M., & Wong, R. O. (2016). Glutamatergic monopolar interneurons provide a novel pathway of excitation in the mouse retina. *Current Biology*, *26*(15), 2070-2077.

Ding, H., Smith, R. G., Poleg-Polsky, A., Diamond, J. S., & Briggman, K. L. (2016). Species-specific wiring for direction selectivity in the mammalian retina. *Nature*, *535*(7610), 105–10.

Dong, C. J., & Werblin, F. S. (1998). Temporal contrast enhancement via GABAC feedback at bipolar terminals in the tiger salamander retina. *Journal of Neurophysiology*, *79*(4), 2171–2180.

Dong, C.-J., & Hare, W. a. (2003). Temporal modulation of scotopic visual signals by A17 amacrine cells in mammalian retina in vivo. *Journal of Neurophysiology*, *89*(4), 2159–2166. https://doi.org/10.1152/jn.01008.2002

Duan, X., Krishnaswamy, A., De La Huerta, I., & Sanes, J. R. (2014). Type II cadherins guide assembly of a direction-selective retinal circuit. *Cell*, *158*(4), 793–807.

Dumitrescu, O. N., Pucci, F. G., Wong, K. Y., & Berson, D. M. (2012). Ectopic Retinal ON Bipolar Cell Synapses in the OFF Inner Plexiform Layer: Contacts with Dopaminergic Amacrine Cells and Melanopsin Ganglion Cells. *J Comp Neurol*, *517*(2), 226–244.

Dunn, F. a., & Wong, R. O. L. (2012). Diverse Strategies Engaged in Establishing Stereotypic Wiring Patterns among Neurons Sharing a Common Input at the Visual System's First Synapse. *Journal of Neuroscience*, *32*(30), 10306–10317.

Euler, T., & Wässle, H. (1995). Immunocytochemical identification of cone bipolar cells in the rat retina. TL - 361. *The Journal of Comparative Neurology*, *361 VN*-(3), 461–478.

Euler, T., & Masland, R. H. (2000). Light-evoked responses of bipolar cells in a mammalian retina. Journal of Neurophysiology, 83(4), 1817-1829.

Euler, T., Haverkamp, S., Schubert, T., & Baden, T. (2014). Retinal bipolar cells: elementary building blocks of vision. *Nature Reviews Neuroscience*, *15*(8), 507–519.

Famiglietti, E. V., & Kolb, H. (1975). A bistratified amacrine cell and synaptic circuitry in the inner plexiform layer of the retina. *Brain research*, *84*(2), 293-300.

Franke, K., Baden, T. (2017). General features of inhibition in the inner retina. Journal of Physiology, Accepted Article.

Fransen, J. W., & Borghuis, B. G. (2017). Temporally Diverse Excitation Generates Direction-Selective Responses in ON- and OFF-Type Retinal Starburst Amacrine Cells. *Cell Reports*, *18*(6), 1356–1365.

Fuerst, P. G., Bruce, F., Tian, M., Wei, W., Elstrott, J., Feller, M. B., Burgess, R. W. (2009). DSCAM and DSCAML1 Function in Self-Avoidance in Multiple Cell Types in the Developing Mouse Retina. *Neuron*, *64*(4), 484–497.

Ghosh, K. K., Bujan, S., Haverkamp, S., Feigenspan, A., & Wässle, H. (2004). Types of Bipolar Cells in the Mouse Retina. *Journal of Comparative Neurology*, *469*(1), 70–82.

Greene, M. J., Kim, J. S., & Seung, H. S. (2016). Analogous Convergence of Sustained and Transient Inputs in Parallel On and Off Pathways for Retinal Motion Computation. *Cell Reports*, *14*(8), 1892–1900.

Grimes, W. N., Zhang, J., Graydon, C. W., Kachar, B., & Diamond, J. S. (2010). Retinal Parallel Processors: More than 100 Independent Microcircuits Operate within a Single Interneuron. *Neuron*, *65*(6), 873–885.

Grimes, W. N., Li, W., Chávez, A. E., & Diamond, J. S. (2009). BK channels modulate pre- and postsynaptic signaling at reciprocal synapses in retina. *Nature Neuroscience*, *12*(5), 585–592.

Hack, I., Peichl, L., & Brandstätter, J. H. (1999). An alternative pathway for rod signals in the rodent retina: rod photoreceptors, cone bipolar cells, and the localization of glutamate receptors. *Proceedings of the National Academy of Sciences of the United States of America*, *96*(24), 14130–14135.

Hartveit, E. (1999). Reciprocal synaptic interactions between rod bipolar cells and amacrine cells in the rat retina. *Journal of Neurophysiology*, *81*(6), 2923–2936.

Haverkamp, S., Wässle, H., Duebel, J., Kuner, T., Augustine, G. J., Feng, G., & Euler, T. (2005). The primordial, blue-cone color system of the mouse retina. Journal of Neuroscience, 25(22), 5438-5445.

Haverkamp, S., Specht, D., Majumdar, S., Zaidi, N. F., Brandstätter, J. H., Wasco, W., Tom Dieck, S. (2008). Type 4 OFF cone bipolar cells of the mouse retina express

calsenilin and contact cones as well as rods. *Journal of Comparative Neurology*, *507*(1), 1087–1101.

Hirasawa, H., & Kaneko, A. (2003). pH changes in the invaginating synaptic cleft mediate feedback from horizontal cells to cone photoreceptors by modulating Ca2+ channels. *J Gen Physiol*, *122*(6), 657–671.

Hirasawa, H., Yamada, M., & Kaneko, A. (2012). Acidification of the synaptic cleft of cone photoreceptor terminal controls the amount of transmitter release, thereby forming the receptive field surround in the vertebrate retina. *Journal of Physiological Sciences*, *62*(5), 359–375.

Hoshi, H., Liu, W. L., Massey, S. C., & Mills, S. L. (2009). ON inputs to the OFF layer: bipolar cells that break the stratification rules of the retina. *J Neurosci*, *29*(28), 8875–8883.

Ishida, A. T., Stell, W. K., & Lightfoot, D. O. (1980). Rod and cone inputs to bipolar cells in goldfish retina. Journal of Comparative Neurology, 191(3), 315-335.

Jacobs, A. L., & Werblin, F. S. (1998). Spatiotemporal Patterns at the Retinal Output Spatiotemporal Patterns at the Retinal Output. *Journal of Neurophysiology*, *80*, 447–451.

Joo, H. R., Peterson, B. B., Haun, T. J., & Dacey, D. M. (2011). Characterization of a novel large-field cone bipolar cell type in the primate retina: Evidence for selective cone connections. *Visual Neuroscience*, *28*(1), 29–37.

Kamermans, M. (2001). Hemichannel-Mediated Inhibition in the Outer Retina. *Science*, *292*(5519), 1178–1180.

Kamermans, M., & Fahrenfort, I. (2004). Ephaptic interactions within a chemical synapse: Hemichannel-mediated ephaptic inhibition in the retina. *Current Opinion in Neurobiology*, *14*(5), 531–541.

Kaneko, A. (1970). Physiological and morphological identification of horizontal, bipolar and amacrine cells in goldfish retina. *The Journal of Physiology*, *207*(3), 623–33.

Kaneko, A. (1973). Receptive field organization of bipolar and amacrine cells in the goldfish retina. *Journal of Physiology*, *235*, 133–153.

Ke, J. Bin, Wang, Y. V., Borghuis, B. G., Cembrowski, M. S., Riecke, H., Kath, W. L., … Singer, J. H. (2014). Adaptation to background light enables contrast coding at rod bipolar cell synapses. *Neuron*, *81*(2), 388–401.

Keeley, P. W., & Reese, B. E. (2010). Morphology of dopaminergic amacrine cells in the mouse retina: independence from homotypic interactions. Journal of Comparative Neurology, 518(8), 1220-1231.

Keeley, P. W., Madsen, N. R., St. John, A. J., & Reese, B. E. (2014). Programmed cell death of retinal cone bipolar cells is independent of afferent or target control. *Developmental Biology*, *394*(2), 191–196.

Keeley, P. W., Kim, J. J., Lee, S. C., Haverkamp, S., & Reese, B. E. (2017). Random spatial patterning of cone bipolar cell mosaics in the mouse retina. Visual Neuroscience, 34.

Kim, J. S., Greene, M. J., Zlateski, A., Lee, K., Richardson, M., Turaga, S. C., … Seung, H. S. (2014). Space–time wiring specificity supports direction selectivity in the retina. *Nature*, *509*(7500), 331–336.

Koike, C., Obara, T., Uriu, Y., Numata, T., Sanuki, R., Miyata, K., Furukawa, T. (2010). TRPM1 is a component of the retinal ON bipolar cell transduction channel in the mGluR6 cascade. *Proc Natl Acad Sci U S A*, *107*(1), 332–337.

Kolb, H. (1970). Organization of the outer plexiform layer of the primate retina: electron microscopy of Golgi-impregnated cells. *Philosophical Transactions of the Royal Society of London B: Biological Sciences*, *258*(823), 261-283.

Kolb, H., & Famigilietti, E. V. (1974). Rod and cone pathways in the inner plexiform layer of cat retina. *Science*, *186*(4158), 47-49.

Lee, S. C. S., Cowgill, E. J., Al-Nabulsi, A., Quinn, E. J., Evans, S. M., & Reese, B. E. (2011). Homotypic regulation of neuronal morphology and connectivity in the mouse retina. *The Journal of Neuroscience : The Official Journal of the Society for Neuroscience*, *31*(40), 14126–33. https://doi.org/10.1523/JNEUROSCI.2844-11.2011

Lefebvre, J. L., Kostadinov, D., Chen, W. V, Maniatis, T., & Sanes, J. R. (2012). Protocadherins Mediate Dendritic Self-Avoidance in the Mammalian Nervous System. *Nature*, *488*(7412), 517–521.

Li, W., & DeVries, S. H. (2006). Bipolar cell pathways for color and luminance vision in a dichromatic mammalian retina. *Nature Neuroscience*, *9*(5), 669–675.

Li, Y. N., Tsujimura, T., Kawamura, S., & Dowling, J. E. (2012). Bipolar cell–photoreceptor connectivity in the zebrafish (Danio rerio) retina. Journal of Comparative Neurology, 520(16), 3786-3802.

Lukasiewicz, P. D., & Werblin, F. S. (1994). A novel GABA receptor modulates synaptic transmission from bipolar to ganglion and amacrine cells in the tiger salamander retina. *The Journal of Neuroscience : The Official Journal of the Society for Neuroscience*, *14*(3 Pt 1), 1213–23.

Marc, R. E., & Liu, W. L. S. (2000). Fundamental GABAergic amacrine cell circuitries in the retina: Nested feedback, concatenated inhibition, and axosomatic synapses. *Journal of Comparative Neurology*, *425*(4), 560–582.

Marc, R. E., Liu, W.L. S., Kalloniatis, M., Raiguel, S. F., & van Haesendonck, E. (1990). Patterns of Glutamate in the Goldfish. *Journal of Neuroscience*, *10*, 4006–4034.

Mataruga, A., Kremmer, E., & Müller, F. (2007). Type 3a and type 3b OFF cone bipolar cells provide for the alternative rod pathway in the mouse retina. *Journal of Comparative Neurology*, *502*(6), 1123-1137.

Molnar, A., Hsueh, H. A., Roska, B., & Werblin, F. S. (2009). Crossover inhibition in the retina: Circuitry that compensates for nonlinear rectifying synaptic transmission. *Journal of Computational Neuroscience*, *27*(3), 569–590.

Molnar, A., & Werblin, F. (2007). Inhibitory feedback shapes bipolar cell responses in the rabbit retina. *Journal of Neurophysiology*, *98*(October 2007), 3423–3435.

Morgan, J. L., Dhingra, A., Vardi, N., & Wong, R. O. (2006). Axons and dendrites originate from neuroepithelial-like processes of retinal bipolar cells. *Nat Neurosci*, *9*(1), 85–92.

Morgans, C. W., Zhang, J., Jeffrey, B. G., Nelson, S. M., Burke, N. S., Duvoisin, R. M., & Brown, R. L. (2009). TRPM1 is required for the depolarizing light response in retinal ON-bipolar cells. *Proceedings of the National Academy of Sciences of the United States of America*, *106*(45), 19174–8.

Pan, Z. H., & Lipton, S. A. (1995). Multiple GABA receptor subtypes mediate inhibition of calcium influx at rat retinal bipolar cell terminals. *The Journal of Neuroscience*, *15*(4), 2668–79.

Pang, J.-J., Gao, F., Lem, J., Bramblett, D. E., Paul, D. L., & Wu, S. M. (2010). Direct rod input to cone BCs and direct cone input to rod BCs challenge the traditional view of mammalian BC circuitry. *Proceedings of the National Academy of Sciences*, *107*(1), 395–400.

Park, S. J. H., Kim, I., Looger, L. L., Demb, J. B., & Borghuis, B. G. (2014). Excitatory Synaptic Inputs to Mouse On-Off Direction- Selective Retinal Ganglion Cells Lack Direction Tuning, *34*(11), 3976–3981.

Pourcho, R. G., & Goebel, D. J. (1983). Neuronal subpopulations in cat retina which accumulate the GABA agonist,(3H) muscimol: a combined Golgi and autoradiographic study. Journal of Comparative Neurology, 219(1), 25-35.

Puller, C., Ondreka, K., & Haverkamp, S. (2011). Bipolar cells of the ground squirrel retina. *Journal of Comparative Neurology*, *519*(4), 759–774.

Puthussery, T., Venkataramani, S., Gayet-primo, J., Smith, R. G., & Taylor, W. R. (2013). Na V 1.1 Channels in Axon Initial Segments of Bipolar Cells Augment Input to Magnocellular Visual Pathways in the Primate Retina, *33*(41), 16045–16059.

Ribelayga, C., Cao, Y., & Mangel, S. C. (2008). The Circadian Clock in the Retina Controls Rod-Cone Coupling. *Neuron*, *59*(5), 790–801.

Saito, Takehiko, Kujiraoka, Toru, Yonaha, Tomohide, Chino, Y. (1985). Reexamination of Photoreceptor-Bipolar Connectivity Patterns in Carp Retina: HRP-EM and Golgi-EM Studies. *Journal of Comparative Neurology*, *236*(2), 141–160.

Sakai, H. M., & Naka, K.-I. N. (1983). Synaptic organization of the cone horizontal cells in the catfish retina. *Vision Research*, *23*, 339–351.

Seeliger, M. W., Brombas, A., Weiler, R., Humphries, P., Knop, G., Tanimoto, N., & Müller, F. (2011). Modulation of rod photoreceptor output by HCN1 channels is essential for regular mesopic cone vision. Nature communications, 2, 532.

Sharpe, L. T., & Stockman, A. (1999). Rod pathways: The importance of seeing nothing. *Trends in Neurosciences*, *22*(11), 497–504.

Shekhar, K., Lapan, S. W., Whitney, I. E., Tran, N. M., Macosko, E. Z., Kowalczyk, M., Sanes, J. R. (2016). Comprehensive Classification of Retinal Bipolar Neurons by Single-Cell Transcriptomics. *Cell*, *166*(5), 1308–1323.e30.

Sherry, D. M., & Yazulla, S. (1993). Goldfish bipolar cells and axon terminal patterns: A Golgi study. *Journal of Comparative Neurology*, *329*(2), 188–200.

Soucy, E., Wang, Y., Nirenberg, S., Nathans, J., & Meister, M. (1998). A novel signaling pathway from rod photoreceptors to ganglion cells in mammalian retina. *Neuron*, *21*(3), 481–493.

Sterling, P. (1983). Microcircuitry of the cat retina. *Annual review of neuroscience*, *6*(1), 149-185.

Strettoi, E., Raviola, E., & Dacheux, R. F. (1992). Synaptic connections of the narrow-field, bistratified rod amacrine cell (AII) in the rabbit retina. Journal of Comparative Neurology, 325(2), 152-168.

Strettoi, E., Novelli, E., Mazzoni, F., Barone, I., & Damiani, D. (2010). Complexity of retinal cone bipolar cells. *Progress in retinal and eye research*, *29*(4), 272-283.

Sukeena, J. M., Galicia, C. A., Wilson, J. D., McGinn, T., Boughman, J. W., Robison, B. D., & Fuerst, P. G. (2016). Characterization and Evolution of the Spotted Gar Retina. *Journal of Experimental Zoology Part B: Molecular and Developmental Evolution*, *326*(7), 403-421.

Suzuki, S., & Kaneko, A. (1990). Identification of bipolar cell subtypes by protein kinase C-like immunoreactivity in the goldfish retina. *Visual Neuroscience*, *5*, 223–230.

Szél, Á., Röhlich, P., Caffé, A. R., & Van Veen, T. (1996). Distribution of cone photoreceptors in the mammalian retina. *Microscopy Research and Technique*, *35*(6), 445–462.

Taylor, W. R. (1999). TTX attenuates surround inhibition in rabbit retinal ganglion cells. *Visual Neuroscience*, *16*(2), 285–90.

Tsukamoto, Y., Morigiwa, K., Ueda, M., & Sterling, P. (2001). Microcircuits for night vision in mouse retina. *The Journal of Neuroscience : The Official Journal of the Society for Neuroscience*, *21*(21), 8616–23.

Tsukamoto, Y., & Omi, N. (2014). Some OFF bipolar cell types make contact with both rods and cones in macaque and mouse retinas. *Frontiers in Neuroanatomy*, *8*(September), 105.

Vaney, D. I., Sivyer, B., & Taylor, W. R. (2012). Direction selectivity in the retina: symmetry and asymmetry in structure and function. *Nature Reviews. Neuroscience*, *13*(3), 194–208.

Villar-Cheda, B., Abalo, X. M., Anadón, R., & Rodicio, M. C. (2006). Calbindin and calretinin immunoreactivity in the retina of adult and larval sea lamprey. *Brain research*, *1068*(1), 118-130.

Wassle, H., Puller, C., Muller, F., & Haverkamp, S. (2009). Cone contacts, mosaics, and territories of bipolar cells in the mouse retina. *J Neurosci*, *29*(1), 106–117.

Werblin, F. S. (1972). Lateral interactions at inner plexiform layer of vertebrate retina: antagonistic responses to change. *Science*, *175*(25), 1008–1010.

West, R. W. (1976). Light and electron microscopy of the ground squirrel retina: functional considerations. *Journal of Comparative Neurology*, *168*(3), 355-377.

Yang, X. L., & Wu, S. M. (1989). Modulation of rod-cone coupling by light. *Science*, *244*(4902), 352–354.

Yang, X. L., & Wu, S. M. (1991). Feedforward lateral inhibition in retinal bipolar cells: input-output relation of the horizontal cell-depolarizing bipolar cell synapse. *Proceedings of the National Academy of Sciences of the United States of America*, *88*(8), 3310–3313.

Figures

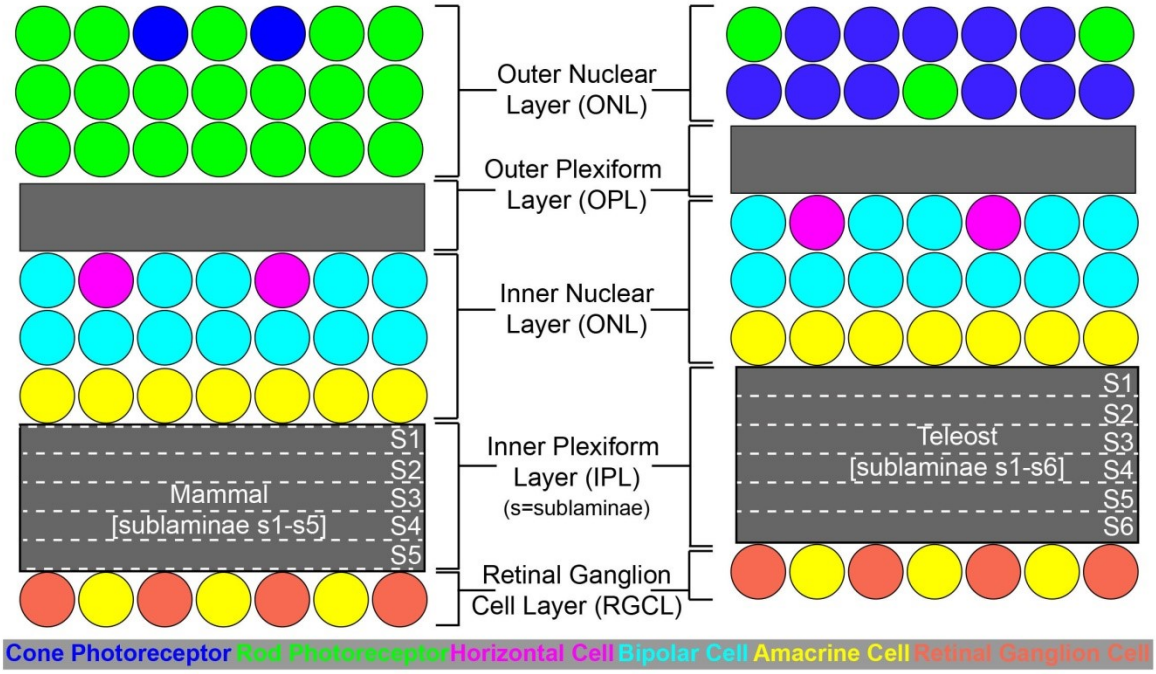

Figure 2.1. Cellular organization of the retina. The retina is composed of three nuclear layers and two synaptic layers. The outermost layer, closest to the eye socket, is the outer nuclear layer (ONL). The ONL contains the cell bodies of cone and rod photoreceptors. The middle nuclear layer is the inner nuclear layer (INL). The INL contains the cell bodies of amacrine cells (AC), horizontal cells (HC), bipolar cells (BC), and Müller glia (MG). The innermost nuclear layer of the retina is the retinal ganglion cell layer (RGL). The RGL contains the cell bodies of RGCs and ACs. The two synaptic layers of the retina are the outer plexiform layer (OPL) and inner plexiform layer (IPL). The OPL contains the synapses between photoreceptors, BCs, and HCs. The IPL contains the synapses between BCs, ACs, and RGCs. The IPL is divided into two halves that largely contain circuitry devoted light increment (ON) and decrement (OFF). The OFF synapses are located proximal to the INL. The ON synapses are located proximal to the RGL. The IPL can be further divided into sublaminae to specify location of BC axon terminal. For mammalian retinas (left), there are five sublaminae: s1-s5. For teleost retina (right), the IPL is divided into sublaminae s1-s6.

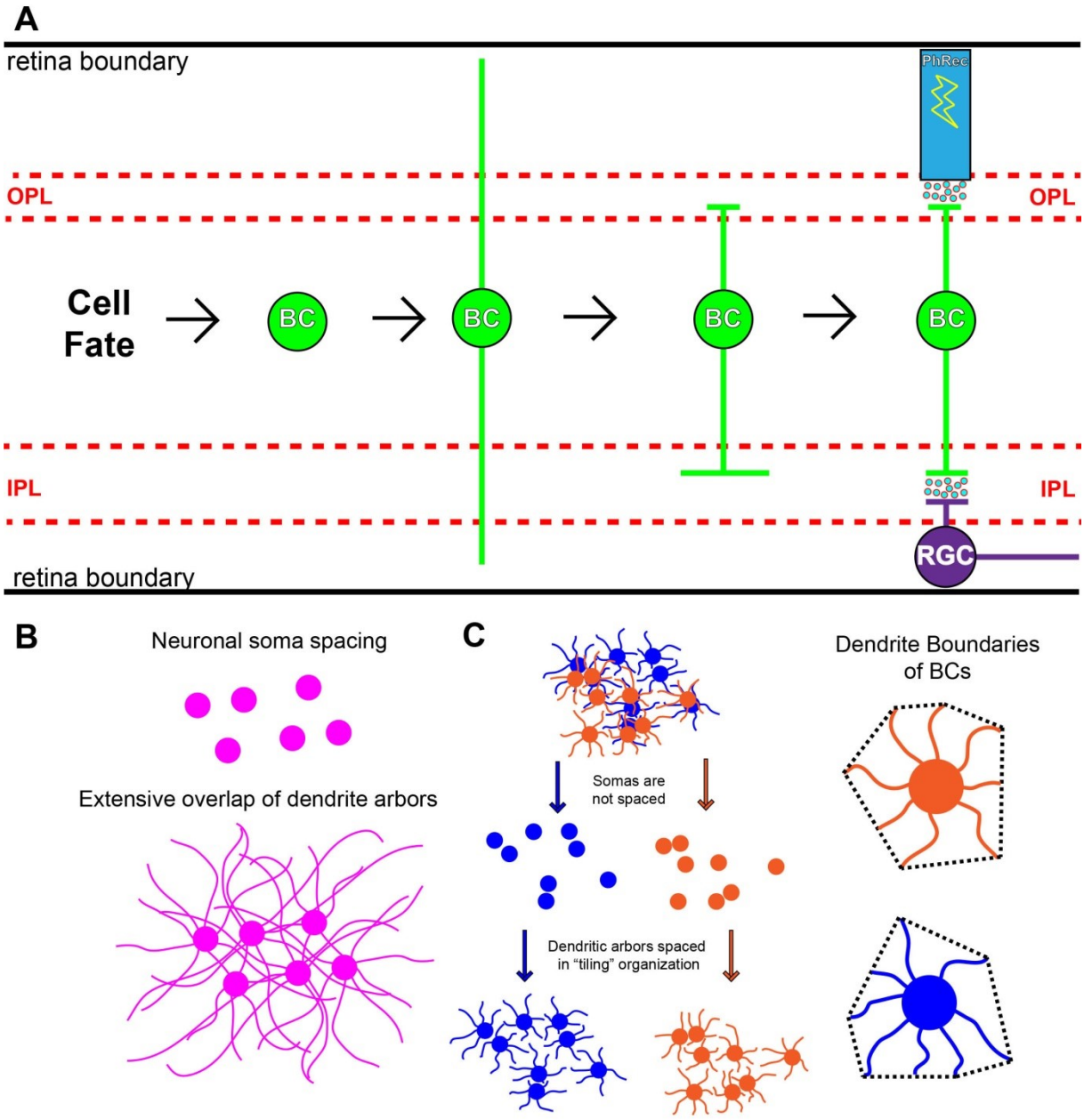

Figure 2.2. Bipolar cell morphology and development. A) Following cell fate determination, the bipolar cell (BC) extends processes that span from the RGL to ONL. Their cell body migrates to its location in the INL, and then the apical and basal processes retract to the appropriate location for a BC of a given subtype. **B)** Most retinal neurons space themselves to increase distance to nearest cells of the same type and project overlapping dendritic arbors. **C)** BCs don't space their cell bodies with respect to the soma of BCs of the same type, but their dendritic and axonal arbors tile, that is they do not overlap. Tiling occurs between like-BCs only.

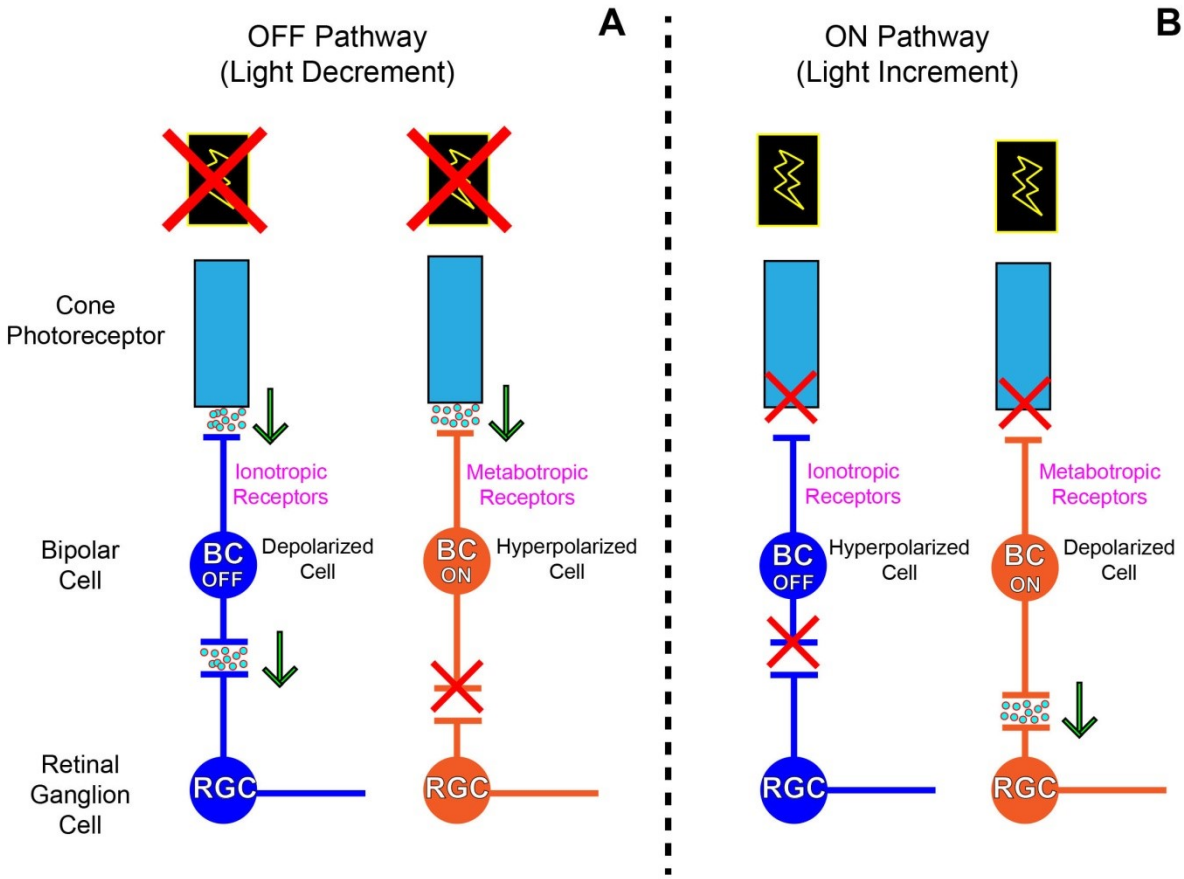

Figure 2.3. Bipolar cells light response. Photoreceptors release glutamate onto the dendritic tips of bipolar cells (BC). OFF and ON BCs respond differently to the glutamate release based on the receptors that they express at their dendrite tips. **A**) OFF BCs (blue) respond to release of glutamate through ionotropic receptors, resulting in depolarization. In turn, the OFF BC releases glutamate from its axon terminal in the IPL. **B**) For ON BCs, the glutamate released from the photoreceptor will activate metabotropic receptors, mGluRs, which signal inactivates TRPM1 cation channels. When glutamate is released signaling through mGluR6 results in closure of TRPM1 channels, which hyperpolarizes the cell. This results in a lack of glutamate release in the IPL.

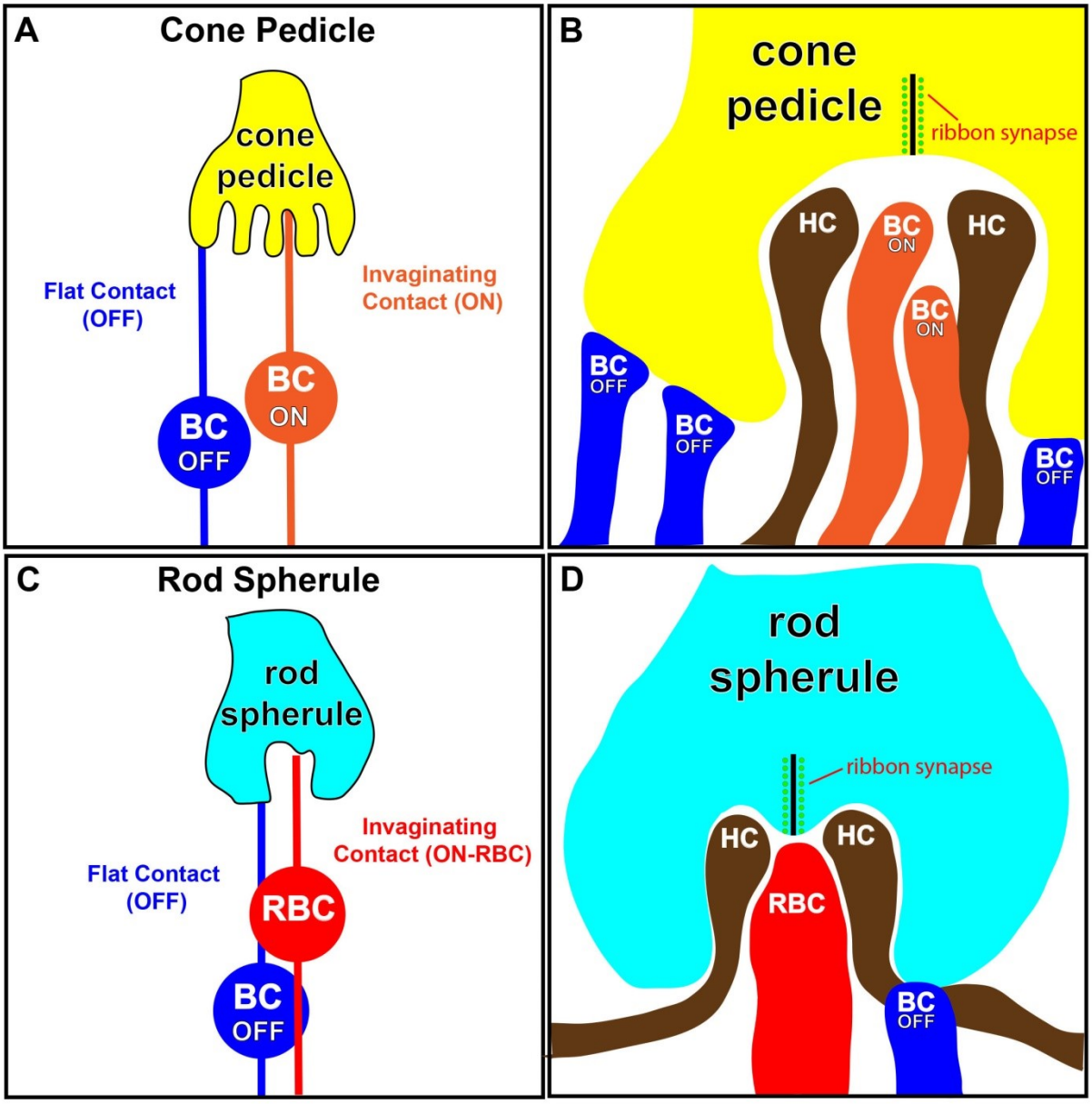

Figure 2.4. Photoreceptor - bipolar cells contacts. A-B) Cone photoreceptors release glutamate at their axon terminal in the outer plexiform layer (OPL), termed pedicles. Two types of contacts are made between cone photoreceptors and bipolar cells (BCs). The first is a flat contact typical of OFF BC populations (blue). The second is an invaginating contact (orange) that is made by ON BCs only in the mammalian retina, or by both ON and OFF tips on the fish retina. HC dendrites tips invaginate alongside BC dendrite tips. **C-D)** The rod spherule is located at the rod axon terminal. The rod bipolar cells (RBC) make invaginating

contacts with the rod spherule, as do HC axon tips. Flat contacts made by OFF BCs are observed at about 10 percent of rod spherules.

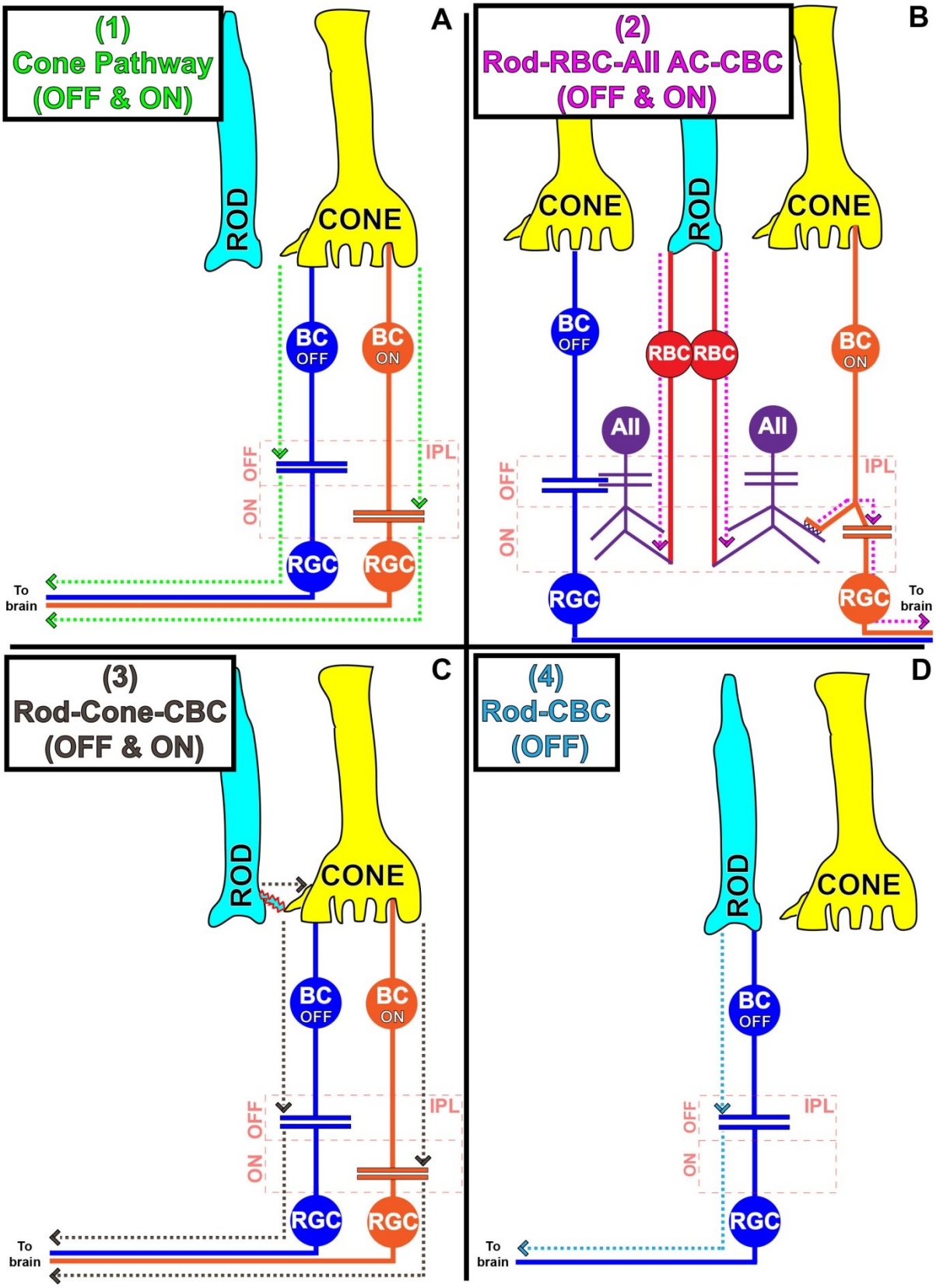
(1)
Cone Pathway
(OFF & ON)
A
ROD
CONE
BC
OFF
BC
ON
OFF
ON
IPL
RGC
RGC
To
brain
(2)
Rod-RBC-AII AC-CBC
(OFF & ON)
B
CONE
ROD
CONE
BC
OFF
RBC
RBC
BC
ON
AII
AII
OFF
ON
IPL
RGC
RGC
To
brain
(3)
Rod-Cone-CBC
(OFF & ON)
C
ROD
CONE
BC
OFF
BC
ON
OFF
ON
IPL
RGC
RGC
To
brain
(4)
Rod-CBC
(OFF)
D
ROD
CONE
BC
OFF
OFF
ON
IPL
RGC
To
brain

Figure 2.5. Four bipolar cell pathways in the retina. A) The cone photoreceptor to cone bipolar cell (BC) pathway (C->CBC) involves a cone photoreceptor coupling to cone bipolar cells through chemical synapses, the activity of which is then conveyed to retinal ganglion cells (RGCs) through excitatory chemical synapses. **B)** The rod photoreceptor makes a direct chemical synapse with RBCs, which, in the mammalian retina, make chemical synapses with the AII AC in the IPL. AII ACs then transmit signal to cone BC axons through gap junctions. The cone BCs then relay the signal to RGCs through chemical synapses. **C)** Rod photoreceptors and cone photoreceptors are also directly connected to each other. This results in an alternative rod pathway by which rod signal is sent to cones via gap junctions. The signal is then relayed through to RGCs via chemical synapses along the cone -> cone BC pathway shown in panel A. **D)** Some rod photoreceptors make flat contacts with certain OFF BCs, forming chemical synapses that provide another alternative rod pathway through the retina.

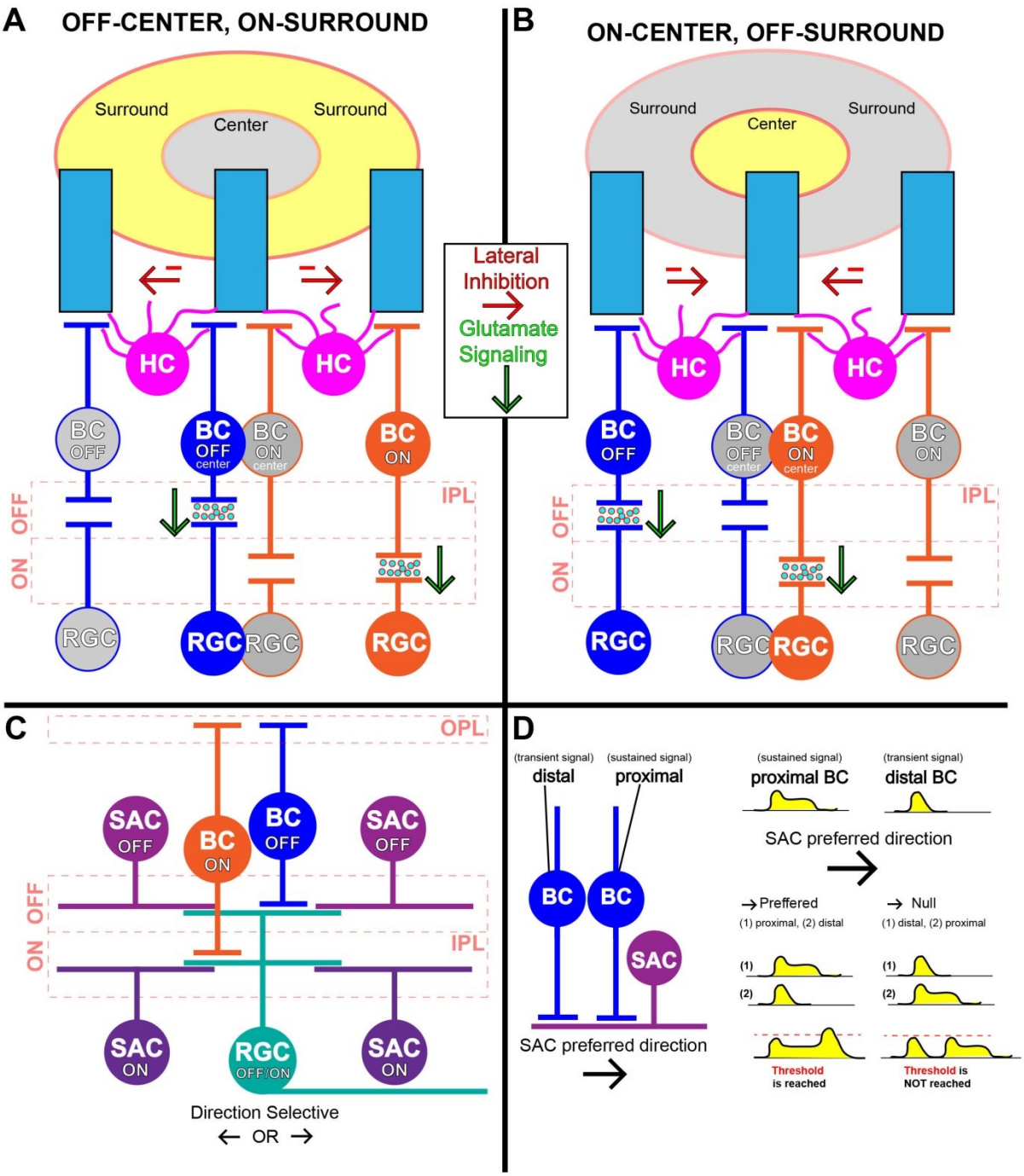

Figure 2.6. Bipolar cells and lateral inhibition. Horizontal cell (HC) mediated inhibition of bipolar cells (BCs) alters signal as it passes through the retina and is thought to underlie several features of visual encoding such as center surround by lateral inhibition **(A-B)**. Models for HC inhibition of BCs near the cone terminal. **A)** HCs in the OPL will inhibit surrounding (neighboring) BCs. When the "center" is in light decrement compared to the edges, the OFF BC in the center will fire intensely and activate both OFF BCs and HCs, the

latter which inhibit neighboring OFF BCs. Likewise, the ON BCs in the surround will fire intensely due to glutamate release from photoreceptor being lessened by lateral inhibition, thereby activating the ON pathway. **B)** Lateral inhibition and ON center response. In ON center response the ON pathway is activated by lack of glutamate release and HCs no longer inhibit surrounding cells. **C-D)** Direction selectivity (DS) in the retina has been observed in retinal ganglion cells (RGCs) that respond to moving visual stimuli. **C)** DSGCs are contacted by populations of BCs and starburst amacrine cells (SACs). BCs influence DS through their synapses with SACs and current models suggest these synapses are the physiological origin of DS. **D)** SACs receive different BCs input types at their proximal and distal dendrites. This creates spatiotemporal interactions of functionally diverse excitatory inputs (from BCs), and result in differences in sustained (proximal) and transient (distal) signaling. *Figures were generated based on Park et al., 2014 and Fransen & Borghuis, 2017.*

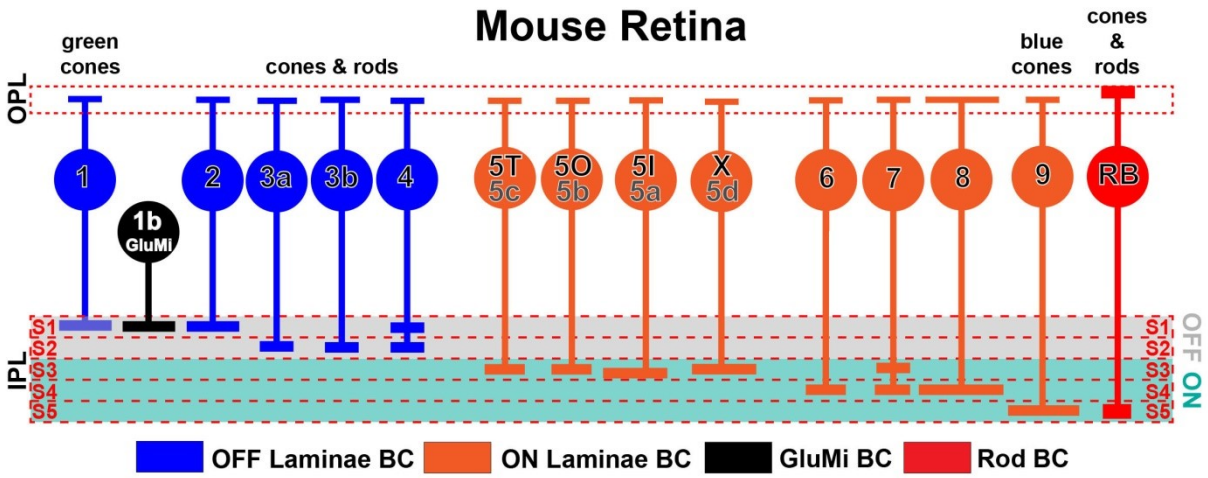

Figure 2.7. Bipolar cell types in the mouse retina. There are currently sixteen classified types of bipolar cell (BC) in the mouse retina. Axon terminal depth increases in BC types from BC1 to RB (left to right in figure). There are five types of BCs that terminate in the OFF region of the IPL. These are types 1, 2, 3a, 3b, and 4 BCs. BC3a, BC3b, and BC4 contact cones and rods. The dendrite lacking “GluMI” cell terminates in the OFF region. The mouse retina contains at least nine BC types that terminate in the ON region of the IPL. These include BC6, BC7, BC8, BC9, rod bipolar cells (RBCs), and four distinct populations of BC5s: BC5a, BC5b, BC5c, and BCd (Shekhar et al., 2016) or as BC5T, BC5O, BC5I, and BCX (Behrens et al., 2016). RBCs make contacts at rod spherules and relay information from rod to RGCs via AII amacrine cells.

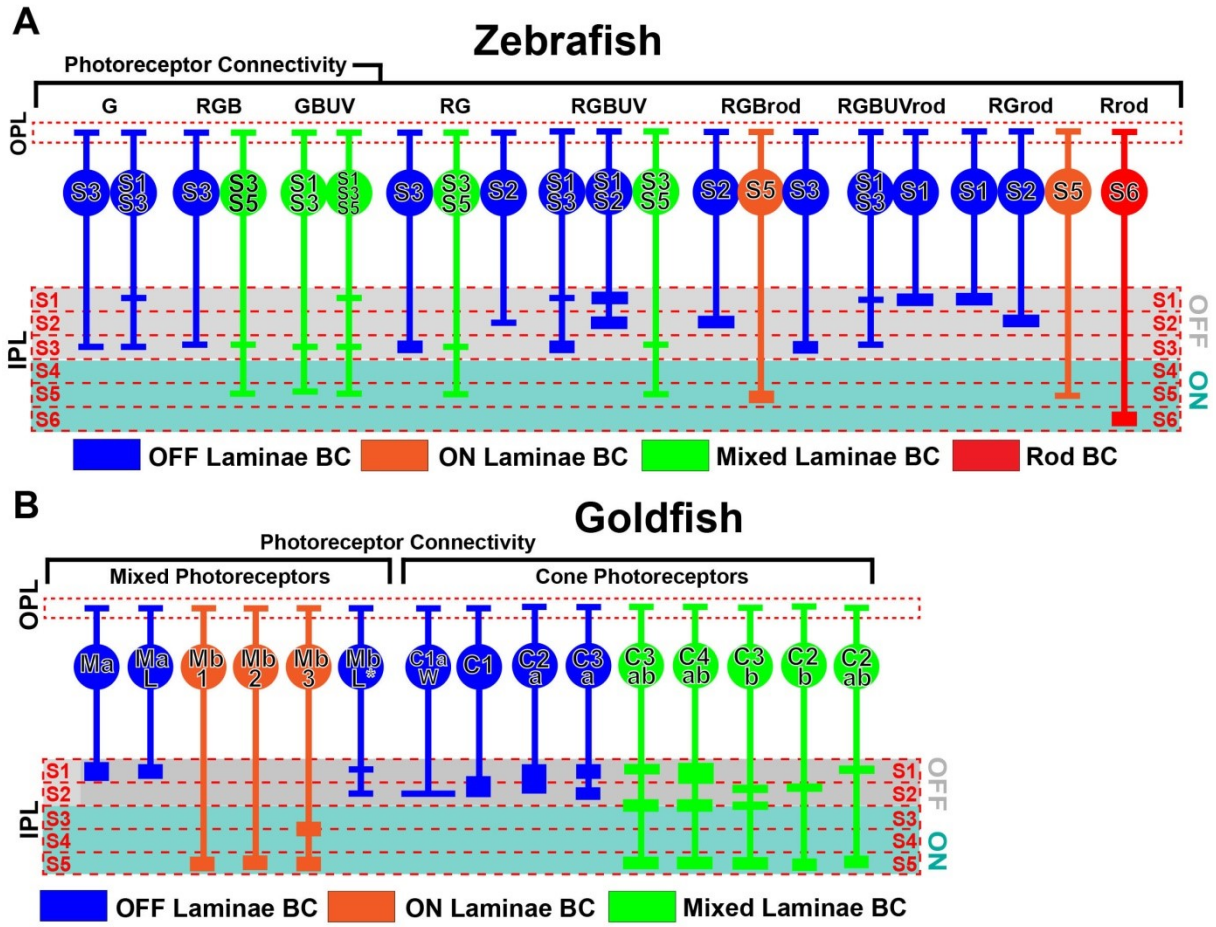

Figure 2.8. Bipolar cell types in the teleost retina. Bipolar cell (BC) populations based on morphology, connectivity, and physiology. **A)** Up to 21 types of BC have been described in the zebrafish retina, based on photoreceptor connectivity and axon terminal location(s). There are nine possible combinations of photoreceptor connectivity groups that include green cones (G), red cones (R), blue cones (B), ultraviolet cones (UV), and rhodopsin-positive photoreceptors (rod). The groups are as follows: G, RGB, GBUV, RG, RGBUV, RGBrod, RGBUVrod, RGrod, and Rrod (L to R in figure). The corresponding label is shown directly above each distinct cell type. BCs in the goldfish retina include 15 known types that vary based on axon terminal depth and photoreceptor connectivity.

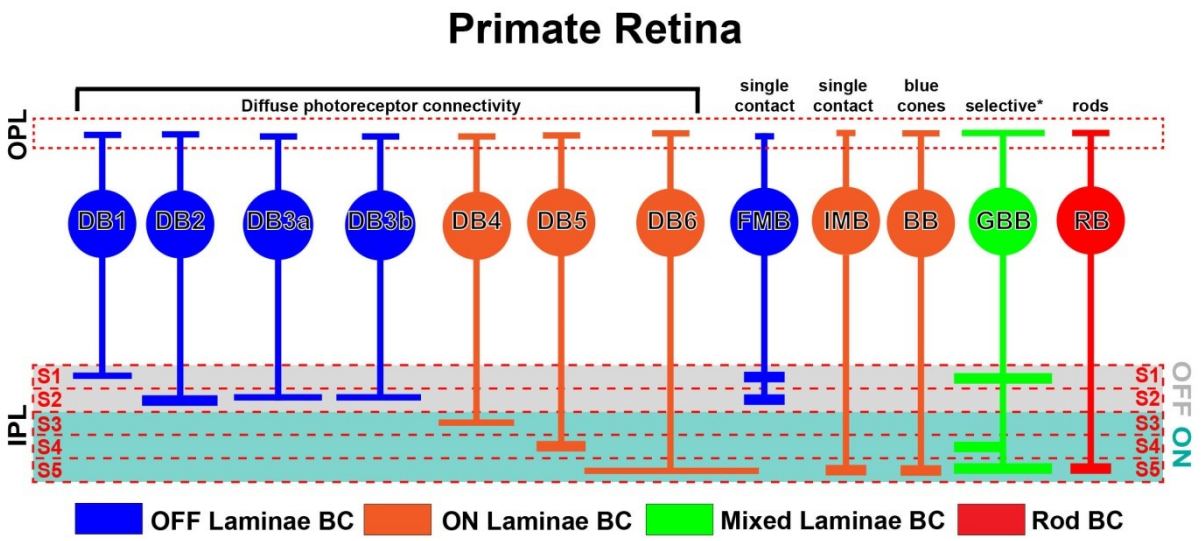

Figure 2.9. Bipolar cell types in the primate retina. 12 types of bipolar cells (BCs) have been described in the primate retina. Diffuse bipolar cells (DB) are named because they contact a diffuse array of cone photoreceptors in their dendritic field, without preference or selectivity. There are seven described types of diffuse BCs in the primate retina. The OFF DBs are DB1, DB2, DB3a, and DB3b. The ON DBs include DB4, DB5, and DB6. The primate retina also contains a unique-to-primates BC type, the midget bipolar cell (MB). There are two types of described MBs in the primate retina. The OFF MB is called FMB due to its flat contact with a cone pedicle, and the ON MB is called IMB due to its invaginating contact with a cone pedicle. Both of the MBs in the primate retina are high in density, small, and only make a contact with a single cone. The primate retina also contains a blue cone specific bipolar cell (BB), which exclusively makes contacts with blue cone photoreceptors. The giant bipolar cell (GBB) is a large BC that contains axon terminals in both the OFF and ON layer of the IPL. GBBs possess large dendritic terminals, yet contact a select number of cones within the terminal, leaving many of them un-sampled. The selectivity of the GBBs remains unknown. The primate retina contains a rod bipolar cell (RBC) that is morphologically similar to the RBC in other mammalian species.

Chapter 3: Synaptic compensation preserves cone projective field in Bax null mice

Joshua M. Sukeena[1], Aaron B. Simmons[1], Samuel Bloomsburg[1], Donson Cook-Gallardo[3], and Peter G. Fuerst[1, 2]

1 University of Idaho, Department of Biological Sciences, Moscow, Idaho 83844, USA, 2 University of Washington School of Medicine, WWAMI Medical Education Program, Moscow, Idaho 83844, USA, 3 Carleton College, Department of Biology, Northfield, Minnesota 55057, USA

Abstract

The intrinsic and environmental cues that drive neuronal organization and connectivity are not currently well understood. In the present study, we used a *Bax* null mouse model to eliminate BAX-mediated programmed cell death, and observe its effect on cellular and synaptic organization in the mouse retina. More specifically, we sought to understand whether OFF bipolar cells (BCs) are organized according to similar principles as ON BCs, and whether their synaptic organization is influenced by cell density. We observed the cellular interactions between neighboring cells, as well as their dendritic connectivity with afferent cone terminals and axon projections in the inner plexiform layer. We found that type 4 OFF bipolar cells (BCs) maintain tiling organization in *Bax* null retina, however, a small increase in overlap of their dendritic areas is seen primarily at cone terminals. This is likely due to an increase in the number of multiply innervated (MI) cones that can be observed in the *Bax* null retina. We also observed a significant increase in dystroglycan-positive ribbon puncta at the cone terminals in *Bax* null retinas. An overall increase in ON BCs and rod BCs was also observed in *Bax* null retinas compared to wild type. Lastly, we observed a possible mechanism for synaptic compensation in the cone projective field, where an increase in MI cones could potentially offset smaller dendritic areas seen in Bax null retinas as well as in

more densely populated regions of wild type retinas.

Introduction

The retina is the primary light sensing tissue of the central nervous system (CNS) that is responsible for converting light stimuli into a signal that can be interpreted by the vision producing areas of the brain. Relay of signal in the retina begins with the photoreceptors. Photoreceptors send signal to retinal bipolar cells (BCs) which then connect with retinal ganglion cells (RGCs). Along this pathway, horizontal cells (HCs) and amacrine cells (ACs) are able to mediate and influence the signal as it passes through the retina. Despite a complex system of signaling in the retina, the organization of the cells and synapses are ordered simply with three nuclear layers and two synaptic layers. The outer nuclear layer (ONL) sits at the back of the eye near the retinal pigment epithelium (RPE), and contains rod and cone photoreceptors. The inner nuclear layer (INL) contains the cell bodies of HCs, BCs, and ACs. The innermost layer, the retinal ganglion cell layer (GCL) contains RGCs and ACs. Between the ONL and INL is the outer plexiform layer (OPL) that contains synapses of both photoreceptor types, HCs, and BCs. Between the INL and GCL is the inner plexiform layer (IPL) which contains synapses between BCs, ACs, and RGCs (Kolb & Famigilietti, 1974; Jeon et al., 1998; Haverkamp & Wassle, 2000; Wassle, 2004; Masland, 2012). The IPL possesses an additional feature of laminar specificity where synapses are located in distinct ON and OFF layers that correspond to light signal from changes in light increment and light decrement respectively.

Retinal neurons are organized in mosaic patterns in which their cell bodies are spaced to different degrees to maximize the space between other cells of the same type. This is thought to ensure even distribution of cells and circuits devoted to detecting different aspects of the visual field, such as contrast, edges or motion (Reese & Keeley, 2015). While the cell bodies of retinal bipolar cells (BCs) are not organized in mosaics, their axonal and dendritic fields are organized in a non-overlapping fashion, referred to as tiling (Keeley et al.,

2017). ON BCs scale the size of their receptive field in response to changes in cellular density (Lee et al., 2011). The synaptic organization of OFF BCs, those that respond to light decrement, is significantly different to that of ON BCs in the mammalian retina (Haverkamp & Wassle, 2000) and we wished to determine if they are organized according to similar principles and how their synaptic organization is influenced by cell density.

We compared the organization of type 4 OFF BCs in different regions of the retina and between wild type (wt) and *Bax* null mice, which have an increased number of cells. We found that, like ON BCs, OFF BCs resize their dendritic arbors in response to changes in density; however, a second type of density adaptation was also observed. As the receptive field of OFF BCs become smaller individual cones were more likely to be sampled by multiple OFF BCs. Measurements of the cone projective field indicate that this change in wiring pattern preserves the size of the cone projective field despite the reduction in the OFF BC dendritic field.

Materials and Methods

Mouse Housing, Care, Strains and Genotyping

All mice were housed in the University of Idaho Live Animal Research Facility (LARF). They were kept on a 12-hour light:dark cycle and fed ad libitum. Mice used in this study were maintained on a mixed C57 BL/6J, C3H/HeJ and 129/P background. All procedures performed on mice used in this study were approved by the University of Idaho Animal Care and Use Committee. Three transgenic mouse lines were used in this study. The first manipulated the *Bax* gene and was acquired from the Jackson Laboratory. The second was Gt(ROSA)26Sortm9(CAG-tdTomato)Hze (referred to as *Ai9*, Jax stock number 007909), a fluorescent reporter strain. The third strain was a Cre transgenic mouse line Tg(Htr2a-cre)KM207Gsat (referred to as *HTR:Cre*, MMRRC, stock no:036750).

Tissue processing for histological analyses

Adult mice were anesthetized using 1 mL of 2,2,2-Tribromoethanol (0.5 g/mL ethanol) via intraperitoneal injection and perfused with PBS (10x stock at 1L with pH=7.4: 80g NaCl, 2g KCl, 26.8g Na_2HPO_4, 2.4g KH_2PO_4). Following removal, eyes were placed into PBS and dissected by removing the cornea and lens. Eyes were then fixed in 4% paraformaldehyde in PBS for 30 minutes at room temperature. Eyes were washed in PBS three times before soaking in a solution of 30% sucrose with PBS overnight at 4^{o} C and/or until the tissue sank to the bottom of the container. Eyes were then placed in a solution containing a 50/50 ratio of 30% sucrose solution and optimal cutting temperature (OCT; Sakura® Finetek Inc.) solution and frozen in liquid nitrogen. Eyes were cut into sections of 10 µm using *Leica GM 1510 S* cryostat. Sections were stored at -20^{o} C until used. If eyes were not to be used right away, they were stored at -80^{o} C in the 30% sucrose with PBS solution in which they were sunk in.

Antibody staining

Tissue was incubated in a blocking solution composed of PBS, 5% normal donkey serum and 0.1% triton (for staining sections) or 0.4% triton (for staining whole retinas) for 45 minutes (for staining sections) or overnight at 4^{o}C (for staining whole retinas). Following application of primary antibodies, the sections were incubated overnight at 4^{o}C, after which they were washed three times for fifteen minutes in PBS at room temperature. Following incubation with secondary antibodies, sections were washed again three times for fifteen minutes in PBS at room temperature. Slides were mounted with cover slips using 80% glycerol as a mounting medium. Whole retinas were stained in a similar manner except for the following two differences. First, both primary and secondary incubations lasted four to five days and they were performed at 4^{o}C with constant rocking movement of the sample.

Also, washes following secondary antibodies were carried out for one hour each in ~5 mL volume of PBS (first two washes) followed by a two to four hour wash in 0.4% triton blocking solution (third wash) at 4^{o}C. All images were collected on an Olympus DSU spinning disc microscope, Nikon spinning disc microscope, and/or an Olympus Fluoview 1000 Confocal/multiphoton microscope.

Antibodies and Stains

The following antibody and lectins were utilized in this study: Rabbit anti-cone arrestin (cones; Millipore; AB15282; 1:1000), mouse anti-PKARIIβ (type 3B cone bipolar cells; BD Biosciences; P54720; 1:500), mouse anti-dystroglycan (OPL synapses; Developmental Studies Hybridoma Bank; 1:500, mouse (IgG1) anti-calsenillin (type 4 cone bipolar cells; Millipore; 05-756; 1:500), mouse (IgG1) anti- Goα (ON bipolar cells; Millipore; MAB3073; 1:1000), Peanut agglutinin (PNA) (cone pedicle; Molecular Probes; L21409; 1:1000), mouse (IgG2a) anti-GFP (green fluorescent protein; NeuroMab; 75-132; 1:500), rabbit anti-PKCα (rod bipolar cells; Santa Cruz Biotechnology; sc-10800; 1:500). Secondary antibodies were used at a concentration of 1:1000. DAPI was used in PBS at room temperature and was included in the second wash at a dilution of 1:50,000 of a 1 mg/ml stock. Peanut lectin (PNA): PNA, conjugated to alexa 488 or alexa 647, was incorporated into the secondary antibody incubation at a dilution of 1:1000 of the manufacturer's recommended concentration (Invitrogen).

Imaging

Images were taken from multiple microscopes including an Olympus Fluoview 1000 confocal/multiphoton and Nikon spinning disc.

Retina region determination

For much of the imaging and analysis, the retina was divided into regions of central, middle, and periphery. For central retina, the optic nerve was found and then all images were taken within 230 μm of it. In order to find peripheral retina, the far outer edge of the retina was found. Then all images were taken no more than 345 μm towards the optic nerve head. The middle retina was considered the region between 230 μm from the optic nerve head (cutoff point for central retina) and 345 μm from the edge of the retina (cutoff point for peripheral retina).

Image density analysis

Image stacks were carefully taken to ensure that no slices were obtained past the cell bodies of BC4s in the INL. Images were imported into ImageJ software to view (Schindelin et al., 2012). To count BC4 number, the antibody staining for calsenillin was used. All visible cell bodies were counted. Cell bodies were excluded when they did not have dendrites projecting to the OPL, as these were likely amacrine cells. This density value will be referred to as local density throughout this study.

BC4 Analysis

All images used were taken on Nikon spinning disc microscope at 60x (oil immersion) and sampled at 0.3 μm across the z-axis. Any changes made for analysis were done in ImageJ software and done uniformly across the entire image. Images for dendrite arbor analysis were taken from above the PNA location through to the approximate beginning of the IPL. Image Stacks were loaded into ImageJ software for analysis. Total number of BC4 cells and cones were recorded for each image giving us a value for local density. For each image, between 2 and 10 cells were selected for analysis. Only cells that were positive for Ai9 expression were used for whole cell analysis; however the determination of single innervated

(SI) and multiply innervated (MI) cones also included non-Ai9 cells when necessary. In this case the cells were identified with *Htr2a*-GFP or calsenillin staining. A convex polygon was drawn around the soma of the cell to determine its area. Next, the dendrite area was collected by drawing a convex polygon around the entirety of the dendritic arbor. The number of cones contacted was determined by counting the number of PNA-positive cells (cones) where a dendritic arbor from the BC4 of interest forms a contact at. Each cone contacted by the BC4 of interest was then labeled as SI (contacted by only one BC4) or shared (contacted by two or more BC4s). For each BC4, the number of MI cones was divided by the total number of cones contacted to determine the percentage of MI cones. This process was repeated for each BC4 that was selected in the image. *Cell Tracing* was done in ImageJ software using plug in simple neurite tracer (Longair et al., 2011). Using the image stack, the individual neurites were manually traced to create a skeleton on the entire dendritic arbor. This was only done in cells that were Ai9-positive.

Neighboring Cell Overlap; analysis of tiling

Following the analysis of a BC4 (see section 2.7), paired overlap between neighboring cells was analyzed. The convex polygons, or dendritic areas, of two neighboring cells were compared. The amount of space in which they overlapped with determined. This number was divided by the full measure of dendritic area to given a percentage of overlap. If neighboring cells did not overlap in their convex polygon, a value of “0” was recorded.

Cone Predictive Field Assays: Dendrites

We first identified each individual cone that the BC4 of interest made a contact at. All cones were then given a distinction of “single innervated” (SI) or “multiply innervated” (MI). For all MI cones, the other BC4 (or multiple BC4s) was measured for its dendritic area in the same way as the BC4 of interest. Next each cone for the BC4 of interest was given a value equal

to the area of the first BC4 (if SI) or the area of the BC4 of interest plus the area(s) of all other BC4s that contacted it. Next the dendritic area(s) contacting each cone (SI and MI cones) for the BC4 of interest were averaged together to produce a cone projective field. Therefore, the cone projective field was the combined average size of the BC4 dendritic arbor(s) that contacted it.

Cone Predictive Field Assays: Axons

The cone projective field for axons was determined in the following way. Images were taken along the z-axis in the retina from the outer nuclear layer (ONL) to the retinal ganglion cell layer (RGCL). BC4s were chosen based on the visibility of their dendrite arbors and axon arbors. Convex polygons were used to determine the dendrite area and axon area. The area of each individual axon that was measured was characterized as “axon area”. Next, all cones were given a distinction of “SI” or “MI” just as previously described. In situations where an MI cone contacted two (or more) BC4s where both dendrite arbor and axon arbor were also visible, the process was repeated for that cell, then both axons were recorded and summed, then categorized as “MI cone axon projective field”. Following analysis of WT retinas and *Bax* null retinas, we used the percentage of MI cones value to determine how many cones would have an axon projective field of a single BC4, and how many would have an “MI axon projective field”. To do so, we made the predictive axon fields proportional to the percentage of SI cones (average axon area), and the percentage of MI cones (MI axon projected field). Because the percentages were out of a maximum of 100%, we scaled it to 100 cones. For example, the *Bax* null retinas were found to have 31% SI cones and 59% MI cones. Therefore 31 cones were given values equal to the average axon size and 59 cones were given values equal to the average of the ”MI axon projected field” were used. These 100 values were then averaged together to determine our predictive axon field for the local density.

Presynaptic density puncta counts

In order to determine the number of ribbon puncta present at each cone terminal, tissue was stained with antibodies against cone arrestin (to visualize the cone terminal), distroglycan (to label synapses), and PNA (to visualize invaginating contact points). Images were taken on an Olympus Fluoview1000 multiphoton microscope at 60x (oil immersion). Images were classified by central, middle, and peripheral retina. In order to do so, sections were taken with the optic nerve head visible in the cryosection. Immediately adjacent to the optic nerve head was considered central retina (~200 μm). Peripheral retina was considered directly adjacent to the edge of the retina. Any space between these two points was then considered middle retina. While imaging, the zoom feature up to level 3.0 was used depending on tissue sample. The image stacks were imported into ImageJ for evaluation. Points in the tissue where dystroglycan and PNA “overlapped” were counted as one ribbon puncta. The number of ribbon puncta was determined for as many cones as possible in a given image stack which ranged from usually from 5-20 total cones.

Cone volume and PNA volume analysis

Whole mount staining with antibodies against cone arrestin (to label the cone terminals) and PNA (to label invaginating contacts) were used to visualize the cone area and PNA area for analysis. The measurements were conducted simultaneously on the same image stack. First, the image stack was imported into ImageJ software. The image containing PNA labeling was loaded first, and 10 were quickly selected at random throughout the field and saved to an ROI. The ten selected cones were then measured beginning with PNA. A convex polygon was drawn around the outer most edges of the PNA labeling (in a similar manner to the dendrite arbors in previous section describing BC4 analysis). The channels were flipped and the same ten cells were then measured for the cone area using the cone arrestin labeling. Similarly, a convex polygon was drawn around the outer edges of the visible cone terminal.

Any teledenria was ignored and not counted towards the area. At least three images were analyzed from central, middle, and peripheral regions of each retina used.

ON bipolar cell counts.

We determined the number of ON bipolar cells and rod bipolar cells in WT and *Bax* null retinas. We began by labeling cells with antibodies against PKCα (rod bipolar cells) and Goα (all ON bipolar cells). The images were taken on an Olympus scanning laser multiphoton microscope at 60x oil at 4 μm/second with a 1.0 zoom. Central, middle, and peripheral retina was determined in the same way as previously described in retina region determination section. The image stacks were imported into ImageJ software. The channels were combined to form a composite image of the PKCα-positive cells, Go-positive cells, and DAPI (nuclear label) staining. First all Goα-positive cells were counted and saved to an ROI. Then the Goα channel was turned off and all PKCα-positive cells were counted. This gave us the number of rod bipolar cells. The two counts were combined, and all Goα-positive cells that were not also positive for PKCα were considered ON bipolar cells. The length of retina was determined by measuring the portion of the INL that was analyzed. The number of cells counted was divided by the length of the INL to give the value of cells/μm.

Cone smothering

The cone smothering assay was done to determine the ratio of dendritic arbors (via calsenillin staining) to the overall PNA volume of the cone terminal. Image stacks were loaded into ImageJ software. An algorithm was used on images to adjust and normalize their brightness to consistent levels between images. A convex polygon was drawn around the outer most area of the PNA. The drawn PNA area was then combined with the calsenillin positive staining for the same area. Pixels in the drawn area that were also positive for

calsenillin staining were calculated as well as the region that was positive for PNA. From this data, a value of calsenillin labeling was calculated.

Results

Most types of retinal neurons vary in density from the central retina, adjacent to the optic nerve, to the peripheral retina. An increase in non-photoreceptor neuron populations is also observed in the *Bax* KO retina due to the loss of BAX-mediated programmed cell death (PCD) (Ogilvie et al., 1998; Pequignot et al., 2003) (Figure 1 A-B). We took advantage of these differences to determine how OFF BC wiring would respond to changes in cell density and the ratio of OFF BCs to the rods and cones from which they receive synaptic input, focusing on type 4 OFF BCs (BC4s), which could be easily labeled using antibodies and transgenic markers. To quantify the role of cell density in development we divided the retinas into central, middle, and peripheral regions, where we changes in BC4 density from the central (highest) to peripheral (lowest) (Figure 1 C-F). Significant increases in cell number were observed for BC4s when comparing different regions of the *Bax* null and wild type retina (Figure 1 G). Cone density was unaffected by the knockout of *Bax* as previously reported (Figure 1 H) (Ogilvie et al., 1998). The relationship between BC4s and cone number was evaluated by determining the ratio of BC4s per cone and varied over two fold (Figure 1 I).

Differential labeling of BC4s was accomplished using *5Htr2a*-Cre coupled to the ai9 reporter in combination with *5Htr2a*-GFP and the calsenillin antibody, which resulted in labeling of single BC4s against a backdrop of the entire population. Activation of the Ai9 red fluorescent protein (RFP) reporter results in RFP expression in approximately 70% of BC4s in the retina (Figure 2A-C) (Lu et al., 2009). The activation of the Ai9 reporter in BC4s allows for highly fine resolution of individual cells (Figure 2D), including their dendrite area (Figure 2E and F), in the wild type (Figure 2D-F) and *Bax* null retina (Figure 2 G-I).

Having a system to differentially label the afferent connections of a BC population (Figure 3 A), all cells of that population and individual cells allowed us to reconstruct the receptive fields of BC4s in high resolution in the wild type (Figure 3 B) and *Bax* null retina (Figure 3 C). We first measured what influence cell density would have on the number of afferent connections made by each bipolar cell. The number of cones contacted decreased as BC4 density increased (Figure 3G), consistent with results reported for ON BCs (Lee et al., 2011) and no significant difference was detected comparing the wild type and *Bax* null retina. We also measured the frequency at which cones were sampled by more than one BC4. Both wild type and *Bax* null cones were more likely to be contacted by multiple BC4s (multiply innervated; MI) but to our surprise there was also a density-independent increase in the frequency at which *Bax* null cones were contacted by multiple BC4s compared to wild type (Figure 3 H; whole fields and I; all individual cells). We measured if the density of BC4 dendrites at individual cones and found dendrite density to be increased (Figure 3 I and J) comparing *Bax* null cones to wild type using the density of peanut lectin staining, which labels the sites of invaginations made by ON BCs and overlaps with mGluR6 and TrpM1 staining (Koike et al., 2010) to normalize cone volume.

To explore why T4BCs in the *Bax* null retina project additional dendrites to cones we measured other components of the cone synapse. ON BCs project dendrites that invaginate into the cone terminal and we hypothesized that an increase in the number of ON cone BCs could result in changes to the cone synapse. Previous reports show an increase in type 7 ON BCs in the *Bax* null retina (Keeley, 2014; Lee, 2011), a finding that we found to be true of ON BCs generally (Figure 4A-H). The invaginating contacts made by ON BCs can be labeled with PNA, which overlaps with the mGluR receptors produced by ON BCs. We observed a significant increase in the area of the cone terminal covered by PNA (Figure 4 I-K), as well as an increase in the overall size of the cone terminal (Figure 4 L). We next sought to test if

there was an increase in presynaptic elements at the cone synapse and measured the number of foci positive for dystroglycan, a marker localized to the cone synapse. A significant increase in the number of foci positive for dystroglycan was observed in the *Bax* null retina compared to wild type (Figure 4 M-O).

A surprising result of this study is the increased frequency at which wild type and *Bax* null BC4s sampled multiple cones. We found that wild type and *Bax* null cones are both increasingly more likely to be sampled by multiple BC4s as BC4 density increases and that this frequency in the *Bax* null retina is higher regardless of density. To test how these wiring pattern differences influence information flow from photoreceptors we compared the predicted cone projective field by measuring the BC4 dendritic and axonal fields using the middle region of the wild type and *Bax* null retina as test regions. First we mapped wild type and *Bax* null cones to the bipolar cells that they contacted (Figure 5 A-D). We then measured the predicted cone projective field based on the area occupied by BC4 dendrites for singly innervated cones (Figure 5 E) and multiply innervated cones (Figure 5 F). We found that while the dendrite area of *Bax* null BC4 is reduced compared to wild type (Figure 5 G), at the level of the cone this difference disappears because the *Bax* null cones are more likely to be innervated by multiple smaller BC4s (Figure 5 H). We repeated this measurement for axon area and found that the *Bax* null BC4 axon area was significantly smaller (Figure 5 I-K), however the predicted axon projective field from the cones perspective was not significantly different (Figure 5 L).

4. Discussion

The mouse retina contains at least 10 types of retinal bipolar cells that very in their size, organization, and activity (Ghosh et al., 2004; Wässle et al., 2009; Euler et al., 2014;

Behrens et al., 2016; Shekhar et al., 2016). BPCs in the retina organize using homotypic interactions between neighboring cells. Communication between cells establishes boundaries, and there is little overlap in their respective dendritic territories (Wassle et al., 2009; Lee et al., 2011). Additionally, BPCs establish afferent synaptic connections with photoreceptors and efferent synapses with retinal ganglion cells, allowing them to relay signal from the OPL to the IPL (Soucy et al., 1998; Sharpe & Stockman, 1999; Bloomfield & Dacheux, 2001; Tsukamoto et al., 2001; Deans et al., 2002; Mataruga et al., 2007; Haverkamp et al., 2008). Recently, the development of several ON BPCs has been closely observed. BC7s grow large dendrite arbors and overlap with neighbors at cone pedicles before a period of refinement that results in tiling. BC6s and BC8s grow directly to their afferent partners and refinement has not been observed (Dunn & Wong, 2012, Reese). In this study we find that OFF BCs scale their dendrites in response to density and that multiple sampling of cones and a reduction in the dendrite and axon field size results in a conservation of the cone projective field.

We initiated this study by characterizing how differences in BC4 density would influence connectivity with cone photoreceptors using natural variation in the wild type retina and in the *Bax* null retina. The loss of BAX-mediated PCD has been shown to cause cellular spacing and neurite avoidance phenotypes in ACs and RGCs (Keeley et al., 2012, Chen et al., 2012). Previous work in *Bax* null retinas found decreases in dendritic area and the number of cones contacted for ON type 7 bipolar cells (Lee et al., 2011). We observed that the tiling and organization of BC4s was still maintained similarly to what has been reported for ON cells with very little invasion of dendritic territory between cells. In *Bax* null retinas, a slight increase in dendritic territory invasion was observed between neighboring cells ($p=0.009$). Upon further investigation, we found that overlap of dendrite territories would often occur at the cone terminal at which the BC4s were making contacts. When we focused our

attention on connections at the cone between neighboring BC4s, we observed that they would often both innervate the cone terminals between them. With further analysis, we observed that this innervation pattern was normal for BC4s in wild type, but occurred at a higher rate in *Bax* null retinas. So we next turned out attention to the cone terminals.

We hypothesized that the density independent increase in multiple innervation of cones by BC4s could be explained by changes in other components of the synapse. We observed several significant differences to the morphology of the cone terminal in *Bax* null retinas. We used retinal sections to perform an analysis of ON cell number and found a significant increase overall in *Bax* null compared to wild type as previously reported. Due to the increase in ON BC number, we measured ON cell invaginating contacts in two ways. The first was to look at ribbon puncta number by labeling ribbon synapses at the base the cone terminals using a combination of antibody labeling for dystroglycan and PNA. We found an increase in the number of ribbon puncta per cone terminal for *Bax* null retina compared to WT. Looking at whole mounts (N=2), we also found an increase in the area of PNA labeling and an increase in total area of the cone terminal in *Bax* null retinas. These changes to size and number suggest the possibility that there is a feedback mechanism or some sort of communication between the cone and developing BC dendrites. According to this model the increase in size at the cone terminal could result in a greater capacity to establish and keep connections with many BPCs including BC4s.

We were curious as to what the potential effect of this alteration in wiring could have on the relay of signal through the retina. Cones in the mammalian retina relay signal to a large number of BCs, and are generally sampled by one BC of each type. We found that BC4s largely maintained tiling despite the increase in their overall number, they now had significantly smaller dendrite arbors. In the middle retina, we found that the average cone projective fields were not significantly different between wild type and *Bax* null. This appears

to be due to the increased number of MI cones compared to the wild type as MI cones will almost always have larger cone projective fields compared to SI cones. By projecting to two are more BC4s at a higher rate, the original difference in dendrite area is essentially negated. We observed a similar finding at the axons level. Whether this is an actual compensatory mechanism to preserve the projective filed size of the cone, a result of BCs that multiply innervate cones not dying in the *Bax* null retina or a coincident finding will be the focus of future studies.

References

Behrens, C., Schubert, T., Haverkamp, S., Euler, T., & Berens, P. (2016). Connectivity map of bipolar cells and photoreceptors in the mouse retina. *eLife*, *5*, e20041.

Euler, T., Haverkamp, S., Schubert, T., & Baden, T. (2014). Retinal bipolar cells: elementary building blocks of vision. *Nature Reviews Neuroscience*, *15*(8), 507-519.

Ghosh, K. K., Bujan, S., Haverkamp, S., Feigenspan, A., & Wässle, H. (2004). Types of bipolar cells in the mouse retina. *Journal of Comparative Neurology*, *469*(1), 70-82.

Haverkamp, S., & Wässle, H. (2000). Immunocytochemical analysis of the mouse retina. Journal of Comparative Neurology, 424(1), 1-23.

Haverkamp, S., Grünert, U., & Wässle, H. (2000). The cone pedicle, a complex synapse in the retina. *Neuron*, *27*(1), 85-95.

Jeon, C. J., Strettoi, E., & Masland, R. H. (1998). The major cell populations of the mouse retina. *Journal of Neuroscience*, *18*(21), 8936-8946.

Keeley, P. W., & Reese, B. E. (2010). Role of afferents in the differentiation of bipolar cells in the mouse retina. *Journal of Neuroscience*, *30*(5), 1677-1685.

Keeley, P. W., Whitney, I. E., Madsen, N. R., John, A. J. S., Borhanian, S., Leong, S. A., ... & Reese, B. E. (2014). Independent genomic control of neuronal number across retinal cell types. Developmental cell, 30(1), 103-109.

Keeley, P. W., Kim, J. J., Lee, S. C., Haverkamp, S., & Reese, B. E. (2017). Random spatial patterning of cone bipolar cell mosaics in the mouse retina. *Visual Neuroscience*, *34*.

Koike, C., Obara, T., Uriu, Y., Numata, T., Sanuki, R., Miyata, K., … Furukawa, T. (2010). TRPM1 is a component of the retinal ON bipolar cell transduction channel in the mGluR6 cascade. *Proc Natl Acad Sci U S A*, *107*(1), 332–337.

Kolb, H., & Famigilietti, E. V. (1974). Rod and cone pathways in the inner plexiform layer of cat retina. *Science*, *186*(4158), 47-49.

Lee, S. C. S., Cowgill, E. J., Al-Nabulsi, A., Quinn, E. J., Evans, S. M., & Reese, B. E. (2011). Homotypic regulation of neuronal morphology and connectivity in the mouse retina. *The Journal of Neuroscience : The Official Journal of the Society for Neuroscience*, *31*(40), 14126–33.

Longair, M. H., Baker, D. A., & Armstrong, J. D. (2011). Simple Neurite Tracer: open source software for reconstruction, visualization and analysis of neuronal processes. Bioinformatics, 27(17), 2453-2454.

Lu, Q., Ivanova, E., & Pan, Z. H. (2009). Characterization of green fluorescent protein–expressing retinal cone bipolar cells in a 5-hydroxytryptamine receptor 2a transgenic mouse line. Neuroscience, 163(2), 662-668.

Masland, R. H. (2012). The neuronal organization of the retina. *Neuron*, *76*(2), 266-280.

Ogilvie, J. M., Deckwerth, T. L., Knudson, C. M., & Korsmeyer, S. J. (1998). Suppression of developmental retinal cell death but not of photoreceptor degeneration in Bax-deficient mice. *Investigative ophthalmology & visual science*, *39*(9), 1713-1720.

Pequignot, M. O., Provost, A. C., Salle, S., Taupin, P., Sainton, K. M., Marchant, D., ... & Abitbol, M. (2003). Major role of BAX in apoptosis during retinal development and in

establishment of a functional postnatal retina. *Developmental dynamics*, *228*(2), 231-238.

Reese, B. E., & Keeley, P. W. (2015). Design principles and developmental mechanisms underlying retinal mosaics. *Biological Reviews*, *90*(3), 854-876.

Schindelin, J., Arganda-Carreras, I., Frise, E., Kaynig, V., Longair, M., Pietzsch, T., ... & Tinevez, J. Y. (2012). Fiji: an open-source platform for biological-image analysis. Nature methods, 9(7), 676-682.

Shekhar, K., Lapan, S. W., Whitney, I. E., Tran, N. M., Macosko, E. Z., Kowalczyk, M., ... & McCarroll, S. A. (2016). Comprehensive classification of retinal bipolar neurons by single-cell transcriptomics. *Cell*, *166*(5), 1308-1323.

Wässle, H. (2004). Parallel processing in the mammalian retina. Nature Reviews Neuroscience, 5(10), 747-757.

Wässle, H., Puller, C., Müller, F., & Haverkamp, S. (2009). Cone contacts, mosaics, and territories of bipolar cells in the mouse retina. *Journal of Neuroscience*, *29*(1), 106-117.

Figures

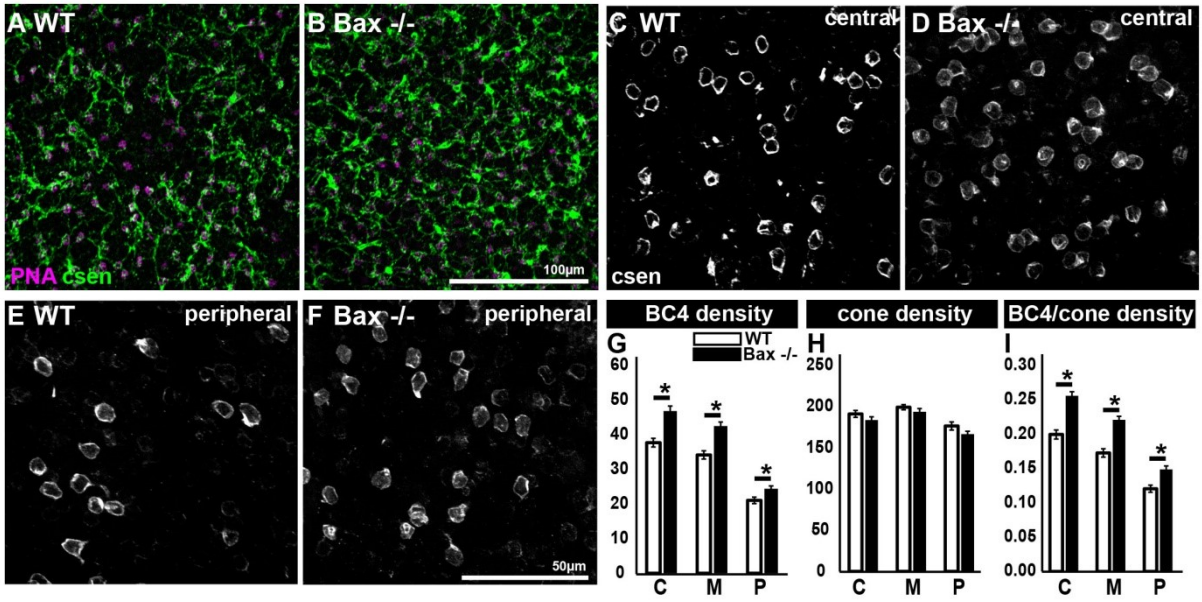

Figure 3.1. Comparison of WT and *Bax* null retinas following loss of Bax-mediated programmed cell death. A-B) Comparison of BC4 dendrites using antibodies against calsenillin (green) in (A) WT and (B) *Bax* null retinas. The density of BC4s varies depending on approximate region of cell. Here we designate central, middle, and peripheral retina regions. **C-D)** BC4 cells at the central retina for WT (C) and *Bax* null (D). **E-F)** BC4 cells in the peripheral retina for WT (E) and *Bax* null (F). **G)** In all three regions, we observed significantly more BC4s in the *Bax* null retina compared to WT. **H)** Consistent with previous findings, cone number is not significantly affected in *Bax* null retina compared to WT. **I)** For all three regions, the ratio of BC4/cone is significantly higher in *Bax* null retina compared to WT. Abbreviations: WT= wild type; BC4= type 4 OFF bipolar cell; C= central retina; M=middle; P=peripheral; csen= calsenillin; PNA= peanut agglutinin. Scale bar in B is equal to 100µm and is the same for A. Scale bar in F is equal to 50µm and is the same for C-E.

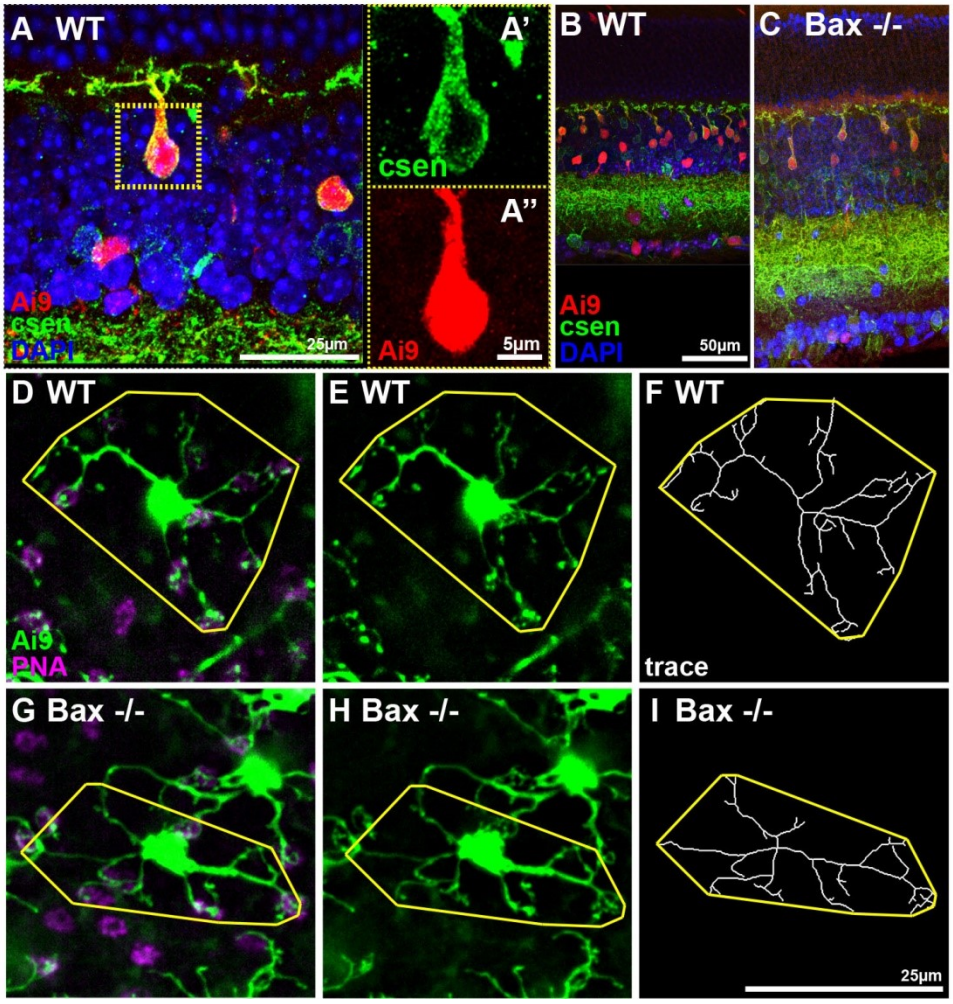

Figure 3.2. LoxP recombination and Ai9 used to target BC4 population in mouse retina. A majority of BC4s express Htr promoter allowing the use of LoxP recombination to drive Cre expression and induce RFP expression in BC4s. **A)** Retina section showing antibodies against calsenillin (green cells; **A'**) and Ai9 recombination (red cells; **A''**) with some BC4s not showing Ai9 recombination. Retina sections show the vertical organization in **B)** WT retina, and **C)** *Bax* null retina (Panel in "C" is a montage consisting of two images). The *Bax* null retina has a thicker INL and RGCL due to loss of Bax-mediated programmed cell death during development. Individual BC4s are visualized with dendritic boundary (yellow lines) and cones contacted (visualized with antibodies against PNA) in the **D-F)** WT retina and **G-I)** *Bax* null retina. Abbreviations: WT= wild type; BC4= type 4 OFF bipolar cell; csen=

calsenillin; PNA= peanut agglutinin. Scale bar in A is equal to 25μm. Scale bar in B is equal to 50μm and is the same for C. Scale bar in I is equal to 25μm and is the same for D-H.

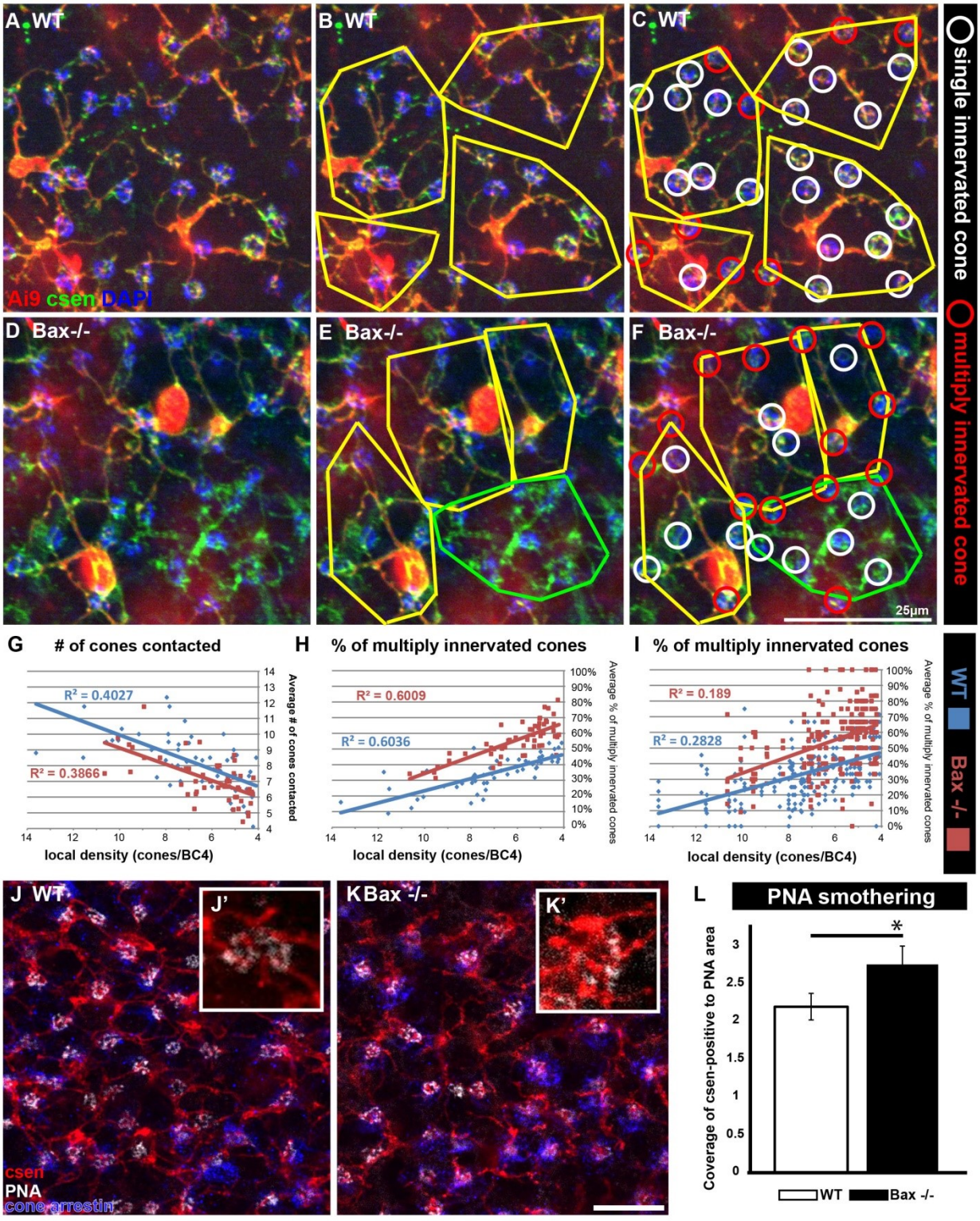

Figure 3.3. Increased cell density minimizes synaptic competition between neighboring BC4 cells in *Bax* null retina. Neighboring cells in WT and *Bax* null retinas

maintained tiling associated with homotypic interactions between like cells during bipolar cell development. However, neighboring cells multiply innervated a higher percentage of cones at the edge of their respective dendritic areas as a result of decreased competition at the cone synapse. **A)** BC4 organization in WT retina**. B)** Dendritic boundary of neighboring WT BC4s shows tiling is maintained and **C)** majority of cones between neighboring cells are innervated by a single BC4 (white circles). **D)** BC4 organization in *Bax* null retina. **E)** Dendritic boundary of neighboring *Bax* null BC4s shows tiling is maintained and **F)** majority of cones between neighboring cells are innervated by multiple BC4s (red circles). The synaptic connections between cones and BC4s is affected by changes in local density of BC4s. **G)** The number of cones contacted by BC4s is correlated with density for both WT (blue diamonds) and *Bax* null (red squares) retinas. As density of BC4s increases, the number of cones contacted decreases for WT (R^2=0.4027) and *Bax* null (R^2=0.3866) retinas. Each symbol represents the average number of cones contacted (2-9 cells total) for a given local density that was analyzed. **H)** As local density of cones/BC4 increases, the percentage of multiply innervated cones also increases for both WT (R^2=0.6036) and *Bax* null (R^2=0.6009) retinas with the percentage of multiply innervated cones consistently higher between neighboring BC4s in *Bax* null retinas. **I)** This trend can still be seen when the presented on a single cell basis: WT (R^2=0.2828) and *Bax* null (R^2=0.1890). **J-K)** Smothering of dendrite area against PNA area was found to be significantly higher in the *Bax* null retina. **L)** Quantification of csen-positive dendrite coverage to PNA area for WT and *Bax* null retinas. Abbreviations: WT= wild type; BC4= type 4 OFF bipolar cell; csen= calsenillin; PNA= peanut agglutinin. Scale bar in F is equal to 25μm and is the same for A-E.

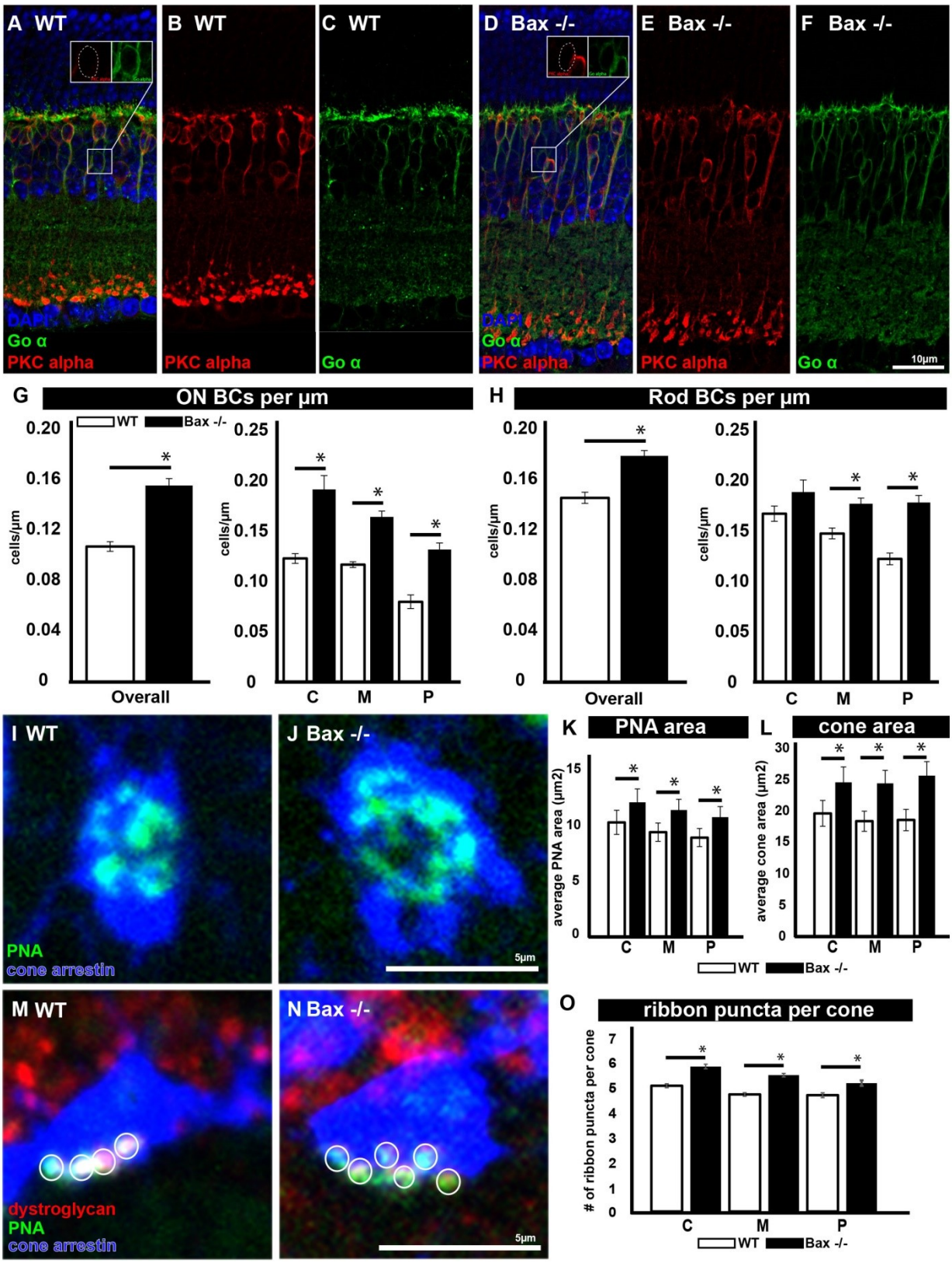
A WT
B WT
C WT
D Bax -/-
E Bax -/-
F Bax -/-
DAPI
Go α
PKC alpha
10μm
G
ON BCs per μm
WT
Bax -/-
cells/μm
Overall
C
M
P
H
Rod BCs per μm
I WT
J Bax -/-
PNA
cone arrestin
5μm
K
PNA area
average PNA area (μm2)
L
cone area
average cone area (μm2)
M WT
N Bax -/-
dystroglycan
O
ribbon puncta per cone
# of ribbon puncta per cone

Figure 3.4. Increased bipolar cell density results in changes at the cone terminal. We present quantification of ON bipolar cell (BPC) differences, PNA area per cone, overall cone area, and the average number of ribbon puncta observed at each cone in WT and *Bax* null retinas. Antibodies against Go α and antibodies against PKC α were used to visualize ON BCs and rod bipolar cells (RBC) respectively. **A-C)** Section of WT retina showing ON BPCs and RBCs. **D-F)** Section of *Bax* null retina showing ON BPCs and RBCs. **G)** Significant increases in the number of ON BPCs was found in the *Bax* null retina compared to WT (evaluated by cells/μm) ($p<0.001$). This was true for comparisons of central, middle, and peripheral regions. **H)** Similarly, we found a significant increase in RBCs in the *Bax* null retina compared to WT ($p<0.001$). **I-J)** Cone Arrestin (rabbit) and PNA were used to determine the area of the cone and area of PNA coverage in WT (I) and *Bax* null (J) retinas. **K)** Overall PNA area per cone was found to be significantly increased in the *Bax* null retina for the central, middle, and peripheral regions (C- $p<0.001$; M- $p<0.001$; P- $p<0.001$). **L)** A significant increase in the average cone area was also found between WT and *Bax* null in central, middle, and peripheral regions (C- $p<0.001$; M- $p<0.001$; P- $p<0.001$). **M-N)** Cone Arrestin (rabbit), Mandag (mouse), and PNA were used to visualize the immuno-positive ribbons in (M) WT and (N) *Bax* null retinas. Each white circle represents a single counted ribbon puncta. **O)** In a comparison of the number of immuno-positive ribbon puncta for WT and *Bax* null retinas, we found a significant increase for all three regions in *Bax* null retinas (C- $p<0.001$; M- $p<0.001$; P-$p=.002$). Abbreviations: WT= wild type; C= central retina; M=middle; P=peripheral; csen= calsenillin; PNA= peanut agglutinin; BC= bipolar cell; RBC= rod bipolar cell. Scale bar in F is equal to 10μm and is the same for A-E. Scale bar in J is equal to 5μm and is the same for I. Scale bar in N is equal to 5μm and is the same for M.

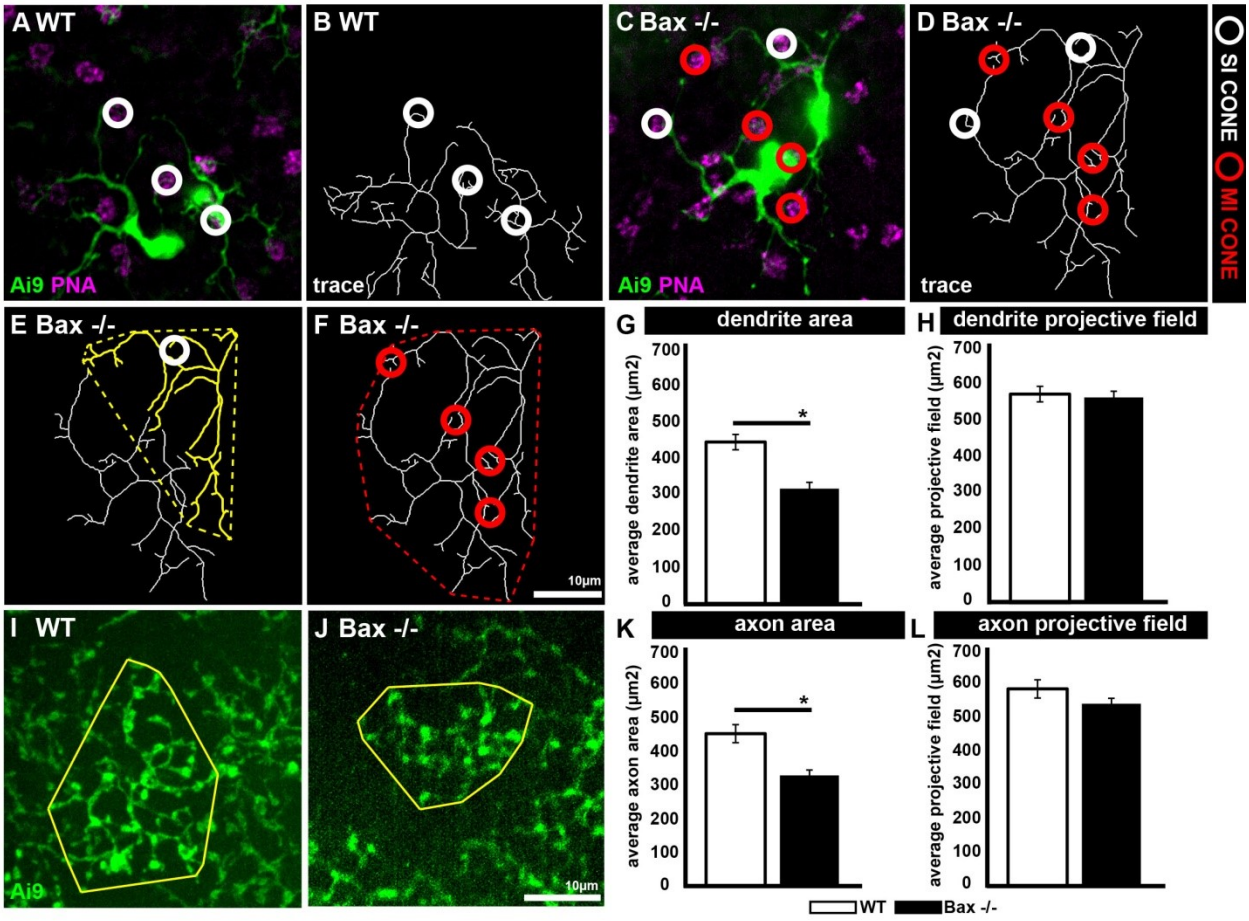

Figure 3.5. The predicted cone field and predicted axon fields are affected by increases in cell density and subsequent increases in multiply innervated cone terminals in the middle retina. A-D) Neighboring cells in the middle retina for WT (A-B) and *Bax* null (C-D) were used to analyze the projective cone field for single innervated cone (SI) and multiply innervated cones (MI). A cone was considered SI if only a single BC4 was contacted, and MI if it was contacted by two or more BPC4s. For A-F, a white circle represents an SI cone, and a red circle represents an MI cone. **E)** We predict that a cone contacting a single BC4 (labeled in yellow to distinguish between neighboring cells) will send a signal to the dendritic arbor (area) associated with that particular cell. **F)** Likewise, we predict that an MI cone will possess a larger dendrite projective field as it is sending signal to two or more BC4s. **G)** For this set of BC4s in the middle retina region, the dendritic area was

found to be significantly larger in the WT retina compared to *Bax* null (p=0.0151). **H)** However, when all SI and MI cones were combined together to get the average dendrite predictive field, there was not a significant difference between WT and *Bax* null retinas (p=0.4601) in cone projective field. **I-J)** We also looked at axons in BC4s in WT (I) and *Bax* null (J) retinas. **K)** Axon area (via convex polygon measurement) was found to be significantly larger in WT retinas compared to *Bax* null (p=0.0002). Additionally, the predicted axon projective field (as determined by the average of SI and MI cones proportional to the average axon size respectively) sizes also showed little difference between WT and *Bax* null . This indicates the possibility of a compensatory mechanism by cones to maintain some consistency in projective field following significant changes in cell density and wiring organization in *Bax* null retinas. Abbreviations: WT= wild type; C= central retina; M=middle; P=peripheral; PNA= peanut agglutinin; SI= single innervated; MI= multiply innervated. Scale bar in F is equal to 10μm and is the same for A-E. Scale bar in J is equal to 10μm and is the same for I.

Chapter 4: DSCAM Promotes Refinement in the Mouse Retina through Cell Death and Restriction of Exploring Dendrites

Shuai Li[1]*, Joshua M. Sukeena[1]*, Aaron B. Simmons[1], Ethan J. Hansen[1], Renee E. Nuhn[1,4], Ivy S. Samuels[2,3], and Peter G. Fuerst[1,4]

1University of Idaho, Department of Biological Sciences, Moscow, Idaho 83844, 2Cole Eye Institute, Cleveland Clinic, Cleveland, Ohio 44106, 3Louis Stokes Cleveland VA Medical Center, Cleveland, Ohio 44195, and 4WWAMI Medical Education Program, Moscow, Idaho 83844

*Co-First Authors

Abstract

In this study we develop and use a gain-of-function mouse allele of the Down syndrome cell adhesion molecule (*Dscam*) to complement loss-of-function models. We assay the role of *Dscam* in promoting cell death, spacing, and laminar targeting of neurons in the developing mouse retina. We find that ectopic or overexpression of *Dscam* is sufficient to drive cell death. Gain-of-function studies indicate that *Dscam* is not sufficient to increase spatial organization, prevent cell-to-cell pairing, or promote active avoidance in the mouse retina, despite the similarity of the *Dscam* loss-of-function phenotype in the mouse retina to phenotypes observed in *Drosophila* Dscam1 mutants. Both gain- and loss-of-function studies support a role for *Dscam* in targeting neurites; DSCAM is necessary for precise dendrite lamination, and is sufficient to retarget neurites of outer retinal cells after ectopic expression. We further demonstrate that DSCAM guides dendrite targeting in type 2 dopaminergic amacrine cells, by restricting the stratum in which exploring retinal dendrites stabilize, in a *Dscam* dosage-dependent manner. Based on these results we propose a single model to account for the numerous *Dscam* gain- and loss-of-function phenotypes reported in the mouse retina whereby DSCAM eliminates inappropriately placed cells and connections.

Introduction

Proper retinal neuron circuitry is achieved by an elegant orchestration of signaling mediated by transmembrane molecules and synaptic activity (Masland, 2012; Randlett et al., 2013; Okawa et al., 2014). Organization of retinal neurites into the inner and outer plexiform layers (IPL and OPL) is accomplished in part by transmembrane semaphorins and their cognate plexin receptors (Matsuoka et al., 2011a,b; Sun et al., 2013). Homophilic cell adhesion molecules, including cadherins (Duan et al., 2014), contactins (Yamagata and Sanes, 2012), Down syndrome cell adhesion molecules (Dscams), and sidekicks (Yamagata and Sanes, 2008), regulate neurite targeting through adhesion. Avoidance is also essential for development of the retina, with multiple EGF-like domains proteins (Kay et al., 2012), DSCAMs (Fuerst et al., 2009), and the γ-protocadherin proteins (Lefebvre et al., 2012) required to prevent interactions.

As noted, DSCAM proteins provide both adhesive and repulsive developmental cues. DSCAM proteins have been most thoroughly studied in *Drosophila*, where the splice diversity of Dscam1 (Schmucker et al., 2000; Neves et al., 2004) facilitates neuron-specific avoidance (Chen et al., 2006), synaptic pairing (Zhu et al., 2006), neurite outgrowth (Hutchinson et al., 2014), and projection of axon collaterals (He et al., 2014). Extensive *Dscam* alternative splicing is not observed in non-insect model organisms (Schmucker and Chen, 2009), and yet many of the functions Dscam1 mediates in *Drosophila* are conserved in other systems. Dscam plays a role in synaptic pairing in *Aplysia* (Li et al., 2009), and mediates axon guidance in zebrafish (Yimlamai et al., 2005), chick (Ly et al., 2008), mouse (Liu et al., 2009), and *Xenopus* (Morales Diaz, 2014). Importantly, requirements for *Dscam* in avoidance in mouse (Fuerst et al., 2008, 2009) and targeting in chick (Yamagata and Sanes, 2008, 2010) have been identified in development of the retina.

These roles are consistent with findings that implicate *Dscam* in contributing to human neurological disorders. Changes to the branching and spine density of cortical neurons observed in *Dscam* mutant mice mirror changes observed in humans with Down syndrome (DS) (Maynard and Stein, 2012). This is further supported by overexpression studies in hippocampal neuron cultures, in which DSCAM inhibits branching (Alves-Sampaio et al., 2010). Misregulation of *Dscam* levels in fragile X syndrome has also been linked to synaptic defects and mistargeting (Cvetkovska et al., 2013; Kim et al., 2013). *Dscam* dose-dependent phenotypes have been identified in the visual system (Blank et al., 2011) and

people with DS have a high incidence of visual deficiency (Creavin and Brown, 2009). Given the large number of disorders associated with *Dscam*, it is essential to determine the precise nature of the gene's function in model organisms.

Here we report that *Dscam* is sufficient to drive cell death but not avoidance in the mouse retina. Gain- and loss-of-function analysis is then combined to assay *Dscam* function in neurite targeting and refinement. We find that mouse *Dscam* is both necessary and sufficient to target retinal neurites. We further demonstrate mechanisms by which DSCAM promotes refinement of dendrites.

Materials and Methods

DSCAM^{FLOXGOF} Mice.

A conditional expression construct with a dual fluorescent reporter under control of the CAG promoter was generated. The backbone of this construct is the pCAG-IG (Internal Ribosome Entry Sequence GFP) plasmid (obtained from Addgene; courtesy of Dr. Connie Cepko; Matsuda and Cepko, 2004). A floxed tandem dimer RFP was PCR amplified from the brainbow 2.1 plasmid, including the poly-A sites from the pcDNA series vectors (obtained from Addgene; courtesy of Dr. Joshua Sanes; Livet et al., 2007). This sequence was inserted into the EcoRI/NotI sites of the pCAG-IG plasmid (NCBI Bankit ID: 1714400). Full-length mouse *Dscam* was amplified from mouse brain cDNA in four individual segments and inserted into the vector pSL1180 (courtesy of Drs. Daniel Voytas and Robert Burgess; NCBI Bankit ID: 1714413). DNA was linearized to remove the viral replication sequences incorporated into the CAG series of plasmid and then microinjected into one-cell mouse embryos by the University of Washington transgenic facility. Five founders were generated from 150 injections. All experiments in this manuscript were performed with mice resulting from a single founder to ensure consistency of expression. This strain is available through The Jackson Laboratory (stock number: 025543).

Mouse Strains and Handling.

*Pax6*α-Cre mice effectively targeted the *Dscam*^{floxGOF} transgene in retinal neurons and Müller glia in the lateral retina, while inactivation of RFP and expression of *Dscam* and GFP was limited to a subset of amacrine cells in a dorsoventral wedge of the retina, as previously reported by others (Stacy et al., 2005; Lefebvre et al., 2008). At the margins of these two domains mixed columns in which only amacrine cells were targeted or in which all neurons

and Müller glia were targeted were often observed intermixed. *Dscam*^{2J} mice, which do not make a DSCAM protein that is detectable by either Western blot analysis or immunohistochemistry, were used in physiology experiments (Schramm et al., 2012; de Andrade et al., 2014). *Dscam*^{FD} mice are derived from germline targeting of a previously reported conditional allele of *Dscam* and were used in all experiments except for physiology recordings (Fuerst et al., 2012). The exon encoding the *Dscam* transmembrane domain was flanked by loxP sites, and was deleted in this allele, and as a result the protein fails to target to the plasma membrane. Both *Dscam*^{FD} and *Dscam*^{2J} alleles are referred to as *Dscam* loss-of-function (*Dscam*^{LOF}) to contrast them with the gain-of-function allele (*Dscam*^{GOF}). *Dscam*^{LOF} refers to homozygous mutants, while heterozygotes are referred to as *DscamLOF*$^{J+}$. Bax-null mice were acquired from The Jackson Laboratory (Knudson et al., 1995). TH-GFP mice express GFP brightly in type 2 dopaminergic amacrine cells (DACs) and more dimly in type 1 DACs (Knop et al., 2011). TH-GFP mice were a kind gift from Dr. Suzy Appleyard, Washington State University. All mice were housed on a 12 h light/dark cycle and fed *ad libitum*. Mice used in this study were maintained on a mixed C57 BL/6J, C3H/HeJ, and 129/P background except for mice carrying the *Dscam*^{2J} allele, which are carried on an inbred C3H/HeJ background. The defective allele of *Pde6b* was crossed out of the C3H/HeJ mice. Mice of either sex were used for analysis in all experiments. All procedures performed on mice used in this study were approved by the University of Idaho Animal Care and Use Committee or by the Cleveland Clinic Institutional Animal Care and Use Committee and were in accordance with the Institute for Laboratory Animal Research Guide for Care and Use of Laboratory Animals.

Genotyping.

Tissue biopsies were boiled in sodium hydroxide and neutralized in Tris Cl, pH 5.0. PCR was performed using one-shot master mix supplemented with primers. Genotyping has previously been described for all strains (Fuerst et al., 2010, 2012). *Dscam*^{GOF} mice were genotyped by the presence of RFP (carries transgene), GFP (carries recombined transgene), or no fluorescent protein (does not carry the transgene).

Immunocytochemistry and immunohistochemistry.

Mice were perfused with PBS. Retinas were hemisected and fixed in 4% PFA for either 30 min at room temperature (worked for all staining except for DSCAM) or for 50 min on ice (worked for all staining but is suboptimal for staining of some cytoplasmic proteins). Tissues

to be embedded in wax were fixed in 1:3 acetic acid:methanol for 2–12 h (paraffin sections gave equivalent antibody staining except for DSCAM, melanopsin, and vglut3 staining). Tissue was stained as previously described (de Andrade et al., 2014).

Antibodies and Stains.

Mouse anti-DSCAM (R&D Technologies; MAB36661; 1:25), rabbit anti-cone arrestin (cones; Millipore; AB15282; 1:5000), rabbit anti-recoverin (rods; Millipore; AB5585; 1:2000), rabbit anti-Iba1 (microglia; Wako; 1:500), rabbit anti-Dab1 (AII-amacrine cells; generous gift from Brian Howell; 1:500), goat anti-ChAT (starburst amacrine cells; Millipore; AB144P; 1:400), rabbit anti-calbindin (horizontal cells; Swant; CB38a; 1:1000), rabbit anti-bNOS (bNOS-amacrine cells; Sigma-Aldrich; NZ280; 1:15,000), mouse anti-PKCα (rod bipolar cells; Santa Cruz Biotechnology; sc8393; 1:500), mouse anti-HCN4 (type 3A cone bipolar cells; Alomone Labs; 1:500), mouse anti-PKARIIβ (type 3B cone bipolar cells; BD Biosciences; P54720; 1:500), mouse anti-dystroglycan (OPL synapses; Developmental Studies Hybridoma Bank; 1:500), rabbit anti-TH (type 1 DACs; Millipore Bioscience Research Reagents; 1:500), mouse anti-GS (Müller glia; BD Transduction Laboratories; 610517; 1:2000), mouse anti-PSD-95 (OPL synapses; NeuroMab; 75-028; 1:200), rabbit anti-melanopsin (melanopsin-positive retinal ganglion cells; generous gift from Ignacio Provencio; 1:5000), mouse anti-TH (type 1 DACs; Novacastra; 1:50), guinea pig anti-vglut3 (vglut3-amacrine cells; Millipore; 1:5000), and rabbit anti-phosphohistone H3 (Cell Signaling Technology; 1:500). DAPI reagent was mixed into the second wash after incubation with secondary antibodies at a dilution of 1:50,000 of a 1 mg/ml stock. DRAQ5 (Cell Signaling Technology) was used at a 1:1000 dilution incorporated with secondary antibodies. For TUNEL staining sections were stained with an *in situ* cell death kit (Roche). Secondary antibodies were acquired from Jackson ImmunoResearch and used at a concentration of 1:1000.

Cell Counts.

Tissue was coded before analysis and counts were performed in a blinded fashion. TUNEL or phosphohistone H3 (pH3)-positive cells were counted in images of retina sections. The position of TUNEL-positive cells was recorded based on which of the three retinal layers they were localized within. Cell type counts: Müller glia, type 1 and 2 DACs, AII amacrine cells, horizontal cells, and starburst amacrine cells were counted in at least four whole retinas. Other cell types were counted in at least four sections from at least three retinas and normalized per length of retina. Nuclei counts: retinal sections were stained with DRAQ5 and

imaged intermediate between the optic nerve and periphery. Columns of cells in the outer nuclear layer, inner nuclear layer, and retinal ganglion cell layer were counted in four areas for each of nine images collected from three different retinas. The number of cells in the IPL was counted for each image in a given area. For type 2 DAC lamination analysis the number of type 2 DAC cells that have dendrites running through S1, both those that terminate in S1 and those that later ascend to S3, were counted in at least six sections from at least three retinas for each age and genotype and reported as the percentage of cells that extend dendrites into S1. Each cell was given a binary value depending on whether it projected dendrites into S1. These numbers were used to test the significance using a Student's *t* test.

Microscopy.

An Olympus DSU spinning disk confocal microscope and Olympus FluoView confocal microscope were used to capture all fluorescent images. A Nikon epifluorescent microscope was used to capture images of H&E sections. Any modification to images, for example, to brightness, was performed across the entire image in accordance with the journal's standards.

Density recovery profile, nearest neighbor analysis, and voronoi analysis.

Spacing analysis was conducted as previously described (Rodieck, 1991; Khiripet et al., 2012). Density recovery profile (DRP) analysis is a measure of the tendency of cells of the same subtype to occupy space located in close proximity to other cells of the same subtype. Cells that avoid cells of the same subtype result in a DRP that includes an exclusion zone, which is evidenced by annuli cell densities that fall below the average cell density. To control for cell density, the packing index was used in statistical tests. The packing index is a measure of organization compared with the most highly spaced possible organization of a given number of cells, that is, if cells were arranged in a hexagonal pattern. Nearest neighbor analysis (NNA) measures the distance from one cell to the nearest cell of the same subtype, which is increased compared with random simulations if cells space themselves to avoid cells of the same subtype. To control for cell density the nearest neighbor regularity index (NNRI) was used in statistical tests. Spacing of cells using Voronoi analysis measures the regularity of spacing with respect to cells of the same subtype. The Voronoi domains (VDs) of different populations can be compared using the coefficient of variance (CoV), the ratio of the SD to the mean.

The programs winDRP or Ka-me (Khiripet et al., 2012) were used to assay the spacing of type 1 and 2 DACs, AII amacrine cells, horizontal cells, and starburst amacrine cells. Whole retinas were imaged in analysis of type 1 and 2 DACs. The -640^2 μm fields of OFF starburst amacrine cells, AII amacrine cells, and horizontal cells were sampled from dorsal, ventral, and lateral planes midway between the optic disk and periphery of the retina. A minimum of six fields sampled from at least three mice was used for each analysis.

Electron microscopy.

Retinas were fixed in cacodylate/glutaraldehyde buffer. Serial electron micrographs were taken at 7 nm resolution every 40–60 nm by Renovo Imaging. Representative synapses were identified by analyzing serial images of rod and cone photoreceptors.

ERG.

After overnight dark adaptation, mice were anesthetized with ketamine (80 mg/kg) and xylazine (16 mg/kg). Eye drops were used to anesthetize the cornea (1% proparacaine HCl) and to dilate the pupil (2.5% phenylephrine HCl, 1% tropicamide, and 1% cyclopentolate HCl). Mice were placed on a temperature-regulated heating pad throughout the recording session.

Strobe flash ERGs were recorded using a stainless steel electrode in contact with the corneal surface. Needle electrodes were placed in the cheek and the tail for reference and ground leads, respectively. Dark-adapted responses were presented within an LKC Ganzfeld and recorded using flash intensities that ranged from −3.6 to 2.1 log cd s/m^2. Stimuli were presented in order of increasing intensity, and the number of successive responses averaged together decreased from 20 for low-intensity flashes to 2 for the highest intensity stimuli. Conversely, the duration of the interstimulus interval increased from 4 s for low-intensity flashes to 90 s for the highest intensity stimuli. Following completion of the dark-adapted responses, a steady rod-desensitizing adapting field (1.5 log cd/m^2) was presented within the Ganzfeld bowl. After allowing a 7 min period of light adaptation, cone ERGs were recorded to flashes superimposed on an adapting field. Flash intensity ranged from −0.8 to 1.9 log cd s/m^2, and responses to 25 flashes were presented at 2.1 Hz and averaged at each intensity level. Responses were differentially amplified (0.3–1500 Hz), averaged, and stored using a UTAS E-3000 signal averaging system (LKC Technologies).

ERG Analysis.

The amplitude of the a-wave was measured at 8 ms after flash presentation from the prestimulus baseline. The amplitude of the b-wave was measured to the b-wave peak from the a-wave trough.

Western Blot Analysis.

Western blot analysis was performed as previously described with the following modifications (Schramm et al., 2012): 30 µg of total protein, including both the cytosolic and membrane fractions, was loaded into each well, and protein was transferred to a nitrocellulose membrane.

IPL lamination analysis

The locations of the inner nuclear layer, retinal ganglion cell layer, and peak intensities of the cholinergic amacrine cell dendrites in S2 and S4 were used to demarcate the IPL into strata for analysis. Peak intensity and band percentages were automatically segmented using custom software run in R based on the location of cholinergic amacrine cell dendrites, the retinal ganglion cell layer, and the inner nuclear layer. Nine images from each genotype were analyzed. Mann–Whitney *U* test *p* value thresholds for significance (0.01) were determined by comparing groups of wild-type retina sections to each other and setting the threshold below values observed in these tests. Tissue was coded before analysis and lamination analysis was performed in a blinded fashion.

Cell culture

Amacrine cells were grown in culture as previously described (Kunzevitzky et al., 2013). Cells were collected at P2 and incubated 2 d before being fixed and stained for DSCAM.

Results

Generation of a conditional *Dscam* gain-of-function mouse model

We generated a gain-of-function mouse model of *Dscam* to extend analysis of phenotypes identified in studies using loss-of-function models (Fuerst et al., 2008; Maynard and Stein, 2012). We generated a transgenic mouse model that conditionally expresses *Dscam* under control of the constitutive CAG promotor (Miyazaki et al., 1989). This allele, denoted as $Dscam^{floxGOF}$ before Cre-mediated recombination, expresses either

RFP, or *Dscam* and GFP, after Cre-mediated recombination removes the RFP sequence (Fig. 1*A*). Mice produced by germline activation of *Dscam* expression (*Dscam*^{GOF}) are viable and fertile, though smaller than littermate controls (Fig. 1*B*; quantified at P11: WT 9.09 ± 1.8 g SD vs 4.25 ± 1.08 g SD; *t* test < 0.0001; *n* = 28), and exhibit circling behavior. The transgene is expressed throughout the retina, the focus of this study (Fig. 1*C*). Increased DSCAM protein was detected in tissue lysates and sections collected from *Dscam*^{GOF} mice, including tissues in which the protein is absent or present in low concentrations such as heart (Grossman et al., 2011), and neural tissues (Fig. 1*D*; data not shown). Tissue-specific conditional activation of recombination was achieved, and resulted in elimination of RFP and production of DSCAM in areas in which Cre recombinase was expressed (Fig. 1*E*). Localization of DSCAM protein in the *Dscam*^{GOF} retina is very similar to the DSCAM localization pattern observed in the wild-type retina (de Andrade et al., 2014; Fig. 1*F*), except for the presence of DSCAM protein in the outer limiting membrane of the *Dscam*^{GOF} allele (Fig. 1*E*, arrows).

To confirm that the *Dscam*^{GOF} allele makes functional protein we complemented the dendrite and soma clumping phenotype associated with the *Dscam*^{LOF} allele. The cell bodies and dendrites of melanopsin-positive retinal ganglion cells (mRGCs) and type 1 DACs are spaced and arborized, respectively, in the wild-type retina (Fig. 1*G*,*H*). Clumping phenotypes observed in the *Dscam*^{LOF}retina (Fig. 1*I*,*J*) were rescued by the *Dscam*^{GOF} transgene, demonstrated for both cell types (Fig. 1*K*,*L*).

Using the gain-of-function allele alongside previously developed loss-of-function alleles, we set out to assay *Dscam*^{LOF} phenotypes by testing the protein's role in (1) developmental cell death, (2) avoidance and cell spacing, and (3) dendrite lamination and refinement.

Gain-of-function analysis confirms *Dscam* expression is sufficient to drive cell death

In the first part of this study we examined the role of *Dscam* in developmental cell death using *Dscam*^{LOF} and *Bax*-null alleles in conjunction with the *Dscam*^{GOF} model.

A decrease in cell death was previously reported in the *Dscam*^{LOF} retina (Fuerst et al., 2008). Compared with the wild-type, the *Dscam*^{GOF} retina displayed a decrease in cell number at postnatal stages, in addition to aberrant pockets of rods and microglia mixed in with the photoreceptor inner and outer segments (observed in every retina section; Fig. 2*A*,*B*,

arrowheads). Cells were identified based on immunoreactivity with recoverin but not cone arrestin, which accounted for most cells, or with Iba1 (data not shown). To test if increased *Dscam* expression levels promote cell death we investigated whether the reduction in cell number in the $Dscam^{GOF}$ retina was due to changes in cell birth, cell death, or both, by counting the number of dividing and apoptotic cells during development (Fig. 2*C*,*D*). A significant increase in cell death, but not cell birth, was observed at time points aligned with the points at which normal developmental cell death occurs in the mouse retina (Fig. 2*E*). Apoptosis of misplaced rods (Fig. 2*B*, arrowheads) at P15 (Fig. 2*E*, ONL P15) and beyond resulted in the elimination of the cell clusters by 8 months of age (Fig. 2*F*). Individual cell populations were counted to determine whether *Dscam* expression level selectively increased cell death in different cell populations. A significant decrease in most cell types of the inner retina was observed compared with wild-type (Fig. 2*G*). Of note, the one neuron type that was not reduced in number in the inner retina, the type 1 DAC, is also unchanged in total number in the $Dscam^{LOF}$ retina (Keeley et al., 2012). These results indicate that *Dscam* expression is sufficient to drive developmental cell death.

We next sought to test if BAX, a terminal activator of cell death that accounts for most cell death in the inner, but not outer, retina (Péquignot et al., 2003), was responsible for the increased apoptosis in the $Dscam^{GOF}$ mouse. Cell number was quantified in wild-type, $Dscam^{LOF/+}$, $Dscam^{LOF}$, *Bax*-null ($Bax^{-/-}$), $Dscam^{LOF}/Bax^{-/-}$, $Dscam^{GOF}$, and $Dscam^{GOF}/Bax^{-/-}$ retinas (Fig. 3*A*–*G*). We first quantified the presence of misplaced neurons in the IPL. Loss of *Dscam* or *Bax* resulted in a significant increase in the number of neurons located in the IPL (Fig. 3*H*). Elimination of both genes resulted in a significant additive increase in the number of neurons in the IPL, while a significant reduction in IPL cell number was detected in the $Dscam^{GOF}/Bax^{-/-}$ retina compared with the $Bax^{-/-}$ retina. This revealed that DSCAM and BAX can independently function to eliminate misplaced cells.

Next we assayed cell number in the three nuclear layers of the retina. No significant difference in the number of cells in the outer nuclear layer (ONL) was detected when comparing any of these genotypes (Fig. 3*I*, ONL; wild-type cell number values are provided in the figure legend; misplaced cells in the $Dscam^{GOF}$ subretinal space were not included in counts). Notable significant differences were detected within the inner retina. We found a significant increase in cell number in the $Dscam^{LOF}/Bax^{-/-}$ retina compared with the $Dscam^{LOF}$ or $Bax^{-/-}$ retina (INL), and decreases in cell number when comparing the $Dscam^{GOF}/Bax^{-/-}$ retina to the $Bax^{-/-}$ retina [INL and retinal ganglion layer (RGL); Fig. 3*I*].

This revealed that DSCAM and BAX can independently drive cell death in the retinal nuclear layers. A significant rescue of cell number comparing the *Dscam*^{GOF}/*Bax*$^{-/-}$ retina to the *Dscam*^{GOF} retina was also detected (Fig. 3*I*). This indicated that although *Dscam* can influence cell number independent of *Bax*, *Bax*-dependent cell death is the main driver of *Dscam*-mediated changes in cell number in the *Dscam*^{GOF} retina. These results are consistent with findings that DSCAM promotes cell death by acting through BAX and at least one other cell death pathway, and that this additional pathway is sufficient to decrease disorganization by elimination of misplaced cells.

Gain-of-function analysis indicates DSCAM is not sufficient to drive cell spacing and avoidance in the mouse retina

In the second part of this study we set out to test if *Dscam* can drive avoidance. *Dscam* is required to prevent cell type-specific adhesion in the dendrites and soma of mouse retinal neurons. Dscam1 in *Drosophila* is required to mediate repulsion, in which case the protein actively promotes avoidance of dendrites extending from the same cell (Hughes et al., 2007). To test if mouse DSCAM is sufficient to promote soma and dendrite avoidance, we extended previous spacing analysis comparing *Dscam*^{LOF} alleles and wild-type to the *Dscam*^{GOF} allele. Spacing analysis was performed on starburst amacrine cells (SACs) and horizontal cells (HCs), two retinal neuron types that do not normally express *Dscam* or its homolog *Dscaml1* (de Andrade et al., 2014). We also assayed spacing of type 1 DACs, which express and require *Dscam* for normal spacing, and AII amacrine cells, which express and require *Dscaml1* for normal spacing. Spatial organization was measured by DRP analysis, NNA, and VD analysis (see Materials and Methods; Rodieck, 1991; Reese and Keeley, 2014).

Spatial organization of SACs was decreased by expression of *Dscam*, and this decrease correlated with a reduction in cell density (Fig. 4*A*,*B*,*E*). Rescue of lost cells in the *Dscam*^{GOF}/*Bax*$^{-/-}$ retina eliminated spacing defects as measured by DRP and Voronoi analysis, but not NN analysis (Fig. 4*C*–*E*). This indicated that disruption of SAC spatial organization in the *Dscam*^{GOF}retina was largely the result of cell death, and that in the absence of this cell death, spatial organization remained equivalent to or less than wild-type. Spacing of HCs was also analyzed. HCs project neurites that overlap extensively in the wild-type retina, and this overlap was still evident in the *Dscam*^{GOF} retina (Fig. 4*F*,*G*). There was also no significant increase in the spatial organization after expression of *Dscam* in these

cells. Instead, we found a slight decrease in the NNRI observed in the *Dscam*^{GOF} retina compared with wild-type (Fig. 4*F–H*). These results indicate that ectopic expression of *Dscam* is not sufficient to increase the organization of the spacing of these cell types.

Next we assayed soma placement and dendrite organization of type 1 DACs and AII ACs, which express and require *Dscam* or *Dscaml1*, respectively, for normal spacing and dendrite arborization.

We had previously speculated that both *Dscam* and *Dscaml1* were required in the retina to facilitate spacing and avoidance, while their differential expression would allow close interactions, for example, between type 1 DACs and AII ACs (Fuerst et al., 2009). Therefore, we assayed if these interactions continued to form after expression of *Dscam* in AII ACs. Type 1 DACs continue to make contacts with AII ACs in the *Dscam*^{GOF} retina, despite the expression of *Dscam* in these cells in the *Dscam*^{GOF} retina (Fig. 4*I*,*J*, arrows). Extensive overlap of type 1 DAC dendrites also continued in the *Dscam*^{GOF} retina (Fig. 4*I*,*J*). This indicates that *Dscam* expression from the *Dscam*^{GOF} transgene is not sufficient to prevent interactions between or within the assayed cell types.

The spacing of wild-type and *Dscam*^{GOF} type 1 DACs was not significantly different compared with each other, with both being significantly different from random simulations in the case of nearest neighbor analysis (Fig. 4*M*). Interestingly, type 1 DACs require *Bax* for normal spacing, and elimination of *Bax* has previously been shown to disrupt spacing of these cells (Keeley et al., 2012). This spacing defect is not rescued by the *Dscam*^{GOF} transgene and both *Bax*-deficient genotypes had nearest neighbor regularity values that were not significantly different from random controls (Fig. 4*K–M*). We also assayed spacing of AII ACs, which were reduced in number in the *Dscam*^{GOF} retina (Fig. 2*G*). Increased cell death resulted in a decrease in AII AC density (Fig. 4*N*,*O*), but this did not change the spatial organization of this cell type (Fig. 4*P*).

These results indicate that DSCAM is not sufficient to drive spatial organization, inhibit dendrite crossing within cell types, or prevent cell-to-cell pairing between AII and DACs. Pairing between AII amacrine cells and rod or cone bipolar cells was also intact in the *Dscam*^{GOF} retina (data not shown). This suggests that *Dscam* loss-of-function phenotypes do not reflect an active role for mouse DSCAM in repulsion or avoidance in the mouse retina.

DSCAM and dendrite lamination

In the third part of this study we investigated the influence of DSCAM on dendrite targeting by testing if the protein is necessary and sufficient to direct placement of dendrites. DSCAM has previously been demonstrated to direct neurite placement in the chick retina, in which the protein is concentrated in a single stratum of the IPL, S5 (Yamagata and Sanes, 2008). We therefore tested whether broadly distributed DSCAM in the mouse retina functioned in a similar manner. We then extended this analysis and demonstrated a mechanism by which the widely distributed DSCAM protein is able to act in dendrite targeting.

DSCAM and BAX are necessary to restrict dendrite placement in the mouse inner retina

Similarities between the *Bax* and *Dscam* mutant retinas have previously been reported, consistent with both proteins' role in cell death (Keeley et al., 2012; Chen et al., 2013). Because *Dscam* and *Bax* regulate cell death in an additive manner (Fig. 3), we hypothesized that compensatory activity of these proteins could promote dendrite lamination by redundantly eliminating cells that misproject dendrites. We reasoned that this could generate the weak dendrite lamination phenotypes observed in either mutant retina. To test this hypothesis, we quantified lamination in the IPL based on the convention of dividing the IPL into five stratum established by Ramon y Cajal (1893) (Fig. 5*A*). Lamination of dendrites spanning these stratum (Fig. 5*B*) was quantified, using the ON and OFF SAC dendrite bands to set S2 and S4, with each of the five strata further subdivided into an inner and outer band (for example, S1 inner and S1 outer). The percentage of dendrites in each stratum was measured using software to automate band demarcation based on peak intensity of cholinergic dendrites and the boundaries of the RGL and INL (see Materials and Methods section for more details). These percentages were then used to quantify differences in lamination when comparing across genotypes. This method of quantification precluded analysis of the $Dscam^{GOF}$ genotype because SAC dendrites collapsed into a single band (Fig. 5*C*, arrow), laminar banding was very inconsistent in these mice, and because dendrites often projected into spaces where RGCs would otherwise be localized (Fig. 5*D*, arrow). Despite the loss of precisely stratified lamina, dendrites in the $Dscam^{GOF}$ retina qualitatively projected to the same lamina as their wild-type counterparts (Fig. 5*C*–*E*).

Laminar targeting of neurites was plotted and quantified for the wild-type, *Bax*$^{-/-}$, *Dscam*^{LOF}, *Dscam*^{LOF}/*Bax*$^{-/-}$, and *Dscam*^{GOF}/*Bax*$^{-/-}$ genotypes (Fig. 5*F*). Significant differences in the lamination of bNOS amacrine cells were not detected when comparing wild-type and *Bax*$^{-/-}$retinas (Fig. 5*G*); however, significant differences in dendrite targeting were detected in two layers of both the *Dscam*^{GOF}/*Bax*$^{-/-}$ retina and the *Dscam*^{LOF} retina compared with wild-type (Fig. 5*G*). Significant differences were also detected in dendrite targeting in 6 of the 10 layers in the *Dscam*^{LOF}/*Bax*$^{-/-}$ retina compared with wild-type, consistent with *Bax* and *Dscam* acting to redundantly refine dendrite lamination (Fig. 5*G*).

Limited disorganization of the lamination of type 1 DAC neurites was observed in the *Bax*$^{-/-}$, *Dscam*^{LOF}, and *Dscam*^{GOF}/*Bax*$^{-/-}$ retinas compared with wild-type, with an increase in the number of neurites (presumably axons) projecting into the INL of these genotypes (Fig. 5*H*). Distribution of type 1 DAC dendrites was increased in both of the OFF strata (S1 and S2) of the *Dscam*^{LOF}/*Bax*$^{-/-}$ retina compared with wild-type (Fig. 5*H*).

An increase in the number of ectopic vglut3-positive AC dendrites projecting to a single layer was detected in the *Bax*$^{-/-}$ retina compared with wild-type (Fig. 5*I*). Conversely, a decrease in the number of vglut3-positive AC dendrites laminating at their native targets, along with an increase in the number of ectopic dendrites, was detected in the *Dscam*^{LOF} and *Dscam*^{LOF}/*Bax*$^{-/-}$ retinas compared with wild-type (Fig. 5*I*). A decrease in the number of vglut3-positive AC dendrites laminating at their native targets was detected in the *Dscam*^{GOF}/*Bax*$^{-/-}$ retina compared with wild-type, but a corresponding increase in ectopic dendrites was not detected.

These results indicate that DSCAM is required for neurite targeting in the mouse retina, an environment where the protein is widely distributed (Fig. 1*F*), and that *Bax*-dependent cell death limits this phenotype in the *Dscam*^{LOF} retina.

DSCAM is sufficient to retarget outer retinal circuitry

DSCAM is widely localized in the mouse IPL, and we therefore turned to the OPL to better test if ectopic *Dscam* expression could retarget neurites. HCs mistargeted neurites into both the IPL and ONL of the *Dscam*^{GOF} retina: close to one-quarter of HCs projected a bipolar cell-like axon into the IPL of the *Dscam*^{GOF} retina (Fig. 6*A*,*B*,*J*, arrows). The few HC projections contacting the *Dscam*^{GOF}/*Bax*$^{-/-}$ IPL were located at the thinner peripheral retina,

suggesting the depth of the INL could serve as a barrier to formation of these projections (Fig. 6*J*; data not shown).

HC neurites also projected ectopically into the ONL (Fig. 6*C*,*D*, arrows). The earliest time point at which this phenotype was detected was P11, but it was evident in all retinas by P13. The dendrites of rod bipolar cells were observed ectopically projecting with HC neurites into the ONL by P18 (Fig. 6*E*, arrows). Invading neurites terminated in the ONL at puncta of synaptic markers (Fig. 6*F*,*G*, arrows), and the presence of morphologically normal ribbon synapses within the ONL of the $Dscam^{GOF}$ retina was confirmed by electron microscopy (Fig. 6*H*, arrow and inset). Projection of HC neurites occurred at a similar frequency in the absence of *Bax*, although these neurites terminated closer to the OPL, rather than projecting through gaps in the outer limiting membrane, which were not observed in the $Dscam^{GOF}/Bax^{-/-}$ retina (Fig. 6*I*; arrowheads; data not shown). Quantification of these results confirmed that the number of HC projections into the ONL, and the number of synapses within the ONL, were significantly increased in the $Dscam^{GOF}$ allele compared with wild-type (Fig. 6*J*). In older retinas (8+ months), in which the transgene is inactivated in many rods, HC neurites targeted rods that continued to express *Dscam*, including those projecting an axon to the OPL (Fig. 6*K*). These results indicate that ectopic expression of *Dscam* results in retargeting of retinal neurites.

DSCAM promotes IPL dendrite lamination by restricting dendrite target choice

To identify potential developmental mechanisms by which DSCAM promotes dendrite targeting in ACs, we used GFP-tagged type 2 DACs (Knop et al., 2011) because this cell type had uniform and reproducible lamination defects in the *Dscam* mutant retina. Type 2 DACs normally target dendrites exclusively to S3 of the IPL (Fig. 7*A*; Bruggen et al., 2014). In the *Dscam* heterozygous and homozygous mutant retina, these cells target dendrites to both S1 and S3 (Fig. 7*B*,*C*, arrows). DSCAM protein was produced by type 2 DACs and was localized to the dendrite tips of these cells *in vitro*, consistent with it functioning to regulate dendrite lamination in this cell population (Fig. 7*D*).

We confirmed that the dendrites projecting to S1 are distinct from type 1 DACs by immunoreactivity with TH, which stains type 1, but not type 2, DACs. Type 1 DACs project dendrites to S1 in the wild-type retina (Fig. 7*E*), whereas we observed an absence of type 2 DAC dendrites in S1 of the wild-type retina (Fig. 7*F*,*G*). In the $DscamLOF^{J+}$ retina, type 2 DACs project dendrites to both S1 and S3 (Fig. 7*H*, arrow). Confocal analysis of layer S1 of

the *DscamLOF*$^{/+}$retina confirmed that these bright GFP-positive dendrites lack TH (Fig. 7*I*,*J*, arrows).

Cell density was assayed to determine whether type 2 DACs that projected neurites were simply cells that did not undergo cell death in the *DscamLOF*$^{/+}$ retina. Type 2 DAC cell number was not significantly changed when comparing *DscamLOF*$^{/+}$ retinas to wild-type retinas (Fig. 7*K*). A significant increase in cell number was observed in the *Dscam*^{LOF} retina compared with either wild-type or *DscamLOF*$^{/+}$ retinas (Fig. 7*K*). Spacing of type 2 DACs was also assayed, to determine whether their cell bodies were abnormally spaced in the absence of *Dscam*. Spacing of type 2 DACs was dependent on *Dscam* in a dose-dependent manner, with significantly lower NNRI and DRP packing index values detected as *Dscam* dosage decreased (Fig. 7*L*,*M*).

These data demonstrate that type 2 DACs require *Dscam* for regulation of cell number, spacing, and lamination. Because the layers (S1 and S3) are sufficiently separated and the heterozygous *Dscam* mutant pups do not have a growth defect, we could for the first time readily examine the influence of *Dscam* dosage on the development of lamination defects in the mouse retina.

First we assayed development of type 2 DACs in wild-type and *DscamLOF*$^{/+}$ retinas. A similar number of wild-type and *DscamLOF*$^{/+}$ type 2 DACs projected dendrites into S1 at early time points, indicating that these cells have a normal tendency to ramify dendrites in both S1 and S3 (Fig. 8*A*,*B*, arrows, *H*, P3). A significant increase in cells that project dendrites into S1 was observed in the *DscamLOF*$^{/+}$ retina compared with wild-type by P5, and these cells accounted for the majority of type 2 DACs by this age (Fig. 8*C*,*D*, arrows, *H*, P5). By P10 GFP fluorescence in this cell type was sufficiently brighter than GFP produced by other cells in the *Dscam*^{GOF} retina, allowing us to assay the effect of *Dscam* overexpression on laminar targeting of type 2 DACs. A significant decrease in the number of type 2 DACs that project dendrites into S1 was observed in the *Dscam*^{GOF} retina compared with wild-type or the *DscamLOF*$^{/+}$ retina, while significantly more neurites targeted S1 in the *DscamLOF*$^{/+}$ retina compared with wild-type (Fig. 8*E*–*G*, arrows, *H*, P10). These results indicate that *Dscam* promotes refinement of type 2 DACs during development by preventing stabilization of dendrites and that *Dscam* expression levels positively correlated with the degree of S1 dendrite pruning.

Extensive remodeling of pyramidal cell dendrites is observed in the *Dscam*-deficient cortex over extended postnatal periods (Maynard and Stein, 2012), and we were curious if a similar remodeling would occur with age in the type 2 DACs. Dendrites that projected into S1 of the *DscamLOF*$^{J+}$ retina were stable and observed in the majority of cells after eye opening and visual function and at all subsequent time points assayed (up to 6 months; data not shown; Fig. 8*H*). Analysis of whole retinas indicated that by P15, wild-type dendrites localized in S1 invariably dove into S3 after projecting a short distance in S1, whereas *DscamLOF*$^{J+}$ dendrites terminated in S1 (data not shown). Many type 2 DACs also projected dendrites into S1 in the *Bax*$^{-/-}$ retina (Fig. 8*H*). A large increase in the number of these cells was observed in the *Bax*$^{-/-}$ retina (P15: *Bax*$^{-/-}$488 ± 94 cells/mm^2 vs wild-type sibling controls 181 ± 27 cells/mm^2; *t* test $p < 0.01$), consistent with these being cells that failed to undergo developmental cell death.

These data address the question of how the broadly distributed DSCAM protein in the mouse IPL can promote the specificity of dendrite lamination and indicate that DSCAM promotes dendrite targeting in the mouse IPL by selectively inhibiting stability of exploring dendrites.

Function follows form

ERGs were performed to test if the morphological abnormalities observed in the *Dscam* gain- and loss-of-function retinas influenced the synaptic activity of the retina. *Dscam*^{GOF} mice displayed significant reductions in the dark-adapted, rod-driven a-wave amplitude; the b-wave amplitudes; and the light-adapted cone-mediated response at 4 months of age (Fig. 9*A*–*E*). The normalized b-wave of *Dscam*^{GOF} mice (0.455) is more severely reduced than the decrease in the amplitude of the a-wave (0.723), demonstrating that the reduction in the b-wave is not secondary to a decreased a-wave. These findings persist at 6 months, with the normalized b-wave amplitude more severely affected than the a-wave amplitude (a-wave, 0.579; b-wave, 0.289; data not shown). At this point we cannot determine whether a decrease in the b-wave is entirely due to a reduction in bipolar cell number, or if synaptic transmission at the rod spherule is also disrupted. Therefore misregulation of *Dscam* expression alters both the morphology and physiology of the retina.

Discussion

The major findings of this study are as follows: (1) DSCAM is sufficient to drive cell death and can regulate cell death independent of *Bax*, (2) dendrite avoidance defects in the *Dscam* loss-of-function retina do not reflect a role for DSCAM in repulsion analogous to *Drosophila* Dscam1, and (3) DSCAM is necessary and sufficient to target neurites, even in systems in which the protein is widely distributed such as the mouse IPL, and that it does so by restricting the locations in which exploring dendrites are able to stabilize.

Dscam drives cell death in the retina

Gain- and loss-of-function results support a role for *Dscam* as a critical driver of developmental cell death in the developing mouse retina. Previous analysis of the loss-of-function *Dscam* brain suggested that this might hold true for other parts of the nervous system; for example, a small increase in the size of the *Dscam*-null hindbrain has been reported (Amano et al., 2009). Further analysis of the *Dscam* mutant brain identified an overall increase in brain/body size ratio in mutant mice, and regions of the brain that were increased or decreased in size were identified, but changes to cell death or birth were not identified in the cortex, which was the focus of the study (Maynard and Stein, 2012). Changes in brain size could therefore be the result of reduced or increased neurite elaboration and changes to the visual system. Further work assisted by conditional gain- and loss-of-function analysis will help clarify the extent to which *Dscam* can drive cell death outside of the retina. Identifying the *Bax*-independent mechanism by which DSCAM drives cell death in the inner retina will also be an important line of future research. The *Bax* homolog *Bak1* is an excellent target for further analysis (Hahn et al., 2003).

DSCAM and dendrite avoidance

Previous studies have identified roles for vertebrate *Dscam* in both adhesion and avoidance in the developing vertebrate nervous system. Loss of *Dscam* or *Dscaml1* function results in a soma and dendrite-clustering phenotype that superficially resembles a similar dendrite self-avoidance phenotype observed in *Drosophila* Dscam1 mutants (Zhu et al., 2006; Hattori et al., 2007; Matthews et al., 2007). Dscam1 has been shown to actively drive avoidance through repulsion, which limits dendrites of a given cell from crossing other dendrites originating from the same cell (Hughes et al., 2007). Several differences between the anatomy of the systems analyzed in mouse and *Drosophila* suggest that these processes

might not be analogous. First, mouse *Dscam* is not extensively alternatively spliced, and functional alternative splice forms have not been reported (Yamakawa et al., 1998). Second, analyzed cell types arborizing dendrites in the mouse retina overlap extensively (Keeley and Reese, 2010), and do not approximate the tiling observed, for example, in type IV DA cells in *Drosophila* (Soba et al., 2007). Third, many different cell types in the mouse inner retina require *Dscam* to prevent a cell type-specific avoidance that occurs in its absence, suggesting that this phenotype is the result of other cell type-specific adhesion molecules.

In this study, we tested if *Dscam* is sufficient to induce avoidance or increase regularity of spacing. We found that its overexpression in cells that express either *Dscam* or *Dscaml1*, or its ectopic expression in SACs or HCs, all failed to increase spatial organization as assayed (Fig. 4). These results suggest that the role of mouse *Dscam* may be better reflected by some of the other *Drosophila* Dscams or phenotypes (Millard et al., 2010; Hutchinson et al., 2014), with the role of *Drosophila* Dscam1 in mouse likely provided by other molecules, such as the γ-protocadherins (Lefebvre et al., 2008, 2012).

DSCAM and dendrite targeting

In addition to being required for avoidance, *Dscam* has also been implicated in providing neurite-targeting cues during lamination of the chick retina (Yamagata and Sanes, 2008). In previous studies, limited dendrite lamination defects were identified in the mouse retina and we show here that this limited defect is partially explained by *Bax*-dependent cell death that occurs in the *Dscam*-deficient retina. Gain-of-function studies did indicate that *Dscam* expression in the outer retina is sufficient to retarget neurites to both the IPL and ONL. Projection of HC neurites into the ONL is observed in several other models, including the aging retina (Liets et al., 2006; Samuel et al., 2011, 2014), plexin and semaphorin-deficient retinas (Matsuoka et al., 2012), and retinas in which physiology is disrupted (Claes et al., 2004; Michalakis et al., 2013). The targeting of individual *Dscam*-expressing rods by HC neurites in the older $Dscam^{GOF}$ retina suggests that the DSCAM protein is sufficient to attract HC neurites, but we cannot rule out that individual rods have defective synaptic structure and act to recruit input secondary to this.

Dscam and dendrite refinement

By analyzing the role of DSCAM in dendrite lamination during development, we identified a novel role for DSCAM in restricting the location that retinal dendrites can stabilize. Mature type 2 DAC cells normally project dendrites to a single layer of the IPL (Bruggen et al., 2014), but as *Dscam* dosage decreases they adopted a bistratified morphology. Further analysis found that the dendrites of these cells, like those of other retinal neurons (Huckfeldt et al., 2009; Reese and Keeley, 2014), initially project dendrites that later retract. A limited and nonsignificant increase in cell number in the *Dscam* heterozygous mutant retina indicated that deficiency in cell death is not sufficient to explain the presence of bistratified type 2 DACs, which account for the majority of these cells in the *DscamLOF*$^{/+}$ retina. Gain-of-function analysis identified a precocious refinement of type 2 DACs, consistent with loss-of-function results.

A simple model for how DSCAM mediates phenotypes in the mouse retina could involve the destabilization of dendrites. DSCAM-mediated signaling has been demonstrated to activate the tyrosine receptor kinases Fyn and Fyk, and induce collapse of growth cones in axon outgrowth assays (Purohit et al., 2012). A model wherein DSCAM signaling results in destabilization and retraction of weakly adhesive contacts would explain both the gain- and loss-of-function phenotypes described in the mouse retina. In this model, adhesive tendencies between cells of the same type are strengthened and cause ectopic clumping in the *Dscam*-deficient retina, while weak connections are not eliminated, resulting in a lack of refinement and the observation of non-native dendrite projections. Increasing or decreasing dendrite stability could then influence the likelihood that cells would form connections and survive developmental cell death. While we propose that our results are most consistent with DSCAM-weakening adhesion, consistent with the ectopic clumping observed in the *Dscam*-deficient retina, we cannot rule out the possibility that DSCAM–DSCAM interactions strengthen a subset of interactions, and therefore cause weaker connections to retract. In either case, the end result on a cellular level would be the same, with weaker connections eliminated. The necessity of a system to eliminate misplaced connections is evidenced by studies investigating how retinal circuitry is established, particularly given the broad overlap of adhesive molecules such as cadherins (Duan et al., 2014) and Ig-domain proteins such as contactins (Yamagata and Sanes, 2012).

Dscam and Down syndrome

An important human health implication of this research is in understanding the role of *Dscam* in DS, the most common form of genetic mental retardation. DS is caused by overexpression of genes on chromosome 21, including a subset of 33 genes in a minimal critical region that encompasses *Dscam*, which are sufficient to give rise to a diagnosis of DS (Lejeune et al., 1959; Rahmani et al., 1990). A hallmark of the developing DS brain is hypocellularity in the cortex, cerebellum, and other regions of the brain, accompanied by changes to dendritic architecture (Reeves et al., 1995; Holtzman et al., 1996; Aylward et al., 1997; Haydar and Reeves, 2012). We used a gain-of-function model and demonstrated that overexpression of *Dscam* is sufficient to reduce cellularity through increased cell death, and that *Dscam* plays a role in dendrite targeting. While people with DS frequently have visual deficiencies (Creavin and Brown, 2009), this is likely not caused by *Dscam*-mediated changes to retinal cell number, as overexpression of another minimal critical region gene, *Dyrk1a*, in DS mouse models inhibits caspase 9 and results in an increase in retinal cell number (Laguna et al., 2013). Previous studies have identified a role for *Dscam* in proper dendrite branching in the hippocampus (Alves-Sampaio et al., 2010) and cortex (Maynard and Stein, 2012), with the latter mirroring changes in the DS brain in which cortical neurons initially project more branches than euploid individuals, before adopting an arbor with fewer projections. These studies identify *Dscam* as an excellent candidate underlying DS pathologies such as hypocellularity observed outside of the retina and dendrite branching defects throughout the brain.

References

Alves-Sampaio A, Troca-Marín JA, Montesinos ML (2010) NMDAmediated regulation of DSCAM dendritic local translation is lost in a mouse model of Down's syndrome. J Neurosci 30:13537–13548.

Amano K, Fujii M, Arata S, Tojima T, Ogawa M, Morita N, Shimohata A, Furuichi T, Itohara S, Kamiguchi H, Korenberg JR, Arata A, Yamakawa K (2009) DSCAM deficiency causes loss of pre-inspiratory neuron synchroneity and perinatal death. J Neurosci 29:2984 –2996.

Aylward EH, Habbak R, Warren AC, Pulsifer MB, Barta PE, Jerram M, Pearlson GD (1997) Cerebellar volume in adults with Down syndrome. Arch Neurol 54:209 –212.

Blank M, Fuerst PG, Stevens B, Nouri N, Kirkby L, Warrier D, Barres BA, Feller MB, Huberman AD, Burgess RW, Garner CC (2011) The Down syndrome critical region regulates retinogeniculate refinement. J Neurosci 31:5764 –5776.

Chen BE, Kondo M, Garnier A, Watson FL, Pu¨ettmann-Holgado R, Lamar DR, SchmuckerD (2006) The molecular diversity of Dscam is functionally required for neuronal wiring specificity in *Drosophila*. Cell 125:607–620.

Chen SK, Chew KS, McNeill DS, Keeley PW, Ecker JL, Mao BQ, Pahlberg J, Kim B, Lee SC, Fox MA, Guido W, Wong KY, Sampath AP, Reese BE, Kuruvilla R, Hattar S (2013) Apoptosis regulates ipRGC spacing necessary for rods and cones to drive circadian photoentrainment. Neuron 77:503–515.

Claes E, SeeligerM,Michalakis S, BielM,HumphriesP,HaverkampS (2004) MorphologicalcharacterizationoftheretinaoftheCNGA3(_/_)Rho(_/_)mutant mouse lacking functional cones and rods. Invest Ophthalmol Vis Sci 45:2039–2048.

Creavin AL, Brown RD (2009) Ophthalmic abnormalities in children with Down syndrome. J Pediatr Ophthalmol Strabismus 46:76–82.

Cvetkovska V, Hibbert AD, Emran F, Chen BE (2013) Overexpression of Down syndrome cell adhesion molecule impairs precise synaptic targeting. Nat Neurosci 16:677– 682.

de Andrade GB, Long SS, Fleming H, Li W, Fuerst PG (2014) DSCAM localization and function at the mouse cone synapse. J Comp Neurol 522: 2609–2633.

Duan X, Krishnaswamy A, De la Huerta I, Sanes JR (2014) Type II cadherins guide assembly of a direction-selective retinal circuit. Cell 158:793– 807.

Fuerst PG, Koizumi A, Masland RH, Burgess RW (2008) Neurite arborization and mosaic spacing in the mouse retina require DSCAM. Nature 451:470–474.

Fuerst PG, Bruce F, Tian M, Wei W, Elstrott J, Feller MB, Erskine L, Singer JH, Burgess RW (2009) DSCAM and DSCAML1 function in self-avoidance in multiple cell types in the developing mouse retina. Neuron 64:484– 497.

Fuerst PG, Harris BS, Johnson KR, BurgessRW (2010) A novel null allele of mouse DSCAM survives to adulthood on an inbred C3H background with reduced phenotypic variability. Genesis 48:578 –584.

Fuerst PG, Bruce F, Rounds RP, Erskine L, Burgess RW (2012) Cell autonomy of DSCAM function in retinal development. Dev Biol 361:326 – 337.

Grossman TR, Gamliel A, Wessells RJ, Taghli-Lamallem O, Jepsen K, Ocorr K, Korenberg JR, Peterson KL, Rosenfeld MG, Bodmer R, Bier E (2011) Over-expression of DSCAM and COL6A2 cooperatively generates congenital heart defects. PLoS Genet 7:e1002344.

Hahn P, Lindsten T, Ying GS, Bennett J, Milam AH, Thompson CB, Dunaief JL (2003) Proapoptotic bcl-2 family members, Bax and Bak, are essential for developmental photoreceptor apoptosis. Invest Ophthalmol Vis Sci 44:3598 –3605.

Hattori D, Demir E, Kim HW, Viragh E, Zipursky SL, Dickson BJ (2007) Dscam diversity is essential for neuronal wiring and self-recognition. Nature 449:223–227.

Haydar TF, Reeves RH (2012) Trisomy 21 and early brain development. Trends Neurosci 35:81–91.

He H, Kise Y, Izadifar A, Urwyler O, Ayaz D, Parthasarthy A, Yan B, Erfurth ML, Dascenco D, Schmucker D (2014) Cell-intrinsic requirement of Dscam1 isoform diversity for axon collateral formation. Science 344: 1182–1186. CrossRef Medline

Holtzman DM, Santucci D, Kilbridge J, Chua-Couzens J, Fontana DJ, Daniels SE, Johnson RM, Chen K, Sun Y, Carlson E, Alleva E, Epstein CJ, Mobley WC (1996) Developmental abnormalities and age-related neurodegeneration in a mouse model of Down syndrome. Proc Natl Acad Sci U S A 93:13333–13338.

Huckfeldt RM, Schubert T, Morgan JL, Godinho L, Di Cristo G, Huang ZJ, Wong RO (2009) Transient neurites of retinal horizontal cells exhibit columnar tiling via homotypic interactions. Nat Neurosci 12:35– 43.

Hughes ME, Bortnick R, Tsubouchi A, Ba¨umer P, Kondo M, Uemura T, Schmucker D (2007) Homophilic Dscam interactions control complex dendrite morphogenesis. Neuron 54:417– 427.

Hutchinson KM, Vonhoff F, Duch C (2014) Dscam1 is required for normal dendrite growth and branching but not for dendritic spacing in *Drosophila* motoneurons. J Neurosci 34:1924 –1931.

Kay JN, Chu MW, Sanes JR (2012) MEGF10 and MEGF11 mediate homotypic interactions required for mosaic spacing of retinal neurons. Nature 483:465–469.

Keeley PW, Reese BE (2010) Morphology of dopaminergic amacrine cells in the mouse retina: independence from homotypic interactions. J Comp Neurol 518:1220 –1231.

Keeley PW, Sliff BJ, Lee SC, Fuerst PG, Burgess RW, Eglen SJ, Reese BE (2012) Neuronal clustering and fasciculation phenotype in Dscam- and Bax-deficient mouse retinas. J Comp Neurol 520:1349 –1364.

Khiripet N, Khantuwan W, Jungck JR (2012) Ka-me: a Voronoi image analyzer. Bioinformatics 28:1802–1804.

Kim JH, Wang X, Coolon R, Ye B (2013) Dscam expression levels determine presynaptic arbor sizes in *Drosophila* sensory neurons. Neuron 78:827– 838.

Knop GC, Feigenspan A, Weiler R, Dedek K (2011) Inputs underlying the ON-OFF light responses of type 2 wide-field amacrine cells in TH::GFP mice. J Neurosci 31:4780–4791.

Knudson CM, Tung KS, Tourtellotte WG, Brown GA, Korsmeyer SJ (1995) Bax-deficient mice with lymphoid hyperplasia and male germ cell death. Science 270:96 –99.

Kunzevitzky NJ, Willeford KT, Feuer WJ, Almeida MV, Goldberg JL (2013) Amacrine cell subtypes differ in their intrinsic neurite growth capacity. Invest Ophthalmol Vis Sci 54:7603–7613.

Laguna A, Barallobre MJ, Marchena MA´ , Mateus C, Ramírez E, Martínez-Cue C, Delabar JM, Castelo-Branco M, de la Villa P, Arbone´s ML (2013) Triplication of DYRK1A causes retinal structural and functional alterations in Down syndrome. Hum Mol Genet 22:2775–2784.

Lefebvre JL, Zhang Y, Meister M, Wang X, Sanes JR (2008) gamma- Protocadherins regulate neuronal survival but are dispensable for circuit formation in retina. Development 135:4141– 4151.

Lefebvre JL, Kostadinov D, Chen WV, Maniatis T, Sanes JR (2012) Protocadherins mediate dendritic self-avoidance in the mammalian nervous system. Nature 488:517–521.

Lejeune J, Turpin R, Gautier M (1959) [Chromosomic diagnosis of mongolism]. Arch Fr Pediatr 16:962–963.

Li HL, Huang BS, Vishwasrao H, Sutedja N, Chen W, Jin I, Hawkins RD, Bailey CH, Kandel ER (2009) Dscam mediates remodeling of glutamate receptors in *Aplysia* during de novo and learning-related synapse formation. Neuron 61:527–540.

Liu G, Li W, Wang L, Kar A, Guan KL, Rao Y, Wu JY (2009) DSCAM functions as a netrin receptor in commissural axon pathfinding. Proc Natl Acad Sci U S A 106:2951–2956.

Livet J, Weissman TA, Kang H, Draft RW, Lu J, Bennis RA, Sanes JR, Lichtman JW (2007) Transgenic strategies for combinatorial expression of fluorescent proteins in the nervous system. Nature 450:56–62.

Ly A, Nikolaev A, Suresh G, Zheng Y, Tessier-Lavigne M, Stein E (2008) DSCAM is a netrin receptor that collaborates with DCC in mediating turning responses to netrin-1. Cell 133:1241–1254.

Masland RH (2012) The neuronal organization of the retina. Neuron 76:266–280.

Matsuda T, Cepko CL (2004) Electroporation and RNA interference in the rodent retina in vivo and in vitro. Proc Natl Acad Sci U S A 101:16 –22.

Matsuoka RL, Nguyen-Ba-Charvet KT, Parray A, Badea TC, Che´dotal A, Kolodkin AL (2011a) Transmembrane semaphorin signalling controls laminar stratification in the mammalian retina. Nature 470:259 –263.

Matsuoka RL, Chivatakarn O, Badea TC, Samuels IS, Cahill H, Katayama K, Kumar SR, Suto F, Che´dotal A, Peachey NS, Nathans J, Yoshida Y, Giger RJ, Kolodkin AL (2011b) Class 5 transmembrane semaphorins control selective Mammalian retinal lamination and function. Neuron 71:460– 473.

Matsuoka RL, Jiang Z, Samuels IS, Nguyen-Ba-Charvet KT, Sun LO, Peachey NS, Che´dotal A, Yau KW, Kolodkin AL (2012) Guidance-cue control of horizontal cell morphology, lamination, and synapse formation in the mammalian outer retina. J Neurosci 32:6859–6868.

Matthews BJ, Kim ME, Flanagan JJ, Hattori D, Clemens JC, Zipursky SL, Grueber WB (2007) Dendrite self-avoidance is controlled by Dscam. Cell 129:593– 604.

Maynard KR, Stein E (2012) DSCAM contributes to dendrite arborization and spine formation in the developing cerebral cortex. J Neurosci 32: 16637–16650.

Michalakis S, Scha¨ferhoff K, Spiwoks-Becker I, Zabouri N, Koch S, Koch F, Bonin M, Biel M, Haverkamp S (2013) Characterization of neurite outgrowth and ectopic synaptogenesis in response to photoreceptor dysfunction. Cell Mol Life Sci 70:1831–1847.

Millard SS, Lu Z, Zipursky SL, Meinertzhagen IA (2010) *Drosophila* dscam proteins regulate postsynaptic specificity at multiple-contact synapses. Neuron 67:761–768.

Miyazaki J, Takaki S, Araki K, Tashiro F, Tominaga A, Takatsu K, Yamamura K (1989) Expression vector system based on the chicken beta-actin promoter directs efficient production of interleukin-5. Gene 79:269 –277.

Morales Diaz HD (2014) Down syndrome cell adhesion molecule is important for early development in *Xenopus tropicalis*. Genesis 52:849–857.

Neves G, Zucker J, Daly M, Chess A (2004) Stochastic yet biased expression of multiple Dscam splice variants by individual cells. Nat Genet 36:240– 246.

Okawa H, Hoon M, Yoshimatsu T, Della Santina L, Wong RO (2014) Illuminating the multifaceted roles of neurotransmission in shaping neuronal circuitry. Neuron 83:1303–1318.

Pe´quignot MO, Provost AC, Salle´ S, Taupin P, Sainton KM, Marchant D, Martinou JC, Ameisen JC, Jais JP, Abitbol M (2003) Major role of BAX in apoptosis during retinal development and in establishment of a functional postnatal retina. Dev Dyn 228:231–238.

Purohit AA, Li W, Qu C, Dwyer T, Shao Q, Guan KL, Liu G (2012) Down syndrome cell adhesion molecule (DSCAM) associates with uncoordinated-5C (UNC5C) in netrin-1-mediated growth cone collapse. J Biol Chem 287:27126 –27138.

Rahmani Z, Blouin JL, Cre´au-Goldberg N, Watkins PC, Mattei JF, Poissonnier M, Prieur M, Chettouh Z, Nicole A, Aurias A, et al. (1990) Down syndrome critical region around D21S55 on proximal 21q22.3.AmJ Med Genet Suppl 7:98 –103.

Ramon y Cajal S (1893) La re_tine des verte_bre_s. La Cellule 9:119 –257. Randlett O, MacDonald RB, Yoshimatsu T, Almeida AD, Suzuki SC, Wong RO, HarrisWA (2013) Cellular requirements for building a retinal neuropil. Cell Rep 3:282–290.

Reeves RH, Irving NG, Moran TH, Wohn A, Kitt C, Sisodia SS, Schmidt C, Bronson RT, Davisson MT (1995) A mouse model for Down syndrome exhibits learning and behaviour deficits. Nat Genet 11:177–184.

Rodieck RW (1991) The density recovery profile: a method for the analysis of points in the plane applicable to retinal studies. Vis Neurosci 6:95–111.

Samuel MA, Zhang Y, Meister M, Sanes JR (2011) Age-related alterations in neurons of the mouse retina. J Neurosci 31:16033–16044.

Samuel MA, Voinescu PE, Lilley BN, de Cabo R, Foretz M, Viollet B, Pawlyk B, Sandberg MA, Vavvas DG, Sanes JR (2014) LKB1 andAMPKregulate synaptic remodeling in old age. Nat Neurosci 17:1190 –1197.

Schmucker D, Chen B (2009) Dscam and DSCAM: complex genes in simple animals, complex animals yet simple genes. Genes Dev 23:147–156.

Schmucker D, Clemens JC, Shu H, Worby CA, Xiao J, Muda M, Dixon JE, Zipursky SL (2000) *Drosophila* Dscam is an axon guidance receptor exhibiting extraordinary molecular diversity. Cell 101:671– 684.

Schramm RD, Li S, Harris BS, Rounds RP, Burgess RW, Ytreberg FM, Fuerst PG (2012) A novel mouse Dscam mutation inhibits localization and shedding of DSCAM. PLoS One 7:e52652.

Soba P, Zhu S, Emoto K, Younger S, Yang SJ, Yu HH, Lee T, Jan LY, Jan YN (2007) *Drosophila* sensory neurons require Dscam for dendritic selfavoidance and proper dendritic field organization. Neuron 54:403– 416.

Stacy RC, Demas J, Burgess RW, Sanes JR, Wong RO (2005) Disruption and recovery of patterned retinal activity in the absence of acetylcholine. J Neurosci 25:9347–9357.

Sun LO, Jiang Z, Rivlin-Etzion M, Hand R, Brady CM, Matsuoka RL, Yau KW, Feller MB, Kolodkin AL (2013) On and off retinal circuit assembly by divergent molecular mechanisms. Science 342:1241974.

Yamagata M, Sanes JR (2008) Dscam and Sidekick proteins direct laminaspecific synaptic connections in vertebrate retina. Nature 451:465– 469.

Yamagata M, Sanes JR (2010) Synaptic localization and function of Sidekick recognition molecules require MAGI scaffolding proteins. J Neurosci 30: 3579–3588.

Yamagata M, Sanes JR (2012) Expanding the Ig superfamily code for laminar specificity in retina: expression and role of contactins. J Neurosci 32:14402–14414.

Yamakawa K, Huot YK, Haendelt MA, Hubert R, Chen XN, Lyons GE, Korenberg JR (1998) DSCAM: a novel member of the immunoglobulin superfamily maps in a Down syndrome region and is involved in the development of the nervous system. Hum Mol Genet 7:227–237.

Yimlamai D, Konnikova L, Moss LG, Jay DG (2005) The zebrafish down syndrome cell adhesion molecule is involved in cell movement during embryogenesis. Dev Biol 279:44 –57.

Zhu H, Hummel T, Clemens JC, Berdnik D, Zipursky SL, Luo L (2006) Dendritic patterning by Dscam and synaptic partner matching in the *Drosophila* antennal lobe. Nat Neurosci 9:349 –355.

Figures

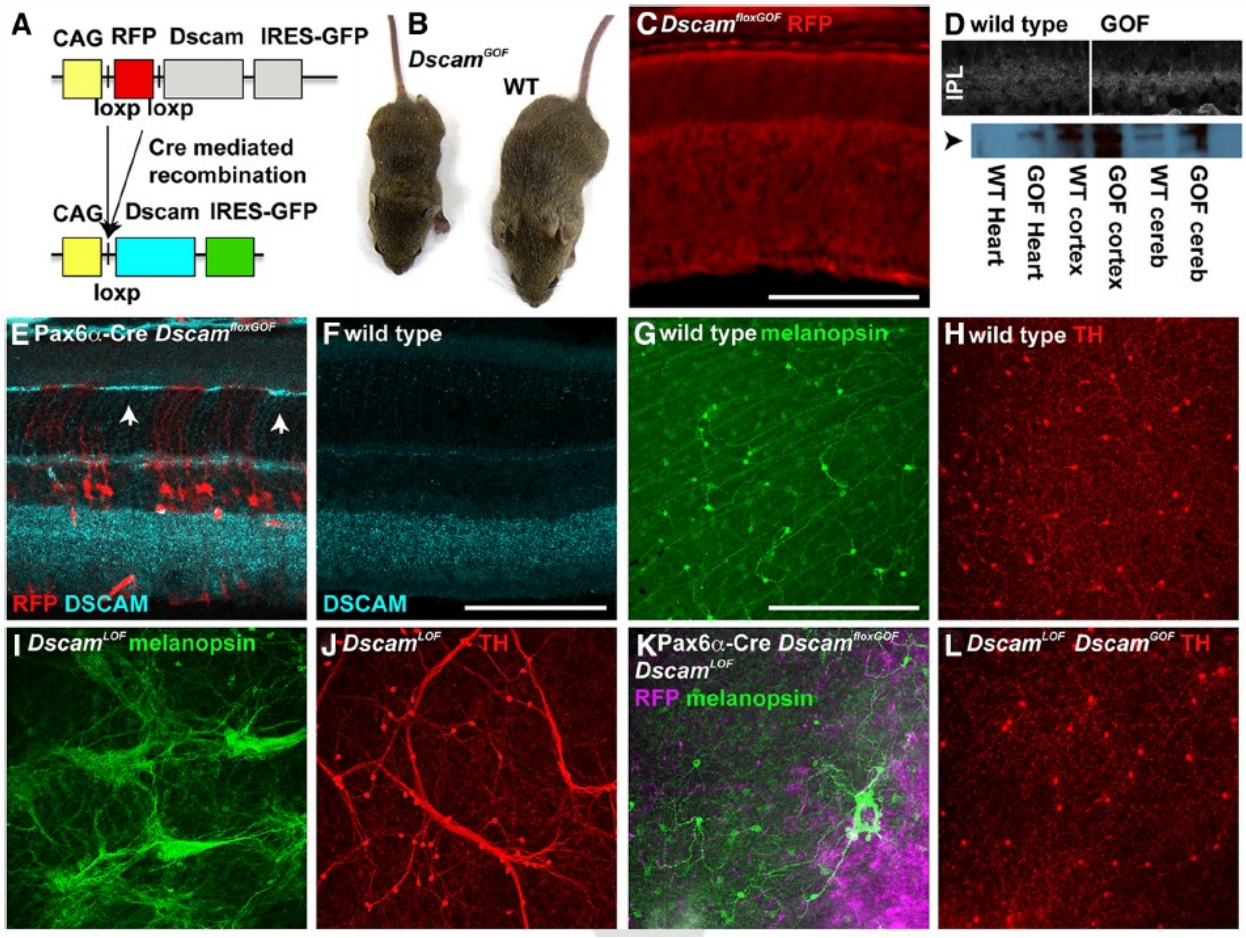

Figure 4.1. *Dscam* gain-of-function allele. *A*, A conditional gain-of-function allele of mouse *Dscam* was generated.*B*, Germline activation of recombination resulted in viable mice that were smaller than littermate controls. *C*, The transgene was expressed throughout the retina during development. *D*, Immunofluorescence of the retinal IPL and Western blot analysis of DSCAM protein in tissue and tissue lysates from wild-type and *DscamGOF* mice. *E*, Mosaic Cre-mediated recombination of the *DscamGOF* transgene. *F*, Distribution of DSCAM in the wild-type retina. *G*, *H*, Spacing and arborization of wild-type mRGCs and DACs. *I*, *J*, Clustering of *DscamLOF* mRGC and DAC cell bodies and dendrites. *K*, *L*, Expression of the *DscamGOF* transgene is sufficient to rescue loss-of-function clumping phenotypes. P15: *B*, *E*, *F*; P10: *C*; P7: *D*; P28 –P42: *G*–*L*. *N*_3 for all genotypes. Scale bars: (in *C*) *C*, *E*, 100_m; *F*, 100_m; (in *G*) *G*–*L* 400_m.

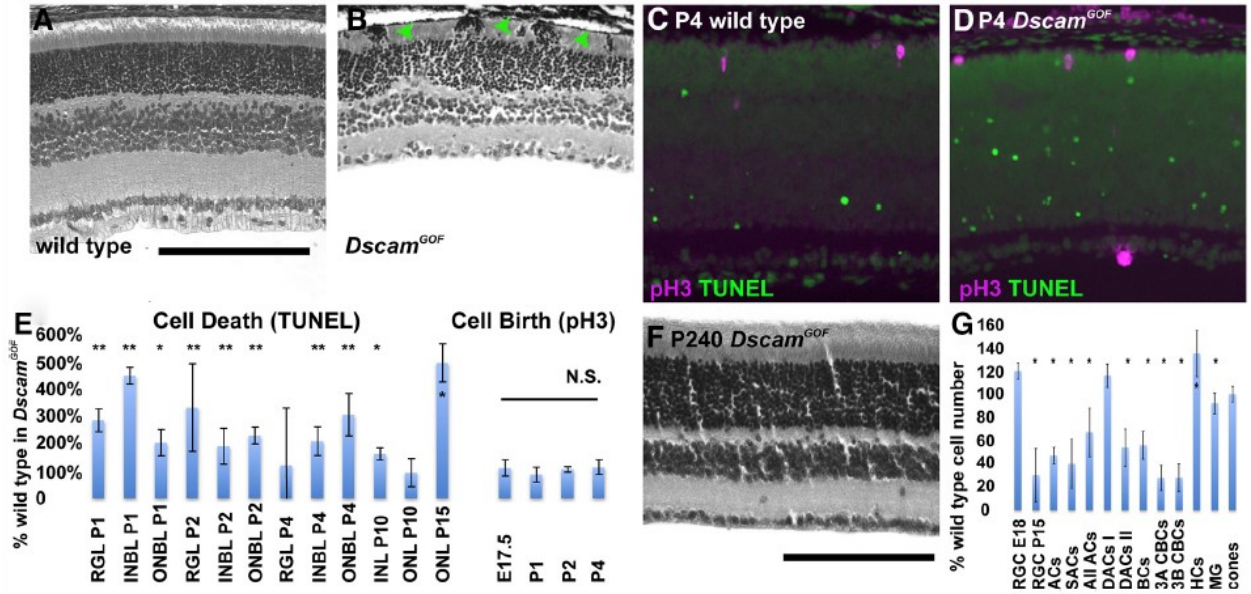

Figure 4.2. *Dscam* expression is sufficient to drive cell death. *A*, *B*, H&E stained sections of wild-type and *DscamGOF* retina. Arrowheads in *B* indicate location of ectopic rod photoreceptors in the *DscamGOF* retina. *C*, *D*, P4 sections of wild-type and *DscamGOF* retina stained with antibodies to phosphohistone H3 and TUNEL. *E*, Quantification of cell birth and death indicated a significant increase in cell death during development of the *DscamGOF* retina compared with wild-type, while no changes in cell birth were detected. The bold line in *E* is at 100% wild-type value. *F*, H&E stained section of P240 *DscamGOF* retina. Ectopic photoreceptors are absent. *G*, Quantification of cell number in the *DscamGOF* retina compared with wild-type. Assayed cells of the inner retina, except for type 1 dopaminergic amacrine cells, were significantly depleted in the *DscamGOF* retina. Cone number was unchanged while an increase in HCs was detected. The bold line in *G* is at 100% wild-type value. INBL, inner neuroblast layer; ONBL, outer neuroblast layer; E, embryonic; P, postnatal; BC, bipolar cell; CBC, cone bipolar cell; MG,Mu¨ller glia. P15: *A*,*B*. *N*_3 for all genotypes. Scale bars: (in *A*)*A*–*D*, 100_m; *F*, 120_m. Mean_SD; **p*_0.05, ***p*_0.01 (Student's *t* test).

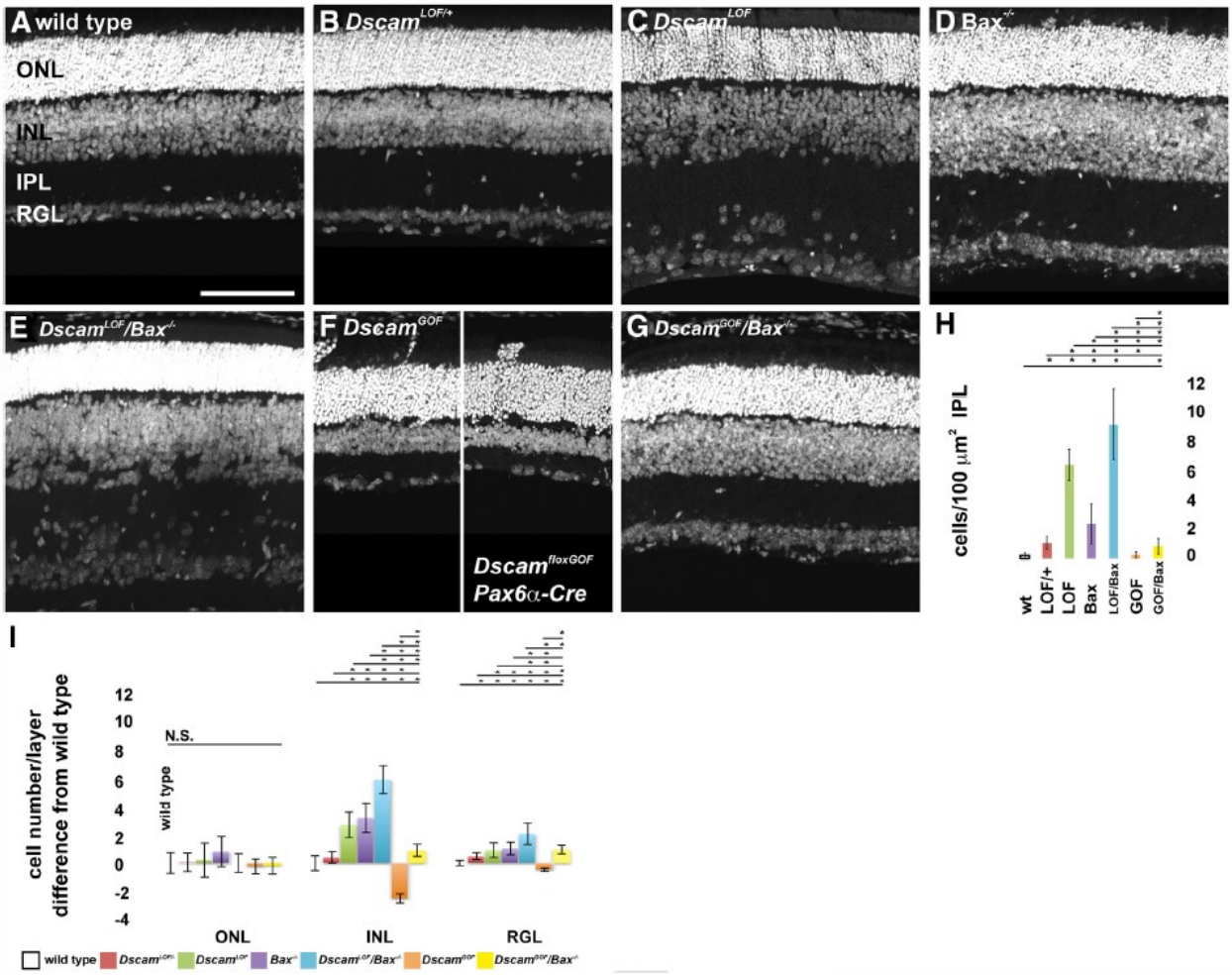

Figure 4.3. DSCAM regulates cell number in *Bax*-dependent and -independent manners. *A*–*G*, DRAQ5 stained retina sections: wild-type (*A*), *DscamLOF/_*(*B*), *DscamLOF* (*C*), *Bax_/_*(*D*), *DscamLOF/ Bax_/_* (*E*), *DscamGOF* (also depicts *DscamfloxGOF* targeted with Pax6_-Cre; *F*), *DscamGOF/Bax_/_*(*G*). *H*, Quantification of displaced neurons in the IPL. *I*, Quantification of cell number in retinal layers. Values are plotted as average difference from wild-type. Wild-type cell number in ONL: 10.5_0.08, INL: 6.64_0.53, RGL:1.17_0.18. RGL: retinal ganglion layer. P18 *N*_3 for all genotypes. Scale bars: (in *A*) *A*–*G*, 100_m. Mean_SD; *p_0.01 (Student's *t* test).

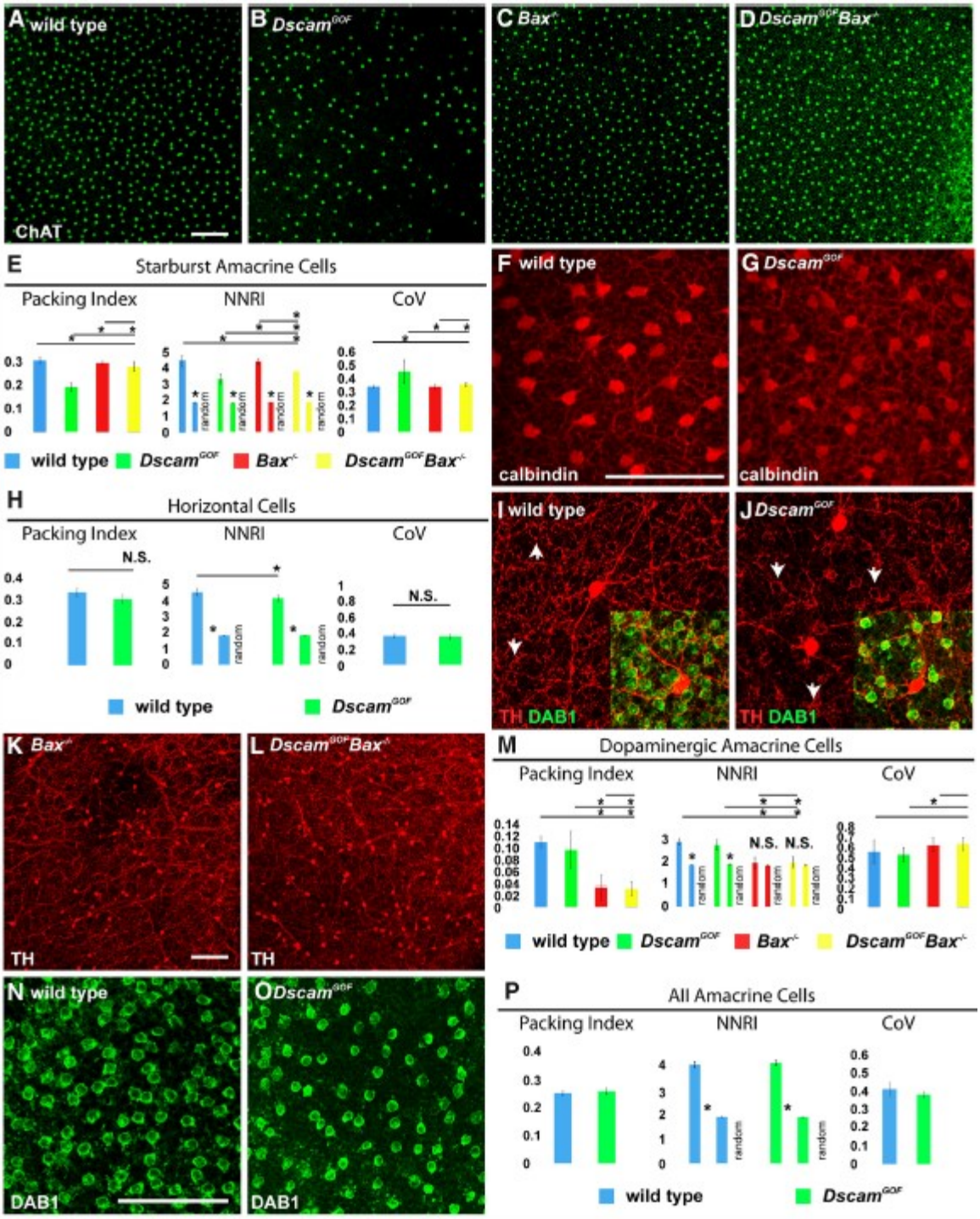

Figure 4.4. DSCAM is not sufficient to increase spacing or avoidance in the mouse retina. *A–D*, Confocal images of OFF SACs. *E*, Quantification of DRP (based on packing index),NNA(based on NNRI), and VD analysis (based on CoV) for wild-type, *DscamGOF*, *Bax_/_*, and *DscamGOF/Bax_/_*SACs. *F*, *G*, Confocal images of horizontal cells in the wild-type and *DscamGOF* retina. *H*, Quantification of packing index, NNRI, and CoV for wild-type

and *DscamGOF* horizontal cells. *I*, *J*, Confocal image of type 1 dopaminergic amacrine and AII amacrine cells. Type 1 DACs wrap dendrites around AII amacrine cells in wild-type and *DscamGOF* retinas (arrowheads). *K*, *L*, Confocal image of type 1 DACs in *Bax_/_*and *DscamGOF/Bax_/_*retinas.*M*, Quantification of packing index, NNRI, and CoV for wild-type, *DscamGOF*, *Bax_/_*, and *DscamGOF/Bax_/_*type 1 DACs.*N*,*O*, Confocal images of AII ACs in wild-type and *DscamGOF* retinas.*P*, Quantification of packing index, NNRI, and CoV for wild-type and *DscamGOF* AII ACs. P28 –P42. *N*_4 for all genotypes. Scale bars: (in *A*) *A*–*D*, 100_m; (in *F*) *F*, *G*, *I*, *J*, 100_m; (in *K*) *K*, *L*, 100_m; (in*N*)*N*,*O*, 100_m. Mean_SD; **p*_0.05 (Student's *t* test).

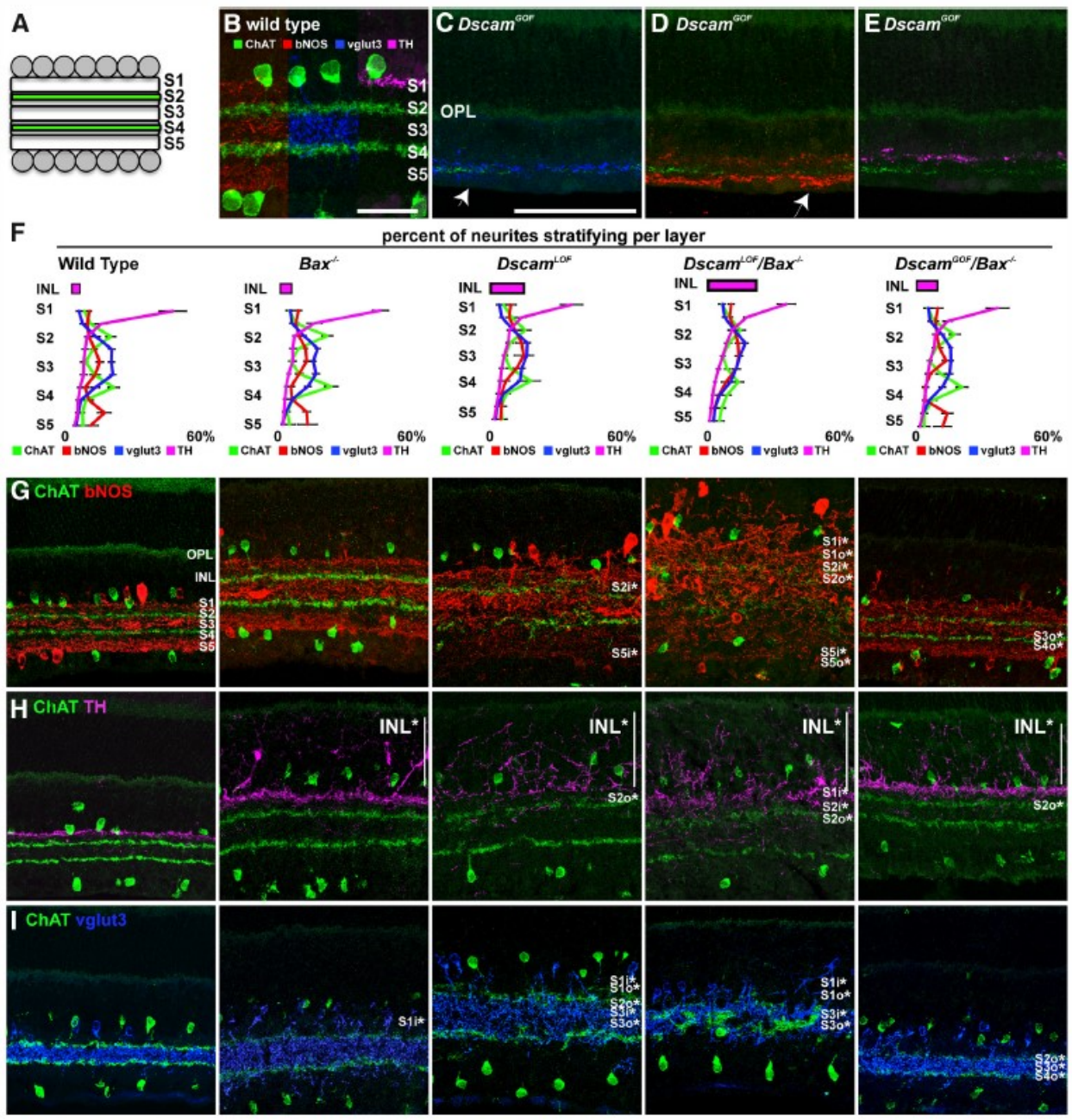

Figure 4.5. *Dscam* is necessary for IPL lamination. *A*, Diagram depiction of the retinal IPL divided into five strata, S1–S5. Locations of SAC dendrites are shown in green. *B*, Location of assayed dendrites in the wild-type retina.*C–E*, Lamination of SAC, bNOS_AC, vglut3_AC, and type 1 DAC dendrites in the *DscamGOF* retina. *C*,Asingle SAC band was observed in most of the *DscamGOF* retina (arrow).*D*, Dendrites projected to regions of the RGL not occupied by cell bodies (arrow). *F*, Plot of percentage dendrites laminating in S1–S5 in the wild-type, *Bax_/_*, *DscamLOF*, *DscamLOF/Bax_/_*, and *DscamGOF/Bax_/_* genotypes. Each

stratum was divided into an inner and outer half for plotting and quantifying percentage lamination. Asterisks in *G–I* denote a Mann–Whitney *U* test *p* value_0.01 compared with wild-type.*G*, Lamination of bNOS_amacrine cell dendrites.*H*, Lamination of type 1 DAC neurites. *I*, Lamination of vglut3_AC dendrites. P18:*N*_3 for all genotypes. Scale bars: *B*, 25_m; (in *C*) *C–E*, *G–I*, 100_m. Mean_SD; **p*_0.01 (Mann–Whitney *U* test).

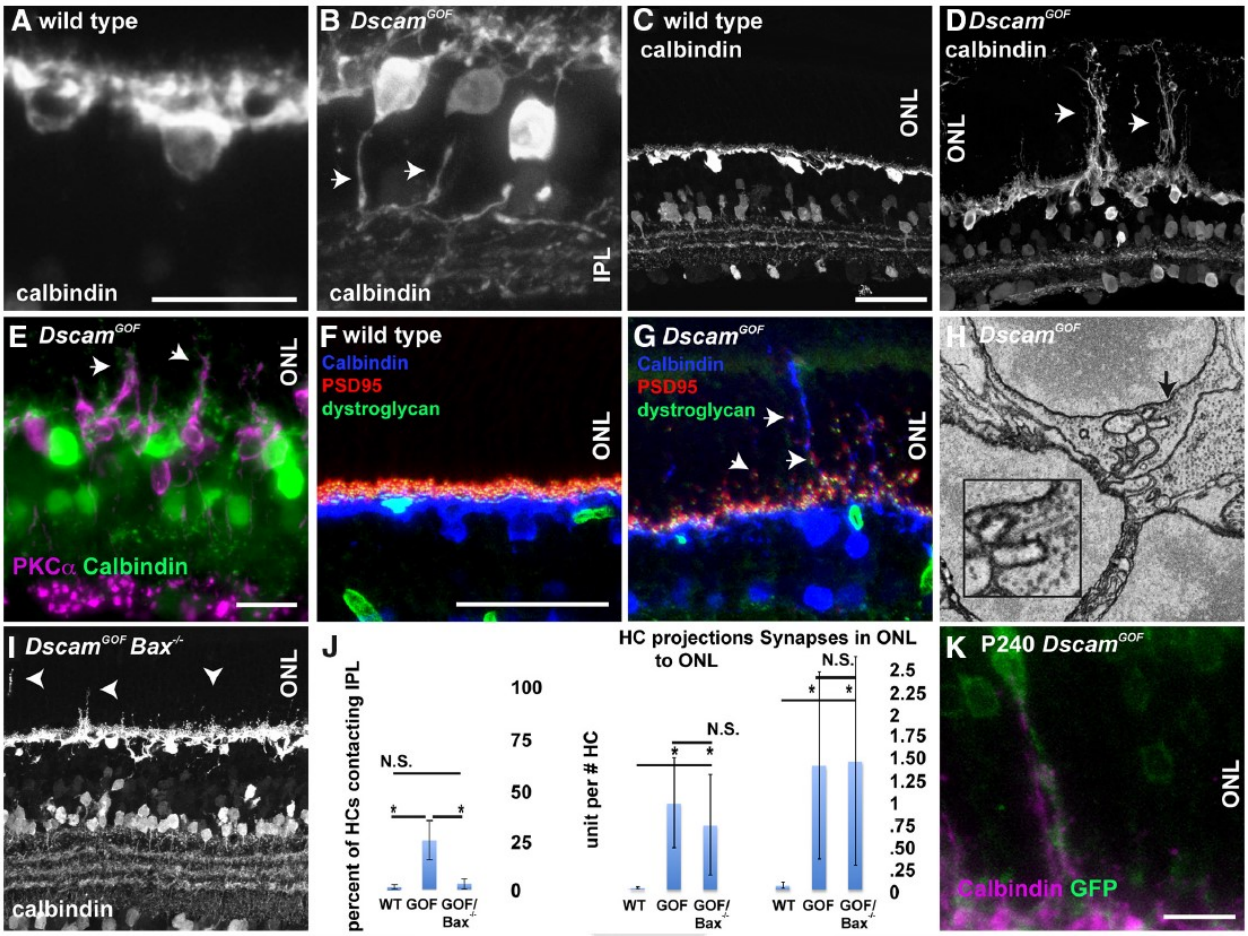

Figure 4.6. DSCAM is sufficient to retarget neurites in the outer retina. *A*–*D*, HCs in the wild-type and *DscamGOF* retina. *A*, *B*, Nearly 25% of *DscamGOF* HCs projected a neurite through the INL to the IPL (*B*, arrows). *C*, *D*, HCs projected neurites into the ONL in the *DscamGOF* retina (*D*, arrows). *E*, Bipolar cell dendrites projected into the ONL after HC neurites (*E*, arrows). *F*, *G*, The synaptic markers PSD-95 and dystroglycan were localized to the tips of HC neurites in the *DscamGOF* ONL (*G*, arrows). *H*, Ribbon synapses were observed in the *DscamGOF* ONL by electron microscopy. *I*, HC neurites projected into the *DscamGOF/Bax_/_*ONL (*I*, arrowheads). *J*, Quantification of HC projections into the IPL, ONL, and synapse number in the ONL for wild-type, *DscamGOF*, and *DscamGOF/Bax_/_*. *K*, HC neurites projecting into the *DscamGOF* ONL-targeted *Dscam*-expressing rods, including those that projected an axon to the OPL. P15:*A*–*G*; P42:*H*; P18: *I*, *J*; P240: *K*.*N*_4 for all assays/genotypes. Scale bars: (in *A*) *A*, *B*, 25_m; (in *C*) *C*, *D*, *I*, 50_m; *E*, 10_m; (in *F*) *F*, *G*, 50_m; *K*, 10_m; *H*, 3.5_m2. Mean_SD; **p*_0.05 (Student's *t* test).

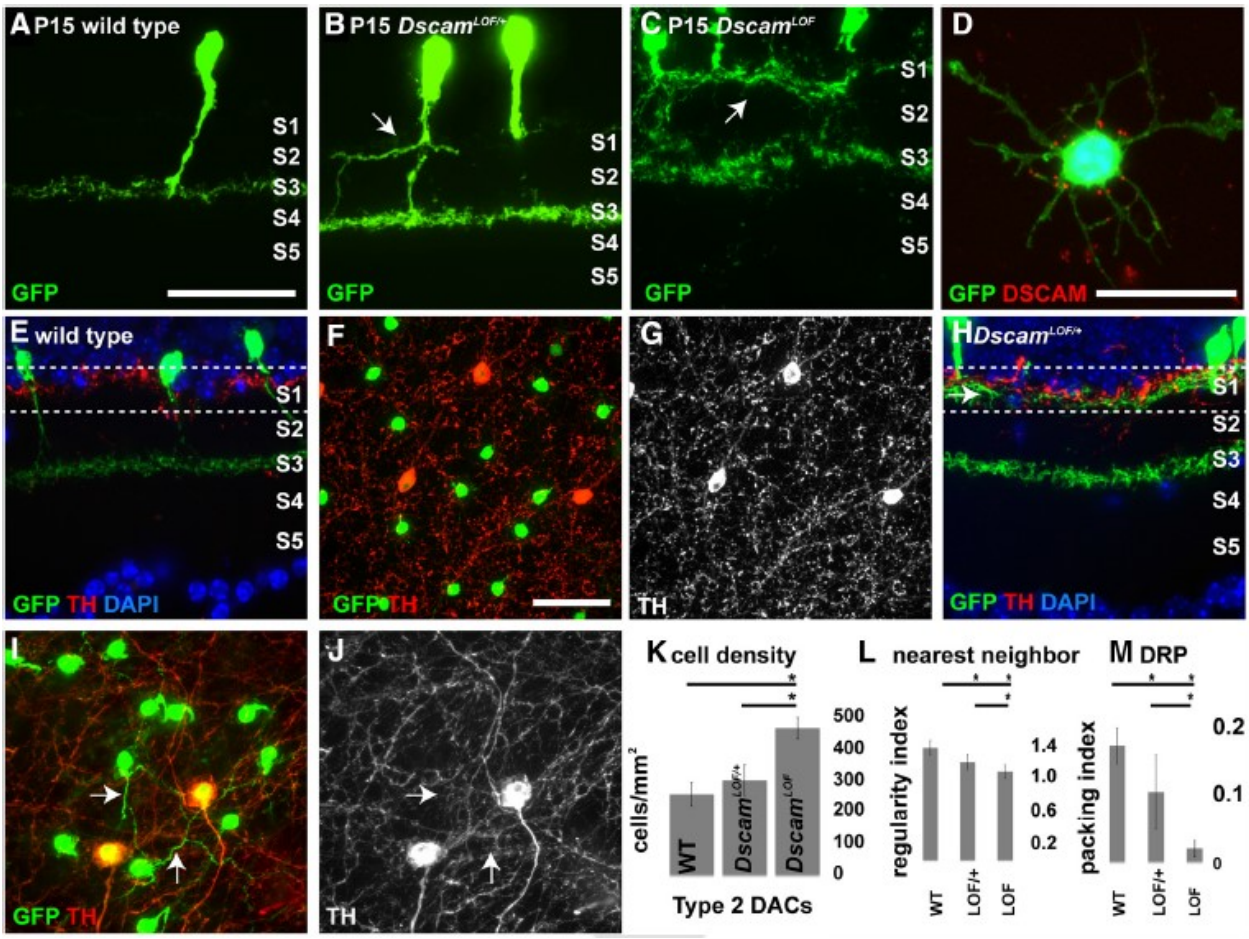

Figure 4.7. Type 2 DAC lamination defects are dependent on *Dscam* dosage. *A*–*C*, Type 2 DACs labeled with a GFP-expressing transgene. *A*, Type 2 DACs project dendrites to S3 at P15 in the wild-type retina. *B*, *C*, Type 2 DACs in the *DscamLOF/_*or *DscamLOF* retina project dendrites to both S1 and S3 (arrows). *D*, Type 2 DAC *in vitro* labeled with an antibody to DSCAM. DSCAM protein was localized to dendrites. *E*, Section of wild-type retina with type 1 and 2 DACs labeled (type 1_dim GFP and TH, type 2_GFP only). Dotted lines show the depth of confocal images in *F* and *G*. *F*, *G*, Type 1 and 2 DACs in a confocal section of layer S1 of the wild-type retina. Dendrites in S1 are those of type 1 DACs.*H*, Section of *DscamLOF/_*retina with type 1 and 2 DACs labeled (type 1_dim GFP and TH, type 2_GFP only). Dotted lines show the depth of confocal images in *I* and *J*. Dendrites of type 2 DACs laminate in S1 of the *DscamLOF/_*retina as evidenced by the lack of TH staining in bright GFP-positive dendrites (arrows). *K*, Quantification of type 2 DAC cell number in the wild-type, *DscamLOF/_*, and *DscamLOF* retinas. Cell density was significantly increased in the *DscamLOF* retina compared with wild-type and *DscamLOF/_*retina. Significant differences were not detected comparing the wild-type and *DscamLOF/_*retina. *L*, Nearest neighbor (NN)

analysis of type 2 DACs. NN regularity significantly decreased as *Dscam* dosage decreased.*M*, DRP analysis of type 2 DACs. Packing index values significantly decreased as *Dscam* dosage decreased. P15: *N*_10: *A*–*C*, *E*,*H*; *N*_ 3: *D*; *N*_4: *F*, *G*, *I*, *J*. Scale bars: (in *A*) *A*–*C*, *E*, *H*, 50_m; *D*, 25_m; (in *F*) *F*, *G*, *I*, *J*, 50_m. Mean_SD; *p_0.05 (Student's *t* test).

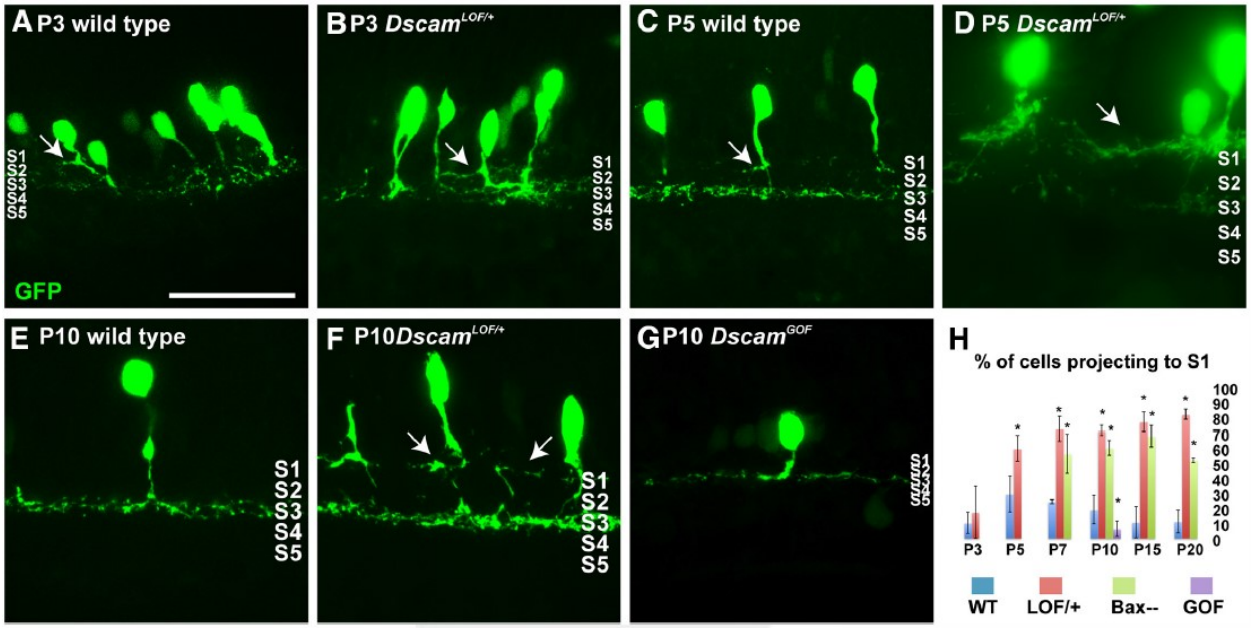

Figure 4.8. DSCAM prevents stabilization of exploring dendrites. *A*–*G*, Type 2 DACs. *A*, *B*, Type 2 DACs in the wild-type and *DscamLOF/_*retina at P3. A statistically similar number of type 2 DACs project into S1 comparing the wild-type and *DscamLOF/_* retina (arrows; *H*, P3). *C*, *D*, Type 2 DACs in the wild-type and *DscamLOF/_* retina at P5. A statistically significant increase in the number of type 2 DACs that project dendrites into S1 of the *DscamLOF/_* retina was observed as compared with controls (arrows; *H*, P5). *E*–*G*, Type 2 DACs in the wild-type, *DscamLOF/_*, and *DscamGOF* retina at P10. A statistically significant increase in the number of type 2 DACs project dendrites into S1 of the *DscamLOF/_* retina was observed compared with wild-type or *DscamGOF* cells (*F*, arrows). A statistically significant decrease in the number of type 2 DACs projecting dendrites into S1 was observed in the *DscamGOF/_*retina compared with wild-type or *DscamLOF/_* cells (*H*, P10). *H*, Quantification of type 2 DAC projections into S1. *N*_3: P3, P5, P10, and P15; *N*_2 WT and *Bax_/_* P7 and P20. Scale bars: (in *A*) *A*–*G*, 50 _m. Mean_SD; *p_0.05 (Student's *t* test).

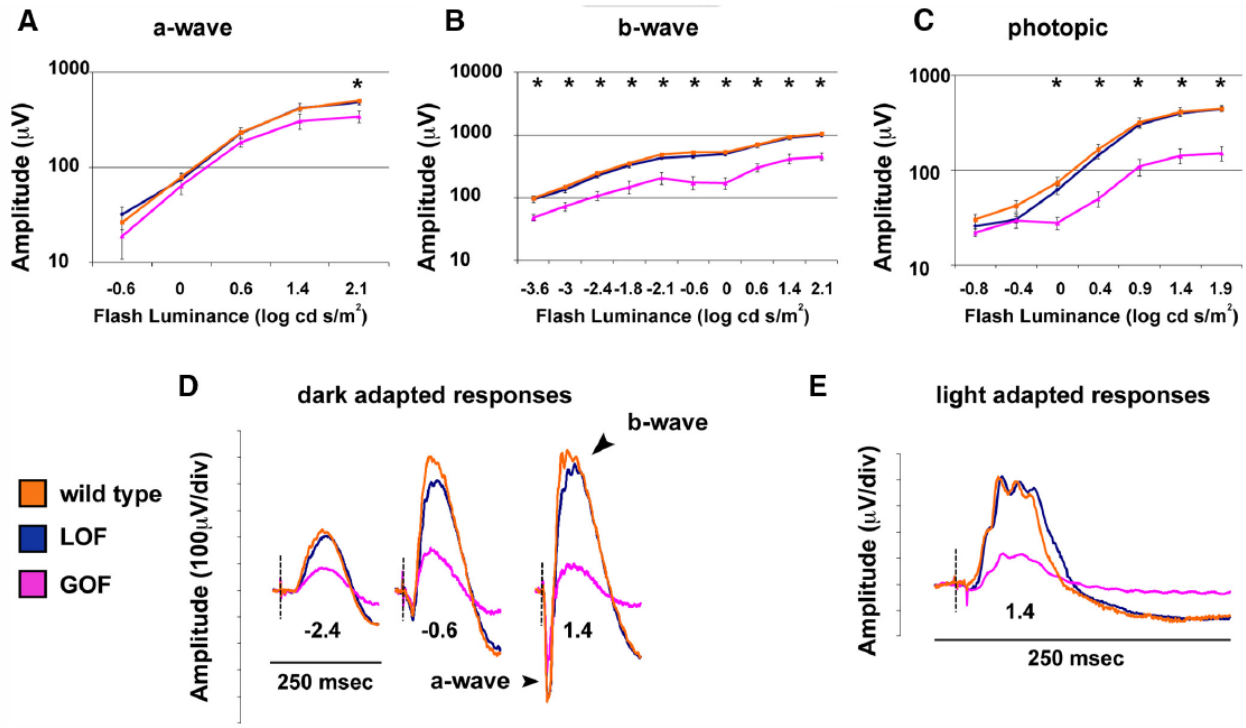

Figure 4.9. *Dscam* overexpression disrupts physiology of outer plexiform layer circuitry. *A–E*, Light- and dark-adapted physiology of the wild-type, *DscamLOF*, and *DscamGOF* retina measured by ERG. *A*, *D*, The a-wave of *DscamGOF* mice was significantly reduced compared with wild-type or *DscamLOF* mice. *B*, *D*, The b-wave of *DscamGOF* mice was significantly reduced compared with wild-type or *DscamLOF* mice. *C*, *E*, The photopic wave of *DscamGOF* mice was significantly reduced compared with wild-type or *DscamLOF* mice. *N*_6 for all genotypes. Mean_SD; **p*_0.01 (Student's *t* test).

Chapter 5: Expression Patterns of DSCAM and SDK Gene Paralogs in Developing Zebrafish Retina

Carlos A. Galicia[1]*, Joshua M. Sukeena[1]* Deborah L. Stenkamp[1], and Peter G. Fuerst[1, 2]

1 University of Idaho, Department of Biological Sciences, Moscow, Idaho 83844, USA, 2 University of Washington School of Medicine, WWAMI Medical Education Program, Moscow, Idaho 83844, USA.

*Co-First Authors

Abstract

The DSCAM, DSCAMl1, SDK1 and SDK2 proteins belong to the immunoglobulin super family of cell adhesion molecules (CAM). Cell adhesion molecules are responsible for the aggregation of cells into tissues and organs. Because of the teleost genome duplication, the zebrafish possesses two copies of each CAM gene except dscaml1. Here we describe the spatial expression patterns of the six genes in the zebrafish embryo retina (96hpf) as well as the co-expression or lack of it among the CAM genes. We found that *dscama* and *dscamb* are co-expressed in the GCL and the basal portion of the INL, however the ONL only showed expression of *dscamb*. *Sdk1a* and *sdk1b* were mostly co-expressed in the GCL and basal portion of the INL. *Sdk2a* and *sdk2b* also showed co-expression in the GCL and basal portion of the INL. An alternate pattern of co-expression and exclusive expression of the dscam and sdk1 paralogs was observed in the GCL and INL. The same pattern was observed between sdk1 and sdk2 paralogs and sdk2 and dscam paralogs. Dscaml1 was observed in the INL and GCL and points of co-expression of *dscaml1* and *dscama* were observed in the basal portion of the INL.

Introduction

The differential adhesion hypothesis proposes that organization of an organism's body plan is mediated by expression of cell adhesion molecules that result in aggregation of cells into different tissues and organs. Experimental evidence for the differential adhesion hypothesis in the nervous system, where it is invoked to explain the exquisite connectivity pattern, is robust. Neuroligins and neurexins have been experimentally demonstrated to provide specificity during neural pairing by partnering pre and post synaptic cells (Dean & Dresbach, 2006). Members of the cadherin and immunoglobulin superfamily of cell adhesion molecules (CAMS), have also been implicated in patterning the nervous system by promoting adhesion or avoidance (Galli-Resta et al., 2008; Sanes and Yamagata, 2009).

Many studies of the role of differential adhesion in neural development are conducted in the retina. Unlike most neural tissues, retinal neurons are coupled in the absence of synaptic input (Nevin et al., 2008), which plays a more local role in sculpting precise synaptic structure (Mumm et al., 2005). The retina is organized in three layers, the outer nuclear layer (ONL), which contains rod and cone photoreceptors, the inner nuclear layer (INL), which contains bipolar, amacrine and horizontal cells, and the retinal ganglion cell layer (RGL), which contains ganglion and amacrine cells (Masland, 2001). Retinal synapses are localized to two synaptic layers located in between the cellular layers; the outer nuclear layer (ONL) and inner nuclear layer (INL). The abundance of tools to label and manipulate retinal neurons and the importance of the tissue in our species dominant sense, vision, has made the retina a valuable model to study mechanisms of neural connectivity.

Zebrafish, as members of the teleost lineage of fishes, underwent a whole genome duplication (WGD) approximately 400 million years ago (Jaillon et al., 2004). As a result most genes represented by a single copy in mammals have two homologues in zebrafish. Subfunctionalization and neofunctionalization of paralogous zebrafish gene products over 400 mya offer the opportunity to genetically dissect the function of genes that play multiple roles in development and an elegant system to test the differential adhesion hypothesis. Therefore, the zebrafish retina is a good model system for evolutionary studies that seek to determine the mechanisms by which differential adhesion sculpts neural architecture.

As a first step we have characterized the expression of Down syndrome cell adhesion molecule (*Dscam*) and sidekick (*Sdk*) paralogs in the zebrafish retina. DSCAM and SDK proteins have been implicated in multiple developmental roles including axon guidance,

avoidance and neuron pairing. The zebrafish genome has three *Dscam* and four *Sdk* genes, compared to two each in chick and mammals. In this study we compared the expression of *Dscam* and *Sdk* paralogs in the zebrafish retina. Additionally, we have cloned *Dscama* and *Dscamb* for use in cellular interaction assays.

Materials and Methods

Zebrafish embryos

Wild type strains of Zebrafish (*Danio rerio*) were maintained at the University of Idaho on a 14 hour:10 hour light:dark cycle in monitored, recirculating system water according to standard protocols as previously described (Westerfield 2007). Embryos were collected and maintained in at approximately 28 ^{o}C until harvesting at 96 hours post fertilization (hpf). Regardless of collection time, the time of spawn was considered as 0 hpf. Following administration of anesthesia with 0.02% MS-222, they were fixed in solution of 4% paraformaldehyde in 5% buffered sucrose solution. Following fixation, embryos were washed in phosphate buffer solution (PBS) and transferred to a mixture consisting of a 1:1 ratio of 30% sucrose in PBS and OCT (optimal cutting temperature embedding medium; Sakura Finetek USA, Torrance CA). Embryos were frozen and cut into 5 µm sections using Microm HM 550.

Sequence analysis

Sequences for zebrafish *dscama*, *dscamb*, *dscaml1 sdk1a*, *sdk1b*, *sdk2a*, *sdk2b* were obtained from the Ensembl genome browser (ensmbl.org release 82). An unrooted tree with the amino acid sequences was generated by performing an alignment with Cobalt and phylogenetic analysis with PAUP 4.0 (Swofford 2003) using the Neighbor Joining algorithm (Fig. 1b). The amino acid sequence of the genes was analyzed using SMART (Letunic 2005) and Prosite (De Castro 2006) to determine the number and identity of protein domains (Fig. 1a). Similarity between sequences was obtained from alignments generated by the blastn suite (Fig. 1d, 1e, 1f, 1g).

Probe preparation

Embryos were homogenized in 1.0 mL of TRIzol Reagent (Invitrogen, Waltham, MA) and RNA was extracted using PureLink RNA Micro Kit (Invitrogen). The extracted RNA was used to generate cDNA with qScript cDNA SuperMix (Quanta Bioscience, Saskatoon, SK). The

resulting cDNA library was subjected to PCR using gene specific primers. Promoter sequences for T7 and SP6 were incorporated into amplicons as previously described (Fuerst et al., 2008). The primers and promoter sequences corresponding with each gene target are summarized in (Table 1).

Histological processing and In situ hybridization

Embedding and in situ hybridization was performed as previously described in at least 4 slides containing tissue from at least 3 different embryos (Barthel and Raymond, 1990; Nelson et al., 2009; Stevens et al., 2011) with minor changes to temperatures of probe hybridization and 1:1 formamide:2xSSC stringency washes. Tissue was vacuum dried for 24 hours prior to hydration using sequential ethanol treatments at concentrations of 100%, 95%, 70%, and 50%. Proteinase K was used to permeabilize the tissue following an acetylation step with triethanolamine (TEA) and acetic anhydride. This was followed by a dehydration step with sequential ethanol treatments at concentrations of 50%, 75%, 95%, and 100% before air drying for one or more hours. Tissues were hybridized with probes for *dscama*, *dscamb*, and *dscaml1* at 68^{o}C and the stringency wash of 1:1 formamide and 2xSSC was performed at 65 ^{o}C. Probes for *sdk1a*, *sdk1b* were hybridized at 70^{o}C and the stringency wash was performed at 56^{o}C. Probes for *sdk2a* and *sdk2b* were hybridized at 70^{o}C and underwent a stringency wash at 68^{o}C. Following stringency washes, tissue was treated with RNAse A and then incubated overnight at room temperature in Anti-Digoxigenin-AP, FAB fragments or Anti-Fluorescein- AP, Fab fragments (Roche). NBT/BCIP solution and/or Fast Red was used to generate colored precipitates. Double in situ hybridization was performed as previously described (Mitchell et al., 2015). Upon completion of color development, slides were washed in alkaline phosphatase (AP) buffer and mounted with 80% glycerol. Images were collected using a Leica DMR microscope and SPOT camera. Expression pattern variability was minimal and mainly caused by differences in time of color development.

Cloning and Transfection

Hek 293 cells were cultured in DMEM with 10% fetal calf serum (FBS) with added antibiotics streptomycin and penicillin. Transfection was done using FuGENE® transfection reagent (Promega). Cells were incubated at 37 ^{o}C with 5.0% CO_2. Cells were stained with antibodies against MYC sequence EQKLISEEDL following a 20 minute fixation (4% paraformaldehyde/1X PBS at room temperature). Co-transfection was done using vectors

with actin GFP and mRFP. The construct for Actin GFP was driven by a CAG promoter in a poly-vector. The construct for mRFP was driven by a CAG promoter in poly-vector.

Results

Overview of the cell adhesion molecule genes and genetic analysis

DSCAM and SDK proteins belong to the immunoglobulin superfamily (IgSF) of cell adhesion molecules (CAM). Their general structure is composed of a variable number of immunoglobulin-like domains and fibronectin domains (type III), a single pass transmembrane domain, and an intracellular domain with a C-terminus that are predicted to bind a PDZ domain (Doyle et al., 1996; Takahashi et al., 1999) (Figure 1A). Genome analysis revealed that zebrafish *dscama*, *dscamb*, *dscaml1, sdk1a, sdk1b*, *sdk2a* and *sdk2b* each possess similar protein domain patterns which correspond to what has been shown previously in their respective orthologs in other vertebrates (Yamagata and Sanes, 2008). In order to assess the relationships between these CAM gene paralogs, we generated a cladogram using amino acid sequences. As predicted, the resulting tree grouped the paralogs together; *dscama* and *dscamb*, *sdk1a* and *sdk1b*, and *sdk2a* and *sdk2b* (Figure 1B). It also showed a closer relationship between Sdk1 and Sdk2 paralog pairs to each other than to any of the Dscam genes. *Dscaml1*, a homolog to *dscama* and *dscamb*, was placed closer to the pair of Dscam paralogs than any of the Sdk genes (Agarwala et al., 2001). Data obtained from ensmbl.org indicated the chromosomal location of *dscaml1* and *dscamb* to be in chromosome 15, *dscama* in chromosome 10, *sdk1a* and *sdk2a* in chromosome 3, *sdk1b* in chromosome 1 and *sdk2b* in chromosome 12 (Fig. 1C). Each pair of paralogs was compared to its single orthologue in human, chick, spotted gar and mice. The comparison of *dscama* and *dscamb* in zebrafish to *dscam* genes in the other species showed an small but consistent higher similarity with *dscamb* (Fig. 1D). Similarly, when comparing *sdk1a* and *sdk1b* to the sdk1 gene across species, *sdk1a* showed a consistent higher similarity (Fig. 1E) and the comparison of *sdk2a* and *sdk2b* to sdk2 showed a higher similarity with *sdk2b* (Fig. 1G). *Dscaml1* was also aligned against the *dscaml1* gene of human, chick, spotted gar and mice and as predicted showed a higher similarity to spotted gar than to the other vertebrates. Data obtained from *Ensembl*® indicated the chromosomal location of *dscaml1* and *dscamb* to be in chromosome 15, *dscama* in chromosome 10, *sdk1a* and *sdk2a* in chromosome 3, *sdk1b* in chromosome 1 and *sdk2b* in chromosome 12 (Fig. 1C). Each pair of paralogs was compared to its single orthologue in human, chick, spotted gar and mice.

Comparisons between zebrafish orthologs *dscama* and *dscamb* to *dscam* genes in other species were consistently observed to be more similar to *dscamb* (Fig. 1D). Similarly, when comparing sdk1a and sdk1b to the sdk1 genes across the aforementioned species, sdk1a was observed to be more similar to the genes of other species (Fig. 1E). Additionally, in comparisons between sdk2a and sdk2b to sdk2 genes in other species, there was more similarity to sdk2b than sdk2a (Fig. 1G). *Dscaml1* was also aligned against the dscaml1 gene of human, chick, spotted gar and mice and as predicted showed a higher similarity to spotted gar than to the other vertebrates.

Differential expression patterns of Dscam paralogs during retinogenesis.

We used *in situ* hybridization to examine expression patterns for the Dscam paralogs in the developing zebrafish retina. Target sequences were amplified from zebrafish cDNA and used to produce digoxigenin (DIG) labeled anti-sense cRNA probes. Each probe was applied to cryosectioned retinal tissue from 96 hours post fertilization (hpf). 96 hpf was chosen as the time point for our experiments to more easily localize the expression of the CAM genes within the layers of the retina since they would be fully shaped. *Dscama* mRNAs were found to be expressed by a subset of cells located in the GCL, and the basal portion of the INL which corresponds to the location of amacrine cells (Fig. 2A). This is consistent with the expression pattern of Dscam observed in the developing mouse retina (Fuerst et al., 2009). However, this pattern differs with the expression observed in the developing chick retina, where subsets of cells in the ONL, all areas of the INL, and GCL express Dscam (Yamagata and Sanes, 2008). *Dscamb* mRNAs were also detected in subsets of cells located in the GCL and basal portions of INL. However, unlike *dscama*, *dscamb* transcripts were observed to be expressed in cells of the ONL (Fig. 2B). Similarly, expression of dscam and dscaml1 in the ONL has also been reported in the developing chick retina (Enright 2014, Yamagata and Sanes 2008).

Differential expression patterns of Sdk paralogs during embryogenesis

We used *in situ* hybridization to determine the mRNA expression patterns for the gene paralog pairs, *sdk1a* and *sdk1b*, as well as *sdk2a* and *sdk2b*. Antisense probes detected expression of transcripts for all four genes in the basal region of the INL and GCL (Fig. 2D-G). This predicts their expression in amacrine cells and retinal ganglion cells. However, sections that were sampled closer to the peripheral regions of the retina showed expression of *sdk1b* and *sdk2b* in subsets of cells in the ONL (Fig. 2E and 2G). This is

similar to the expression pattern that was seen for *dscamb* (Fig. 2B). Our observations in zebrafish retina differ from that of the developing mouse retina. The expression of sidekick-1 and sidekick-2 in mouse retina was observed in subsets of cells in the GCL and throughout the INL, but very little expression was seen in the ONL (Krishnaswamy et al., 2015). *Sdk1b* and *sdk2b* expression in zebrafish retina appear similar to the developing chick retina, where expression of sidekick-1 and sidekick-2 has been reported in subsets of cells in the ONL, throughout the INL, and GCL (Yamagata et al., 2002; Yamagata and Sanes, 2008).

Co-expression patterns of CAM gene paralogs during embryogenesis

In order to determine whether our target paralogs are co-expressed in the same cell populations, we used double *in situ* hybridization assays. In zebrafish, co-expression of *dscama* and *dscamb* was observed within a subset of cells located in the GCL and INL (Figure 3A-C). However, only *dscamb* was found to be expressed in the ONL (Figure 3B). We also used double *in situ* hybridization assays for the Sdk gene paralogs to determine whether or not they are co-expressed during development. *Sdk1a* and *sdk1b* were co-expressed by a subset of cells in the GCL as well as the basal portion of the INL (Fig. 3D-F). Similarly, *sdk2a* and *sdk2b* were also found to be co-expressed by a subset of cells in the GCL and basal portion of the INL (Figure 3 G-I).

Expression of CAM genes does not exclude expression of other CAM genes.

We next sought to determine the prevalence of co-expression for Dscam and Sdk genes in the same cell. Previous observations in chick and mouse showed mRNAs for sidekick-1 and sidekick-2 were rarely found to overlap in neuron subsets, and overlap was only observed within the GCL (Yamagata et al., 2002; Yamagata and Sanes, 2008; Krishnaswamy et al., 2015). In the developing chick retina, Dscam, dscaml1, Sidekick-1 and Sidekick-2 are all expressed exclusively in subsets of retinal neurons and specific laminae of the IPL (Y&S, 2008; Y&S, 2010). A similar expression pattern has been observed for Dscam in mouse retina, where *dscama* and *dscaml1* are expressed in exclusive cells (Fuerst et al., 2009). However, occurrences of sidekick-1 and sidekick-2 co-expression in mouse retina have been observed for cells in the GCL (Krish, 2015).

We performed double *in situ* hybridization with the following CAM gene pairs: *dscama* with *dscaml1, sdk1b* with *dscamb, and sdk2b* with *sdk1b*. We sought to determine whether expression of different CAM types was mutually exclusive in zebrafish retina. The expression

patterns of *dscama* (Fig. 4J) and *dscaml1* (Fig. 4K) showed co-expression in cells located in the basal part of the INL (Fig. 4L). Other areas of the INL only showed expression of *dscaml1*. Results of *sdk1b* (Fig. 4D) and *dscamb* (Fig. 4E) revealed co-expression in cells located in the INL and GCL (Fig. 4F). Additionally, we observed *sdk2b* (Fig. 4G) and *dscamb* (Fig. 4H) had a similar pattern of co-expression within INL neurons (Fig. 4I).We observed similar regions of expression for *sdk2b* (Fig. 4A) and *sdk1b* (Fig. 4B), with a cell mosaic of exclusive expression and co-expression within the INL (Fig. 4C). For all target mRNAs, the expression pattern of exclusivity that was observed in the developing chick retina (cite) was not seen. However, full co-expression was not observed either. This lack of a complete exclusion of expression or a complete co-expression resembled the results found for sidekick-1 and sidekick-2 in mice (Krish, 2015).

Cloning of DSCAM A and DSCAM B proteins

We were able to successfully clone the full coding sequence for both *dscama* and *dscamb* into vector pcDNA 3.1+ (cite). The cloning was done sequentially in regions of 1000 base pairs at a time, with an overlap of ~100 base pairs. PCR was used to join fragments together. A full table of primers and the restriction sites that were used can be found in table 2. For *dscama*, nucleotide blast revealed identities at 99% (6050/6075) between Ensembl databased and our cloned gene. Peptide blast revealed identities at 100% (2024/2024). For *dscamb*, nucleotide blast revealed identities at 99% (6050/6063) between Ensembl database and our cloned gene. Peptide blast revealed 100% identity (2020/2020). For both *dscama* and *dscamb*, this suggests that the mismatches in nucleotide sequence were isolated to the third codon site, and did not affect the protein sequence. In order to verify expression of the individual genes *in vitro*, we fused a MYC tag sequence (EQKLISEEDL) to the N-terminus of each nucleotide sequence followed immediately by a stop codon (N-EQKLISEEDL-stop). We then individually co-transfected them into hek293A cells with vectors containing other fluorescent markers. For *dscamba*, a membrane bound red fluorescent protein was used (mRFP). For *dscamb*, a green fluorescent protein fused to actin was used (actin GFP). Our results show that expression of *dscama* and *dscamb* was occurring in these cells (Figure 5).

Discussion

Our results suggest that retinal expression patterns of Dscam and Sdk genes are dissimilar across species during embryonic development. These expression patterns can vary both across sets of CAM genes (Dscam and Sdk genes) and between gene paralogs (*dscama*

and *dscamb*). In chick retina, there is non-overlapping expression in subsets of interneurons and retinal ganglion cells, with further expression at the synapses in distinct sublaminae of the IPL. This is true both across CAM genes, and within paralog pairs. In mouse, the paralogs show no overlap in expression, but co-expression of Dscam and Sdk genes has been observed. Our observations in zebrafish show that paralogs are co-expressed in subsets of cells within the GCL and INL. However, when comparing across CAM genes, there was a mixture of co-expression and exclusive expression in the INL and GCL, possibly depending on cell type. Taken together, it appears that CAM expression patterns vary across species, and more functional data will be required to understand their roles during early retinal development.

Abbreviations

Dscam= Down syndrome cell adhesion molecule; Sdk= Sidekick. hpf= hours post fertilization; ONL=outer nuclear layer; INL=inner nuclear layer; GCL=ganglion cell layer; IPL=inner plexiform layer.

References

Agarwala, K. L., Ganesh, S., Tsutsumi, Y., Suzuki, T., Amano, K., & Yamakawa, K. (2001). Cloning and functional characterization of *DSCAML1*, a novel DSCAM-like cell adhesion molecule that mediates homophilic intercellular adhesion. *Biochemical and biophysical research communications*, *285*(3), 760-772.

Doyle, D. A., Lee, A., Lewis, J., Kim, E., Sheng, M., & MacKinnon, R. (1996). Crystal structures of a complexed and peptide-free membrane protein–binding domain: molecular basis of peptide recognition by PDZ. *Cell*,*85*(7), 1067-1076.

Fuerst P.G., Bruce F., Tian M., Wei W., Elstrott J., Feller M.B., Erskine L., Singer J.H., Burgess R.W. (2009). DSCAM and *DSCAML1* function in self-avoidance in multiple cell types in the developing mouse retina. *Neuron*, *64*(4), 484-497.

Gumbiner, B. M. (1996). Cell adhesion: the molecular basis of tissue architecture and morphogenesis. *Cell*, *84*(3), 345-357.

Jaillon O., Aury J.M., Brunet F., Petit J.L., Stange-Thomann N., Mauceli E., Bouneau L., Fischer C., Ozouf-Costaz C., Bernot A., Nicaud S., Jaffe D., Fisher S., Lutfalla G., Dossat C., Segurens B., Dasilva C., Salanoubat M., Levy M., Boudet N., Castellano S., Anthouard V., Jubin C., Castelli V., Katinka M., Vacherie B., Biémont C., Skalli Z., Cattolico L., Poulain J., De Berardinis V., Cruaud C., Duprat S., Brottier P.,

Coutanceau J.P., Gouzy J., Parra G., Lardier G., Chapple C., McKernan K.J.,McEwan P., Bosak S., Kellis M., Volff J.N., Guigó R., Zody M.C., Mesirov J., Lindblad-Toh K., Birren B., Nusbaum C., Kahn D., Robinson-Rechavi M., Laudet V., Schachter V., Quétier F., Saurin W., Scarpelli C., Wincker P., Lander E.S., Weissenbach J., Roest Crollius H. (2004). Genome duplication in the teleost fish Tetraodon nigroviridis reveals the early vertebrate proto-karyotype. *Nature*,*431*(7011), 946-957.

Krishnaswamy, A., Yamagata, M., Duan, X., Hong, Y. K., & Sanes, J. R. (2015). Sidekick 2 directs formation of a retinal circuit that detects differential motion. *Nature*, *524*(7566), 466-470.

Masland, R. H. (2001). The fundamental plan of the retina. *Nature neuroscience*, *4*(9), 877-886.

Dean, C., & Dresbach, T. (2006). Neuroligins and neurexins: linking cell adhesion, synapse formation and cognitive function. *Trends in neurosciences*, *29*(1), 21-29.

Mumm, J. S., Godinho, L., Morgan, J. L., Oakley, D. M., Schroeter, E. H., & Wong, R. O. (2005). Laminar circuit formation in the vertebrate retina.*Progress in brain research*, *147*, 155- 169.

Nevin, L. M., Taylor, M. R., & Baier, H. (2008). Hardwiring of fine synaptic layers in the zebrafish visual pathway. *Neural development*, *3*(1), 1.

Takahashi, K., Nakanishi, H., Miyahara, M., Mandai, K., Satoh, K., Satoh, A., Nishioka H, Aoki J, Nomoto A, Mizoguchi A, Takai, Y. (1999). Nectin/PRR: an immunoglobulin-like cell adhesion molecule recruited to cadherin-based adherens junctions through interaction with afadin, a PDZ domain–containing protein. *The Journal of cell biology*,*145*(3), 539-549.

Schmucker, D., Clemens, J. C., Shu, H., Worby, C. A., Xiao, J., Muda, M., Dixon J.E., Zipursky, S. (2000). Drosophila Dscam Is an Axon Guidance Receptor Exhibiting Extraordinary Molecular Diversity. *Cell*, 101(6).

Yamagata, M., & Sanes, J. R. (2008). Dscam and Sidekick proteins direct lamina-specific synaptic connections in vertebrate retina. *Nature*, *451*(7177), 465-469.

Zhang, J. (2003). Evolution by gene duplication: an update. *Trends in ecology & evolution*, *18*(6), 292-298.

Figures

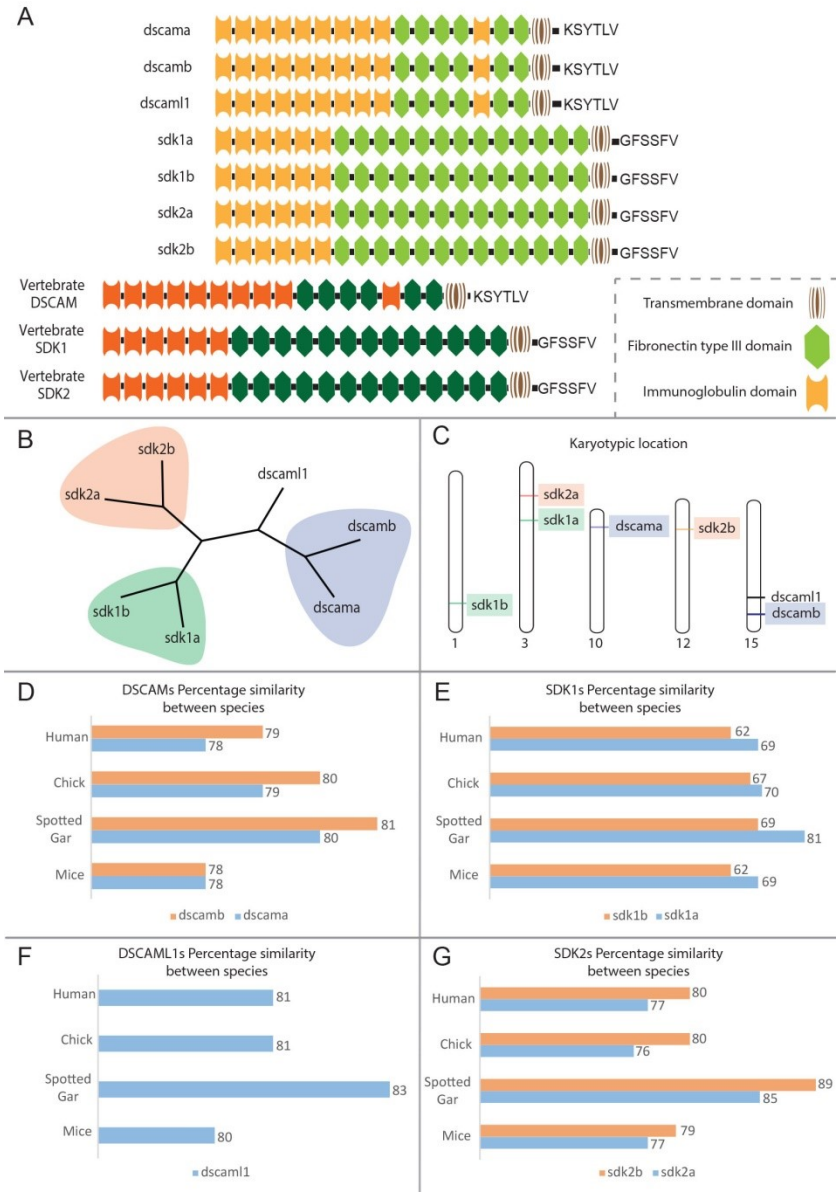

Figure 5.1. Compositional and genetic comparison of Dscam and Sdk genes. The zebrafish genome contains paralogs for Dscam (*dscama* & *dscamb*), Sdk1 (*sdk1a* & *sdk1b*), and Sdk2 (*sdk2a* & *sdk2b*). *Dscaml1* is a homolog for *dscama* and *dscamb*. Both Dscam and Sdk are members of the immunoglobulin superfamily of proteins, and play roles in cell adhesion. They consist of different combinations of the following protein domain(s); a single pass transmembrane domain, fibronectin (type III) domains, and immunoglobulin domains. **A)** The combination of domain structures for *dscama*, *dscamb*, *dscaml1*, *sdk1a*, *sdk1b*, *sdk2a*, and *sdk2b* as obtained from the zebrafish genome. The corresponding structures for

DSCAM, SDK1, and SDK2 for other non-teleost vertebrates are also displayed. Key is displayed in lower right of panel by dashed line. **B)** A cladogram was generated to show relationships between the nucleotide sequences of all genes that were targeted. Predicted relationships were found between Sdk and Dscam paralogs (see colors), with *dscaml1* homolog showing divergence prior to duplication event. **C)** Visual representation of gene locus for Dscam and Sdk genes in zebrafish. Chromosome numbers are shown as 1, 3, 10, 12, and 15. **D-G)** Nucleotide sequences for Dscam and Sdk genes were assembled and blasted against the sequences for orthologs in the following species: human, chick, spotted gar and mouse. **D)** Percentages of similarity for *dscamb* (orange) and *dscama* (blue) were determined against the singular Dscam that is found in the genomes of human, chick, spotted gar, and mouse. **E)** Percentages of similarity for *sdk1b* (orange) and *sdk1a* (blue) were determined. **F)** Percentages of similarity for *dscaml1* were determined. **D)** Percentages of similarity for *sdk2b* (orange) and *sdk2a* (blue) were determined. Abbreviations: Dscam= Down syndrome cell adhesion molecule; Sdk= Sidekick.

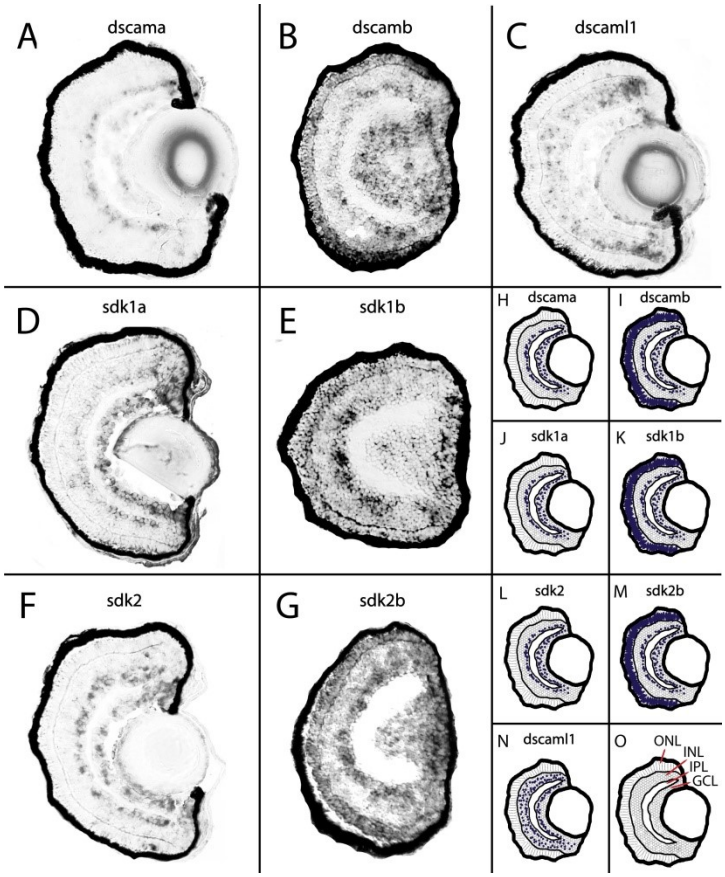

Figure 5.2. Expression of cell adhesion molecules in developing zebrafish retina at 96hpf. Expression patterns of cell adhesion molecules, Dscam and Sdk, were observed and found to vary between paralogs. *In situ* hybridization using cryosections of 96 hpf zebrafish retina is shown for **A)** *dscama*, **B)** *dscamb*, **C)** *dscaml1*, **D)** *sdk1a*, **E)** *sdk1b*, **F)** *sdk2a*, **G)** *sdk2b*. Consistent labeling of mRNA was found in the INL and GCL, however expression in the ONL was observed only for *dscamb* **(B)**, *sdk1b* **(E)**, and *sdk2b* **(G)**. Cartoon representations in **H-N** display the expression patterns for each mRNA that was targeted. Here, paralogs are displayed side-by-side with labeling of ONL, INL, GCL, and IPL as represented in **(O)**. All images displayed are of antisense probe. Abbreviations: hpf= hours post fertilization; Dscam= Down syndrome cell adhesion molecule; Sdk= Sidekick; ONL=outer nuclear layer; INL=inner nuclear layer; GCL=ganglion cell layer; IPL=inner plexiform layer.

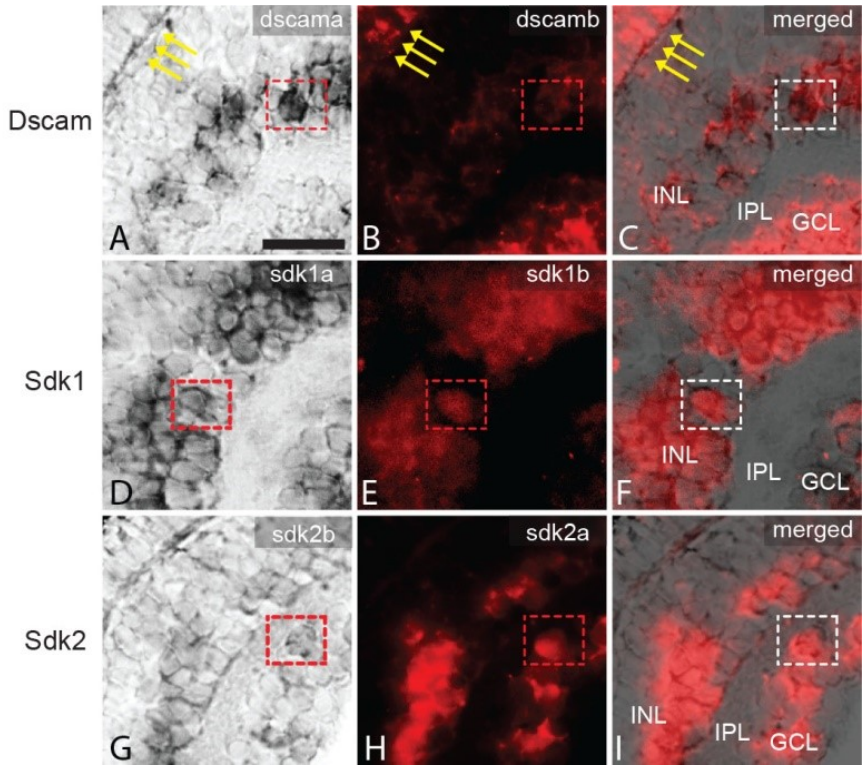

Figure 5.3. Expression of Dscam and Sdk paralogs in developing zebrafish central retina at 96 hpf. Relative expression levels of *dscama*, *dscamb*, *sdk1a*, *sdk1b*, *sdk2a*, and *sdk2b* were shown using *in situ hybridization*. **A)** Expression of *dscama* was observed in the INL and at low levels in the GCL, but no expression was observed in the ONL (arrows). **B)** Expression of *dscamb* was observed at low levels in the INL and strongly in the GCL and ONL (arrows). **C)** Gene paralogs, *dscama* and *dscamb* are co-expressed in cells in the INL and GCL, but only *dscamb* is expressed in the ONL (arrows). **D)** Expression of *sdk1a* was observed in the INL and GCL. **E)** Expression of *sdk1b* was seen in the INL and at low levels in the GCL. **F)** Gene paralogs, *sdk1a* and *sdk1b* were shown to be co-expressed in cells in the INL and GCL. **G)** Expression of *sdk2b* was observed in the INL and GCL. **H)** Expression of *sdk2a* was observed in the INL and GCL. **I)** Gene paralogs, *sdk2b* and *sdk2a* were shown to be co-expressed in cells in the INL and GCL. Dashed line boxes show the identical area of interest for panels A-C, D-F, and G-I. The red boxes correspond to the region for single expression panels of A, B, D, E, G, and H White boxes in C, F, and I show regions of co-expression between paralogs. All images displayed are of antisense probe. Abbreviations: hpf= hours post fertilization; Dscam= Down syndrome cell adhesion molecule; Sdk= Sidekick; ONL=outer nuclear layer; INL=inner nuclear layer; GCL=ganglion cell layer.

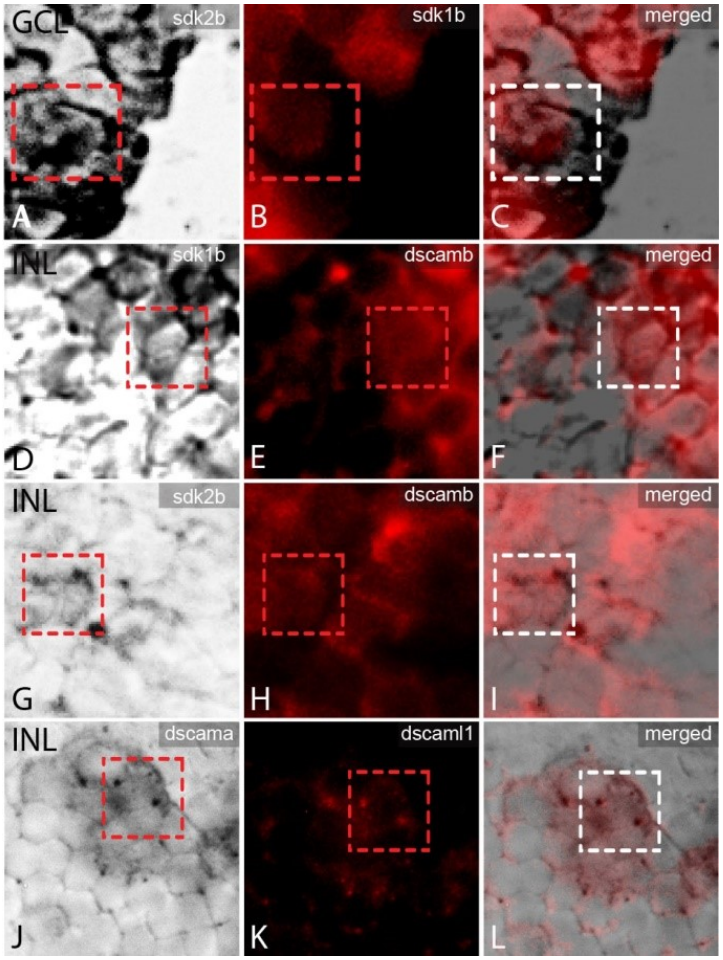

Figure 5.4. Expression of Dscam and Sdk homologs in the central inner retina of developing zebrafish 96 hpf. Relative expression levels for gene homologs were shown using double *in situ hybridization.* **A)** *sdk2b* is shown to be expressed in a subset of cells within the GCL. **B)** *sdk1b* expression is also observed in cells in the GCL. **C)** The merging of *sdk2b* and *sdk1b* reveals that some overlap exists between positive cells. **D)** *sdk1b* is shown to be expressed in a subset of cells within the basal INL. **E)** *dscamb* was also observed in the basal INL. **F)** The merging of *sdk1b* and *dscamb* shows some level of overlap for positive cells. **G)** *sdk2b* expression was observed within the INL. **H)** *dscamb* transcripts were also observed in the INL, and **I)** merging the two reveals low levels of overlap for positive cells. The expression results for **J)** *dscama* and **K)** *dscaml1*. **L)** The merging of *dscama* and *dscaml1* reveals some level of overlap for positive cells within the INL. For all comparisons, we observed a mosaic of cells expressing the two targeted transcripts; some that express both transcripts and other cells that express only one or the other. Dashed line boxes show the identical area of interest for panels A-C, D-F, G-I, and J-L. The red boxes correspond to

the region for single expression panels of A, B, D, E, G, H, J, and K. White boxes in C, F, I, and L correspond to the same region of tissue from the single expression panels, but with the two probes merged. All images displayed are of antisense probe. Abbreviations: hpf= hours post fertilization; Dscam= Down syndrome cell adhesion molecule; Sdk= Sidekick; INL=inner nuclear layer; GCL=ganglion cell layer.

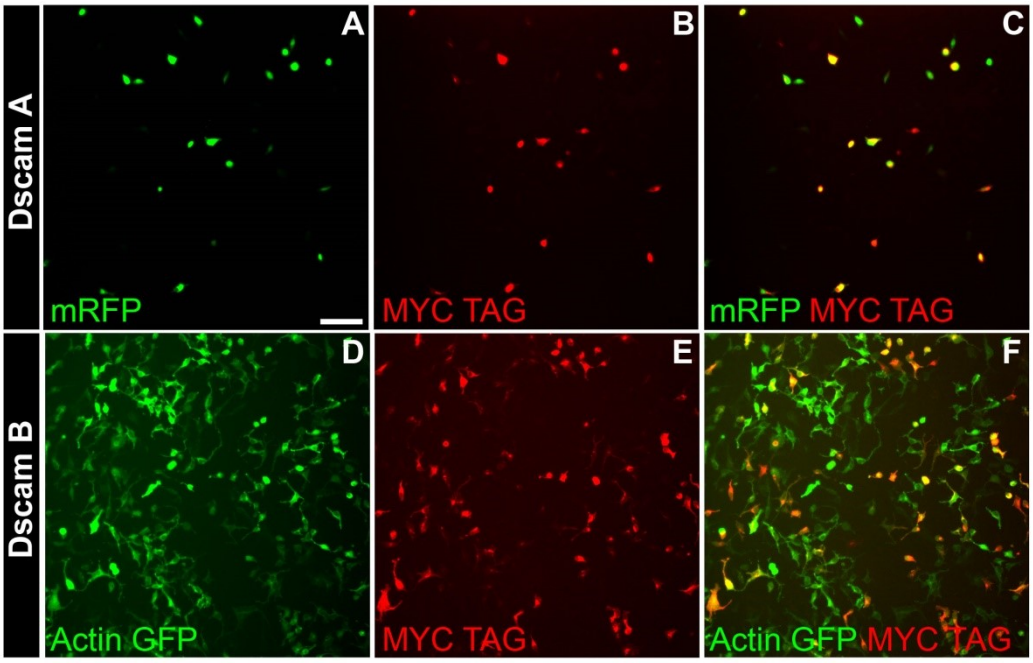

Figure 5.5. Expression of DSCAM A and DSCAM B proteins following cloning. The genomic sequences for *dscama* and *dscamb* were cloned into expression vector pcDNA 3.1+ for use in cellular interaction assays. A MYC tag was used to verify expression and allow for a while to label the cells expressing the genes. A-B) *Dscama* was co-transfected into cells alongside a membrane bound green fluorescent protein (mGFP). Panel C shows the combined expression of the mGFP and antibodies against the MYC tag, verifying its expression in some cells. B-D) *Dscamb* was co-transfected into cells alongside an Actin GFP fused protein. Panel F shows the combined expression of the Actin GFP and antibodies against the MYC tag, verifying its expression in some cells. Scale bar in A is equal to 100 μm, and continues for B-F.

Gene	Forward (5′–3′) SP6	Reverse (5′–3′) T7
dscama	CATACGATTTAGGTGACACTATAGGCTCTGAGTCCAGCTGAGAAA	TAATACGACTCACTATAGGGGGATCCCTGGGACGTTGTAG
dscamb	CATACGATTTAGGTGACACTATAGCGTACACCTGACACCGTGAA	TAATACGACTCACTATAGGGTTGTTTGCTTGTCGTTGCCG
dscaml1	CATACGATTTAGGTGACACTATAGGGGCTCATCCAGCTGACAAA	TAATACGACTCACTATAGGGTCTCCCCATTCTCCATCGGG
sdk1a	CATACGATTTAGGTGACACTATAGCTCTTCCGACCGGAAACCAA	TAATACGACTCACTATAGGGGCTGTTCCACAGCTCTTGT
sdk1b	CATACGATTTAGGTGACACTATAGCAGGTGCTCGCATTTACACG	TAATACGACTCACTATAGGGGCCTGAGGACGCTCTTTTTG
sdk2a	CATACGATTTAGGTGACACTATAGCCCCTACAGTGTGAGGAACC	TAATACGACTCACTATAGGGGGCGTACAGGGCTCATAGAC
sdk2b	CATACGATTTAGGTGACACTATAGGCTGGGCAGAACTCACATCT	TAATACGACTCACTATAGGGTGAAGACAGTCGACACAGGC

Table 5.1. Primer sequences used to amplify genes and generate corresponding probes. T7 and SP6 promoter sequences are underlined.

The resulting PCR products were run and isolated on a 0.75% agarose gel and purified using GeneJet gel extraction kit (Fermentas Life Technologies, Waltham, MA). The purified DNA was used to generate cRNA probes trough in vitro transcription using DIG RNA labeling Mix (Roche, Indianapolis, IN) and T7/SP6 RNA Polymerase (Roche)

DSCAM A		
Forward Primer	Reverse Primer	Name
GAGAAAGCTTCGGATGTGGATATTGG		1
CTTGGCTTCTAATTTTCCCTGAA	TTCAGGGAAAATTAGAAGCCAAG	1R
TCCAGATCTTCCACTTTCCTCC		2
AGGATCTGGCACAAAGAGCC	GGCTCTTTGTGCCAGATCCT	2R
ACGAGACATCGCTACACGTC		3
GAGCTCGAACTCATCGG	CCGATGAGTTCGAGCTC	3R
GCAGCTATGTCTGCGA		4
TCTCACTGAAGGCGGACAAG	CTTGTCCGCCTTCAGTGAGA	4R
GGATGGCGAAGAGTGATGGA		5
CATGTCCCACCCAGCTATGG	CCATAGCTGGGTGGGACATG	5R
GGGGTCTATCGCTGCACAT		6
GGTCACCAGATCGGAC	GTCCGATCTGGTGACC	6R
GTCCACGTCACGGTC		7
CCATCCGCAGAGCAGTTCAA	TTGAACTGCTCTGCGGATGG	7R
CGCCGTGGTCAAATACCAGA		8
GATCATGTGCGACTGCTTCTC	GAGAAGCAGTCGCACATGATC	8R
TCGTATCCCAACAACTCGCT		9
CGTAGCCGGTGATGAG	CTCATCACCGGCTACG	9R
CGATGAGAGAGGATTCGG		10
ATGCAGACGAACTGATGGC	GCCATCAGTTCGTCTGCAT	10R
CGTCACGCTGGAAGCAATCA		11
GAGAGCGGCCGCGCCGTTCAGAGCCT	AGGCTCTGAACGGCGCGGCCGCTCTC	11R

GAGAAAGCTTCTGGCAGACTCCGG		12
CATCCGGGGCCACTTCAAAC	GTTTGAAGTGGCCCCGGATG	12R
TCCTCCGCTAAAGCTGAATGG		13
TCAGGAGGGACTTGAACCTG	CAGGTTCAAGTCCCTCCTGA	13R
ACGCAGCATCCACGGAAAT		14
ACTTTCCAGCGGACG	CGTCCGCTGGAAAGT	14R
AAGACTCATGGGAAAGAGC		15
AGGACGAAGAGCAGCACCAT	ATGGTGCTGCTCTTCGTCCT	15R
CTCTGGTGAAGGACCCCGT		16
GACTGCTCTTACTGGTCCCTG	CAGGGACCAGTAAGAGCAGTC	16R
TTCGGAGAAACTGCCAAGCA		17
CTGGCCAGCTCCTC	GAGGAGCTGGCCAG	17R
ACTGGAGGCTCGGG		18
ACTCCCCGGTTTAGGAGGAA	TTCCTCCTAAACCGGGGAGT	18R
GGTCATCAACATGGCCGTTC		19
GAGAGCGGCCGCTCAGTGTGTAGGAC	GTCCTACACACTGAGCGGCCGCTCTC	19R

DSCAM B		
Forward Primer	Reverse Primer	Name
ATTGAACGCAGCGGGGCATGTGGATATTGG		1
TGTACGGCTCCCGGAATAC	GTATTCCGGGAGCCGTACA	1R
TCCTGCCATCCAGCTTTAGT		2
CCGATGACCCACCATAACCT	AGGTTATGGTGGGTCATCGG	2R
AGGGGAGACCAGACAGAGTA		3

GCCAGTCACACTACAGAAC	GTTCTGTAGTGTGACTGGC	3R
CAGAGTGTATCAGGCCTC		4
TCCCATCTTCCAAGACGACCT	AGGTCGTCTTGGAAGATGGGA	4R
TCACGGGCATTAACAACGAG		5
ACGGGTAACCAATGATGCGA	TCGCATCATTGGTTACCCGT	5R
AAAAATGTCACTGCCATCGCT		6
GATGCAGGTGTAACTGCC	GGCAGTTACACCTGCATC	6R
ACACTCCGACTCTCAGAG		7
CCAGAATTCAAGGCAATGGGC	GCCCATTGCCTTGAATTCTGG	7R
TGAATTGTTCGGCAAAGGGA		8
TCACCATAAGAGTTAATGGCGATG	CATCGCCATTAACTCTTATGGTGA	8R
AAGGAAGTGGGGGATGAGGT		9
CTTCCATGTGACTTTGATGCCC	GGGCATCAAAGTCACATGGAAG	9R
ATCGGAGAAAGCAGACCGAG		10
GCTGTGGTCACAACGTTTTCAG	CTGAAAACGTTGTGACCACAGC	10R
AGCCAATCGAGCAGGAATGG		11
CATCTCCAGCTCGAGTGAAGG	CCTTCACTCGAGCTGGAGATG	11R
TCACTCGAGCTGGAGATGG		12
ACAATGTCCCTCATCCAGGG	CCCTGGATGAGGGACATTGT	12R
TCACCGTAGAGCCCCAAG		13
CCATTGTCTCCGGGGATCC	GGATCCCCGGAGACAATGG	13R
GGGGTTCCGATGAGATCATGC		14
ACCGTTGTTCCAACCAATG	CATTGGTTGGAACAACGGT	14R
TGACTGCACAGAATGCAG		15

AGTCCTTCATTTCCCTGCCTG	CAGGCAGGGAAATGAAGGACT	15R
AAGAGGGTGCTGTTCGCTAC		16
CCAGGTCTAGCATCAGACACG	CGTGTCTGATGCTAGACCTGG	16R
TGACGGACAATGACTTTGGAGA		17
AGCTCCTCATAAGTGGAGG	CCTCCACTTATGAGGAGCT	17R
AGTCGTTATGCCAGCCAG		18
CCATGCGTAGGTAAGGGGG	CCCCCTTACCTACGCATGG	18R
CCAAACCACAGGACGCCAG		19
GAGAGATCTAGATTATACAAGTGTGTA GGACTTTGCGTAGGGG	CCCCTACGCAAAGTCCTACACACTTGT ATAATCTAGATCTCTC	19R

Table 5.2. Primer sequences used to amplify genes and generate corresponding probes. The resulting PCR products were run and isolated on a 0.75% agarose gel and purified using GeneJet gel extraction kit (Fermentas Life Technologies, Waltham, MA).

Chapter 6: Characterization and Evolution of the Spotted Gar Retina

Joshua M. Sukeena[1], Carlos A. Galicia[1], Jacob D. Wilson[4], Tim McGinn[1], Janette W. Boughmann[5], Barrie D. Robison[1], John H. Postlethwait[3], Ingo Braasch[5], Deborah L. Stenkamp[1], and Peter G. Fuerst[1, 2]

1 University of Idaho, Department of Biological Sciences, Moscow, Idaho 83844, USA, 2 University of Washington School of Medicine, WWAMI Medical Education Program, Moscow, Idaho 83844, USA, 3 University of Oregon, Department of Evolution, Development, and Genetics, Eugene, Oregon 97403, USA. 4 Colorado School of Mines, Golden, Colorado 80401, USA, 5 Michigan State University, Department of Integrative Biology and Program in Ecology, Evolutionary Biology and Behavior, East Lansing, Michigan 48824, USA.

Abstract

In this study we characterize the retina of the spotted gar, *Lepisosteus oculatus*, a ray-finned fish. Gar did not undergo the whole genome duplication event that occurred at the base of the teleost fish lineage, which includes the model species zebrafish and medaka. The divergence of gars from the teleost lineage and the availability of a high quality genome sequence make it a uniquely useful species to understand how genome duplication sculpted features of the teleost visual system, including photoreceptor diversity. We developed reagents to characterize the cellular organization of the spotted gar retina, including representative markers for all major classes of retinal neurons and Müller glia. We report that the gar has a preponderance of predicted short-wavelength (SWS) shifted opsin genes, including a duplicated set of SWS1 (ultraviolet) sensitive opsin encoding genes, a SWS2 (blue) opsin encoding gene, and two rod opsin encoding genes, all of which were expressed in retinal photoreceptors. We also report that gar SWS1 cones lack the geometric organization of photoreceptors observed in teleost fish species, consistent with the crystalline photoreceptor mosaic being a teleost innovation. Of note the spotted gar expresses both *exo-rhodopsin* (RH1-1) and rhodopsin (RH1-2) in rods. *Exo-rhodopsin* is an opsin that is not expressed in the retina of zebrafish and other teleosts, but rather is expressed in regions of the brain. This study suggests that *exo-rhodopsin* is an ancestral actinopterygian (ray finned fish) retinal opsin, and in teleosts its expression has possibly been subfunctionalized to the pineal gland.

Introduction

Vision originates within the cells of the neural retina. The vertebrate retina contains six classes of neurons: rod and cone photoreceptors, horizontal cells (HC), bipolar cells (BPC), amacrine cells (AC), and retinal ganglion cells (RGC) (Masland, 2001). Signal detection initiates with the activation of different visual pigments in the photoreceptors and is transmitted from the retinal tissue via the optic nerve, a thick bundle of ganglion cell axons that carry information to the vision processing areas of the brain. The other neurons of the retina modify and/or relay signals as they pass through the tissue, helping to generate different aspects of vision, such as depth and movement detection. The development and organization of the visual system, as the dominant sense of humans, is a priority for biomedical research. Understanding genetic differences in neural development across organisms can provide insight into retina function. With the current study, we provide an anatomical characterization of an emerging model for retina research to better understand the evolution of the visual system.

Several model species have been widely utilized to study the structure and function of the retina. Over the last twenty years, advances in genetic engineering have resulted in the emergence of the mouse and zebrafish as the most popular models to study the visual system (Fadool and Dowling, 2008). Zebrafish and other teleost fish models have an increased repertoire of genes in certain gene families as a result of a whole genome duplication that occurred approximately 350 million years ago, the teleost genome duplication (TGD) (Figure 1 A) (Postlethwait, 1998; Taylor et al., 2003; Braasch and Postlethwait, 2012). As a result of the TGD, zebrafish and other teleost genomes often contain two duplicates of a given human or mouse gene. Teleost species such as zebrafish also have an array of features not observed in mammalian retinas, such as a crystalline mosaic of photoreceptors, a larger number of color detecting circuits and the ability to regenerate their retina (Cameron and Carney, 2000; Fadool, 2003; Raymond and Barthel, 2004; Vihtelic et al., 2006; Kroehne et al., 2011; Stenkamp, 2011; Sherpa et al., 2014). The extent to which the TGD contributed to morphological differences, such as those observed in the retina, or whether they already existed in ray-finned fish before the TGD, is currently a matter of debate that we address in this study (Crow and Wagner, 2006; Braasch and Postlethwait, 2012).

To address this question we characterized the retina of a basal species of ray-finned fish, the spotted gar, *Lepisosteus oculatus.* We choose the spotted gar for this study because of the availability of a high quality sequenced genome, because it did not undergo subsequent genome duplications, and because of its close evolutionary relationship to the teleost fishes (Amores et al., 2011). This lack of genome duplications has left the spotted gar with conserved syntenies much closer to humans than to teleost fish (Jones et al., 2012; Braasch et al., 2016). Additionally, their high fecundity (thousands of eggs during mating season) makes them ideal for housing in a research lab environment (Smith, 2006). The use of the spotted gar as a model system is growing, and therefore the infrastructure and protocols are in place with resources only expected to grow in the future. The gar visual system has been observed previously (Collin & Collin, 1993), however very little is currently known regarding the spotted gar retina tissue.

In the present study, we characterize the retina of the spotted gar. We found that the general structure of the retina is conserved as compared with retinas of other vertebrates, with three nuclear layers and two synaptic layers of varying thickness. A ciliary marginal zone (CMZ), typical of fish retinas, was observed in the far periphery of the spotted gar retina. Genomic analysis, RT-PCR and *in situ* hybridization revealed that the spotted gar retina expresses seven types of photoreceptor opsin genes, with a prevalence of predicted short-wavelength sensitive opsins. Mosaic spacing of SWS1-expressing cones revealed that photoreceptor organization appears to be more similar to that observed in mammals than to that in zebrafish. We also report that the spotted gar expresses RH1-1, ortholog to teleost *exo-rhodopsin,* in retinal rods.

Materials and Methods

Animals

Spotted gar (*Lepisosteus oculatus*) individuals were spawned in Louisiana and then raised and maintained at the University of Oregon in water with 4ppt salinity and a pH around 7.0, with recirculating filtration. Water was kept close to room temperature (22^{o}C). Animals were kept on a light cycle of 14 hour ON/10 hour OFF. Housing tubs were covered ~30% to allow for shade. Spotted gars were fed adult brine shrimps and zebrafish at the University of Oregon. Mice (*Mus musculus*) used were wild type outbred mice of mixed C57Bl6, 129, Balb and C3H backgrounds, and were housed in the University of Idaho Live Animal Research

Facility (LARF). They were fed ad libitum on a light cycle of 12 hour ON/12 hour OFF. The zebrafish (*Danio rerio*) that were used in the experiments were maintained at the University of Idaho on a light cycle of 14 hour ON/10 hour OFF in monitored, recirculating system water according to standard protocols (Westerfield, 2010). Animal use was approved by the University of Idaho and University of Oregon Animal Care and Use Committees.

Tissue processing for histological analyses

Spotted gar specimens were anesthetized by adding MS-222 (0.16g/mL) to 1 L of tank water. For animals that were dark adapted, the procedure was done immediately following 2 hours in a blacked-out tank. Conversely, light adapted animals were maintained under standard fluorescent lighting in their tanks for ≥ 2 hours prior to anesthetization. Following administration of anesthesia gar eyes were surgically removed and placed into phosphate buffer saline (PBS) (pH=7.4). This tissue was taken from gars that were approximately 1 year old and measured 15-20 cm in length. Eyes were fixed in 4% paraformaldehyde in PBS for 30 minutes at room temperature. Eyes were then removed from PBS and dissected to remove the cornea and lens. Following fixation and dissection, eyes were washed in PBS before soaking in a solution of 30% sucrose with PBS until the tissue sank to the bottom of the container. Eyes were then placed in a solution containing a 50/50 ratio of 30% sucrose solution and optimal cutting temperature (OCT; Sakura® Finetek Inc.) solution and frozen in liquid nitrogen. Eyes were cut into sections of 5 and 10 µm using *Leica GM 1510 S* cryostat. Gar eyes that were used for whole mount retina labeling were sent from the University of Oregon to the University of Idaho following the same fixation protocol that we report here. These eyes were immediately dissected to remove the retina. Adult mice were anesthetized using 1 mL of 2,2,2-Tribromoethanol (0.5g/mL ethanol) via needle injection. Following anesthetization, adult mouse tissue was prepared identical to gar eye tissue as just described. Adult zebrafish were anaesthetized by immersion in buffered MS-222 (0.16g/mL) and enucleated eyes were fixed in PO_4-buffered (pH 7.4) 5% sucrose, and processed for cryosectioning on a Microm cryostat as previously described (Nelson et al., 2009). All tissues were stored at -20^{o}C prior to use for analysis using immunohistochemistry (IHC), *in situ* hybridization, and hematoxylin and eosin (H&E) staining.

Hematoxylin and eosin staining

Tissue for H&E staining was placed at room temperature for 30 minutes to air dry. Slides were incubated in 0.1% Mayer's Hematoxylin (MHS-16 Sigma Aldrich; St. Louis, MO) for 10 minutes. Slides were then placed into a coplin jar with running tap water for 5 minutes to wash. Slides were then placed into 0.5% eosin for 1 minute, which was followed by a wash in distilled H_20 until eosin streaks disappeared. Consecutive washes in 50% ethanol (30 seconds), 75% ethanol (30 seconds), 95% ethanol (30 seconds), and 100% ethanol (1 minute). Slides were then dipped into xylene five times and immediately mounted with Permount® (Fisher Scientific; Pittsburgh, PA).

Antibody staining

We have summarized all antibodies used in the present study (including those that did not result in specific staining), the dilution at which they were used, and the source of the reagents (S- Table 1). Retinal tissue used in antibody staining procedures was collected from spotted gars between 1 to 2 years of age. It was incubated in a blocking solution composed of PBS, 5% normal donkey serum and 0.1% triton (for staining sections) or 0.4% triton (for staining whole retinas) for 45 minutes (for staining sections) or overnight at 4^{o}C (for staining whole retinas). Antibodies were diluted in blocking solution according to the concentrations listed (S- Table 1). Following application of primary antibodies, the sections were incubated overnight at 4^{o}C, after which they were washed three times for fifteen minutes in PBS. Secondary antibodies were used at various dilutions according to their recommended value. Following incubation with secondary antibodies, sections were washed three times for fifteen minutes in PBS. A nuclear stain, DAPI, was used in PBS at room temperature and was included in the second wash at a dilution of 1:50,000 of a 1 mg/ml stock. Slides were mounted with cover slips that were applied using 80% glycerol as a mounting medium. Whole retinas were stained in a similar manner except for the following three differences. First, both primary and secondary incubations lasted three to seven days (depending on age of tissue) and were performed at 4^{o}C. Second, washes between applications of primary and secondary antibodies were carried out for one hour each in a PBS with 0.1% triton for a total of three washes. Third, washes following secondary antibodies were carried out for one hour each in PBS (first two washes) followed by a two to four hour wash in 0.4% triton blocking solution (third wash) at 4^{o}C. All images were collected and imaged on an Olympus DSU

spinning disc microscope, a Leica DM2500 microscope with Leica DFC7000T digital camera, and/or an Olympus Fluoview 1000 Confocal/multiphoton microscope.

Nuclear antigen retrieval

Cryosectioned tissue (gar) was permeabilized by 15 minute incubation in PBS + 1% Triton solution (PBST) at room temperature. Tissue was then boiled (at 95-100^{o}C) for 10 minutes in citrate buffer (0.05% tween 20; pH=6.0) and cooled for 10 minutes at room temperature. Tissue was then put through an additional wash in PBST for 5 minutes. The remaining steps were identical to the antibody staining protocol used in this study.

Gar RNA extraction and cDNA preparation

Eyes were shipped from the University of Oregon to the University of Idaho in *RNA-later* (Thermo Fisher Scientific, Waltham, MA) and stored at -80^{o}C. Eyes were removed and homogenized in 1.0 mL of Trizol (Thermo Fisher Scientific, Waltham, MA) reagent for approximately 2 minutes. Chloroform was added at a volume of 0.2 mL and set for ~2 minutes at room temperature before spinning at 12,500 rpm for 15 minutes at 4^{o}C. The top layer, containing the RNA, was removed to a new tube where 2 volumes of lithium chloride were added to the solution. This solution was incubated for 4 hours at -20^{o}C, followed by a 15,000 rpm spin for 15 minutes at 4^{o}C. The pellet was re-suspended in TE buffer and stored at -80^{o}C. Extracted RNA was used to produce cDNA with SuperScript® III First-Strand Synthesis System (Thermofisher Scientific, Waltham, MA).

In situ hybridization primer design

In situ hybridization was used to target seven of the predicted opsin mRNAs encoded within the spotted gar genome. Sequences for these opsin genes were obtained from the Ensembl database. Therefore, we verified the genome annotation and then documented their patterns of expression in spotted gar retina. All primers were designed with the *sp6* forward promoter (5'-CATACGATTTAGGTGACACTATAG-3') or *t7* reverse promoter (5'-TAATACGACTCACTATAGGG - 3'). The promoter sequences were added to the amplicon as previously described (Fuerst et al., 2008). Gene specific primers, target sequences, and sp6/t7 promoter sequences are summarized (S- Table 2).

Sequencing and verification of cRNA probes

Probe samples for *in situ* hybridization were verified via DNA sequencing performed by *ElimBio* (St. Hayward, CA). Results were compared to original genomic sequence using nucleotide blast software and viewed using *Sequencher* genetics software®.

In situ hybridization application

Following verification of probes via sequencing, *in situ* hybridization was performed as previously described for cryosectioned tissue (Nelson et al., 2008; Stevens et al., 2011). Tissue was vacuum dried for 24 hours and then hydrated using sequential ethanol treatments of 100%, 95%, 70%, 50%. Tissue was treated with Proteinase K enzyme and triethanolamine (TEA) + acetic anhydride before another dehydration. Tissue was incubated in anti-sense probe overnight (~12 hours) at 56^{o}C. Following anti-sense probe application, slides were incubated at room temperature with SSC buffer prior to a stringency wash of formamide and 2xSSC (1:1 ratio) at 65^{o}C. Treatment with RNAse A was used prior to incubation with anti-DIG AP fragments overnight at room temperature. Color reaction was completed using NBT/BCIP solution at room temperature. For tissue that was subsequently stained with antibodies, slides were taken directly from color reaction solution into 0.1% blocking solution for incubation at room temperature for 1 hour. Following incubation, they were administered through identical procedure for antibody staining as described previously in section 2.4. Upon completion, slides were washed in alkaline phosphatase (AP) buffer and mounted using 80% glycerol solution. Images were collected using a Leica DMR microscope and SPOT camera or a Leica DM2500 with a Leica DFC7000T digital camera.

Laminar thickness using nuclei number

Following H&E staining, tissue was subjected to analysis of laminar thickness by counting nuclei within defined columns of nuclear layers. Images were collected from three different spotted gar specimens. For both central retina and peripheral retina, five images were used, with six columns being counted on each image. Each column consisted of a straight line (1 μm wide) drawn through the entire retina, and cells in the outer nuclear layer, inner nuclear layer, and ganglion cell layer were counted along each of six separate columns. Nuclei were only counted if they were in contact with the column. Measurements derived from a given

image were averaged. Differences in laminar thickness between central and peripheral retina were compared using a Student's *t*-test.

Density recovery profile analysis (DRP)

DRP analysis of identified cells of retinal whole mounts was performed using WinDRP 1.6.4 (Rodieck, 1991). Images were imported as BMP files and the location of each cell body was marked. The cell diameter was set to 7 μm, the annulus width was set at 10 μm and cells within 10 annuli were counted. The soma correction was used (the first annulus bin is discarded because two cells cannot occupy the same space). The number of cells in each bin was averaged to calculate an average bin density. The packing indexes were used to identify for the overall organization of cells using a Student's *t*-test.

Nearest neighbor analysis (NNA)

NNA was performed using the same software that was used for DRP analysis. The regularity index (RI) of each test was given and was used to compare the newly calculated distribution against random simulations using a Student's *t*-test.

Results

The spotted gar (*Lepisosteus oculatus*) is a ray-finned fish whose lineage diverged from the teleost lineage prior to the TGD and did not undergo subsequent genome duplications, such as the WGD events that have occurred in the sturgeon. Its genomic organization, more similar to the organization of the mammalian genome, together with its evolutionary history, make it an excellent candidate to bridge experimental findings from zebrafish to mammals (Figure 1 A; Amores et al. 2011 Braasch 2016).

Retina organization

The organization of the spotted gar retina is histologically similar to that of both zebrafish and mouse. In all three species, three nuclear layers-the ONL, INL, and GCL-are separated by two synaptic layers, the outer plexiform layer (OPL) and the inner plexiform layer (IPL) (Figure 1 B-D). We performed a laminar thickness assay for spotted gar retina by counting the number of nuclei per layer within defined radial columns. These counts were performed for peripheral and central retina regions to test whether or not they differed across the retina. We found no significant difference in average nuclear layer thickness in central

retina as compared with peripheral retina for the ONL, INL, or GCL of the gar (p= 0.327; ONL, p= 0.325; INL, p= 0.934; GCL, (N=3)).

Presence of Ciliary Marginal Zone

The retinas of most vertebrates see continued neurogenesis through the lifespan. In such retinas, new neurons are added at the peripheral margin, a region termed the ciliary marginal zone (CMZ) (Raymond et al., 2006; Stenkamp, 2007). In teleost retina, new rods are also generated sporadically throughout the retina (Stenkamp, 2011). We confirmed the presence of a CMZ in the spotted gar using antibodies to PCNA, which labeled cells in S-phase, and antibodies to PH3, which labeled cells in M-phase of cell division (Figure 1 E & F). We also observed the presence of numerous cells in the INL of the central retina that were positive for PH3 (Figure 1G), suggesting ongoing proliferation outside the CMZ and similar to the continued generation of rods in teleosts. However, we did not observe cells positive for PH3 or PCNA within the ONL, which has been observed in teleosts (Raymond & Rivilin, 1987; Julian et al., 1998; Otteson et al., 2001; Bernardos et al., 2007; Nelson et al., 2008; Stenkamp, 2011).

Labeling cells of the spotted gar inner retina

Markers for cell populations and neurites in the gar inner retina were identified using antibodies that recognize retinal antigens in mouse and or zebrafish. Hu and islet1 are transcription factors expressed in zebrafish retinal neurons (Link et al. 2000). In gar, antibodies against Hu recognized nuclei in the GCL, INL and occasionally in the ONL (Figure 2 A) of the gar retina. Antibodies against islet1 labeled a subset of nuclei in the GCL and INL (Figure 2 B) similar to what was previously reported in mice (Erskine et al., 2000). The anti-SMI-32 antibody showed strong labeling in the IPL, and faint labeling of a cell population(s) in the ONL (Figure 2 C). Antibodies against SV2 (Figure 2 D) labeled synaptic terminals near the ONL and neurite projections extending towards the outer retina. Strong SV2 labeling throughout the IPL was also observed. Antibodies against Goα (G-protein coupled receptor; alpha subunit), (Figure 2 E) labeled neurites in the OPL and IPL, and faintly labeled a cell population(s) in the INL.

Antibodies against recoverin labeled a presumed population of bipolar cells in the INL (staining of the ONL by recoverin antibodies will be discussed below). The pattern in spotted gar was found to be consistent with the staining pattern observed in other species for type 2

cone bipolar cells (Milam, 1993; Haverkamp, 2003) (Figure 2 F). Anti-parvalbumin labeled a cell type with a neurite morphology and location consistent with a horizontal cell identity (Figure 2 G). Antibodies to bNOS labeled presumed amacrine cells in the INL that had a dendrite stratification pattern in the IPL comparable to that of mouse bNOS+ amacrine cells (Figure 2 H). Antibodies to TH labeled a population of presumed amacrine cells and a single sublaminae (S1) within the IPL (Figure 2 I), and the observed morphology is similar to that of dopaminergic amacrine cells in zebrafish retina (Yazulla and Studholme, 2001). Antibodies to ChAT labeled presumed amacrine cells in the INL and GCL that stratified in two sublaminae of the IPL, similar to what is observed in mouse (Figure 2 J). Finally, Müller glia are the only non-neuronal cell type within the retina that is produced by retinal progenitor cells, and they play a vital role in maintaining the structure of the retinal tissue. They are abundant throughout the retina, where they span the tissue from the ONL to the GCL, with cell bodies located within the INL. Two antibodies labeled this cell population in the spotted gar retina (Figure 2 K & L). The monoclonal antibody Zrf-1, which detects zebrafish glial fibrillary acidic protein (GFAP), labeled glial end-feet within the GCL as well as the distal regions of the Müller glia (Figure 2 K). Antibodies to mammalian GFAP showed strong labeling throughout the Müller glia cells, including the cell body (Figure 2 L).

A displaced population of neurons in the spotted gar ONL

While characterizing the spotted gar outer retina, we observed a population of calbindin-positive cells in the ONL that lacked obvious photoreceptor morphology. Calbindin-positive cells with a similar morphology were also observed in the INL (Figure 3 A). The displaced cells projected processes towards photoreceptor inner segments but did not appear connected to inner and outer segments, and did not accumulate antibodies to SV2 proximal to the OPL (inset; 3 B'), as observed for photoreceptors (Figure 3 B). Axon-like processes projecting to the IPL were observed emanating from the somas of calbindin-positive cells on either side of the OPL (Figure 3 C). Their terminals in the IPL contained SV2 immunoreactivity. Two groups of calbindin-positive cells of different sizes were observed in retina whole mounts, suggesting that this cell population is polymorphic (Figure 3 D and E). Both subpopulations of calbindin-positive cells were distributed in a dorsal-ventral gradient, with highest densities dorsally (Figure 3 F).

Labeling cells of the spotted gar outer retina

We next tested for molecular similarities amongst spotted gar, zebrafish, and mouse photoreceptors by testing antibodies for labeling in the outer retina. Antibodies to recoverin, a protein involved in shutting off the phototransduction cascade, labeled antigen in both rods and cones of gar retina (Figure 4 A). A polyclonal antibody to zebrafish rhodopsin labeled the inner and outer segments and cell bodies of rods, identified by their elongated morphology, but it did not label the more compact cones (Figure 4 B and C). Rods were also labeled brightly by 1D1, a monoclonal antibody used for labeling rod opsins in zebrafish, and this staining was restricted to outer segments (Figure 4 D). Polyclonal antibodies to zebrafish SWS1 or SWS2 opsin labeled a large number of cones compared to the number of cells expressing the opsins as determined by *in situ* hybridization for SWS1-1 and SWS1-2 (described below), suggesting cross reactivity of these antibodies with multiple gar opsins (Figure 4 E-G). Antibodies to mouse SWS opsin labeled a small number of cones in the spotted gar retina (Figure 4 H). The monoclonal antibody ZPR1, which labels the cone arrestin (arr3a) of double cones (LWS/RH2) of zebrafish (Renninger et al., 2011) did not stain any cells in gar retina (data not shown). The lack of staining could be because arr3a diverged substantially between gar and zebrafish following TGD, or that the LWS/RH2 double cones are absent from gar retina.

Synaptic terminals in the OPL were labeled with antibodies to the scaffolding protein, CASK (Figure 4 I). Photoreceptor inner and outer segments were labeled by the antibody Zpr-3 (Figure4 J), which labels both rod opsin and RH2 (green cone opsin) in zebrafish retina (Stevens et al., 2011). Cone outer segments were labeled with peanut agglutinin (PNA) (Figure 4 K). Antibody staining results are summarized in Figure 4 L).

Spotted gar SWS1-2 cone distribution

The distribution of photoreceptors in teleost fish is remarkable based on the geometrically precise distribution of cones (Raymond et al., 1995; Stenkamp et al., 2001; Allison et al., 2010). The origin of this distribution is not understood on a molecular level. We sought to determine if photoreceptors in the spotted gar are organized in a fashion similar to the geometric distribution observed in teleost species, or more similar to the regular spacing of cone photoreceptors in terrestrial vertebrates. Therefore, we measured the distribution of cone photoreceptors that labeled with antibodies to mouse SWS opsin, which appeared to

label a single population of cone based on their spacing across the horizontal plane of the retina (perpendicular to the radial plane extending from photoreceptors to ganglion cells) (Figure 5 A). We confirmed that the antibody labeled a single population of cones by double *in situ* hybridization and antibody staining and were able to conclude that the antibody labels SWS1-2 cones in the gar retina (Figure 5 B and C). Cones in the mouse retina are organized in a sharp dorsal-ventral gradient with green opsin-expressing cones predominant in the dorsal retina and blue opsin-expressing cones in the ventral retina (Haverkamp et al., 2005). Similarly, we observed a gradient of SWS1-2 cones from the dorsal to ventral retina of the gar. The density of SWS1-2 cones in dorsal retina was significantly greater than in ventral retina (Figure 5 E and F). The SWS1-2 cones in both the ventral and dorsal gar retina appeared to be distributed in a nonrandom fashion (Figure 5 G and J). Statistical pattern analysis confirmed that SWS1-2 cones in both the ventral and dorsal retina were found to be locally patterned at more consistent distances from each other than predicted from random simulations of cell distribution (Figure 5 H and K), suggesting some regularity to the pattern. To compare the pattern of SWS1-2 cones in the gar retina to the corresponding patterns for teleost fish and mammals, we applied a measure of pattern regularity termed the Regularity Index (RI) or Conformity Ratio (CR; mean NND/s.d. of the mean NND; Cook, 1996). In ventral gar retina the RI is 4.19 ± 0.44 (N=5) (Figure 5 I), while in dorsal retina this index is 4.61 ± 0.26 (N=5) (Figure 5 L). By comparison, for SWS1-positive cones in adult zebrafish, the CR has been reported as 10.6 across the entire retina outside of the larval remnant (Allison et al., 2010), while for SWS cones in adult mouse the RI has been reported as 4.82 in central and 3.55 in peripheral retina (Fei, 2003). Collectively these observations are consistent with our hypothesis that the spacing and organization of cone photoreceptors in gar retina resembles that observed in terrestrial vertebrates such as mouse.

Opsin expression and distribution in spotted gar retina

In order to further characterize the spotted gar retina, we mapped the distribution of photoreceptor visual pigment opsin mRNAs; opsins initiate visual signal transduction upon being struck and activated by photons. We identified seven predicted photoreceptor opsin genes in the spotted gar genome, confirming a previous report (Lagman et al., 2013; Braasch et al., 2016). There are two predicted UV opsins, SWS1-1 and SWS1-2, as well as two rod opsin genes, RH1-1 and RH1-2. Single opsin genes orthologous to zebrafish opsins of similar sensitivity, LWS (red opsin; long-wavelength sensitive), RH2 (green opsin; medium-wavelength sensitive) and SWS2 (blue opsin; short-wavelength 2) were detected.

Two opsins that are co-orthologous to the zebrafish UV opsins were detected as a local duplication, SWS1-1 (UV opsin 1; short-wavelength sensitive) and SWS1-2 (UV opsin 2; short-wavelength sensitive). In addition, RH1-1 and RH1-2, were also identified, and reside upon Chromosome 5 within 16.6 Mb of each other. RH1-1 contains introns and is homologous to teleost *exo-rhodopsin*, a visual pigment gene expressed outside the retina in zebrafish (Figure 6 A). Previous phylogenetic analyses did not fully resolve the position of gar RH1-1 within the cluster of vertebrate rhodopsin genes, but the presence of introns is consistent with this rhodopsin gene as ancestral (Lagman et al., 2013). RH1-2 is intronless and is orthologous to teleost retinal *rhodopsin* (and in zebrafish, also to *rhodopsin-like*; *rhol*) (Lagman et al., 2013). Products of polymerase chain reaction (PCR) corresponding to each of these opsins were amplified from spotted gar retinal cDNA and their identity was confirmed by sequencing (Figure 6 B).

In situ hybridization assays were performed using probes corresponding to the seven predicted gar opsins. All opsin mRNAs were detected in the photoreceptor cell bodies and/or photoreceptor inner segments, as expected (Figure 6 C-I). Both RH1-1 and RH1-2 were expressed in photoreceptors in cells with rod photoreceptor morphology, based on the rod like structure of the inner and outer segments. The density of opsin expressing cells varied, with low numbers of LWS (isolated to the regions near the optic nerve), SWS1-2 and SWS2 opsin expressing cells observed compared to RH2, SWS1-1, RH1-1 and RH1-2 expressing cells (Figure 4 J). The distribution of the expression of mRNAs predicted to correspond with multiple cone opsins and with rod opsins, suggests that the spotted gar has a duplex retina containing both rods and cones, and with the potential for color vision.

Discussion

The retina is a major focus of biomedical research because of its role in initiating our dominant sense, vision. The spotted gar, *Lepisosteus oculatus*, provides an emerging model in retina research. For example, two of the most common models for studying the retina are the zebrafish, a teleost fish, and mouse, a mammal (Jeon et al., 1998; Fadool and Dowling, 2008). The spotted gar provides an ideal opportunity to complement these studies and to understand the evolutionary origin of features of the teleost retina, such as the geometric pattern of photoreceptors and patterns of rhodopsin gene expression (Figure 1). The fecundity and readily available genomic resources available for study of the spotted gar distinguish it as a preferred model species over other basal ray-finned fish lineages (Braasch

et al., 2015). Significant findings of this study include 1) confirmation of structural and anatomical similarities between the spotted gar retina and those of other common models, 2) a displaced population of bipolar cell-like neurons near the photoreceptor layer, 3) an enriched repertoire of predicted short-wavelength shifted opsins, 4) lack of a geometric cone organization and 5) retinal expression of the gar ortholog of teleost *exo-rhodopsin*. We also generated a database of immunolabeling for all neuronal cell classes and Müller glia in the gar retina (S- Table 3). Today, much remains unknown about the spotted gar retina, and the findings of this study provide an important first step, i.e. its anatomical characterization.

Conservation across lineages

In the current study, we observed high conservation of retinal organization (cellular layers and plexiform layers) for spotted gar tissue when compared to other common retina models. In particular, antibodies against TH, bNOS, and ChAT were striking in their similarity to mouse and zebrafish tissue. These are commonly used mammalian markers designed to label the various populations of BPCs, ACs, RGCs, and laminae of the IPL. We observed very similar patterns among mouse and zebrafish and the spotted gar retina, suggesting a conservation of cellular organization despite the long divergence in genetic relationship.

We propose that the spotted gar is an organism that provides a unique means for understanding the evolution of the visual system. Both similarities and differences can be observed when comparing the spotted gar retina and visual behavior to that of humans and other common model systems such as mouse, zebrafish, and *Drosophila*, as well as less common systems like lamprey (Beamish, 1980; Collin, S. P., et al., 2003; Schwab & Collin, 2005; Villar-Cheda et al., 2006; Lamb et al., 2007) (Figure 7). We have included a diagram comparing all of these species on the basis of their retinal organization. Behavioral differences such as preferred feeding time are different among the species, which can potentially have impacts on the visual system (Figure 7 A) (Allada & Chung, 2010). The organization of light-responsive cells, rods and cones, shows large variation in both organization and wave-length sensitivity and detection. The basic structure of cellular layers and synaptic layers are conserved for all except *Drosophila*, with key differences (Figure 7 B-G). The presence of a ciliary marginal zone (CMZ), a region of the far periphery retina that houses retinal stems cells to aid in the continual growth of the retina through the lifespan, was only observed in gar (as shown in this study) and zebrafish (Figure 7 H). A displaced bipolar cell population(s), originally observed in lamprey, was also found in spotted gar

(Figures 4 & Figure 7 L-M). Across all species displayed, differences in location of horizontal cells have been observed, and large varieties of photoreceptor types; predicted and/or observed (Figure 1 B-D & Figure 7 I-M) (Ali & Anctil, 1976; Dartnall et al., 1983; Boynton, 1988; Applebury et al., 2000; Collin et al., 2003; Connaughton et al., 2004; Roberts et al., 2005; Takechi & Kawamura, 2005; Song et al., 2008; Allison et al., 2010; Lagman et al., 2013; Nivison-Smith et al., 2013). Much remains unknown, but being able to directly compare specialized tissue, such as the retina, across species that have long diverged in evolution provides an opportunity to understand how biological systems develop.

Displaced bipolar cell-like neurons in the ONL of the retina

The calbindin-positive cells in the ONL appear to be a population of displaced bipolar cells. The morphology and antibody labeling pattern correlate with previously reported bipolar cells in the retina (Ghosh et al., 2004; Euler et al., 2014; Li, Y. et al., 2012). This finding is unlike displaced amacrine cells in the GCL, which are commonly observed in other species (Pérez De Sevilla Müller et al., 2007). There is no direct comparison with zebrafish, as anti-calbindin is an ineffective marker in their retinal tissue (Yazulla and Studholme, 2001; and data not shown). Despite their location in the ONL of the gar retina, no antibody staining for photoreceptor populations was successful in colabeling the calbindin+ cells, nor were attempts to label any opsin mRNAs within the cells using *in situ* hybridization. Displaced bipolar cells have also been previously observed in the retinas of other basal species of fish (Braasch et al., 2016) including *Amia calva* (Bowfin) (Ali & Anctil, 1976), and sea lamprey (Villar-Cheda et al., 2006).

Photoreceptor organization

By labeling photoreceptor populations in the spotted gar with immunohistochemistry and *in situ* hybridization, we were able to make observations regarding how spotted gar organization compares to common retina models such as zebrafish and mouse. Teleost fish possess extremely organized photoreceptor mosaics, with regular spacing occurring within and between photoreceptor types (Raymond and Barthel, 2004; Fadool, 2003). The organization of SWS1-2 cones in the spotted gar was more regular than expected compared to random distribution, but not to the precise geometric levels observed in zebrafish. Rather, the organization resembled that of the mammalian retina, where the emphasis is on uniformity rather than specific spacing patterns (Ahnelt, 2000). This suggests that the

photoreceptor organization seen in gar and mouse represents the ancestral condition for bony vertebrates and creates a unique opportunity to study two questions in particular: 1) the conservation of function behind cell spacing and organization in the retina and 2) the potential role of the TGD in the establishment of photoreceptor mosaics seen in zebrafish and most teleosts.

Additionally, a ventral to dorsal gradient was observed in spotted gar for SWS1-2 cones that was not reciprocated in zebrafish retina. However, it is reminiscent of differences in spatial organization and densities among photoreceptor populations that are commonly seen in the retinas of other species. A consistent gradient has been observed in mouse retina, where the expression of medium-wavelength sensitive (MWS) opsins and short-wavelength sensitive (SWS) opsins differ in densities in the dorsal region (Applebury et al., 2000; Roberts et al., 2005). Dorsal-ventral and/or central-peripheral gradients of opsin expression and /or regional specializations are common in the retina. Even in fish with repeated crystalline mosaic patterning of morphological cone subtypes, the expression of opsins, particularly those encoded by tandemly replicated gene arrays, display pronounced topographic and temporal gradients (Takechi and Kawamura, 2005; Dalton et al., 2014; Mitchell et al., 2015). Additionally, previous work in gar retina with UV wavelength sensitivity, Opn5m and Opn5m2, has found that UV photo-sensitive proteins are distributed in a dorsal-ventral gradient (Sato et al., 2016).

Such differences have also observed in other fish species, for example, increases in density at the temporoventral regions has shown to benefit plankton feeders such as the ray-finned fish, *Osmerus eperlanus*, a teleost (Reckel et al., 2003). Increasing cone densities in the far temporal retina was found in the *Pomoxis annularis* (Browman et al 1990), another teleost fish. Past work has shown that increases in single cone density appear to visually aid predators (Browman et al. 1994). More specifically, ultraviolet vision was shown to improve prey search in zooplanktivorous fish by improving prey contrast against a background rich in scattered ultraviolet light (Losey et al., 1999). Spotted gars are night active predators, as previous work reported that 70% of gars collected at night showed food consumption, compared to less than 30% of gars at day and dusk. Additionally, tracking of spotted gar movement revealed significantly more activity during the night compared to daytime. The preference in spotted gar retina for a high number of opsins in a UV shifted spectral range is consistent with their feeding pattern (Snedden, G. et al. 1999, Hunt, 1953).

Photoreceptor diversity in the retina of the spotted gar likely includes a population of rods, and several types of cones that express SWS1-1, SWS1-2, SWS2, RH-2, and LWS, accounting for all of the predicted retinal opsin genes in the gar genome (Lagman et al., 2013). The high density of rods located in the gar retina is consistent with its nocturnal habits that were previously reported. The most abundant cone population expresses SWS1-1, with predicted sensitivity to short wavelengths, based upon homology with other SWS1 opsins with peak sensitivities in the UV range of the spectrum (Braasch et al., 2016). If we extend this prediction to the other opsins expressed in the gar retina, the gar appears to have a preponderance of cones likely sensitive to short wavelengths (approx. 13 cones/100 μm for SWS1-1 + SWS1-2 + SWS2 opsins; Fig. 6K) vs. longer wavelengths (approx. 8 cones/100 μm for RH2 + LWS opsins; Fig. 6K).

Retinal expression of an *exo-rhodopsin* homolog

We observed expression of two rhodopsin genes in rods of the adult gar retina: RH1-1, the ortholog of teleost *exo-rhodopsin*; and RH1-2, the ortholog of teleost retinal rhodopsin (Lagman et al., 2013). *In situ* hybridization assays suggest that both rod opsins are expressed in overlapping photoreceptor populations of the gar, but further studies will be needed to characterize any spatiotemporal and/or quantitative difference in expression. The gar RH1-1 and teleost *exo-rhodopsin* contain introns, and cluster phylogenetically with other vertebrate rhodopsins. Gar RH1-2 and teleost retinal rhodopsin are intronless and likely arose as a consequence of a retrotranscription event (Fitzgibbon et al., 1995; Lagman et al., 2013). Retinal expression of RH1-1 in gar, confirmed by RT-PCR and *in situ* hybridization, raises the question of when this change in expression occurred during evolution of fishes. The results of our *in situ* hybridization assays suggest that both rod opsins (RH1-1 and RH1-2) are expressed in overlapping photoreceptor populations in the spotted gar retina, but further studies will be needed to characterize any spatiotemporal and/or quantitative differences in expression.

In this study, we characterized the *Lepisosteus oculatus* retina as an emerging model for neural and visual research. We have compiled a resource of antigen labeling tools, predicted opsin gene expression, and the basic organization of the retina structure and its cellular organization in the spotted gar. These anatomical findings, along with recent work regarding the *Lepisosteus oculatus* genome and its status as an out-group for teleost fish,

make it an excellent candidate for future research regarding the evolution of the visual system and the role of genome duplication in neural development.

Acknowledgements

This research was supported by NSF Cooperative Agreement DBI #093945 (BEACON) and NSF REU Site Award DBI #1460696. Imaging performed with the help of the IBEST Optical Imaging Core was supported by INBRE Awards P20GM103408. Additional thanks to the University of Oregon Fish Facility for spotted gar husbandry and Allyse Ferrara and Queston Fontenot (Nicholls State University, Louisiana) for providing spotted gar embryos. We would like to thank Ruth Frey for help regarding equipment for housing spotted gar at the University of Idaho as well as *in situ hybridization* work, and Tyler Lankford for technical assistance. The authors are grateful to Dr. David Hyde and Dr. James Fadool for anti-zebrafish opsin antibodies. Zpr-1, zpr-3, and zrf-1 antibodies were obtained from the Zebrafish International Resource Center (ZIRC), which is supported by NIH P40 RR012546. We would also like to thank Aaron Simmons and Dr. Shuai Li for helpful suggestions.

Conflict of Interest The authors have no conflict of interest with respect to this work.

Author Contributions All authors had full access to all the data in the study and take responsibility for the integrity of the data and the accuracy of the data analysis. Study concept and design: JMS, PGF, DLS, BDR, JWB. Acquisition of data: JMS, CAG, JDW, TM. Analysis and interpretation of data: JMS, PGF, DLS. Drafting of the manuscript: JMS, PGF, and DLS. Critical revision of the manuscript for important intellectual content: JMS, PGF, DLS, JHP, IB. Statistical analysis: JMS, CAG, And JDW. Obtained funding: PGF, DLS, BDR, and JWB. Administrative, technical, and material support: PGF, DLS, JHP, IB. Study supervision: PGF, DLS.

References

Ahnelt, P. K., & Kolb, H. (2000). The mammalian photoreceptor mosaic-adaptive design. *Progress in retinal and eye research*, *19*(6), 711-777.

Allada, R., & Chung, B. Y. (2010). Circadian organization of behavior and physiology in Drosophila. *Annual review of physiology*, 72, 605.

Ali, M. A., & Anctil, M. (1976). *Retinas of fishes: An atlas*. Berlin: Springer-Verlag

Allison, W. T., Barthel, L. K., Skebo, K. M., Takechi, M., Kawamura, S., & Raymond, P. A. (2010). Ontogeny of cone photoreceptor mosaics in zebrafish. *Journal of Comparative Neurology*, *518*(20), 4182-4195.

Amores, A., Catchen, J., Ferrara, A., Fontenot, Q., & Postlethwait, J. H. (2011). Genome Evolution and Meiotic Maps by Massively Parallel DNA Sequencing: Spotted Gar, an Out-group for the Teleost Genome Duplication. *Genetics*, 188: 799-808.

Applebury, M. L., Antoch, M. P., Baxter, L. C., Chun, L. L. Y., Falk, J. D., Farhangfar, F., & Robbins, J. T. (2000). The murine cone photoreceptor: a single cone type expresses both S and M opsins with retinal spatial patterning. *Neuron*, *27*(3), 513-523.

Beamish, F. W. H. (1980). Biology of the North American anadromous sea lamprey, Petromyzon marinus. *Canadian Journal of Fisheries and Aquatic Sciences*, 37(11), 1924-1943.

Bernardos, R.L., Barthel, L.K., Meyers, J.R., Raymond, P.A., 2007. Late-stage neuronal progenitors in the retina are radial Muller glia that function as retinal stem cells. *J. Neurosci.* 27, 7028e7040.

Boynton, R. M. (1988). Color vision. Annual review of psychology, 39(1), 69-100.

Braasch, I., & Postlethwait, J. H. (2012). Polyploidy in fish and the teleost genome duplication. In Polyploidy and genome evolution (pp. 341-383). Springer Berlin Heidelberg.

Braasch, I., Peterson, S. M., Desvignes, T., McCluskey, B. M., Batzel, P., & Postlethwait, J. H. (2015). A new model army: Emerging fish models to study the genomics of vertebrate Evo-Devo. *Journal of Experimental Zoology Part B: Molecular and Developmental Evolution*, 324(4), 316-341.

Braasch, I., Gehrke, A. R., Smith, J. J., Kawasaki, K., Manousaki, T., Pasquier, J., & Berlin, A. M. (2016). The spotted gar genome illuminates vertebrate evolution and facilitates human-teleost comparisons. *Nature genetics*, 48(4), 427-437.

Browman, H. I., Gordon, W. C., Evans, B. I., & O'Brien, W. J. (1990). Correlation between histological and behavioral measures of visual acuity in a zooplanktivorous fish, the white crappie (Pomoxis annularis). *Brain, behavior and evolution*, 35(2), 85-97.

Browman, H. 1994. Ultraviolet photoreceptor contributes to pretty search behavior in two species of zooplanktivorous fishes. *J. exp. Biol*., 186: 187-198.

Cameron, D. A., & Carney, L. H. (2000). Cell mosaic patterns in the native and regenerated inner retina of zebrafish: implications for retinal assembly. *Journal of Comparative Neurology*, *416*(3), 356-367.

Chotard, C., & Salecker, I. (2007). Glial cell development and function in the Drosophila visual system. *Neuron glia biology*, 3(01), 17-25.

Collin, S. P., & Collin, H. B. (1993). The visual system of the Florida garfish, *Lepisosteus platyrhincus* (Ginglymodi). *Brain, behavior and evolution*, 42(2), pp. 98-115.

Collin, S. P., Knight, M. A., Davies, W. L., Potter, I. C., Hunt, D. M., & Trezise, A. E. (2003). Ancient colour vision: multiple opsin genes in the ancestral vertebrates. *Current Biology*, 13(22), R864-R865.

Connaughton, V. P., Graham, D., & Nelson, R. (2004). Identification and morphological classification of horizontal, bipolar, and amacrine cells within the zebrafish retina. *Journal of Comparative Neurology*, 477(4), 371-385.

Cook, J. E. (1996). Spatial properties of retinal mosaics: an empirical evaluation of some existing measures. *Visual neuroscience*, 13(01), 15-30.

Crow, K. D., & Wagner, G. P. (2006). What is the role of genome duplication in the evolution of complexity and diversity? *Molecular biology and evolution*, *23*(5), 887-892.

Dalton, B. E., Loew, E. R., Cronin, T. W., & Carleton, K. L. (2014). Spectral tuning by opsin coexpression in retinal regions that view different parts of the visual field. *Proceedings of the Royal Society of London B: Biological Sciences*, 281(1797), 20141980.

Dartnall, H. J., Bowmaker, J. K., & Mollon, J. D. (1983). Human visual pigments: microspectrophotometric results from the eyes of seven persons. *Proceedings of the Royal Society of London B: Biological Sciences*, 220(1218), 115-130.

Erskine, L., Williams, S. E., Brose, K., Kidd, T., Rachel, R. A., Goodman, C. S., & Mason, C. A. (2000). Retinal ganglion cell axon guidance in the mouse optic chiasm: expression and function of robos and slits. *The Journal of Neuroscience*, 20(13), 4975-4982.

Euler, T., Haverkamp, S., Schubert, T., & Baden, T. (2014). Retinal bipolar cells: elementary building blocks of vision. *Nature Reviews Neuroscience*, *15*(8), 507-519.

Fadool, J. 2003. Development of a rod photoreceptor mosaic revealed in transgenic zebrafish. *Developmental Biology*, 258: 277-290

Fadool J, Dowling J. 2008. Zebrafish: A model system for the study of eye genetics. *Progress in Retina and Eye Research*, 27: 89-110

Fei, Y. (2003). Development of the cone photoreceptor mosaic in the mouse retina revealed by fluorescent cones in transgenic mice. *Mol Vis*, *9*(6), 31-42.

Fitzgibbon, J., Hope, A., Slobodyanyuk, S. J., Bellingham, J., Bowmaker, J. K., & Hunt, D. M. (1995). The rhodopsin-encoding gene of bony fish lacks introns. *Gene*, 164(2), 273-277.

Fuerst PG, Bruce F, Tian M, Wei W, Elstrott J, Feller MB, Erskine L, Singer JH, Burgess RW. 2008. DSCAM and DSCAML1 function in self-avoidance in multiple cell types in the developing mouse retina. *Neuron*, 64(4):484-497.

Ghosh, K. K., Bujan, S., Haverkamp, S., Feigenspan, A., & Wässle, H. (2004). Types of bipolar cells in the mouse retina. *Journal of Comparative Neurology*, *469*(1), 70-82.

Haverkamp, S., & Wässle, H. (2000). Immunocytochemical analysis of the mouse retina. *Journal of Comparative Neurology*, *424*(1), 1-23.

Haverkamp, S., Ghosh, K. K., Hirano, A. A., & Wässle, H. (2003). Immunocytochemical description of five bipolar cell types of the mouse retina. *Journal of Comparative Neurology*, *455*(4), 463-476.

Haverkamp, S., Wässle, H., Duebel, J., Kuner, T., Augustine, G. J., Feng, G., & Euler, T. (2005). The primordial, blue-cone color system of the mouse retina. *The Journal of Neuroscience*, 25(22), 5438-5445.

Hunt, B. P. (1953). Food relationships between Florida spotted gar and other organisms in the Tamiami Canal, Dade County, Florida. *Transactions of the American Fisheries Society*, 82(1), 13-33.

Jeon, C. J., Strettoi, E., & Masland, R. H. (1998). The major cell populations of the mouse retina. *The Journal of Neuroscience*, 18(21), 8936-8946.

Jones, F. C., Grabherr, M. G., Chan, Y. F., Russell, P., Mauceli, E., Johnson, J., & Birney, E. (2012). The genomic basis of adaptive evolution in threespine sticklebacks. *Nature*, *484*(7392), 55-61.

Julian, D., Ennis, K., Korenbrot, J.I., 1998. Birth and fate of proliferative cells in the inner nuclear layer of the mature fish retina. *J. Comp. Neurol*. 394, 271e282.

Kay, J. et al., 2001 Retinal Ganglion Cell Genesis Requires lakritz, a Zebrafish atonal Homolog. *Neuron*, 30: 725-736.

Kroehne, V., et al., 2011 Regeneration of the adult zebrafish brain from neurogenic radial glia-type progenitors. *Development*, 138: 4831-4841.

Kumar, J. P. (2001). Signaling pathways in Drosophila and vertebrate retinal development. *Nature Reviews Genetics*, 2(11), 846-857.

Labhart, T., Baumann, F., & Bernard, G. D. (2009). Specialized ommatidia of the polarization-sensitive dorsal rim area in the eye of monarch butterflies have non-functional reflecting tapeta. *Cell and tissue research*, 338(3), 391-400.

Lagman, D., Daza, D. O., Widmark, J., Abalo, X. M., Sundström, G., & Larhammar, D. (2013). The vertebrate ancestral repertoire of visual opsins, transducin alpha subunits and oxytocin/vasopressin receptors was established by duplication of their shared genomic region in the two rounds of early vertebrate genome duplications. *BMC evolutionary biology*, 13(1), 1.

Lamb, T. D., Collin, S. P., & Pugh, E. N. (2007). Evolution of the vertebrate eye: opsins, photoreceptors, retina and eye cup. *Nature Reviews Neuroscience*, 8(12), 960-976.

Link, B. A., Fadool, J. M., Malicki, J., & Dowling, J. E. (2000). The zebrafish young mutation acts non-cell-autonomously to uncouple differentiation from specification for all retinal cells. *Development*, *127*(10), 2177-2188.

Losey, G. S., Cronin, T. W., Goldsmith, T. H., Hyde, D., Marshall, N. J., & McFarland, W. N. (1999). The UV visual world of fishes: a review. *Journal of Fish Biology*, *54*(5), 921-943.

Masland, R. H. (2001). The fundamental plan of the retina. *Nature neuroscience*, 4(9), 877-886.

Milam, A. H., Saari, J. C., Jacobson, S. G., Lubinski, W. P., Feun, L. G., & Alexander, K. R. (1993). Autoantibodies against retinal bipolar cells in cutaneous melanoma-associated retinopathy. *Investigative ophthalmology & visual science*, 34(1), 91- 100.

Mitchell, D. M., Stevens, C. B., Frey, R. A., Hunter, S. S., Ashino, R., Kawamura, S., & Stenkamp, D. L. (2015). Retinoic Acid signaling regulates differential expression of the tandemly-duplicated long wavelength-sensitive cone opsin genes in zebrafish. *PLoS Genet*, 11(8), e1005483.

Nelson, S.M., Frey, R.A., Wardwell, S.L., Stenkamp, D.L., 2008. The developmental sequence of gene expression within the rod photoreceptor lineage in embryonic zebrafish. *Dev. Dyn*. 237, 2903e2917.

Nivison-Smith, L., Collin, S. P., Zhu, Y., Ready, S., Acosta, M. L., Hunt, D. M., & Kalloniatis, M. (2013). Retinal amino acid neurochemistry of the southern hemisphere lamprey, *Geotria australis*. PloS one, 8(3), e58406.

Otteson, D.C., D'Costa, A.R., Hitchcock, P.F., 2001. Putative stem cells and the lineage of rod photoreceptors in the mature retina of the goldfish. *Dev. Biol.* 232, 62e76.

Pérez De Sevilla Müller, L., Shelley, J., & Weiler, R. (2007). Displaced amacrine cells of the mouse retina. *Journal of Comparative Neurology*, *505*(2), 177-189.

Postlethwait, J. et al., 1998 Vertebrate genome evolution and the zebra fish gene map. *Nat. Genet*. 18: 345–349.

Raymond, P.A., Rivlin, P.K., 1987. Germinal cells in the goldfish retina that produce rod photoreceptors. *Dev. Biol*. 122, 120e138.

Raymond, P. A., Barthel, L. K., & Curran, G. A. (1995). Developmental patterning of rod and cone photoreceptors in embryonic zebrafish. *Journal of Comparative Neurology*, *359*(4), 537-550.

Raymond, P. A., & Barthel, L. K. (2004). A moving wave patterns the cone photoreceptor mosaic array in the zebrafish retina. *Int J Dev Biol*, *48*(8-9), 935-945.

Raymond, P. A., Barthel, L. K., Bernardos, R. L., & Perkowski, J. J. (2006). Molecular characterization of retinal stem cells and their niches in adult zebrafish. *BMC developmental biology*, *6*(1), 36.

Reckel, F., Hoffmann, B., Melzer, R. R., Horppila, J., & Smola, U. (2003). Photoreceptors and cone patterns in the retina of the smelt Osmerus eperlanus (L.)(Osmeridae: Teleostei). *Acta Zoologica*, *84*(3), 161-170.

Renninger, S. L., Gesemann, M., & Neuhauss, S. C. (2011). Cone arrestin confers cone vision of high temporal resolution in zebrafish larvae. *European Journal of Neuroscience*, 33(4), 658-667.

Roberts, M. R., Hendrickson, A., McGuire, C. R., & Reh, T. A. (2005). Retinoid X receptor (gamma) is necessary to establish the S-opsin gradient in cone photoreceptors of the developing mouse retina. *Investigative ophthalmology & visual science*, *46*(8), 2897-2904.

Rodieck, RW. 1991. The density recovery profile: a method for the analysis of points in the plane applicable to retinal studies. *Vis Neurosci* 6(2):95-111.

Sanes, J. R., & Zipursky, S. L. (2010). Design principles of insect and vertebrate visual systems. *Neuron*, 66(1), 15-36.

Sato, K., Yamashita, T., Haruki, Y., Ohuchi, H., Kinoshita, M., & Shichida, Y. (2016). Two UV-Sensitive Photoreceptor Proteins, Opn5m and Opn5m2 in Ray-Finned Fish with Distinct Molecular Properties and Broad Distribution in the *Retina and Brain*. PLoS ONE, 11(5), e0155339. http://doi.org/10.1371/journal.pone.0155339

Schwab, I. R., & Collin, S. P. (2005). Are you calling me primitive?. *British Journal of Ophthalmology*, 89(12), 1553-1553.

Sherpa, T., Lankford, T., McGinn, T. E., Hunter, S. S., Frey, R. A., Sun, C., & Stenkamp, D. L. (2014). Retinal regeneration is facilitated by the presence of surviving neurons. *Developmental neurobiology*, *74*(9), 851-876.

Smith, O. A., 2006 Reproductive potential and life history of spotted gar Lepisosteus oculatus in the upper Barataria estuary, Louisiana, pp.116 in *Marine and Environmental Biology*. Nicolls State University, Thibodaux, LA.

Snedden, G. A., Kelso, W. E., & Rutherford, D. A. (1999). Diel and seasonal patterns of spotted gar movement and habitat use in the lower Atchafalaya River Basin, Louisiana. *Transactions of the American Fisheries Society*,128(1), 144-154.

Song, P. I., Matsui, J. I., & Dowling, J. E. (2008). Morphological types and connectivity of horizontal cells found in the adult zebrafish (Danio rerio) retina. *Journal of Comparative Neurology*, 506(2), 328-338.

Stenkamp, D. L., Powers, M. K., Carney, L. H., & Cameron, D. A. (2001). Evidence for two distinct mechanisms of neurogenesis and cellular pattern formation in regenerated goldfish retinas. *Journal of Comparative Neurology*, *431*(4), 363-381.

Stenkamp, D. L. (2007). Neurogenesis in the fish retina. *International review of cytology*, *259*, 173-224.

Stenkamp, D. L. (2011). The rod photoreceptor lineage of teleost fish. *Progress in retinal and eye research*, *30*(6), 395-404.

Stevens, C. B., Cameron, D. A., & Stenkamp, D. L. (2011). Plasticity of photoreceptor-generating retinal progenitors revealed by prolonged retinoic acid exposure. *BMC developmental biology*, *11*(1), 51.

Takechi, M., & Kawamura, S. (2005). Temporal and spatial changes in the expression pattern of multiple red and green subtype opsin genes during zebrafish development. *The Journal of experimental biology*, 208(7), 1337-1345.

Taylor J., Braasch I., Frickey T., Meyer A., Van De Peer Y., 2003 Genome duplication, a trait shared by 22,000 species of ray-finned fish. *Genome Res*. 13:382–390.

Vihtelic, T., Doro, C., Hyde, D., 1999 Cloning and characterization of six zebrafish photoreceptor opsin cDNAs and immunolocalization of their corresponding proteins. *Visual Neuroscience*. 16: 3: 571-585.

Vihtelic, T. S., Soverly, J. E., Kassen, S. C., & Hyde, D. R. (2006). Retinal regional differences in photoreceptor cell death and regeneration in light-lesioned albino zebrafish. *Experimental eye research*, *82*(4), 558-575.

Villar-Cheda, B., Abalo, X. M., Anadón, R., & Rodicio, M. C. (2006). Calbindin and calretinin immunoreactivity in the retina of adult and larval sea lamprey. *Brain research*, 1068(1), 118-130.

Wernet, M. F., & Desplan, C. (2004). Building a retinal mosaic: cell-fate decision in the fly eye. *Trends in cell biology*, 14(10), 576-584.

Wernet, M. F., Mazzoni, E. O., Çelik, A., Duncan, D. M., Duncan, I., & Desplan, C. (2006). Stochastic spineless expression creates the retinal mosaic for colour vision. Nature, 440(7081), 174-180.

Westerfield, M. (2007) The Zebrafish Book. A Guide for the Laboratory Use of Zebrafish (*Danio rerio*), 5th Edition. University of Oregon Press, Eugene, OR.

Yazulla, S., & Studholme, K. M. (2001). Neurochemical anatomy of the zebrafish retina as determined by immunocytochemistry. *Journal of Neurocytology*, *30*(7), 551-592.

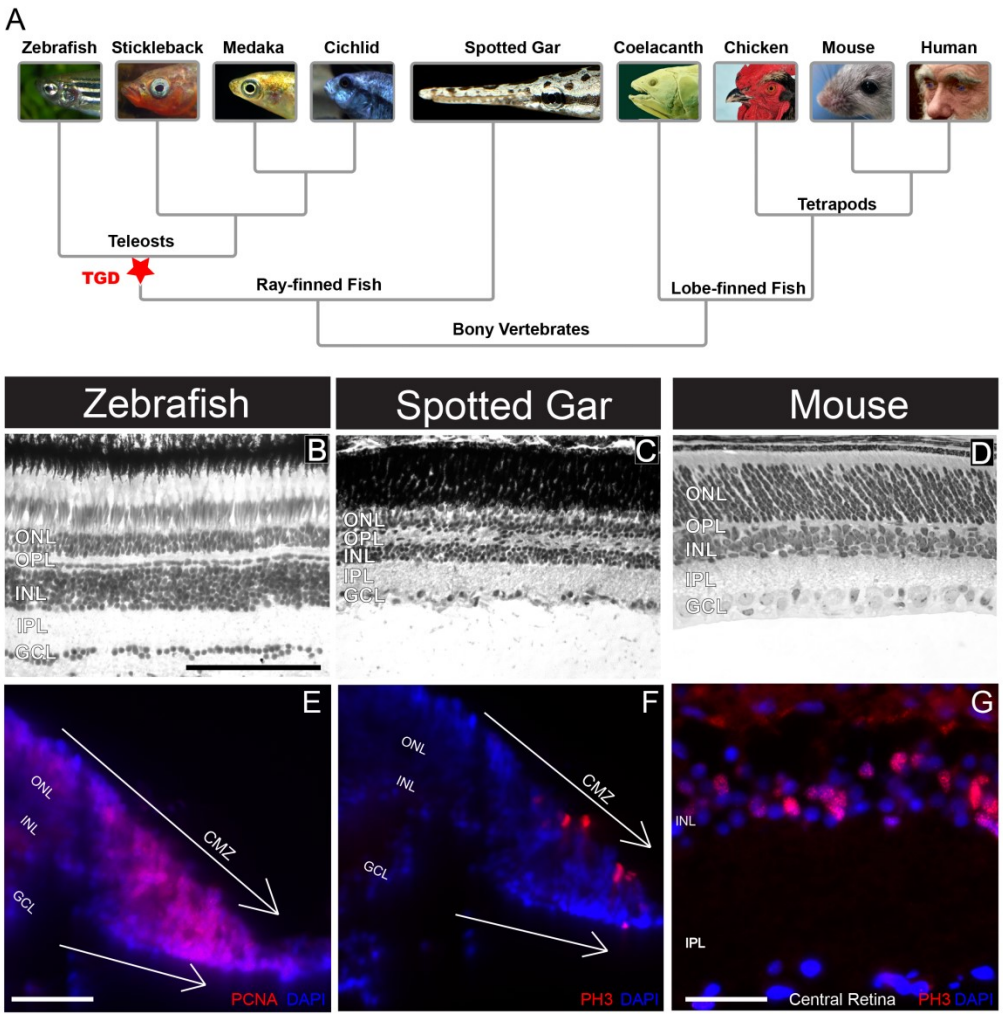

Figure 6.1. A) Phylogenetic and anatomical relationships between the spotted gar and common models and the observation of a ciliary marginal zone in spotted gar retina. Spotted gar, *Lepisosteus oculatus*, is a ray-finned fish that diverged from the teleost fish lineage prior to the teleost genome duplication (TGD, red star). Additionally, the spotted gar has not undergone any subsequent genome duplications, and retains a genome organization and gene complements similar to tetrapods (human, mouse, and chicken). **B)** Zebrafish retina stained with hematoxylin and eosin (H & E) to show nuclear layers and overall organization. **C)** Spotted gar retina tissue stained with H & E. **D)** Mouse retina tissue stained with H & E for comparison. A ciliary marginal zone (CMZ) was observed at the far periphery of the spotted gar retina. **E)** Labeling with antibodies against proliferating cell nuclear antigen (PCNA) was observed in many cells at the periphery of the retina. This is evidence of a pool of proliferating cells that are contributing to the continual growth of the retina. Antibodies against Phospho-Histone H3 (PH3) also show evidence of dividing cells in the **F)** peripheral

region of the retina, as well as evidence of cell proliferation in the **G)** inner nuclear layer (INL); a likely result of the constantly growing retina that was observed for the spotted gar. The arrows in E and F are directed towards the furthest peripheral edge of the retina sections. Abbreviations: ONL=outer nuclear layer; INL=inner nuclear layer; GCL=ganglion cell layer; OPL=outer plexiform layer; IPL=inner plexiform layer. The scale bar in B is equal to 100 μm, and continues for C and D. Scales bar in E is equal to 50 μm, and is the same for F. Scale bar in G is equal to 25 μm.

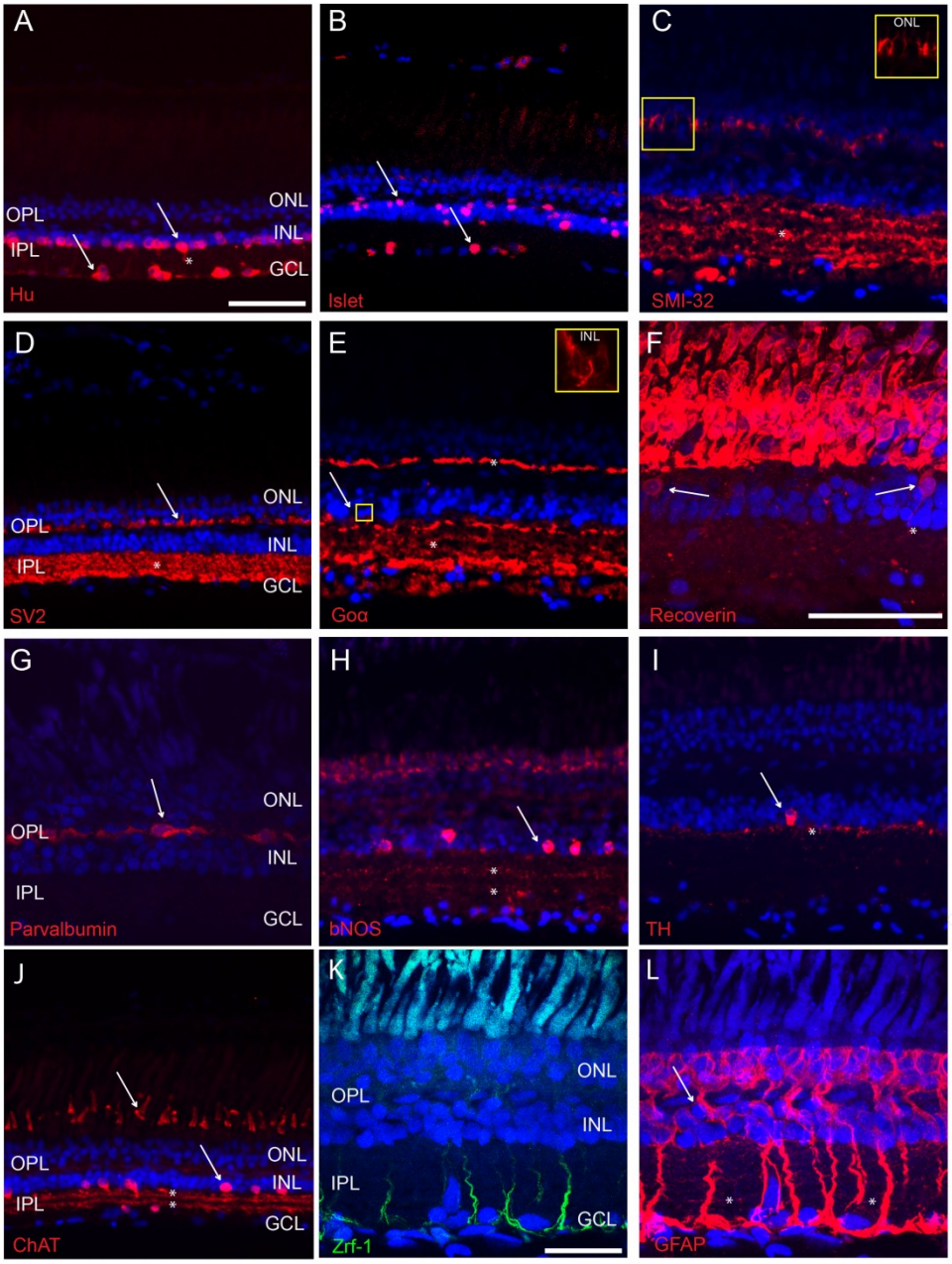

Figure 6.2. Labeling cells in the spotted gar inner retina. A) Antibodies against the transcription factor Hu showed immunoreactivity for cells in the INL and GCL. Additionally, small neurites were shown projecting into the IPL. **B)** Antibodies against Islet1, a transcription factor important for neural development, labeled cells in the INL and GCL. **C)** Antibodies against SMI-32 showed clear labeling of neurites in the IPL as well as a bipolar cell population(s) within the ONL (inset). **D)** Anti-SV2 is an antibody for targeting cone bipolar cells. Additionally, strong labeling of the IPL was observed. **E)** Antibodies to Goα a labeled neurites in the IPL and OPL (asterisks) as well as the outer edge of bipolar cells in the ONL

(inset). **F)** Antibodies to recoverin showed consistent labeling of a bipolar cell population and its axons into the IPL (see arrows). Previous reporting identifies these as type 2 OFF bipolar cells in mammalian retina, and is likely the same for spotted gar. **G)** Antibodies to parvalbumin labeled a population of neurons in the INL, presumably horizontal cells. **H)** Antibodies to bNOS labeled presumed amacrine cells located in the GCL and INL. Clear labeling of cells in the INL as well as distinct sublaminae in the IPL (asterisks). **I)** Antibodies to tyrosine hydroxylase (TH) labeled a cell population that projects dendrites to the outer most portion (anterior) of the IPL, similar to what is observed in the mouse and zebrafish retina. **J)** Antibodies to ChAT labeled populations of cells in the INL and GCL (displaced) in addition to distinct labeling of the S2 and S4 sublaminae in the IPL (asterisks). This is similar to the staining pattern of this antibody in the mouse retina (Haverkamp & Wassle, 2000). Interestingly, consistent labeling of photoreceptor inner segments was observed as well. Müller glia cells, which span the retina, are often targeted in other vertebrates with antibodies against GFAP. Anti-mammalian GFAP and anti-zebrafish GFAP (Zrf-1) were effective in labeling Müller glia cells in the spotted gar retina. **K)** Zrf-1 reveal strong labeling isolated to the Müller glia processes in the inner retina (arrow). **L)** Antibodies to mammalian GFAP reveal effective labeling throughout the entire cell and its processes, including the tangential processes (asterisks) that span the IPL. For A-L, arrows indicate cell bodies, and asterisks indicate dendritic connections and/or sublaminae of the IPL that were positive for the antibodies. Abbreviations: ONL=outer nuclear layer; INL=inner nuclear layer; GCL=ganglion cell layer; OPL=outer plexiform layer; IPL=inner plexiform layer; SV2=synaptic vesicle 2; TH=tyrosine hydroxylase. All tissue is sectioned from wild type retinas from spotted gar aged 1 year to 2 years. Scale bar in A is equal to 50 μm, and is the same for B-E and H-J. The scale bar in F is equal to 50 μm and it continues for G. Scale bar in K is equal to 100 □m, and continues for L.

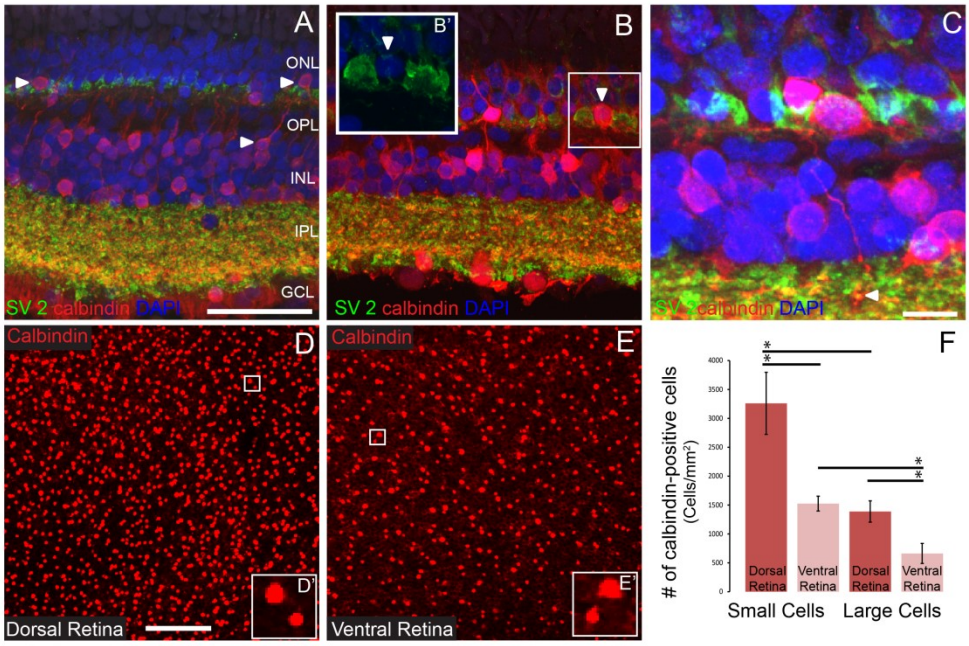

Figure 6.3. Displaced calbindin-positive cells found in spotted gar retina. A population of calbindin-positive cells in the ONL was observed. **A)** Cells stained with antibodies against calbindin (a calcium binding protein) were observed on both sides of the OPL (arrows). **B)** Cells stained with antibodies to calbindin in the ONL did not accumulate SV2, as observed in adjacent photoreceptors (inset **B'**; white arrow). **C)** Calbindin-positive cell in ONL projected an axon-like process into the IPL and punctate SV2 staining was observed in the distal portion of this process. **D, E)** Calbindin-positive cells in the ONL were categorized by size into small and large cells (insets **D'** and **E'**). **F)** An increase in density was observed from ventral to dorsal regions of the retina small and large cells. For A, B and C, arrows indicate cell bodies. Abbreviations: ONL=outer nuclear layer; INL=inner nuclear layer; GCL=ganglion cell layer; OPL=outer plexiform layer; IPL=inner plexiform layer; SV2=synaptic vesicle 2. Scale bar for A is equal to 50 □m, and is the same for B. Scale bar for C is equal to 12.5 □m. Scale bar in D represents 100 □m, and is the same for E.

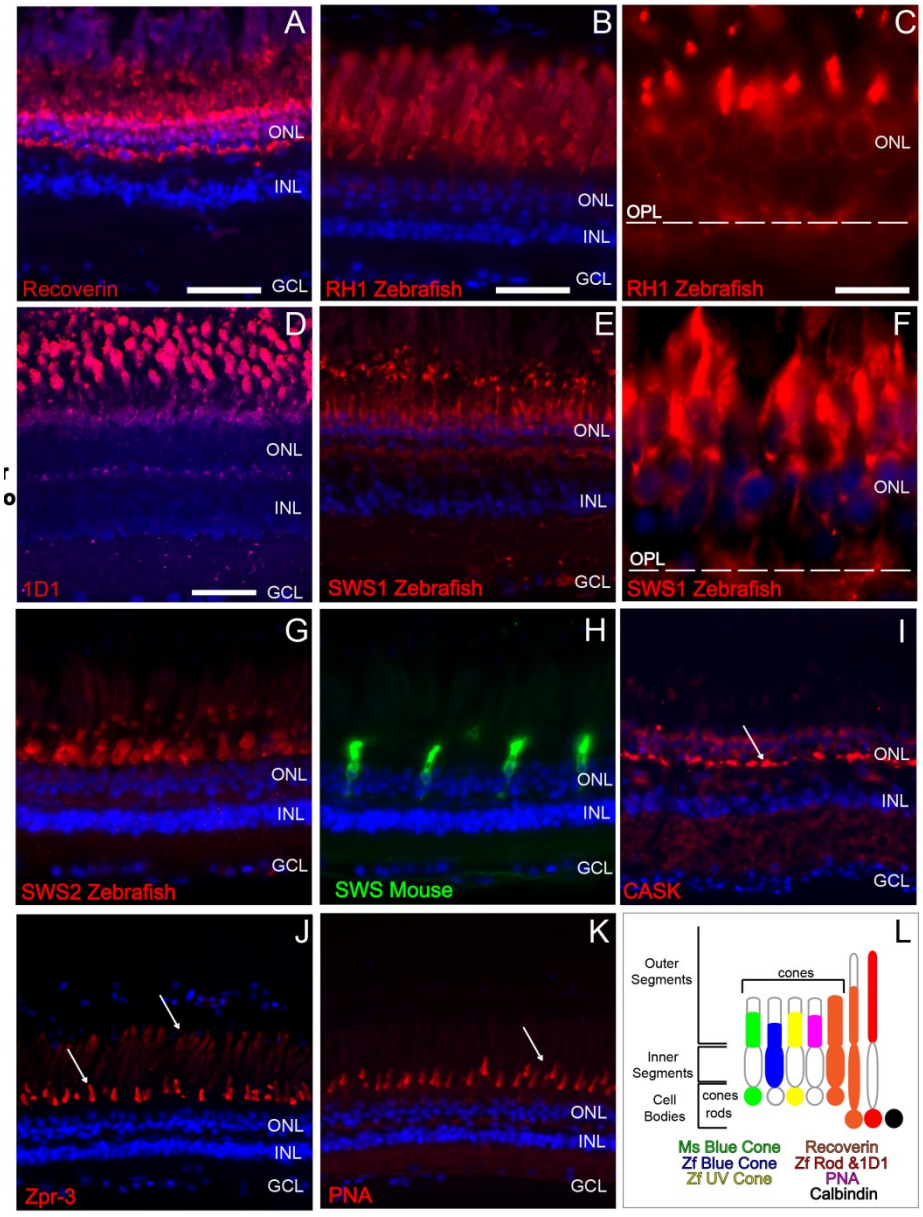

Figure 6.4. Immunohistochemistry labeling for spotted gar outer retina. Sections of spotted gar tissue were stained with specific antibody markers aimed at targeting cells in the photoreceptor layer. We observed successful labeling of entire populations and individual cell types. **A)** Antibodies against recoverin labeled all or most photoreceptors in gar retina. **B-C)** Antibodies against RH1 Zebrafish (antibodies to zebrafish rhodopsin) staining was observed in all rod cells. Strong labeling in the outer segments and fainter labeling of cell bodies was observed. **D)** Rod photoreceptor outer segments were also labeled by the monoclonal antibody 1D1. Individual cone photoreceptor types were labeled with **E-F)** anti-SWS1 Zebrafish (antibodies to zebrafish ultraviolet opsin 1), **G)** Anti-SWS2 Zebrafish (antibodies to

zebrafish blue opsin), and **H)** anti-SWS Mouse (antibodies to mouse blue opsin). Dashed lines in **C** and **F** mark the center of the OPL. Cell bodies belonging to cone photoreceptors were found to be located posterior to rod photoreceptors. Additional staining was shown with **I)** antibodies against CASK, which was found to label synapses in the OPL (see arrow). **J)** Both the inner and outer segments were labeled with antibodies against Zpr-3, with stronger labeling in the inner segments. **K)** Peanut agglutinin (PNA) shows clear and distinct labeling in the photoreceptor inner segments (see arrow). Labeling patterns and cell body organization from A-K are summarized in panel **L)**. Abbreviations: ONL=outer nuclear layer; INL=inner nuclear layer; GCL=ganglion cell layer; OPL=outer plexiform layer; IPL=inner plexiform layer; PNA=peanut agglutinin. Scale bar in A is equal to 50 μm, and it is the same for E, I, J, and K. Scale bar in C is equal to 12.5 μm and it is the same for F. Scale bar in B is equal to 37.5 μm and it is the same for G and H. Scale bar in D is equal to 25 μm.

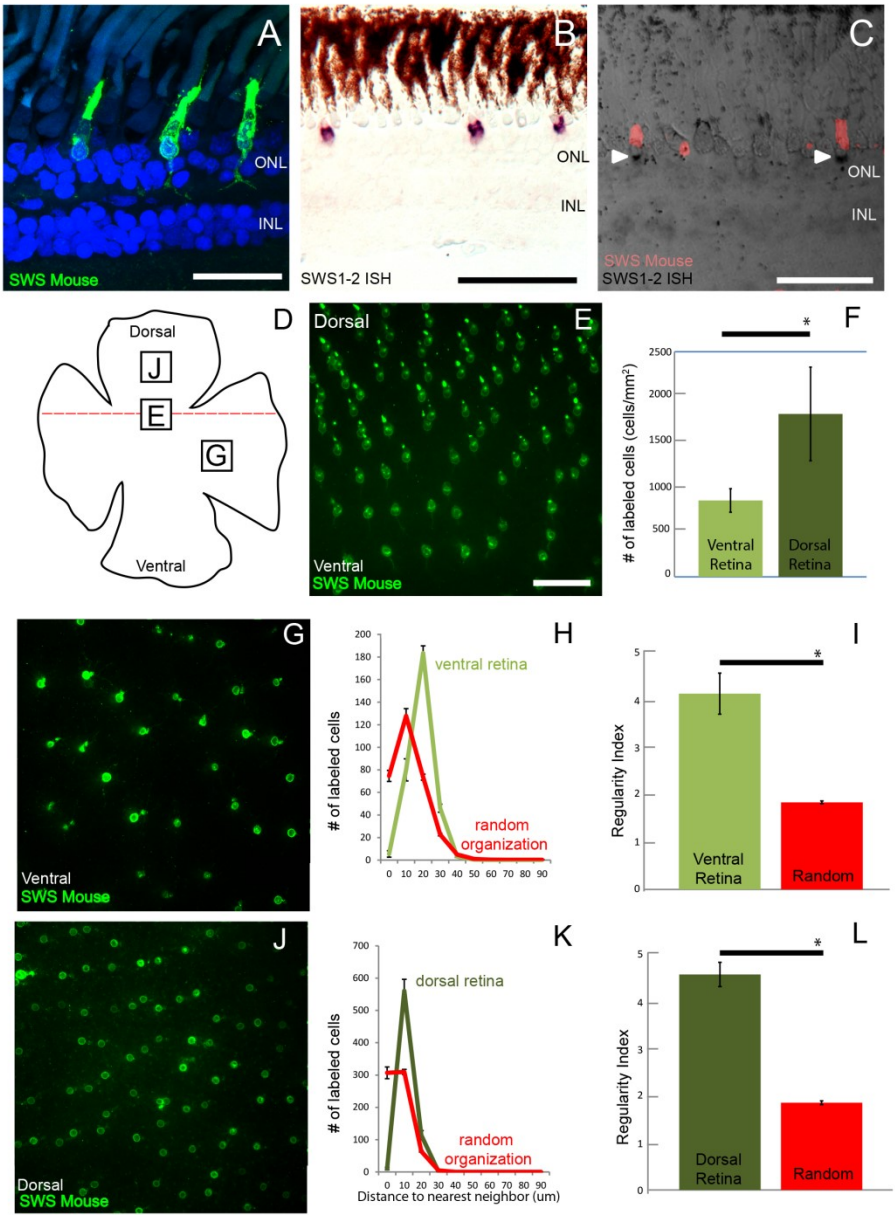

Figure 6.5. Spacing and organization of SWS1-2+ cone photoreceptors. A) Antibodies to SWS Mouse (antibodies to mouse blue opsin) labeled cones in the spotted gar. **B)** *In situ* hybridization (ISH) for SWS1-2 opsin mRNA labeled a similar number of cones. **C)** Double labeling with antibodies to mouse SWS and *in situ* hybridization of SWS1-2 opsin mRNA revealed that they targeted the same cell population. **D)** Diagram showing the approximate locations of sampling from dorsal and ventral retina regions that were used in subsequent figures. The red dashed line represents the transition area where a marked difference between the dorsal and ventral regions can be observed. **E)** SWS1-2 cones (as labeled with Mouse SWS antibodies) in spotted gar whole mount retina showing the transition from dorsal

(top) to ventral (bottom) regions of the spotted gar retina. **F)** The summary of DRP (density recovery profile) results showing the difference in density from dorsal to ventral retina. Density was observed to be significantly different between the two regions ($p=3.0x10^{-43}$ as denoted by "*"). **G)** Whole mount display of cellular organization for SWS1-2 cones in the ventral retina only. **H)** Nearest neighbor analysis (NNA), a measurement that reflects the distance from one cell to its nearest neighboring cell, results for SWS1-2 cones in spotted gar for ventral retina (light green line). Cells were found to be organized significantly different from random simulations of cell placement (red line). **I)** Regularity index (RI) values that were observed for ventral retina (light green) compared with a random simulations (red). RI is a measurement of local pattern regularity, and this measurement for SWS1-2 cones was found to be significantly different from that of random simulations. **J)** Whole mount display of cellular organization for SWS1-2 cones in the dorsal retina only. **K)** NNA results for SWS1-2 cones for dorsal retina (dark green line). Cones from dorsal retina were also found to be organized significantly different from random simulations (red line). **L)** RI values that were observed for dorsal retina (dark green) compared with random simulations of cell placement (red). This organization was found to be significantly different from that of random simulations. Abbreviations: ONL=outer nuclear layer; INL=inner nuclear layer; GCL=ganglion cell layer; OPL=outer plexiform layer; IPL=inner plexiform layer. Scale bars in A, B, and C are equal to 50 μm. Scale bar in E is equal to 50 μm, and continues for G and J.

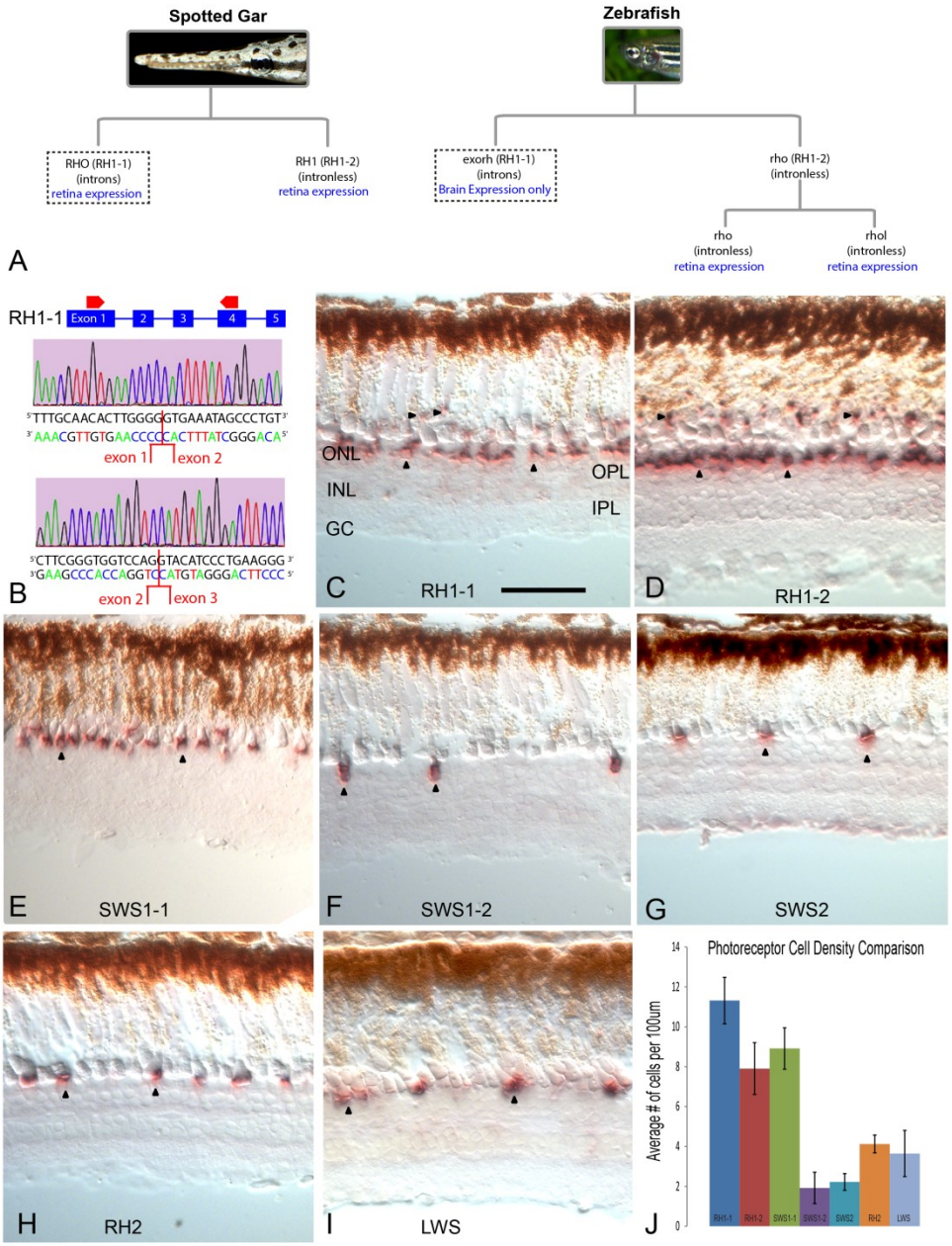

Figure 6.6. **Expression of *exo-rhodopsin* in retinal photoreceptors, as well as other opsin mRNA. A)** Comparison of rod opsins expression in spotted gar retina and zebrafish (teleost) retina. The intron-containing gene, rhodopsin (RH1-1), was found to be expressed in the spotted gar retina, while its orthologue in teleost retina is not expressed in retina tissue. **B)** Representation of RH1-1 gene in spotted gar genome. Forward and reverse primers are noted on exons 1 and 4. Sequencing revealed the splice site junctions for exon 1 and exon 2, as well as exon 2 and exon 3, confirming expression of RH1-1 in the spotted gar retina. *In situ* hybridization assays were conducted for predicted opsin genes in the spotted gar

genome. All seven genes were found to be expressed in the retina. Expression of mRNAs were observed and recorded for **C)** RH1-1 (*exo-rhodopsin*), **D)** RH1-2 (rhodopsin), **E)** SWS1-1 (ultraviolet opsin 1), **F)** SWS1-2 (ultraviolet opsin 2), **G)** SWS2 (blue opsin), **H)** RH2 (green opsin), and **I)** LWS (red opsin). **J)** Comparisons of cellular densities for RH1-1, RH1-2, SWS1-1, SWS1-2, SWS2, RH2, and LWS are shown. Abbreviations: rho= rhodopsin, exorh= *exo-rhodopsin*, ONL=outer nuclear layer; INL=inner nuclear layer; GCL=ganglion cell layer; OPL=outer plexiform layer; IPL=inner plexiform layer. Scale bar in C is equivalent to 50 μm, and is same for D-I.

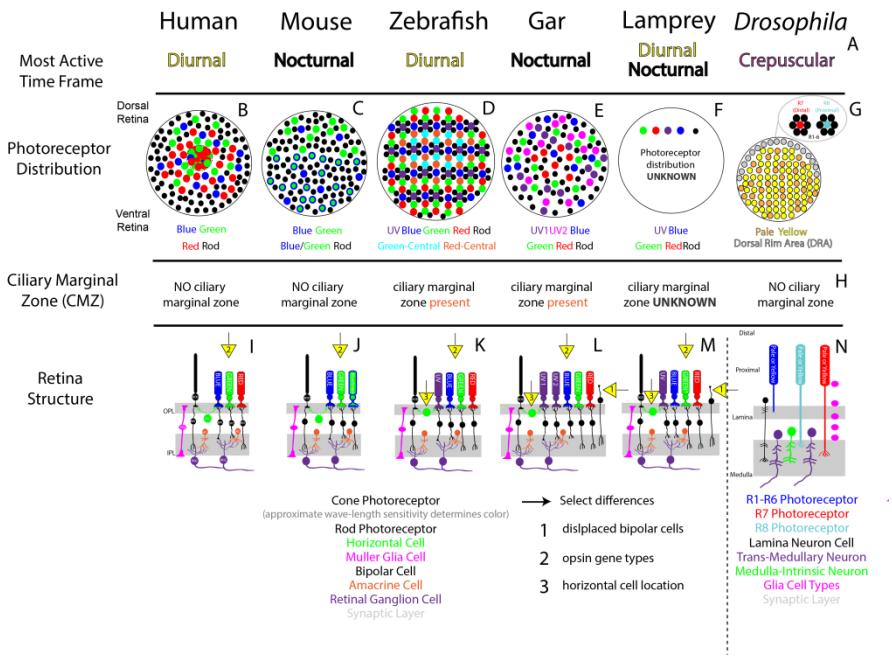

Figure 6.7. Differences and similarities in organization and retinal features were observed across model systems mouse, zebrafish, lamprey, and human. A) The most active time of the day, often used to collect food or avoid being food. The organization of retinal photoreceptor mosaics varies among model organisms. **B)** Humans are among a rare group with an exclusively cone rich region, the fovea. **C)** The mouse retina is rod-dominant with blue, green, and blue-green cones with drastic differences between ventral and dorsal regions. **D)** A crystalline structure of organization shown in zebrafish retina, where photoreceptors organize into a consistent pattern. This is a trait not observed in non-teleost organisms to date (larval remnant not shown) (recreated from Fadool et al., 2003; Takechi & Kawamura, 2005; Allison et al., 2010). **E)** The predicted opsins present in the spotted gar retina, with red-sensitive cones in just the central retina, and a dorsal to ventral gradient for UV-2 cones. **F)** Lamprey photoreceptor mosaic for predicted opsins is unknown. **G)** In *Drosophila*, specialized structures called ommatidia contain eight varying light-sensitive photoreceptor cells, R1-R6, with R7 located distally and R8 proximally. Cells in the dorsal rim area are specialized to detect polarized light, while the rest of the retina produces pale or yellow ommatidia throughout (*Drosophila* mosaic re-created from Wernet & Desplan, 2004; Wernet et al., 2006; Labhart et al., 2009). **H)** The CMZ provides cells for continuous growth of the retina well into adulthood. A CMZ was shown in the spotted gar retina in this study, while previous work showed its presence in zebrafish retina. Humans, mice, and *Drosophila* do not have a CMZ in their retina, and its presence lamprey remains unknown. The basic

structure and organization is conserved for all vertebrates: **I)** human, **J)** mouse, **K)** zebrafish, **L)** spotted gar, and **M**) lamprey (Sanes and Zipursky, 2010). Noted differences are labeled by numbered triangles; 1) photoreceptor types and their distribution, 2) displaced bipolar cells in the photoreceptor layer, 3) placement of horizontal cell bodies respective to OPL. **N)** Organization of *Drosophila* visual system also consists of cellular layers and synaptic layers; the retina, lamina and medulla (Kumar, 2001; Chotard & Salecker, 2007; Sanes and Zipursky, 2010). In *Drosophila*, the visual signal is sent from the photoreceptors to lamina neurons and medulla-intrinsic neurons before it is then sent to the vision processing area, the lobula complex, via trans-medullary neurons. *Images in B-G, I-N are not made to scale, but are based on general organization that has been found in previous work as well as this study. Abbreviations: DRA= dorsal rim area, CMZ= ciliary marginal zone; UV= ultraviolet; AC= amacrine cell; BPC= bipolar cell; HC= horizontal cell; RGC= retinal ganglion cell; R= photoreceptor (*Drosophila*); OPL=outer plexiform layer; IPL=inner plexiform layer.

Antigen	Immunogen	Manufacturer and Details	Dilution Used
bNOS	Synthetic peptide corresponding to the C-terminal fragment of nNOS of rat brain origin (amino acids 1409-1429 with N-terminal added lysine: EDAGVFISRLRDDNRYHEDIF)	Sigma; St. Louis, MO, USA. Catalog Number: N7280. Rabbit Polyclonal.	1:1000
Tyrosine Hydroxylase	Denatured tyrosine hydroxylase from rat pheochromocytoma (denatured by sodium dodecyl sulfate).	Millipore, Billerica, MA, USA. Catalog Number: AB152. Rabbit Polyclonal.	1:1000
Brn3a	Amino acids 1-109 of Brn-3a of mouse origin	Santa Cruz Biotechnology, Santa Cruz, CA, USA. Catalog Number: SC-8429. Mouse Monoclonal IgG1.	1:200
NK3R	Synthetic peptide at the c-terminus of rat NK-3 (SFISSPYTSVDEYS)	Novus Biologicals, Littleton CO, USA. Catalog Number: 300-102. Rabbit Polyclonal.	1:1000
Recoverin	Recombinant human recoverin	Millipore, Billerica, MA, USA. Catalog Number: AB5585. Rabbit Polyclonal.	1:1000
HCN4	Amino acids 119-155 of human HCN4 (HGHLHDSAEERRLIAEGDASP GEDRTPPGLAAEPERP)	Alomone, Jerusalem, Israel. Catalog Number: APC-052. Rabbit Polyclonal.	1:500
PKAR II beta	Amino acids 1-418 (full length) of human protein kinase A, regulatory subunit IIβ	BD Biosciences, Franklin Lakes, NJ, USA. Catalog Number: P54720. Mouse Monoclonal IgG1.	1:1000
Goα	Purified Goα from bovine brain	Millipore, Billerica, MA, USA. Catalog Number: MAB3073. Mouse Monoclonal IgG1.	1:1000
PKC α	An epitope mapping between amino acids 645-672 at the C-terminus of PKCα of human origin (IANIDQSDFEGFSYVNPQFVH	Santa Cruz Biotechnology, Santa Cruz CA, USA. Catalog Number: SC-8393. Mouse Monoclonal IgG1.	1:1000

	PILQSAV)		
Cone arrestin	Synthetic peptide: EEFMQHNSQTQS	Millipore, Billerica, MA, USA. Catalog Number: AB15282. Rabbit Polyclonal.	1:1000
Calbindin	Purified rat calbindin D-28	Swant, Bellinzona, Switzerland. Catalog Number: CB-38a. Rabbit Polyclonal.	1:500
Bassoon	Fusion protein amino acids 738-1075 of ground squirrel bassoon	Custom made courtesy of Wei Li (Covance) Rabbit Polyclonal.	1:100
PSD-95	Fusion protein amino acids 77-299 (PDZ domains 1 and 2) of human PSD-95	UC Davis NeuroMab Facility, Davis, CA, USA. Catalog Number: 75-028.	1:500
ChAT	Human placental choline acetyltransferase	Millipore, Billerica, MA, USA. Catalog Number: AB144P. Goat Polyclonal.	1:500
Disabled (Dab1)	GST-mouse Dab1 fusion protein corresponding to residues 107–243	Generous Gift of Brian Howell. Rabbit Polyclonal.	1:500
Chx10	a peptide encompassing the amino acids 44–61 of human CHX10 (PPSSHPRAALDGLAPGHL)	Santa Cruz Biotechnology, Santa Cruz, CA, USA. Catalog Number: sc-21690. Goat Polyclonal.	1:100
SWS1 Zebrafish (UV opsin)	Ultraviolet opsin amino terminal peptides were expressed as bacterial fusion proteins to generate polyclonal antisera. Initial probe generated from goldfish cDNA. (Hyde & Vihtelic, 1998)	Generous Gift of David Hyde. Rabbit Polyclonal.	1:1000
LWS Zebrafish (red opsin)	Probe produced from zebrafish cDNA to match opsin protein sequence, corresponding to residues 103-271. Expressed as bacterial fusion proteins to generate polyclonal antisera. (Hyde & Vihtelic, 1998)	Generous Gift of David Hyde. Rabbit Polyclonal.	1:500
SWS2 Zebrafish (blue opsin)	Blue opsin amino terminal peptides were expressed as	Generous gift of David Hyde. Rabbit	1:250

	bacterial fusion proteins to generate polyclonal antisera. Initial probe generated from goldfish cDNA. (Hyde & Vihtelic, 1998)	Polyclonal.	
Rhodopsin Zebrafish	Probe produced from zebrafish cDNA to match opsin protein sequence, corresponding to residues 95-117. Expressed as bacterial fusion proteins to generate polyclonal antisera. (Hyde & Vihtelic, 1998)	Generous gift of David Hyde. Rabbit Polyclonal.	1:5000
OPN1SW (SWS Mouse; blue opsin)	Raised against a peptide mapping at the N-terminus of the opsin protein encoded by OPN1SW of human origin.	Santa Cruz Biotechnology, Santa Cruz, CA, USA. Catalog Number: SC-14363. Goat polyclonal.	1:1000
***1D1** (Zebrafish Rhodopsin)	Generated from splenocytes isolated from a BALB/c mouse immunized with whole zebrafish retina in Ribi adjuvant (Ribi protein).	Generous gift of Jim Fadool. Mouse monoclonal.	1:250
Brain3b	Epitope mapping at the C-terminus of Brn-3b of human origin.	Santa Cruz Biotechnology, Santa Cruz, CA, USA. Catalog Number: SC-6026 P. Goat polyclonal.	1:100
Cadherin-8	Mouse cadherin-8 human Fc fusion protein.	Developed by Masatoshi Takeichi and Sachihiro C. Suzuki. Obtained from Developmental Studies Hybridoma Bank, University of Iowa, Department of Biology, Iowa City, IA 52242 Mouse monoclonal IgG1.	1:100
Phospho-ß-Catenin	Synthetic phophopeptide corresponding to residues surrounding Ser33, Ser37 and Thr41 of human ß-catenin. Purified by protein A and peptide affinity chromatography.	Cell Signaling Technology. Gene-ED #1499 Rabbit polyclonal	1:500
2H3	Neurofilament from rat brain membranes	Developed by Thomas M. Jessell and Jane Dodd. Obtained from Developmental Studies	1:500

		Hybridoma Bank, University of Iowa, Department of Biology, Iowa City, IA 52242 Mouse monoclonal IgG1.	
CTBP	Amino acids 361-445 of the mouse CtBP2 protein.	BD Transduction Laboratories (San Juan, CA), mouse monoclonal IgG, #612044	1:500
GABA-alpha2	Synthetic peptide (aa 39-67 of mouse GAGA-A receptor γ2 precuros protein) coupled to key-hole limpet hemocyanin via an added C-terminal cysteine residue.	Synaptic Systems catalogue no. 224 003; polyclonal rabbit	1:1000
GFAP (GA5)	Produced by immunizing animals with native glial fibrillary acidic protein (GFAP) purified from pig spinal cord.	Cell Signaling Technology. Gene-ED #2670 Mouse monoclonal	1:500
Glutamate-R1	KLH-conjugated linear peptide corresponding to human Glutamate receptor 1 (GluR1) at the c-terminus	Millipore, Billerica, MA, USA. Catalog Number: AB1504. Rabbit Polyclonal.	1:500
Glutamate-R2	Produced against fusion protein amino acids 834-883 (cytoplasmic C-terminus) of rat GluR2 (accession number P42262)	UC Davis NeuroMab Facility, Davis, CA, USA. Catalog Number: 75-002. Mouse monoclonal (igG_1)	1:500
Glutamine synthetase	Sheep glutamine synthetase (amino acids 1–373)	BD Transduction Laboratories, Franklin Lakes, NJ, USA. Catalog Number: 610517. Mouse Monoclonal IgG2A.	1:1000
Hu	Isolated from a patient with paraneoplastic encephalomyelitis.	Molecular Probes; catalog #21271 Mouse monoclonal 16A11.	1:500
KV 3.1b potassium channel	Produced against fusion protein amino acids 437-585 (cytoplasmic C-terminus) of rat Kv3.1b (accession number NP_036988)	UC Davis NeuroMab Facility, Davis, CA, USA. Catalog Number: 75-041. Mouse monoclonal (igG_1)	1:500
KV 4.2	Produced synthetic peptide amino acids 209-225 (extracellular S1-S2 loop) of rat	UC Davis NeuroMab Facility, Davis, CA, USA.	1:500

	Kv4.2 (CGSSPGHIKELPSGERY; accession number Q63881)	Catalog Number: 75-016. Mouse monoclonal (igG$_1$)	
Melanopsin	15 N-terminal amino acids of mouse Melanopsin.	Generous gift of Ignacio Provencio. Rabbit monoclonal.	1:5000
NR2A	Produced against fusion protein amino acids 75-325 (extracellular N-terminus) of rat NR2A (AKA Glutamate [NMDA] receptor subunit epsilon-1, N-methyl D-aspartate receptor subtype 2A, Grin2a, NMDAR2A, Accession number Q00959)	UC Davis NeuroMab Facility, Davis, CA, USA. Catalog Number: 75-000. Mouse monoclonal (igG2a)	1:500
Parvalbumin	Purified from frog muscle	Millipore, Billerica, MA, USA. Catalog Number: MAB1572. Mouse monoclonal (igG1)	1:500
Pax6	Chick Pax6 gene corresponding to aa 1-223. Recombinant protein made in E. coli.	Developed by Atsushi Kawakami. Obtained from Developmental Studies Hybridoma Bank, University of Iowa, Department of Biology, Iowa City, IA 52242. Mouse monoclonal IgG1	1:500
Proliferating cell nuclear antigen (PCNA)	Synthetic peptide: DMGHLKYYLAPKIEDEEGS, corresponding to C terminal amino acids 243-261 of Human PCNA	Abcam Inc. (ab2426) Rabbit polyclonal	1:200
Phospho-Histone H3 (PH3)	Produced by immunizing animals with a synthetic phosphopeptide corresponding to residues surrounding Ser10 of human histone H3. Purified by protein A and peptide affinity chromatography.	Cell Signaling Technology. Gene-ED #8352. Rabbit polyclonal	1:500
***PNA**	Lection PNA is isolated from peanuts. It is a 110 kDa tetramer that is specific for terminal B-galactose.	Molecular Probes, Inc. Catalog # L21409	1:1000
CASK	GST fusion-protein corresponding to the CASK specific domain residues 318-415 of human CASK/mLin-2 that lies between the calmodulin binding and PZD domains.	UC Davis NeuroMab Facility, Davis, CA, USA. Catalog Number: 75-000. Mouse monoclonal (igG$_1$)	1:500
N-catenin	Chicken alpha N catenin	Developed by	1:500

	isolated from chicken brain.	Masatoshi Takeichi and Sachihiro C. Suzuki. Obtained from Developmental Studies Hybridoma Bank, University of Iowa, Department of Biology, Iowa City, IA 52242. Rat monoclonal IgG.	
SV2	Purified via synaptic vesicles; ommata electric organ.	Developed by Kathleen Buckley. Obtained from Developmental Studies Hybridoma Bank, University of Iowa, Department of Biology, Iowa City, IA 52242. Mouse monoclonal	1:250
*Zpr-1	Zebrafish cone arrestin a, arr3a.	Zebrafish International Resource Center (ZIRC) University of Oregon; Eugene, OR, 5274. Mouse monocolonal (IgG1).	1:200
***Zpr-3**	Unidentified epitope of rod photoreceptors. Produced from mixture of 48hpf zebrafish embryos.	Zebrafish International Resource Center (ZIRC) University of Oregon; Eugene, OR, 5274. Mouse monocolonal (IgG1).	1:200
Islet (39.4D5)	C-terminal portion of rat Islet-1 homeobox.	Developed by Thomas M. Jessell and Susan Brenner-Mortan. Obtained from Developmental Studies Hybridoma Bank, University of Iowa, Department of Biology, Iowa City, IA 52242. Mouse monoclonal	1:500
***ZRF1**	Antibody designed to target the glial fibrillary acidic protein (GFAP) in zebrafish.	Zebrafish International Resource Center (ZIRC) University of Oregon; Eugene, OR, 5274. Mouse monocolonal (IgG1).	1:500
SMI-32	SMI-32 reacts with a nonphosphorylated epitope in neurofilament H of most mammalian species.	Biolegend (formerly Covance Antibody Products) Dedham, MA 02026. Product#	1:250

		SMI-32R. Mouse monoclonal.	

Table 6.1 Summary of antibodies used

Gene	Forward (5'-3') SP6	Reverse (5'-3') T7	Size of probe (bp)
RH1-1	ACCTCCATGCACGGCTATTT	GGCCCTCTGGGTAGTTTCTG	450
RH1-2	CTGAAACCCGAGGTAAACAACGA	TATTCATGCAGACGTAGATGAGAGG	351
SWS1-1	GAGCCCTCAGAGCTGTAAGTT	AGCCAGAAACATGAGAGTGCT	336
SWS1-2	TGTTCACAAAAAGCTCCTGCAT	ACAATGAATATACAGATGATGCCCA	300
SWS2	GAGCTCCCGGACGACTTTTA	TGTGAAGCCCTCGATCTTGC	345
RH2	GAAGTCTCCTCCACAGCGTC	CACATGTGGCTGTCAGGCTA	499
LWS	GTCCGAGTCCACCCAGAAAG	TTCAACGCGCAGAGAGGAAT	311
	SP6 (5'-3')	CATACGATTTAGGTGACACTATAG	
	T7 (5'-3')	TAATACGACTCACTATAGGG	

Table 6.2 Primer sequences used for *in situ* hybridization.

Antibody Against	Comments	Figure
Hu	Strongly in cell bodies of presumed AC and RGC populations in INL and GCL.	2 A
Islet	Labels various RGC, AC, and BPC cell bodies in the RGCL, INL, and ONL.	2 B
TH	Cell bodies of presumed ACs within the INL and S1 layer of the IPL	2 I
ChAT	Cell bodies and S2 and S4 layers of IPL. Also strong in cell bodies of presumed ACs in INL and GCL. Faint labeling of cone inner segments.	2 J
bNOS	Cell bodies of presumed ACs in the INL and various sublaminae of IPL	2 H
Calbindin	Strong labeling of cell bodies and neurite projections of cells from ONL and INL of varying morphologies. Also strong labeling within the IPL.	3 A-E
DAB	Weak edges of cell bodies and strongly throughout the IPL Strong labeling in the IPL, and faint activity in cell bodies of an ONL population(s).	Not shown
SMI-32	Cell bodies within the OPL of presumed BPCs	2 C
HCN4	Staining of various cells bodies in ONL. Strong labeling of synapses in OPL and IPL.	Not shown 2 E
Goα	Staining strong in cell bodies and/or outer edge of cell bodies. Faint in neurites.	2 G
Parvalbumin	Strong labeling in photoreceptors. Presumed to be mixture of rod outer segments and some cone inner segments.	4 J
*Zpr-3	Strong and specific for cone inner segments	

PNA	Strongly in cell body and edges of outer segments of SWS1-2 cones.	4 K
SWS Mouse	Strongly in outer segments, weakly for cell bodies of SWS1 cones.	4 H, 5 A, E, G, J
SWS1 Zebrafish	Strongly at cone inner segments, Nothing seen in individual cell bodies.	4 E-F
SWS2 Zebrafish	Strongly in outer segments, weakly in rod cell bodies.	4 G
RH1 Zebrafish	Strongly in all photoreceptor cell bodies and outer segments, strong labeling of type 2 bipolar cells in ONL.	4 B-C
Recoverin	Strong labeling of rod outer segments.	4 A, 2 F
*1D1 (rhodopsin)	Strongly in cell bodies and entire length of spanning segments for presumed Muller glia.	4 D
GFAP (glial fibrillary acidic protein)	Strongly in the anterior regions of spanning segments for presumed Muller glia.	2 L
*Zrf-1 (GFAP protein)	Cone pedicle region; OPL	2 K
CTBP	Cone pedicle region; OPL	Not shown
Cask	Cone synapse region; OPL	4 I
KV4.2	Labeled cells in the ONL and their neurite projections extending towards the outer retina. Strong labeling throughout the IPL. Labels various RGC, AC, and BPC cell bodies in the RGCL, INL, and ONL.	Not shown
Cadherin 8		Not shown
SV2		2 D
Proliferating cell nuclear antigen (PCNA)	Cell bodies throughout retina in INL and cell bodies throughout nuclear layers at far periphery of the retina; CMZ region.	1 E

Phospho-Histone H3 (ph3)	Cell bodies throughout retina in INL and cell bodies in the photoreceptor layer at far periphery of the retina; CMZ region.	1 F-G

Table 6.3. Report of effective antibody labeling in spotted gar retina.

*Not an antigen; commercial name of product used. (Antigen name in parentheses if applicable)

Conclusion

The work in this dissertation sought to approach neural development using multiple model organisms. First, we begin by reviewing the form and function of BCs in popular model organisms: mouse, teleost fish, and primate retinas. We intend this as resource for researchers and clinicians to better understand how signal is relayed from photoreceptors to ganglion cells in the retina. In the mouse retina, we determined a novel role of DSCAM in IPL lamination and neurite refinement. We propose a potential compensatory mechanism in which cone photoreceptors ensure the conservation of the size of their projective field through changes in their connectivity with efferent BCs. Furthermore, loss of Bax-mediated PCD strengthens this effect through increases in cellular densities and subsequent changes to BC dendritic fields. We propose an emerging model system, the spotted gar, as a means for studying the effects of genome duplication on neural development.

DSCAM is has previously been shown to play roles in neuron spacing, neurite avoidance, and programmed cell death (PCD). In this work, we provide a model for the role of DSCAM in neurite refinement through restriction of the striatum in which neurites laminate. It achieves order through repulsion, and is critical for proper formation of the IPL. Due to the role of DSCAM in apoptosis, we also sought to understand the mechanism for which DSCAM signals through. A major protein in the cell death pathway is BAX, which triggers cell death via caspase activation. PCD is a necessary aspect of neural development as it plays a role in cellular spacing, causing select cells to undergo apoptosis and therefore contributing to the cell mosaic pattern that is observed in wild type retinas. This development of cellular spacing and organization is of particular interest for the retina as it is the area of the brain responsible for interpreting visual stimulation. We found that in dopaminergic amacrine cells, BAX KO also results in similar lamination errors compared to our observation in DSCAM deficient retinas. However, this phenocopy was not fully corroborated in the OPL with type 4 OFF BCs. Rather, we observed that the loss of BAX-mediated PCD resulted in changes to the cone terminals and the wiring of BCs through the increased number of multiply-innervated cones. We propose the possibility of this as a compensatory mechanism to conserve cone field projection, but further analyses that include physiological assays would be required to confirm that hypothesis.

This work also sought to understand the potential roles of large scale genetic rearrangements on the evolution of the CNS. We have proposed the spotted gar as a

possible model for this type of research as it contains a single genome, and diverged in lineage prior to the TGD. It is has a genome organization that is similar to mammals, as it contains a single genome but has spent the last 300 million years in an environment more similar to teleost fish. The characterization of the spotted gar retina provides researchers with a baseline for comparison to the more complex organization that has been observed in the teleost fish lineage. It provides a potential system for determining whether certain genes have been preferentially retained following TGD. We have also provided potential target genes for this research. The zebrafish contains *Dscama* and *Dscamb*, and both are actively expressed during neural development. They are expressed in overlapping and separate cellular populations. We cloned the coding sequences for both of these genes into vectors, and verified their full expression in vivo. This sets the state for future work involving their functions during neural development, and whether or not they have been subfunctionalized or possibly neofunctionalized over the course of evolution.

Neurological disorders continue to be major challenges in modern medicine and in order to address these issues, it will be important to have a solid understanding of how the CNS is organized and how the organization evolved. These projects that I have been a part of during my doctoral training have allowed me to gain experience skills and develop a strong knowledge base in multiple areas of research. I believe that the future of science relies in the ability of researchers to encompass multiple disciplines and collaborate with researchers with varying backgrounds. The presentation of this work is done with the intention of providing examples of the importance for collaborative research across both fields and model systems.

Appendix A

The Journal of Neuroscience does not require permission to reuse a published article for non-commercial use, such as in this dissertation.

Appendix B

JOHN WILEY AND SONS LICENSE TERMS AND CONDITIONS

Apr 19, 2017

This Agreement between Joshua Sukeena ("You") and John Wiley and Sons ("John Wiley and Sons") consists of your license details and the terms and conditions provided by John Wiley and Sons and Copyright Clearance Center.

License Number	4092750764299
License date	
Licensed Content Publisher	John Wiley and Sons
Licensed Content Publication	Journal of Experimental Zoology Part A: Ecological Genetics and Physiology
Licensed Content Title	Characterization and Evolution of the Spotted Gar Retina
Licensed Content Author	Joshua M. Sukeena,Carlos A. Galicia,Jacob D. Wilson,Tim McGinn,Janette W. Boughman,Barrie D. Robison,John H. Postlethwait,Ingo Braasch,Deborah L. Stenkamp,Peter G. Fuerst
Licensed Content Date	Nov 9, 2016
Licensed Content Pages	19
Type of use	Dissertation/Thesis
Requestor type	Author of this Wiley article
Format	Print and electronic
Portion	Full article
Will you be translating?	No
Title of your thesis / dissertation	Cellular Summer Camp: How Young Neurons Learn to Communicate and Interact With Their Environments
Expected completion date	May 2017
Expected size (number of pages)	200
Requestor Location	Joshua Sukeena 719 S. Deakin St. MOSCOW, ID 83843 United States Attn: Joshua Sukeena

Publisher Tax ID	EU826007151
Billing Type	Invoice
Billing Address	Joshua Sukeena 719 S. Deakin St. MOSCOW, ID 83843 United States Attn: Joshua Sukeena
Total	0.00 USD

Terms and Conditions

TERMS AND CONDITIONS

This copyrighted material is owned by or exclusively licensed to John Wiley & Sons, Inc. or one of its group companies (each a"Wiley Company") or handled on behalf of a society with which a Wiley Company has exclusive publishing rights in relation to a particular work (collectively "WILEY"). By clicking "accept" in connection with completing this licensing transaction, you agree that the following terms and conditions apply to this transaction (along with the billing and payment terms and conditions established by the Copyright Clearance Center Inc., ("CCC's Billing and Payment terms and conditions"), at the time that you opened your RightsLink account (these are available at any time at http://myaccount.copyright.com).

Terms and Conditions

- The materials you have requested permission to reproduce or reuse (the "Wiley Materials") are protected by copyright.
- You are hereby granted a personal, non-exclusive, non-sub licensable (on a stand-alone basis), non-transferable, worldwide, limited license to reproduce the Wiley Materials for the purpose specified in the licensing process. This license, **and any CONTENT (PDF or image file) purchased as part of your order,** is for a one-time use only and limited to any maximum distribution number specified in the license. The first instance of republication or reuse granted by this license must be completed within two years of the date of the grant of this license (although copies prepared before the end date may be distributed thereafter). The Wiley Materials shall not be used in any other manner or for any other purpose, beyond what is granted in the license. Permission is granted subject to an appropriate acknowledgement given to the author, title of the material/book/journal and the publisher. You shall also duplicate the copyright notice that appears in the Wiley publication in your use of the Wiley Material. Permission is also granted on the understanding that nowhere in the text is a previously published source acknowledged for all or part of this Wiley Material. Any third party content is expressly excluded from this permission.
- With respect to the Wiley Materials, all rights are reserved. Except as expressly granted by the terms of the license, no part of the Wiley Materials may be copied, modified, adapted (except for minor reformatting required by the new Publication), translated,

reproduced, transferred or distributed, in any form or by any means, and no derivative works may be made based on the Wiley Materials without the prior permission of the respective copyright owner.**For STM Signatory Publishers clearing permission under the terms of the STM Permissions Guidelines only, the terms of the license are extended to include subsequent editions and for editions in other languages, provided such editions are for the work as a whole in situ and does not involve the separate exploitation of the permitted figures or extracts,** You may not alter, remove or suppress in any manner any copyright, trademark or other notices displayed by the Wiley Materials. You may not license, rent, sell, loan, lease, pledge, offer as security, transfer or assign the Wiley Materials on a stand-alone basis, or any of the rights granted to you hereunder to any other person.

- The Wiley Materials and all of the intellectual property rights therein shall at all times remain the exclusive property of John Wiley & Sons Inc, the Wiley Companies, or their respective licensors, and your interest therein is only that of having possession of and the right to reproduce the Wiley Materials pursuant to Section 2 herein during the continuance of this Agreement. You agree that you own no right, title or interest in or to the Wiley Materials or any of the intellectual property rights therein. You shall have no rights hereunder other than the license as provided for above in Section 2. No right, license or interest to any trademark, trade name, service mark or other branding ("Marks") of WILEY or its licensors is granted hereunder, and you agree that you shall not assert any such right, license or interest with respect thereto

- NEITHER WILEY NOR ITS LICENSORS MAKES ANY WARRANTY OR REPRESENTATION OF ANY KIND TO YOU OR ANY THIRD PARTY, EXPRESS, IMPLIED OR STATUTORY, WITH RESPECT TO THE MATERIALS OR THE ACCURACY OF ANY INFORMATION CONTAINED IN THE MATERIALS, INCLUDING, WITHOUT LIMITATION, ANY IMPLIED WARRANTY OF MERCHANTABILITY, ACCURACY, SATISFACTORY QUALITY, FITNESS FOR A PARTICULAR PURPOSE, USABILITY, INTEGRATION OR NON-INFRINGEMENT AND ALL SUCH WARRANTIES ARE HEREBY EXCLUDED BY WILEY AND ITS LICENSORS AND WAIVED BY YOU.

- WILEY shall have the right to terminate this Agreement immediately upon breach of this Agreement by you.

- You shall indemnify, defend and hold harmless WILEY, its Licensors and their respective directors, officers, agents and employees, from and against any actual or threatened claims, demands, causes of action or proceedings arising from any breach of this Agreement by you.

- IN NO EVENT SHALL WILEY OR ITS LICENSORS BE LIABLE TO YOU OR ANY OTHER PARTY OR ANY OTHER PERSON OR ENTITY FOR ANY SPECIAL, CONSEQUENTIAL, INCIDENTAL, INDIRECT, EXEMPLARY OR PUNITIVE DAMAGES, HOWEVER CAUSED, ARISING OUT OF OR IN CONNECTION WITH THE DOWNLOADING, PROVISIONING, VIEWING OR USE OF THE MATERIALS REGARDLESS OF THE FORM OF ACTION, WHETHER FOR BREACH OF CONTRACT, BREACH OF WARRANTY, TORT, NEGLIGENCE, INFRINGEMENT OR OTHERWISE (INCLUDING, WITHOUT LIMITATION, DAMAGES BASED ON LOSS OF PROFITS, DATA, FILES, USE, BUSINESS OPPORTUNITY OR CLAIMS OF THIRD PARTIES),

AND WHETHER OR NOT THE PARTY HAS BEEN ADVISED OF THE POSSIBILITY OF SUCH DAMAGES. THIS LIMITATION SHALL APPLY NOTWITHSTANDING ANY FAILURE OF ESSENTIAL PURPOSE OF ANY LIMITED REMEDY PROVIDED HEREIN.

- Should any provision of this Agreement be held by a court of competent jurisdiction to be illegal, invalid, or unenforceable, that provision shall be deemed amended to achieve as nearly as possible the same economic effect as the original provision, and the legality, validity and enforceability of the remaining provisions of this Agreement shall not be affected or impaired thereby.

- The failure of either party to enforce any term or condition of this Agreement shall not constitute a waiver of either party's right to enforce each and every term and condition of this Agreement. No breach under this agreement shall be deemed waived or excused by either party unless such waiver or consent is in writing signed by the party granting such waiver or consent. The waiver by or consent of a party to a breach of any provision of this Agreement shall not operate or be construed as a waiver of or consent to any other or subsequent breach by such other party.

- This Agreement may not be assigned (including by operation of law or otherwise) by you without WILEY's prior written consent.

- Any fee required for this permission shall be non-refundable after thirty (30) days from receipt by the CCC.

- These terms and conditions together with CCC's Billing and Payment terms and conditions (which are incorporated herein) form the entire agreement between you and WILEY concerning this licensing transaction and (in the absence of fraud) supersedes all prior agreements and representations of the parties, oral or written. This Agreement may not be amended except in writing signed by both parties. This Agreement shall be binding upon and inure to the benefit of the parties' successors, legal representatives, and authorized assigns.

- In the event of any conflict between your obligations established by these terms and conditions and those established by CCC's Billing and Payment terms and conditions, these terms and conditions shall prevail.

- WILEY expressly reserves all rights not specifically granted in the combination of (i) the license details provided by you and accepted in the course of this licensing transaction, (ii) these terms and conditions and (iii) CCC's Billing and Payment terms and conditions.

- This Agreement will be void if the Type of Use, Format, Circulation, or Requestor Type was misrepresented during the licensing process.

- This Agreement shall be governed by and construed in accordance with the laws of the State of New York, USA, without regards to such state's conflict of law rules. Any legal action, suit or proceeding arising out of or relating to these Terms and Conditions or the breach thereof shall be instituted in a court of competent jurisdiction in New York County in the State of New York in the United States of America and each party hereby

consents and submits to the personal jurisdiction of such court, waives any objection to venue in such court and consents to service of process by registered or certified mail, return receipt requested, at the last known address of such party.